

University of Alberta
Department of Civil &
Environmental Engineering



Structural Engineering Report No. 231

Field Assessment of Crowchild Trail Bridge

by
Kong K. Taing
J.J.R. Cheng
and
S. Afhami

January, 2000

ABSTRACT

The Crowchild Trail Bridge in Calgary, Alberta is a three-span, two-lane, one-way traffic overpass. In 1997, its superstructure was replaced by a steel-free concrete deck supported by five steel plate girders. In order to assess the performance of the bridge, the University of Alberta developed an extensive instrumentation and monitoring program at the time of construction. Initial load tests were carried out in August 1997, before the bridge was open to traffic, to establish the baseline structural characteristics of the bridge. The bridge was tested again in August 1998, one year after opening to traffic. The testing programs include ambient vibration test, static and dynamic load tests using trucks with known axle loads and running at various speeds. In addition to the strain gauges, thermistors, and fibre optic strain gauges installed in the first year, cable transducers and accelerometers were added in the second year tests.

Natural frequencies and mode shapes of the bridge were determined by the ambient vibration tests performed in 1997 and 1998. The investigated frequencies and mode shapes show good correlation with theoretical closed form solutions. However, all the investigated frequencies have shown a reduction of approximately 0.20 Hz after the bridge has been in service for one year. The static and dynamic tests show that the composite action in the positive moment region has not changed during the first year of operation, but there is a shift of 98 mm in the neutral axis in the negative moment region due to the cracking of the concrete deck. Since the mass of the structure has not changed, this may indicate that the stiffness of the bridge has been reduced. Good load sharing between the girders was observed in both positive and negative moment regions. The

damping ratio and dynamic amplification factor was obtained from both the strain gauge and deflection data. The local strain gauge data yielded higher dynamic amplification factors than the ones from the overall deflection results. Both transverse and longitudinal cracks were observed on the bottom surface of the bridge deck. As of August 1998, cracks visible on the deck show no serviceability concern.

TABLE OF CONTENTS

	Page
1. INTRODUCTION	1
1.1 Background and Statement of the Problems	1
1.2 Innovative Structures	2
1.3 Scope and Objectives	4
1.4 Thesis Layout	5
2. LITERATURE REVIEW	7
2.1 Steel-Free Deck in the Positive Moment Region	7
2.1.1 Half-Scale Model	8
2.1.2 Full-Scale Model	9
2.1.3 Salmon River Bridge Project	12
2.1.4 Kent County Road	13
2.2 Steel-Free Deck in the Negative Moment Region	14
2.2.1 Full-Scale Model	15
2.3 Serviceability Issues	16
3. CONSTRUCTION AND INSTRUMENTATION OF THE CROWCHILD TRAIL BRIDGE	18
3.1 Background	18
3.2 Description of Crowchild Trail Bridge	20
3.2.1 General	20
3.2.2 Concrete Bridge Deck	23
3.2.3 Steel Plate Girders	25
3.3 Instrumentation	28
3.3.1 Location of Gauges	28
3.4 Field Testing	43
3.4.1 Tests Performed on Crowchild Trail Bridge	43

4. EXPERIMENTAL RESULTS	45
4.1 Results of the August 1997 Test	45
4.1.1 Ambient Vibration Results from UBC	45
4.1.2 Static Test Results	47
4.1.2.1 Survey Results	51
4.1.2.2 Results from Strain Measurements	53
4.1.3 Crack Pattern for August 1997	56
4.2 Results of the August 1998 Test	60
4.2.1 Ambient Vibration Tests	60
4.2.1.1 Objective and Problems	61
4.2.1.2 Field Testing	61
4.2.1.3 Data Reduction	64
4.2.1.4 Frequencies and Mode shapes	70
4.2.2 Static Test Results	75
4.2.2.1 Cable Transducers Results	78
4.2.2.2 Results from Strain Measurements	80
4.2.2.3 Influence Line	84
4.2.3 Dynamic Tests	86
4.2.3.1 Data Reduction	88
4.2.3.2 Damping Coefficient	95
4.2.3.3 Dynamic Amplification Factor	97
4.2.3.3.1 Dynamic Amplification Factor:	
Local Strain Component	97
4.2.3.3.2 Dynamic Amplification Factor:	
Overall Deflection Component	101
4.2.3.4 Load Sharing	104
4.2.4 Crack Pattern for August 1998	107

5. ANALYSIS AND COMPARISON	111
5.1 Dynamic Behaviour of Crowchild Trail Bridge	111
5.1.1 Theoretical Background	111
5.1.2 Natural Frequencies and Mode Shapes of the Crowchild Trail Bridge	116
5.1.3 Damping of the Crowchild Trail Bridge	119
5.2 Static Behaviour of Crowchild Trail Bridge	120
5.2.1 Shear Transfer in the Transverse Direction	120
5.2.2 Rigidity of the Deck and Load Sharing Among Girders	122
5.2.3 Composite Action in the Longitudinal Direction	124
5.2.4 Change in the Stiffness of the Bridge	125
6. SUMMARY AND CONCLUSIONS	128
6.1 Summary	128
6.2 Conclusions	131
6.3 Recommendations for Future Research	132
REFERENCES	135
APPENDIX A	137
APPENDIX B	144

LIST OF TABLES

	Page
Table 2.1: Concrete Strength	10
Table 3.1: Girder Type and Section Dimensions	25
Table 3.2: Crowchild Trail Bridge Concrete Mix Characteristics/Specifications	26
Table 3.3: Instrumentation	30
Table 3.4: Tests Performed on Crowchild Bridge	44
Table 4.1: Natural Frequencies Between 0 - 20 Hz.	47
Table 4.2: Static Tests – Surveyed Deflections from August 1997 Test	50
Table 4.3: Filenames and Accelerometer Locations	63
Table 4.4: Vertical and Torsional Modes	72
Table 4.5: Filenames, Test Speed and Stage Number	87
Table 4.6: Dynamic Amplification Factor: Local Strain Effects for [Set 1]	101
Table 4.7: Dynamic Amplification Factor: Overall Deflection	103
Table 5.1: Frequency of Single Span and Simply Supported	115
Table 5.2: Frequency of Three Continuous Span and Simply Supported	116
Table 5.3: Crowchild Trail Bridge Concrete Mix Properties	117
Table 5.4: Comparison of Natural Frequencies Results	119
Table 5.5: Section properties of the girders	127
Table B1: Static Test- August '97, Strain Gauge Reading – by Multiplexer	145
Table B2: Strain Gauge Reading for Static Test, August '97 Before and After Asphalt	149
Table B3: Static Test, August '97, Survey Reading – Raw Data	152
Table B4: Static Test, August '97, Reduce Survey Data	153

LIST OF FIGURES

	Page
Figure 1.1: Basic Concept of Arching Action	1
Figure 1.2: Arching Concepts with External Steel Reinforcement	3
Figure 2.1: Typical Cross Section of the Superstructure.	10
Figure 2.2: Plan View: Location of Load Tests (Newhook <i>et al.</i> , 1996)	11
Figure 3.1 Crowchild Trail Bridge: West Elevation	20
Figure 3.2: Crowchild Trail Bridge--Cross Section	22
Figure 3.3: Plan View of Girders and Tension Straps	26
Figure 3.4(a): Instrumentation Used in the Crowchild Bridge--the North Span	32
Figure 3.4(b): Instrumentation Used in the Crowchild Bridge--Region "A"	32
Figure 3.4(c): Instrumentation Used in the Crowchild Bridge--Region "B"	33
Figure 3.4(d): Instrumentation Used in the Crowchild Bridge--Detail "A"	36
Figure 3.4(e): Instrumentation Used in the Crowchild Bridge--Detail "B"	34
Figure 3.4(f): Instrumentation Used in the Crowchild Bridge--Detail "C"	34
Figure 3.5: Instrumentation on Cross Frame	35
Figure 3.6: Embedded Concrete Strain Gauges	38
Figure 3.7: Embedded Thermistors	40
Figure 3.8: Gauges on Steel Straps	40
Figure 3.9: Gauges on Shear Studs	41
Figure 3.10: Strain Gauges on Girders	42
Figure 3.11: Gauges on NEFMAC and Stainless Steel Bar	42
Figure 4.1: Trucks Use in August 97 Test	48
Figure 4.2: Load Points and Survey Points [August 1997]	49
Figure 4.3: Deflection at C1 to C5 for Load Case P5	51
Figure 4.4: Deflection at C1 to C5 for Load Case P1	52
Figure 4.5: Deflection at C1 to C5 for Load Case P9	53
Figure 4.6: Positive Moment Region Strain--Distribution in Girder #1	54
Figure 4.7: Negative Moment Region--Strain Distribution in Girder #1	55

Figure 4.8:	Strain in Positive and Negative Regions for August 1997	56
Figure 4.9:	South Span Crack Pattern [August 1997]	57
Figure 4.10:	Middle Span Crack Pattern [August 1997]	58
Figure 4.11:	North Span Crack Pattern [August 1997]	59
Figure 4.12:	Ambient Vibration Test Layout [August 1998]	65
Figure 4.13	Accelerometer #10-- Raw Data	66
Figure 4.14	Power Spectrum for Accelerometer #10	67
Figure 4.15:	Power Spectrum for Accelerometer # 11	68
Figure 4.16:	Phase Analysis for 2.60 Hz	69
Figure 4.17:	Distinguish between Vertical [4.43 Hz] / Torsional [5.00 Hz] Mode Shapes	70
Figure 4.18:	Power Spectrum for the Sum of All Accelerometers from Eight Files	71
Figure 4.19(a):	Frequencies and Mode Shapes--1 st Fundamental Vertical and Torsional Mode Shapes	73
Figure 4.19(b):	Frequencies and Mode Shapes--2 nd Vertical and Torsional Mode Shapes	73
Figure 4.19(c):	Frequencies and Mode Shapes--3 rd Vertical and Torsional Mode Shapes	74
Figure 4.19(d):	Frequencies and Mode Shapes--4 th Vertical and Torsional Mode Shapes	74
Figure 4.20:	Truck Used in August 1998 Tests	75
Figure 4.21:	Static and Dynamic Tests, Load Points Layout for August 1998	77
Figure 4.22:	North Span Loading Configuration and Strap Numbering	78
Figure 4.23:	Cable Transducers at Strap #13	78
Figure 4.24:	Influence Lines from Cable Transducers at Strap #13	80
Figure 4.25:	The Three Girder Type Used and Strain Gauges Layout	81
Figure 4.26:	Strain Distribution for Aug. '97 and Aug. '98 in Positive Moment Region	82
Figure 4.27:	Strain Distribution for Aug. '97 and Aug. '98 in Negative Region	83
Figure 4.28:	Strain Distribution for Positive and Negative Regions in	

	August 1998	84
Figure 4.29:	Influence Line for Strain Gauge G3	85
Figure 4.30:	3D Influence Surface for Cable Transducer at Strap #13	86
Figure 4.31:	Raw Data for Strain Gauges G3 in 55 km/hr test on August 1998	88
Figure 4.32:	Low Pass Filtered Data of 10 Hz for Gauge G3 [<i>Before correcting for drift</i>]	89
Figure 4.33:	Final Filtered Response for Strain Gauge G3 [<i>After corrected for drifts</i>]	90
Figure 4.34	Final Filtered Response for Strain Gauge ST	91
Figure 4.35:	Filtered Data with Low Pass of 0.8 Hz and Band Pass of [0.8-10] Hz	93
Figure 4.36:	Cable Transducer Raw/Filtered Data [<i>Before Corrected for Shift</i>]	94
Figure 4.37:	Cable Transducer Raw/Filtered Data [<i>After Corrected for Shift</i>]	94
Figure 4.38:	Superimposed of Cable Transducer and Accelerometer Data	96
Figure 4.39:	Accelerometer and Cable Transducer--Damping Curve	96
Figure 4.40(a)	Decouple Response in Strain Gauges G3 for 55 km/hr Test	98
Figure 4.40(b)	Decouple Response in Strain Gauges G3 for 40 km/hr Test	98
Figure 4.40(c)	Decouple Response in Strain Gauges G3 for 30 km/hr Test	99
Figure 4.40(d)	Decouple Response in Strain Gauges G3 for 15 km/hr Test	99
Figure 4.41:	Dynamic Amplification Factor – Local Effect	100
Figure 4.42:	Cable Transducer #1 for 55 km/hr Test	102
Figure 4.43:	Dynamic Amplification Factor – Overall Deflection Effect	104
Figure 4.44:	Overall Deflection Among Girders	105
Figure 4.45(a):	3D Influence Surface – Static Test Results	106
Figure 4.45(b):	3D Influence Surface – Dynamic Test Results	106
Figure 4.46:	South Span Crack Pattern [August 1998]	108
Figure 4.47:	Middle Span Crack Pattern [August 1998]	109
Figure 4.48:	North Span Crack Pattern [August 1998]	110
Figure 5.1:	Idealized Components	111
Figure 5.2:	Simply Supported Beam	115
Figure 5.3:	Three Continuous Span	116

Figure 5.4:	Simplified Model of Bridge Deck	118
Figure 5.5:	Damping Curve	119
Figure 5.6:	Effects of Damping	120
Figure 5.7:	Shear Transfer in the Concrete Deck	121
Figure 5.8:	Load Sharing among Girders Based on the Deflection Measurements	123
Figure 5.9:	Location of the Neutral Axis in the Positive Moment Region	124
Figure 5.10:	Location of the Neutral Axis in the Negative Moment Region	125
Figure 6.1:	Recommended Accelerometer Location for Future Testing	134
Figure A1:	Cross Sectional View of the Crowchild Bridge	138
Figure A2:	West Elevation View of the Crowchild Bridge	139
Figure A3:	Plan View Layout of the Girders and Straps	140
Figure A4:	Overall Instrumentation Layout	141
Figure A5:	Bridge Deck Barrier	142
Figure A6:	Layout of Gauges that are Embedded in Concrete	143
Figure B1:	Static Load Test, August '98 for Cable Transducers at Strap #21	154
Figure B2:	Static Load Test, August '98 for Cable Transducer at Strap #13	154
Figure B3:	Static Load Test, August '98 for Two Cable Transducers for Girder 5 in the Positive and Negative Moment Region	155
Figure B4:	Static Load Test, August '98 from Cable Transducers at Strap #13—3D Plot	155
Figure B5:	Static Load Test, August '98 from Cable Transducers at Strap #21—3D Plot	156
Figure B6:	Static Load Test, August '98 from Cable Transducers at Strap #13	156
Figure B7:	Static Load Test, August '98 from Strain Gauge at Positive Moment Region	157
Figure B8:	Static Load Test, August '98 for Girder 2 in the Positive Moment Region	157
Figure B9:	Static Load Test, August '98 for Girder 3 in the Positive Moment Region	158
Figure B10:	Static Load Test, August '98 for Girder 5 in	

	the Positive Moment Region	158
Figure B11:	Static Load Test, August '98 for Girder 4 in the Positive Moment Region	159
Figure B12:	Static Load Test, August '98 for all Bottom Gauges in the Positive Moment Region	159
Figure B13:	Static Load Test, August '98 for Girder 1 in Negative Moment Region	160
Figure B14:	Static Load Test, August '98 for Girder 2 in Negative Moment Region	160
Figure B15:	Static Load Test, August '98 for all Bottom Gauges in Positive Moment Region	161
Figure B16:	Static Load Test, August '98 for Top Gauges in Negative Moment Region	161
Figure B17:	Static Load Test, August '98 for T4 & ST Gauges	162
Figure B18:	Static Load Test, August '98 for All Cable Transducers at Strap #21	162
Figure B19:	Static Load Test, August '98 for Cable Transducers at Strap #13	163
Figure B20:	Static Load Test, August '98 for Cable Transducers on Girder 5	163
Figure B21:	Static Load Test, August '98 for Strap #8 in the Positive Moment Region	164
Figure B22:	Static Load Test, August '98 for Straps #9, 10, 11 in Positive Moment	164
Figure B23:	Static Load Test, August '98 for Straps in Positive Moment Region	165
Figure B24:	Static Load Test, August '98 for Straps in Positive Moment Region	165
Figure B25:	Static Load Test, August '98 for Strap #8 in the Positive Moment Region	166
Figure B26:	Static Load Test, August '98 for Strap #23 in Positive Moment Region	166
Figure B27:	Static Load Test, August '98 for T4 & Standard Gauges	167
Figure B28:	Static Load Test, August '98 for C-Bar at Cantilever	167

Figure B29:	Static Load Test, August '98 for C-Bar at Cantilever	168
Figure B30:	Static Load Test, August '98 for C-Bar at Pier No.1	168
Figure B31:	Static Load Test, August '98 for C-Bar at Pier No.1	169
Figure B32:	Static Load Test, August '98 for Cable Transducers at Strap #21	169
Figure B33:	Static Load Test, August '98 for Cable Transducers at Strap #13	170
Figure B34:	Static Load Test, August '98 for Cable Transducers on Girder 5	170
Figure B35:	Static Load Test, August '98 for Gauges on NEFMAC & Stainless Bar	171
Figure B36:	Static Load Test, August '98 for Gauges on Shear Stud	171
Figure B37:	Static Load Test, August '98 for Gauges on Cross Frame	172
Figure B38:	Static Load Test, August '98 for Embedded Concrete Gauges	172
Figure B39:	Static Load Test, August '98 for Embedded Concrete Strain Gauges	173
Figure B40:	Static Load Test, August '98 for Embedded Concrete Strain Gauges	173
Figure B41:	Static Load Test, August '98 for Embedded Concrete Strain Gauges	174
Figure B42:	Static Load Test, August '98 for Embedded Concrete Strain Gauges	174
Figure B43:	Static Load Test, August '98 for T4 and St Gauges	175
Figure B44:	Static Load Test, August '98 for Cable Transducers at Strap #21	175
Figure B45:	Static Load Test, August '98 for Cable Transducers at Strap #13	176
Figure B46:	Static Load Test, August '98 for Two Cable Transducers on Girder #5	176
Figure B47:	55 km/hr Test, August '98 for Strap #1 in Positive Moment Region	177
Figure B48:	Comparison of Load Sharing in the Positive Moment Region	177
Figure B49:	Comparison of Load Sharing in the Positive Moment Region	178
Figure B50:	55 km/hr Test, August '98 for Gauge G3	178
Figure B51:	55 km/hr Test, August '98 for Gauge G33 & G34	179
Figure B52:	55 km/hr Test, August '98 for Gauge G3 Filtered Data	179
Figure B53:	55 km/hr Test, August '98 for Gauge G33 Filtered Data	180
Figure B54:	55 km/hr Test, August '98 for Gauge G34 Filtered Data	180
Figure B55:	55 km/hr Test, August '98 for Gauge ST Filtered Data	181
Figure B56:	40 km/hr Test, August '98 for Gauge G3 Filtered Data	181

Figure B57:	40 km/hr Test, August '98 for Gauge G33 & G34 Filtered Data	182
Figure B58:	40 km/hr Test, August '98 for Gauge G3 Filtered Data	182
Figure B59:	40 km/hr Test, August '98 for Gauge G33 Filtered Data	183
Figure B60:	40 km/hr Test, August '98 for Gauge G34 Filtered Data	183
Figure B61:	30 km/hr Test, August '98 for Gauge G3 Filtered Data	184
Figure B62:	30 km/hr Test, August '98 for Gauge G3 Final Filtered Data	184
Figure B63:	30 km/hr Test, August '98 for Gauge G33 Filtered Data	185
Figure B64:	30 km/hr Test, August '98 for Gauge G33 & G34 Filtered Data	185
Figure B65:	15 km/hr Test, August '98 for Gauge G3 Filtered Data	186
Figure B66:	15 km/hr Test, August '98 for Gauge G3 Filtered Data	186
Figure B67:	15 km/hr Test, August '98 for Gauge G33 Filtered Data	187
Figure B68:	15 km/hr Test, August '98 for Gauge G34 Filtered Data	187
Figure B69:	All Four Test Speeds, August '98 for Gauge G3 Filtered Data	188
Figure B70:	All Four Test Speeds, August '98 for Gauge G3 Filtered Data	188
Figure B71:	All Four Test Speeds, August '98 for Gauge G3 Filtered Data Superimposed	189
Figure B72:	Dynamic Amplification Factor versus Speeds from Cable Transducers	189
Figure B73:	Dynamic Amplification Factor versus Speeds from Strain Gauges	190
Figure B74:	55 km/hr Test, August '98 for Gauge #6 Before Corrected for Drifts	190
Figure B75:	55 km/hr Test, August '98 for Gauge #6 After Corrected for Drifts	191
Figure B76:	40 km/hr Test, August '98 for Gauge #6 Before Corrected for Drifts	191
Figure B77:	40 km/hr Test, August '98 for Gauge #6 After Corrected for Drifts	192
Figure B78:	30 km/hr Test, August '98 for Gauge #6 Before Corrected for Drifts	192
Figure B79:	30 km/hr Test, August '98 for Gauge #6 After Corrected for Drifts	193
Figure B80:	55 km/hr Test, August '98 for Cable Transducer #1 Filtered Data Set 1	193
Figure B81:	40 km/hr Test, August '98 for Cable Transducer #1 Filtered Data Set 1	194
Figure B82:	30 km/hr Test, August '98 for Cable Transducer #1	

	Filtered Data Set 1	194
Figure B83:	15 km/hr Test, August '98 for Cable Transducer #1 Filtered Data Set 1	195
Figure B84:	55 km/hr Test, August '98 for Cable Transducer #1 Filtered Data Set 2	195
Figure B85:	40 km/hr Test, August '98 for Cable Transducer #1 Filtered Data Set 2	196
Figure B86:	30 km/hr Test, August '98 for Cable Transducer #1 Filtered Data Set 2	196
Figure B87:	15 km/hr Test, August '98 for Cable Transducer #1 Filtered Data Set 2	197
Figure B88:	55 km/hr Test, August '98 for Cable Transducer #1 Filtered Data Set 3	197
Figure B89:	40 km/hr Test, August '98 for Cable Transducer #1 Filtered Data Set 3	198
Figure B90:	30 km/hr Test, August '98 for Cable Transducer #1 Filtered Data Set 3	198
Figure B91:	15 km/hr Test, August '98 for Cable Transducer #1 Filtered Data Set 3	199
Figure B92:	55 km/hr Test, August '98 for Strain on One Steel Straps, Set 2	199
Figure B93:	55 km/hr Test, August '98 for Cable Transducer #1 and Accelerometer #8 Filtered Data Set 3 for a Low Pass Filtered of 0.8 Hz.	200
Figure B94:	Damping Cure for Free Vibration Phase in Test Set 3	200
Figure B95:	Potential Aliasing Error	201

LIST OF PHOTOS

Photo 1.1: Crowchild Trail Bridge's Superstructure at North Abutment.	3
Photo 1.2: Superstructure of Crowchild Trail Bridge at Pier No. 1 (Looking South)	5
Photo 3.1: Old Crowchild Trail Bridge Superstructure under Demolition	18
Photo 3.2: Crowchild Trail Bridge's Superstructure (Demolition Process)	19
Photo 3.3: New Crowchild Trail Bridge (Looking North-East)	21
Photo 3.4: Underside of Crowchild Trail Bridge (Looking North)	22
Photo 3.5: Reinforcement in Negative Moment Region	24
Photo 3.6: Reinforcement at Cantilever Ends	24
Photo 3.7: Steel Studs on Plate Girders and Steel Straps	27
Photo 3.8: Supports at North Abutment	27
Photo 3.9: Supports at Pier No. 1 (Looking South)	28
Photo 3.10: Gauging Instruments Used on Crowchild Bridge	29
Photo 3.11: Formwork for the Embedded Concrete Strain Gauges	36
Photo 3.12: Formwork for the Embedded Thermistors	36
Photo 3.13: Precast Blocks for Embedded Instruments	37
Photo 3.14: Precast Blocks for Embedded Thermistors (Field Placement)	37
Photo 3.15: Precast Blocks for Embedded Concrete Strain Gauges (Field Placement and Concrete Casting)	38

LIST OF ABBREVIATIONS AND NOTATIONS

NOTATIONS

A, B	Constants
c	Damping Coefficient
c_{cr}	Critical Damping Coefficient
E	Modulus of Elasticity
E_C	Modulus of Elasticity of Concrete
E_S	Modulus of Elasticity of Steel
F	Gauge Factor
F_y	Yield Strength
f'_{C28}	Concrete Strength on the 28 th day
f_{cr}	Ultimate Concrete Strength
f_D	Damping Force
f_I	Inertia Force
f_S	Stiffness Force
G, r	Constants that Depend on Initial Conditions
G_1, G_2	Constants that Depend on Initial Conditions
I	Moment of Inertia
k	Stiffness
l	Length
M	Moment
m	Mass or Number of Successive Peaks
n	Modulus of Elasticity Ratio
P	Concentrated Load
$P(t)$	Force as a function of time, t
$Q(x)$	Spatial function
$R_{internal}$	Internal Reaction
R_x	Reaction in the X direction

R_y	Reaction in the Y direction
T_D	Damping Period
T_n	Undamped Period
$T(t)$	Time function
t	Time
u	Displacement
\dot{u}	Velocity
\ddot{u}	Acceleration
\dot{u}_o	Initial Velocity
\ddot{u}_o	Initial Acceleration
V	Shear Force
ε	Strain
γ_c	Concrete Density
λ	Constant
θ	Phase of Vibration
ρ	Magnitude of Vibration
Ω	Resistance Ohms
w_n	Undamped Angular Frequency
w_D	Damped Angular Frequency
ξ	Damping Ratio

ABBREVIATIONS

AE10	Epoxy for Strain Gauges
CFRP	Carbon Fibre Reinforced Polymers
CHBDC	Canadian Highway Bridge Design Code
GFRP	Glass Fibre Reinforced Polymers
ISIS	Intelligent Sensing of Innovative Structure

NEFMAC	NEw Fiber composite MAterial for reinforcing Concrete
OHBDC	Ontario Highway Bridge Design Code
OBB	Ontario Bridge Barrier
TUNS	Technical University of Nova Scotia
UBC	University of British Columbia
U of A	University of Alberta

1. INTRODUCTION

1.1 Background and Statement of the Problems

Bridges have been built as early as the second century BC. Roman engineers developed and utilized the concept of arching action for centuries (Barker *et al.*, 1997). In fact, some of the oldest stone arch bridges from the ninth century BC still survive and remain functional even today. The basic concept of arching action is shown in Figure 1.1 below. Arch structures have proven themselves to be beautiful, durable and adaptable to ever changing environmental load. Despite its excellent track record, the arch structural form was eventually replaced with lighter weight and cheaper to build structures; such as steel and steel reinforced concrete structures.

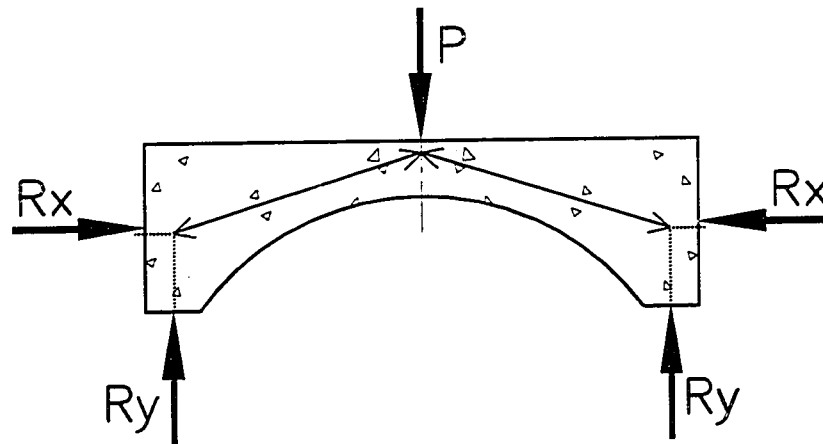


Figure 1.1: Basic Concept of Arching Action

Steel bridges became popular in the mid-eighteenth century, during the Industrial Revolution. By the early nineteenth century, steel reinforced concrete bridges appeared and grew at an exponential rate (Barker *et al.*, 1997). Numerous factors contribute to the popularity of reinforced concrete structures. The cost is competitive and its weight often reduces or eliminates dynamic problems. Nonetheless, reinforced concrete bridges have merely been introduced a few decades ago, yet a great number of them already need to be replaced due to corrosion of steel reinforcement or deterioration of concrete. Costs to

retrofit or replace such structures are both a nuisance to the public and expensive. Because reinforced concrete structures have numerous durability problems in northern climates, an alternative method of construction is needed in such regions.

One of the durability problems encountered with reinforced concrete structures is related to the corrosion of the steel reinforcement inside the concrete deck. Particularly in cold regions where deicing salt is used, the problems are most apparent. Poor quality concrete and inadequate concrete cover for the reinforcing steel account for the majority of the durability problems. Since the steel reinforcement is embedded, it is either difficult or impossible to access without damage to the structure as a whole. Thereby, maintenance, evaluation, and repairs of bridge superstructures are very expensive and sometimes impossible. Therefore, it is necessary to find novel approaches to the use of steel reinforcement and to assess their durability.

1.2 Innovative Structures

A new and innovative approach to bridge deck design is to totally exclude internal reinforcement from the deck, utilizing the steel reinforcement in the form of external tension straps. Figure 1.2 shows the arching action concept with external steel reinforcement. Photo 1.1 shows such innovative concept used in the construction of Crowchild Trail Bridge in Calgary, Alberta. This concept is the same as the traditional reinforced concrete deck except that the steel in tension is now taken out of the deck. The advantages of this system are as follow:

1. It results in a better use of concrete's high compressive strength and steel's high tensile strength;
2. It requires less concrete and therefore material cost is reduced;
3. It reduces the dead weight on the structure;
4. It saves labor cost, since no placement of internal steel reinforcement is needed;

- 5. It allows for better maintenance of the steel reinforcement since it is exposed and the application of protective coating to the steel straps is no longer an impossible task;

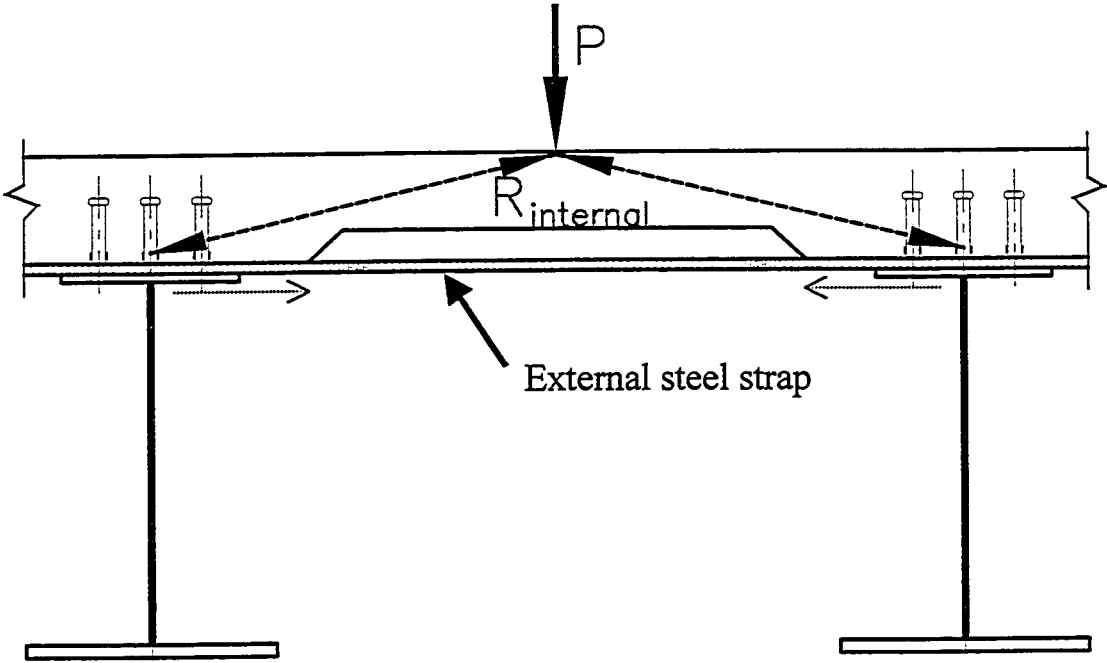


Figure 1.2: Arching Concepts with External Steel Reinforcement

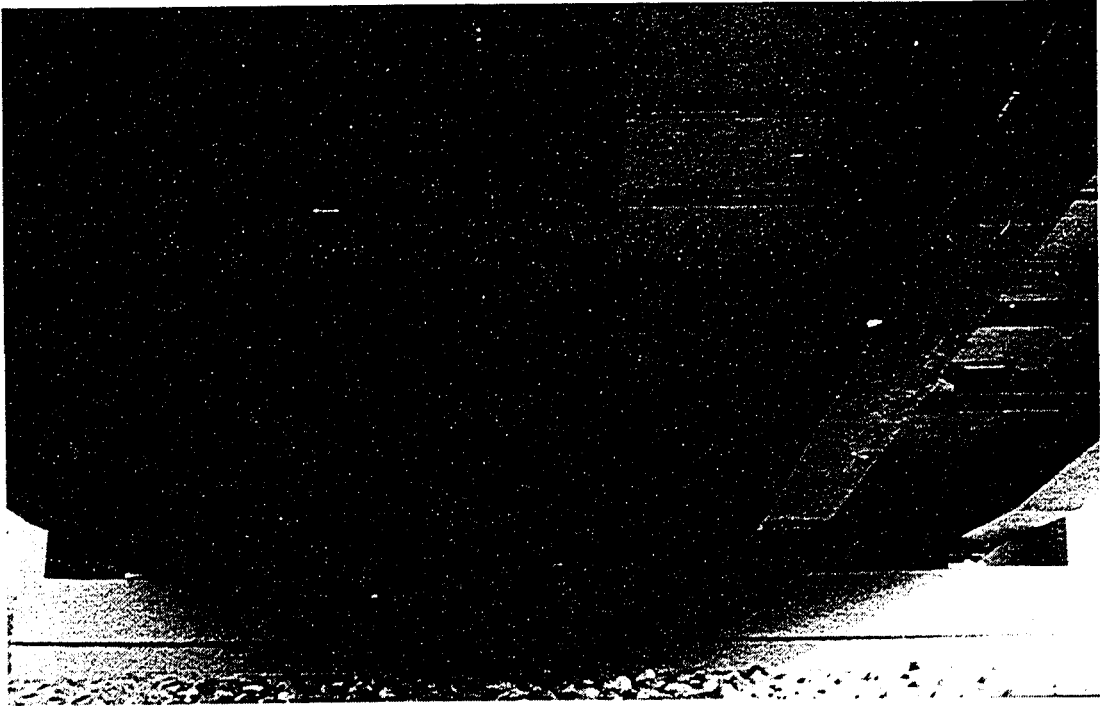


Photo 1.1: Crowchild Trail Bridge's Superstructure at North Abutment.

1.3 Scope and Objectives

The Crowchild Trail Bridge is located at the intersection of Crowchild Trail and University Drive in Calgary, Alberta. It consists of three continuous spans, two-lane, one-way traffic overpass. The total length of the bridge is 92.878 meters with two interior supports. This bridge was built in June 1997 using the innovative steel-free deck approach described in section 1.2, and it is the first of its kind in the world that utilizes this innovative approach of steel-free deck with external reinforcement over the positive and negative moment regions. Photo 1.2 shows the steel-free deck concept used over the negative moment region at Pier No. 1. Although steel-free deck design is believed to solve the internal steel corrosion problem and accessibility of the steel for maintenance and repair issues, it is essential to assess and understand its performance and long-term durability. The objective of this research is to evaluate and assess the performance of Crowchild Trail Bridge by using the field instrumentation and testing on the bridge.

Field assessment of Crowchild Trail Bridge focuses on three main issues: the performance under serviceability conditions, change of major characteristics of the bridge with time, and its long-term durability. In order to assess its performance under serviceability condition, static and dynamic tests were carried out using trucks with known axle loads. Ambient vibration tests were performed to determine the fundamental dynamic characteristics of the bridge. The fundamental structural characteristics obtained from truck tests and ambient vibration tests are evaluated annually and compared to those obtained before the bridge was open to traffic. To study long term durability, the bridge was inspected visually, and the crack patterns were mapped periodically. The scope of this thesis is confined to the field assessment of Crowchild Trail Bridge over its first two years of operation.

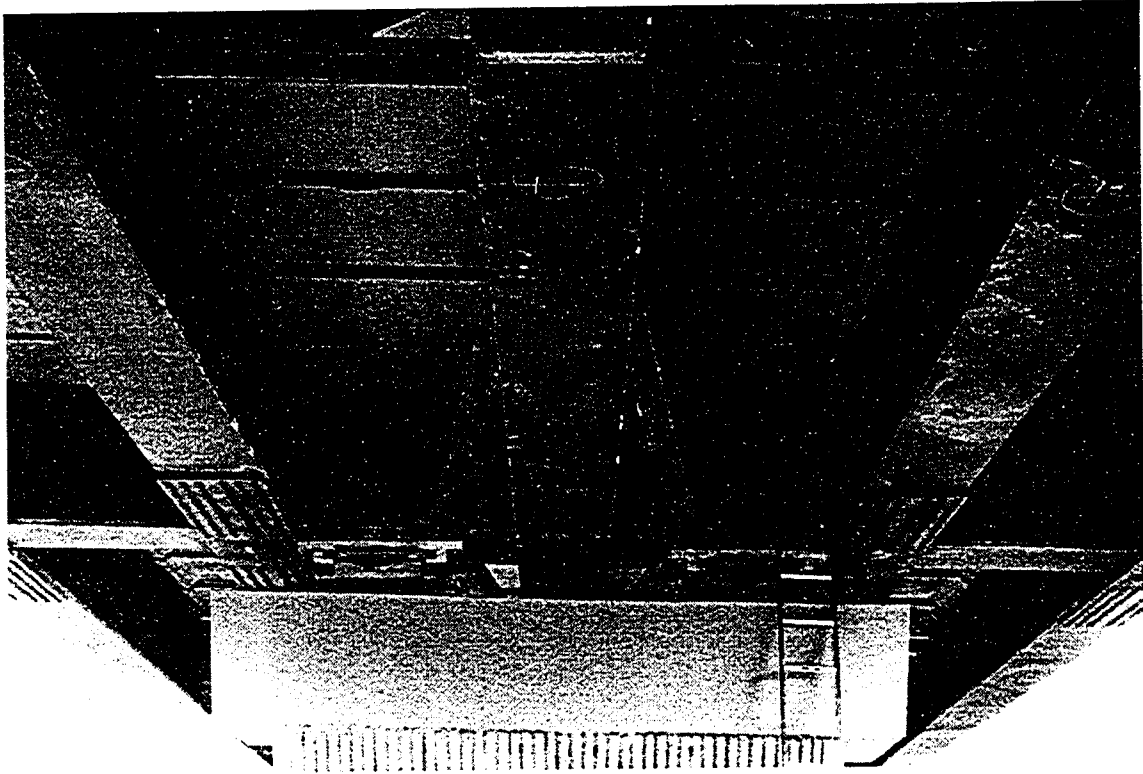


Photo 1.2: Superstructure of Crowchild Bridge at Pier No. 1 (Looking South)

1.4 Thesis Layout

Chapter 2 presents a review of the literature on steel-free decks. Scale model and full-scale model test results on steel-free decks at positive and negative moment region are outlined and summarized. Construction and instrumentation of the Crowchild Trail Bridge are described in detail in Chapter 3. Mechanical properties of materials used, layout of structural elements and final as-built details are documented.

Chapter 4 presents a summary of experimental field test results and experimental analysis obtained from the Crowchild Trail Bridge. Before the bridge was opened to traffic, Phase I test was conducted to establish a reference structural characteristic of the bridge. In Phase II of the tests, static and dynamic tests were performed. Details of Phase II testing are also discussed in terms of fundamental structural characteristics and its changes over time. Crack patterns are also documented and presented in this chapter. The experimental results are used to compare to the theoretical solutions discussed in

Chapter 5. Finally, Chapter 6 presents a summary of the findings for the field assessment of the Crowchild Trail Bridge. Conclusions are drawn and suggestions are made for future research in this field.

2. LITERATURE REVIEW

2.1 Steel-Free Deck in the Positive Moment Region

The concept of steel-free deck started with the work of Kinnunen and Nylander (1960) who proposed a model to predict the punching resistance of simply supported concrete slabs subjected to a concentrated load. Hewitt and Batchelor (1975) later incorporated restraint boundary conditions and the concept of compressive membrane stresses (known as internal arching action) with the model proposed by Kinnunen and Nylander. Hewitt and Batchelor's model, however, was developed for reinforced concrete slabs with internal reinforcement. The proposed restraint factors were empirical and can only be determined through experimentation.

The Technical University of Nova Scotia (TUNS), in collaboration with the Ministry of Transportation of Ontario, initiated a research program on steel-free bridge deck design (Mufti *et al.*, 1993). Five half-scale models of steel-free deck with in-plane restraint provided by external steel straps were constructed and tested. The results of these tests lead Mufti *et al.* (1996) to a gradual refinement of the steel-free deck concept. The majority of their work on this concept has been empirical. Finite element models developed by Wegner and Mufti (1994b) have provided useful guidance to help reduce the amount of experimental work.

Wegner and Mufti (1994b) proposed a method to incorporate internal arching action concept for unreinforced slabs with in-plane restraint provided by external reinforcement. Several of Wegner and Mufti's basic assumptions used in the development of the model were adopted from Kinnunen and Nylander. The finite element results however did not match experimental results with required accuracy and the concept was found to be very complex and sensitive to modeling parameters (Newhook *et al.*, 1995).

After eight years of laboratory studies in the design and testing of steel-free concrete deck concept, the Salmon River Bridge in Halifax, Nova Scotia was built (Newhook *et al.*, 1996). The Salmon River Bridge consisted of two spans, each 31.2 m in length, with a simply supported superstructure. To verify the design, a full-scale model of the superstructure was constructed at the Heavy Structures Laboratory of TUNS. The model was tested for various loading conditions to assess the ultimate strength behaviour.

2.1.1 Half-Scale Model

To optimize the internal arching action in steel-free deck design, Mufti *et al.* (1993) constructed various half-scale models based on the steel-free deck concept as shown in Figure 2.1. The first three of the five half-scale models were constructed as cast-in-place with 100 mm thick concrete deck. The girders were 2.31 m apart and 3.66 m long. A concentrated load was applied to a 127 mm x 254 mm steel plate pad with rubber bearing. The load represented wheel load, and it was applied at half way between the two girders.

In the first half-scale model, three internal diaphragms were used but none at the supports. This specimen failed at 173 kN. The failure mode was a hybrid of flexure and punching shear. Diaphragms were added at the two end supports in the second half-scale model and the failure load increased to 222 kN. The failure mechanism for the second model was similar to the first model; a hybrid of flexure and punching shear. In the third half-scale model, the diaphragm size was increased (Mufti *et al.*, 1993) and eight steel straps were added at 457 mm on centers by welding to the underside of the top flanges of the girders. The third model was tested three times, and the variable was the location of the load along the span. In the first test, the model was loaded at the midspan, this model failed in punching shear at a load of 418 kN. In the second and third tests on this third model, the load was applied at different locations along the span. As the load point approached the edge of the slab, the failure modes again became a hybrid of flexural and punching shear.

Subsequently, a fourth half-scale model was built to investigate the behaviour of a multi-girder system whereby the concrete on top of the interior span may crack under tension due to loads straddling the girder. The test results showed simultaneous punching shear failure under the two loads straddling the interior girder. The failure load was 418 kN for each loading location. Since the failure loads was the same for a single load and dual load straddling the girder, the fourth specimen demonstrated that the proposed design does support multi-girder systems.

Newhook *et al.* (1995) later constructed a fifth half-scale model similar to the fourth model described above. This model was designed to evaluate the following parameters: location of load, edge beams, strap spacing and stiffness, diaphragm contribution, and reduced deck thickness. In the previous four specimens, loads were always applied directly above or adjacent to straps, such that the straps were in the most advantageous position to provide restraint. In the fifth specimen, however, the loads were applied at the midpoint between straps, such that the straps would not be in the optimal position to provide restraint. The fifth specimen was used for several ultimate static load tests; all failure modes were punching shear. The authors concluded that the travelling nature of wheel loads does not present a problem in terms of the ability of the straps to provide the required lateral restraint, provided that the strap spacing is not excessive. Newhook *et al.* (1995) removed a portion of the diaphragm, but no significant effect was found in the punching failure mode. The results further reinforced that straps provide more effective lateral restraint than diaphragms. No dynamic testing was performed.

2.1.2 Full-Scale Model

Based on the fifth half-scale model, Mufti *et al.* (1995) proceeded with a full-scale model of the Salmon River Bridge. Two 12 m long girders were simply supported and spaced at 2700 mm on center. Lateral tie was constructed at each end of the girders with C380 x 50 mm channels bolted to top flange of the girders, which were made composite with the deck using shear studs. At the ends, the deck was thickened to 300 mm. Angles

L100 x 100 x 10 mm were used for the remainder of the K-Type diaphragms at the ends. At the mid-span, angles L100 x 100 x 10 mm were used for the X-Type bracing system with a bottom chord. Concrete strengths for this full-scale model and the Salmon River Bridge are listed in Table 2.1 below.

Table 2.1: Concrete Strength

Component with Fibres	Experimental Model	Salmon River Bridge
Compressive Strength	41.8 MPa	39.0 MPa
Modulus of Rupture	5.2 MPa	5.9 MPa

Figure 2.1 shows typical interior cross section and Figure 2.2 shows typical plan view of the deck. The model consisted of a 200 mm thick slab with 100 mm haunches. The slab was supported by two W610 x 241 steel beams tied together at the top flange with 100 mm x 12.5 mm steel straps spaced at 1200 mm along the entire length of the test specimen. The load patch was 250 mm x 500 mm, centered between the girders.

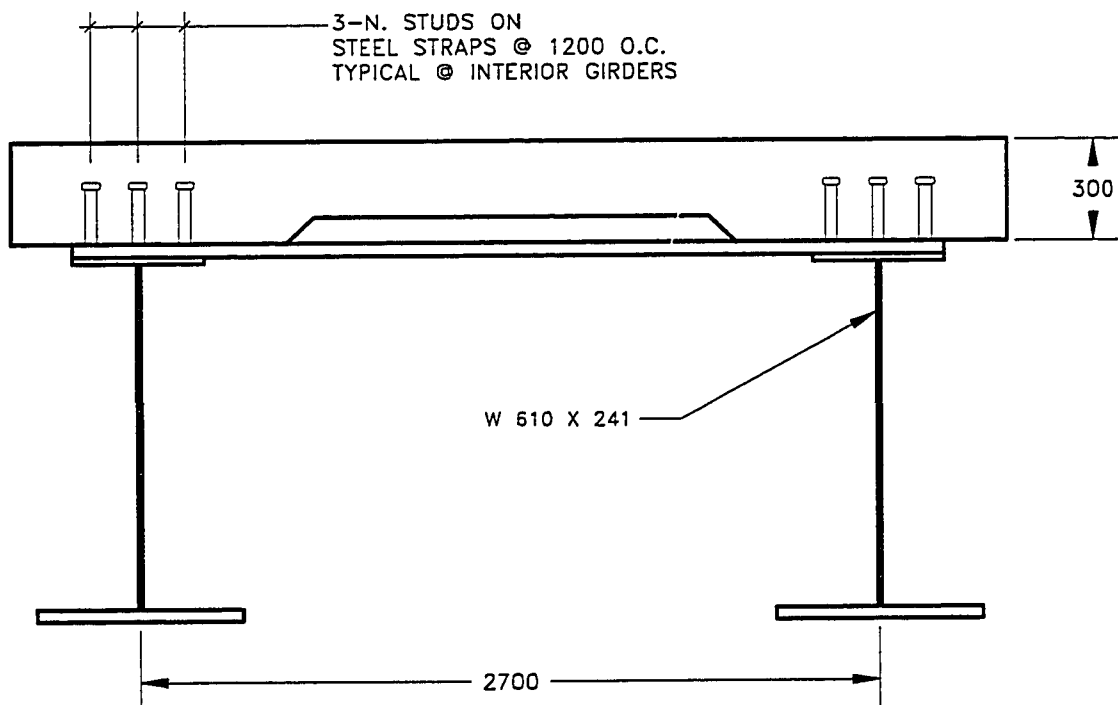


Figure 2.1: Typical Cross Section of the Superstructure.

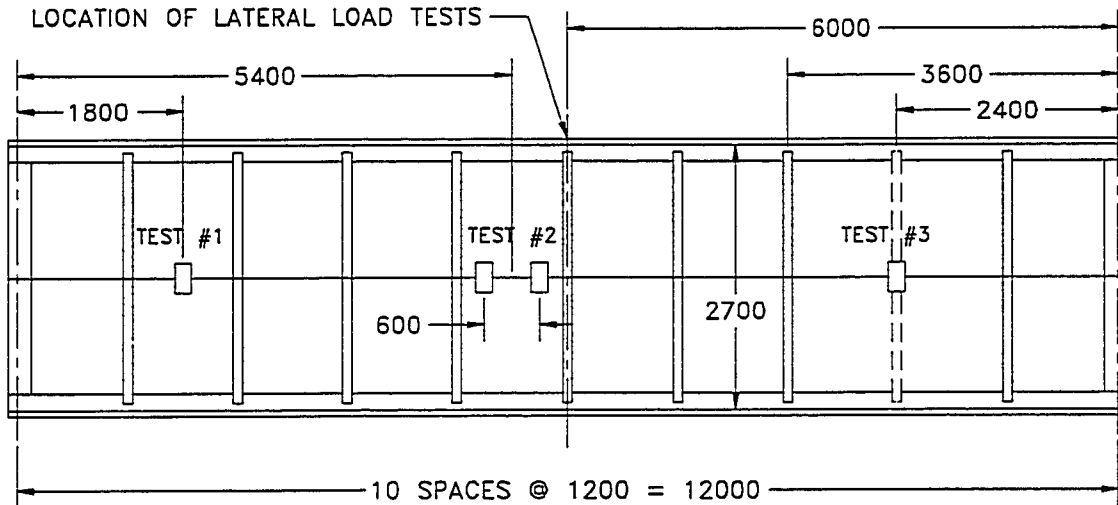


Figure 2.2: Plan View: Location of Load Tests (Newhook *et al.*, 1996)

To determine the contribution of the cross bracing to the lateral stiffness of the system, a series of lateral point loads were applied to the system, as shown in Figure 2.2 above. Before the concrete deck was cast, a series of horizontal loads was applied to the fully braced system, in Test Series 1. Fully braced diaphragms, consisting of K-Type braced plus the top and bottom flanges of the girders were tied together. In the Test Series 2, the bottom chord of the diaphragm was removed leaving K-Type bracing. For Test Series 3, the diaphragm was completely removed. Results from these tests show that the braced diaphragm provide less than 12 percent of the total lateral restraints stiffness at the diaphragm location and quickly diminishes as the load moves away.

After the concrete deck was cast, Newhook *et al.* (1996) conducted the following three destructive tests. Test #1 was conducted to determine the load capacity of the system. Test #2 was conducted to simulate a very severe tandem axle loading. Test #2 was stopped at a load of 1373 kN for safety reasons. Test #3 was conducted to simulate the failure of the strap. The test was terminated at a load of 863 kN without failure. At this point, the deck was severely damaged and longitudinal cracks ran full length along the underside of the deck. The strap directly beneath the load point was removed to simulate strap failure; the deck was loaded to a maximum of 1118 kN and failed at 951 kN.

Newhook *et al.* (1996) made recommendations for the calculation of the lateral restraint stiffness of steel-free deck system by only considering the contribution from steel straps alone. The steel-free deck on the Salmon River Bridge was designed based on this recommendation. The design approach proposed by Newhook *et al.* (1996) leads to very conservative results since it does not include the lateral stiffness contribution from girders, cross bracings, outside restraint from straps, and load sharing of the system as a whole. The lateral restraint contribution from straps compared to the total lateral restraint of the model was only 40 percent of the total lateral stiffness of the system. Newhook *et al.* (1996) recommendations are therefore conservative.

Stress-strain curves plotted by Newhook *et al.* (1996) show that the steel-free deck system seems to suggest plastic deformation after 470 kN. In terms of serviceability, this can be a problem. Authors stated that the significant change in behaviour of the system corresponded to the load at the point where the first crack was observed at the underside of the deck beneath the loading point. It is also important to consider the fatigue of concrete, as the maximum service load range is approximately one fifth of the concrete cracking load.

2.1.3 Salmon River Bridge Project

The first steel-free deck bridge was built on the Trans-Canada Highway in Nova Scotia. It was open to traffic on December 5, 1995. The bridge consists of two 31.2 m simply supported spans. The cross section consists of steel plate girders spaced at 2.7 m with diaphragms spaced at 7200 mm supporting a 200 mm deck with haunches of 130 mm and no overhangs. The diaphragms are built-up of C380 x 50 with the strong axis in the plane of the deck as opposed to conventional practice, which would have the strong axis in the vertical plane. With this new concept, Newhook *et al.* (1996) believed that adequate in-plane restraint would be developed to achieve punching failure capacity of the deck. The concrete is reinforced with chopped polypropylene fibre. Lateral confinement is provided by 100 x 14 mm uncoated weathering steel straps welded to the top of the

girders at 1200 mm on center. Although it is believed that the steel straps need to only be 100 x 12 mm, an extra 2 mm is added to allow for the weathering process.

The predicted ultimate capacity for this configuration was 550 kN; this load capacity was limited by the yielding of the strap adjacent to the maximum wheel load. Testing of a full-scale model of this structure, which accounts for lateral stiffness of the girder, deck haunches and post yield capacity in the straps indicated that the actual capacity was in excess of 1200 kN (Newhook *et al.*, 1996). The weld detail used to attach the steel straps to the top flange of the beam was designed based on the following two design considerations (Newhook *et al.*, 1996):

1. Yielding of the steel straps at the factored load level.
2. Under cyclic service loads the stress range in the weld was limited to 48 MPa as per CSA-S6 requirement for Class W connection detail with over 2 million cycles of load reversal.

Salmon River Bridge was instrumented and monitored by TUNS and the Ministry of Transportation of Ontario (Newhook *et al.*, 1996). Strain sensors were mounted on the steel straps and girders to measure their field performance. Sensors consist of electronic resistance foil gauges and Bragg Grating type fibre optic sensors. In addition, three fibre optic sensors were embedded in the NEw Fiber composite MAterial for reinforcing Concrete (NEFMAC) grids. No field data on Salmon River Bridge were presented (Doncaster *et al.*, 1996). Consequently, this fact further reinforced the need to field evaluate such innovative structure.

2.1.4 Kent County Road

Another steel-free deck was built in Chatham, Ontario, in 1996. The bridge consists of four spans of 13 m, 20 m, 20 m, and 13 m length. The two 13 m long spans were built using the steel-free deck concept. The two interior spans used a conventional steel reinforced concrete deck. The deck consists of a 175 mm slab supported by five

girders spaced at 2.1 meters. The deck slab overhangs 0.9 m beyond the outer girder and the overhangs were reinforced with Glass Fibre Reinforced Polymers (GFRP) bars. The barriers are reinforced with double-headed tension bars made of stainless steel for connection between barrier and deck slab. In the negative moment region of the deck, GFRP bars were used as the reinforcement. The bridge barrier wall used was Ontario Bridge Barrier (OBB) is also free of corrodible steel reinforcement. The bridge was also instrumented with strain gauges but no known field data were reported. Again, this innovative approach to steel-free bridge deck design had been put into use on two different superstructures, yet no field data had been reported in regards to its performance in service.

2.2 Steel-Free Deck in the Negative Moment Region

Dorey *et al.* (1996) investigated the suitability of continuous steel-free deck for multi-span structures. A study was conducted to determine whether the steel-free deck concept would have sufficient uncracked moment capacity over the negative moment region to meet the OHBDC. A full-scale model was constructed and tested at TUNS. Dorey *et al.* showed that the uncracked portion of the superstructure had adequate strength for the specified loads, but not for the factored loads. The test by Dorey *et al.* also showed that the uncracked specified serviceability stresses in the concrete did not meet OHBDC-91 limit of $0.4f_{cr}$ for crack control. This is a potential concern in the development of continuous steel-free deck over negative moment regions. However, researchers at TUNS believe that steel-free deck concept over negative moment region has sufficient reserve tensile capacity to carry the specified tensile loads (Dorey *et al.*, 1996).

2.2.1 Full-Scale Model

Dorey *et al.* (1996) constructed a full-scale test specimen of the negative moment region. The length of the test specimen was taken as approximately 0.2 times the span length of the continuous span. A 12.5 m long test specimen was used to model the negative moment region of a two span 31.2 m bridge. The specimens were tested as simply supported beams with the loads applied to create tension in the top fibers. The first crack appeared near the location of the applied load at 314 kN. This was well below the predicted 715 kN capacity based on measured flexural strength of the concrete. With additional load, additional cracks developed in the transverse direction. The cracks that formed during the test ranged in width between 0.50 mm to 2.20 mm at termination of the test. The load at first cracking of the deck corresponds to a stress of 2.9 MPa, which is close to the lower measured splitting strength of concrete, 3.2 MPa. Dorey *et al.* (1996) suggested that size effect is a factor for lower value in the model than in the material tested.

The load versus deflection curve obtained from the tests conducted by Dorey *et al.* (1996) shows linear relationship before cracking, indicating a constant stiffness and elastic behaviour. After cracking, the slope of the load versus deflection curve decreased, indicating a loss of composite action. The slope of the load versus deflection curve continued to decrease until it reached a lower bound (slope again became constant). Dorey *et al.* have successfully correlated the predicted model to the experimental model in regards to composite action before crack and after crack relationship. The test results raised two important concerns: low cracking load capacity and large crack widths in negative moment regions.

The experimental full-scale model had shown that both strength and serviceability cracking limit states were exceeded in the negative moment region. Dorey *et al.* (1996) suggested that the strength limit states could be easily addressed by

- Proportioning the section such that the neutral axis is higher within the section.
- Increasing the concrete strength.

The writer, however, believes that by cambering the support in the negative moment region before placement of the concrete and lowering the support to its desired location after placement of the concrete, beneficial prestressing forces would be developed in the concrete deck to help counteract the negative moment stresses. Of course, creep must be considered in the design.

2.3 Serviceability Issues

Serviceability must also receive due consideration in addition to the strength issues. Many freeze thaw cycles can deteriorate the concrete around the cracks and the deterioration can be severe enough to cause overall deck failure. In addition, excessive cracking in the negative moment region gives the chloride laden water on the top of the deck easy access to the steel girders, leading to their premature deterioration. Finally, aesthetics of structure needs to be considered.

As suggested in the name '*innovative design*' of steel-free deck, it is essential to field evaluate the durability of such design and its' performance. Steel-free deck is an innovative design proposed by Mufti and his associates, and it has been put into use on both the Salmon River Bridge and the Kent County Road. Although these bridges have been instrumented, no field data have been reported on its performance or durability. TUNS had done extensive laboratory research works on the concept of steel-free deck in collaboration with Ministry of Transportation of Ontario. However, all laboratory work on scale model and full-scale model have been focused on the ultimate strength behaviour and little on the serviceability. In addition, no dynamic testing was investigated for a bridge deck that only performed under dynamic loading.

Use of steel-free deck concept has been extended into the negative moment region of the Crowchild Trail Bridge in Calgary, Alberta near the University of Calgary. Crowchild Trail Bridge's construction and instrumentation are described in detail in Chapter 3. The University of Alberta has extensively developed field instrumentation and monitoring program on this bridge. The purpose of this program was to field assess the bridge's static and dynamic behaviour in service. This program, in turn, established a base structural characteristic of the bridge, thereby allowing a future long term monitoring program on the bridge to be developed and evaluated.

3. CONSTRUCTION AND INSTRUMENTATION OF THE CROWCHILD TRAIL BRIDGE

3.1 Background

The Crowchild Trail Bridge is a two-lane, one-way traffic overpass located on the intersection of Crowchild Trail and University Drive near the University of Calgary. The original superstructure was a three-span prestressed concrete box-girder bridge designed for HS20 truck loading. Each span is simply supported, and pretensioned longitudinally. Due to a large increase in traffic loads and rapid deterioration of the superstructure, it was necessary to replace the superstructure of the bridge. Photo 3.1 shows the old Crowchild Trail Bridge concrete box girder system during demolition.

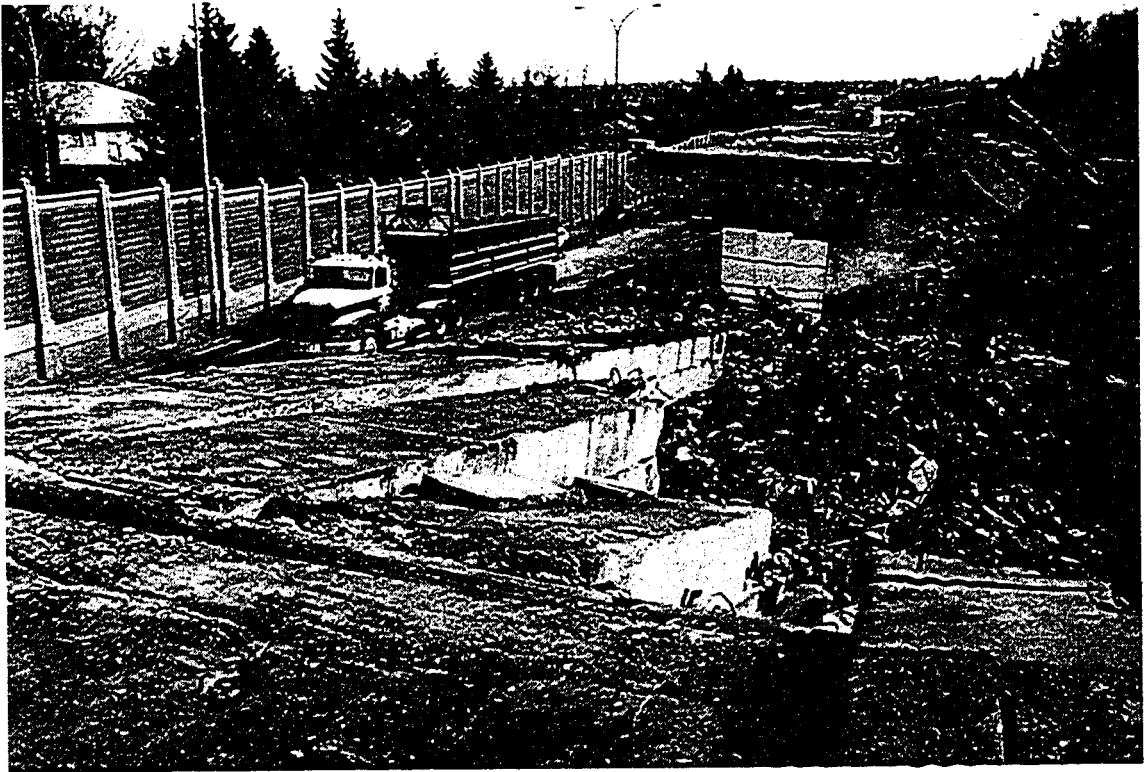


Photo 3.1: Old Crowchild Trail Bridge Superstructure under Demolition

The old Crowchild Trail Bridge was evaluated using Clause 11 of the Ontario Highway Bridge Design Code (OHBDC-1991) and Clause 12 of CSA/CAN-S6-M88 for

a CS-615 design truck. Evaluation showed that the prestressed concrete box girders had insufficient bending capacity. Furthermore, the development and quantity of reinforcement in the draped connection and T-Beam corbel were inadequate. Therefore, the bridge was upgraded in July 1997. Two options for the upgrade were considered. The first option was to replace the concrete box girders with new concrete girders. With this option, it would have been necessary to also strengthen the existing foundations. The second option was to replace the superstructure with lighter structure, thereby eliminating the need to modify the supporting foundation.

After 20 years of operation, the original Crowchild Trail Bridge superstructure was already in need of replacement. It was therefore necessary to find a better method of construction, which would make better use of the concrete strength and would improve durability in northern regions. For economic and durability reasons, it was decided to replace the old Crowchild Trail bridge superstructure by a steel-free deck on steel girders. With this option, the bridge could carry the CS-750 truck load, and the existing piers were reused without any need of modification. The design for the typical overload trucks is based on the Ultimate Limit State load rating, using Clause 12 of CAN/CSA-S6-M88.

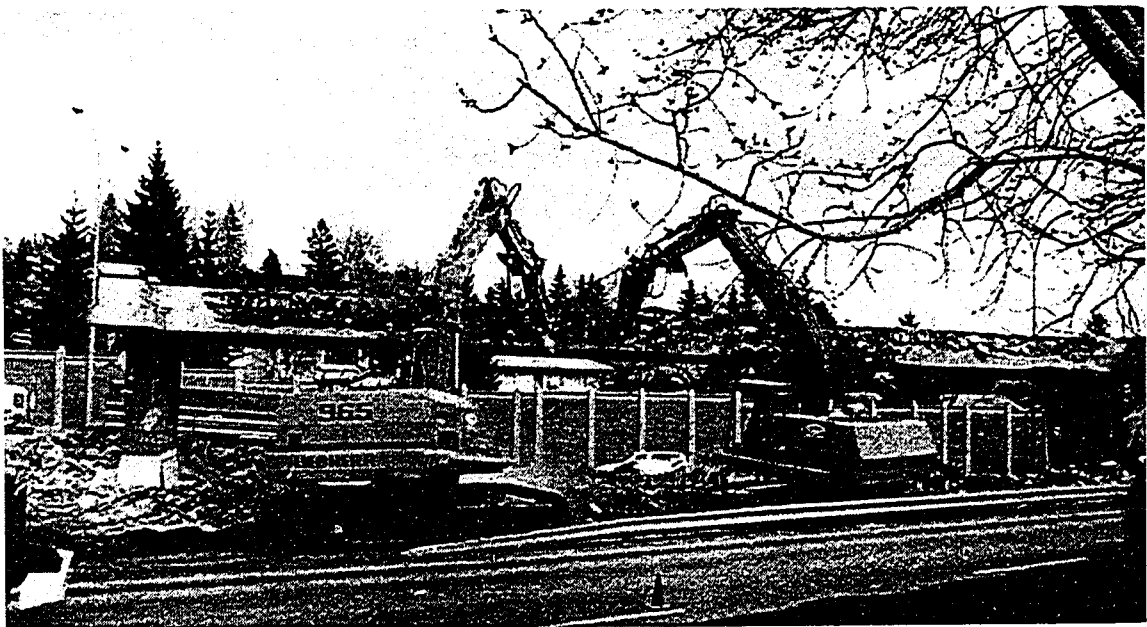


Photo 3.2: Crowchild Trail Bridge's Superstructure (Demolition Process)

Photos 3.1 and 3.2 show the demolition process of the previous concrete box girder superstructure. Furthermore, it shows how care was taken to protect the existing piers so that they could be reused in the new construction without any modification. Nonetheless, the steel-free deck concept is relatively new, and it is therefore necessary to field evaluate its performance in the field from the points of view of strength and serviceability.

3.2 Description of Crowchild Trail Bridge

3.2.1 General

Crowchild Trail Bridge has three continuous spans, 29830 mm, 32818 mm, and 30230 mm long from the North abutment. The superstructure is a composite structure with a cast-in-place fiber reinforced concrete deck continuous over positive and negative moment regions. The deck is supported on five built-up steel plate girders. This is the first continuous steel-free deck in the world. Figure 3.1 shows the West elevation of the new Crowchild Trail Bridge. Photo 3.3 shows the new Crowchild Trial Bridge after construction.

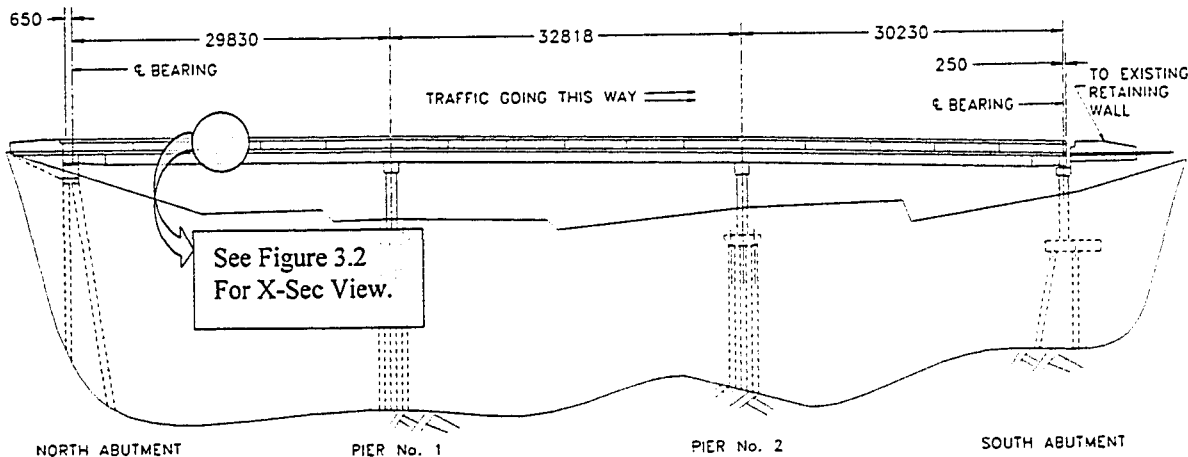


Figure 3.1: Crowchild Trail Bridge: West Elevation



Photo 3.3: New Crowchild Trail Bridge (Looking North-East)

The major problem with the conventional reinforced concrete deck is the corrosion of the internal steel reinforcement in severe winter climates. The new Crowchild Trail Bridge has a deck width of 9030 mm and it has no internal steel reinforcement. Figure 3.2 shows the overall cross-sectional view of the Crowchild Trail Bridge superstructure. Refer to drawing Figure A1 in Appendix A for more detailed information.

Within each span, there are four cross frames equally spaced. These cross frames serve as diaphragms and provide for lateral stability of the girders and load sharing between the girders. The deck behaves much like a conventional reinforced concrete deck, except that there is no internal tension steel reinforcement, which was replaced by external steel straps. Photo 3.4 shows the completed deck view from under the bridge. In this case, the exposed steel reinforcement consists of tension straps as shown in the photo.

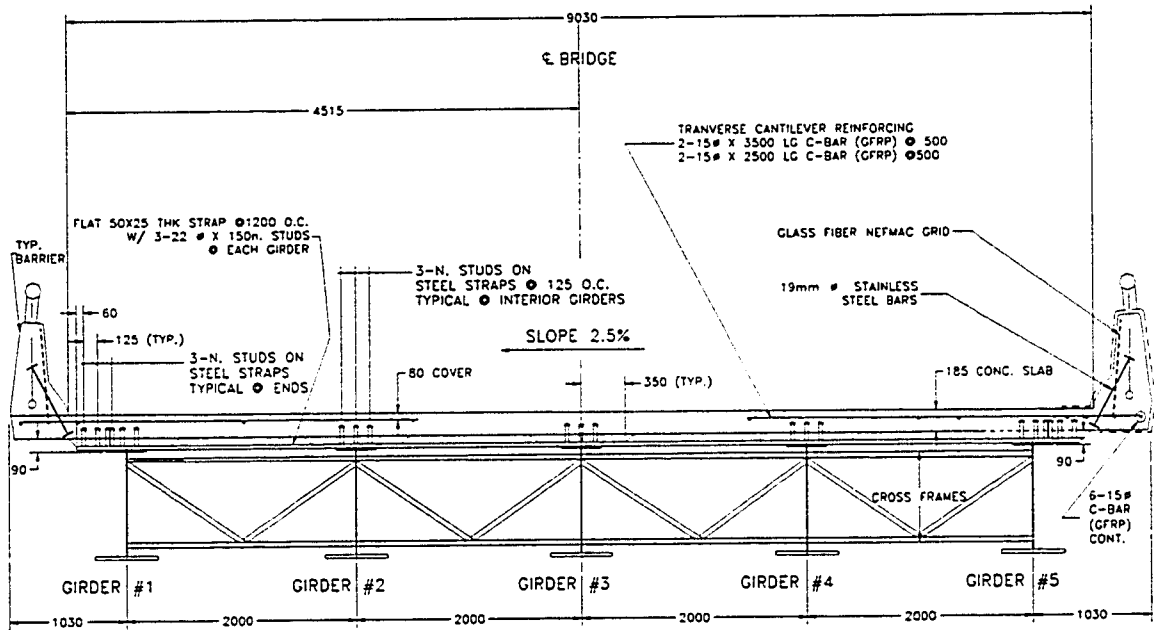


Figure 3.2: Crowchild Trail Bridge--Cross Section



Photo 3.4: Underside of Crowchild Trail Bridge (Looking North)

3.2.2 Concrete Bridge Deck

With the configuration shown in Figure 3.2, the main part of the concrete deck is only 175 mm thick with a 90 mm haunch spanning between the girders parallel to the tension straps. The main purpose of the tension straps is to provide the necessary lateral constraints to develop the internal arching action in the concrete deck. The tension-straps are 50 x 25 mm bars spaced at 1.2 m on center. Loss of section due to the weathering process has been considered in the design of the straps. A plan view of the strap layout is presented in drawing Figure A3 of Appendix A. The drawing also presents the plan view of the girder layout and cross sections of the girders along the length of the bridge.

The primary concern in the use of steel-free deck over negative moment regions is the potential excessive flexural cracks width in the concrete deck, which may affect the internal arching action required for the steel-free deck to function. Tests at TUNS have tried to address this negative moment region issue. Tests confirmed that cracks in the transverse direction do not significantly affect the internal arching capacity of the slab (Dorey *et al.*, 1996). Although transverse cracks consist mainly of shrinkage cracks and do not cause structural concerns, in the negative moment region these cracks could increase beyond the limits set out by the OHBDC (1991). To take care of the concern in regards to transverse crack, Glass Fiber Reinforced Polymer (GFRP) bars are utilized over the piers. Photo 3.5 shows the GFRP bars over the intersection of the bridge Girders and Pier No. 1 diaphragm.

GFRP reinforcement is also used on both sides of the cantilevers of the deck, as shown in Figure 3.2 and in Photo 3.6. Prefabricated glass fiber reinforcing grids, NEFMAC, are used for the reinforcement of bridge barriers and double headed stainless steel bars are used to anchor the barriers to deck.

The specified 28-day concrete compressive strength is 35 MPa. The concrete was mixed with 0.45 percent by volume of chopped polypropylene fibers. Concrete mixes

used are in conformance with CAN3-A23.1-M90. Table 3.2 shows the concrete mix characteristics for the Crowchild Trail Bridge.

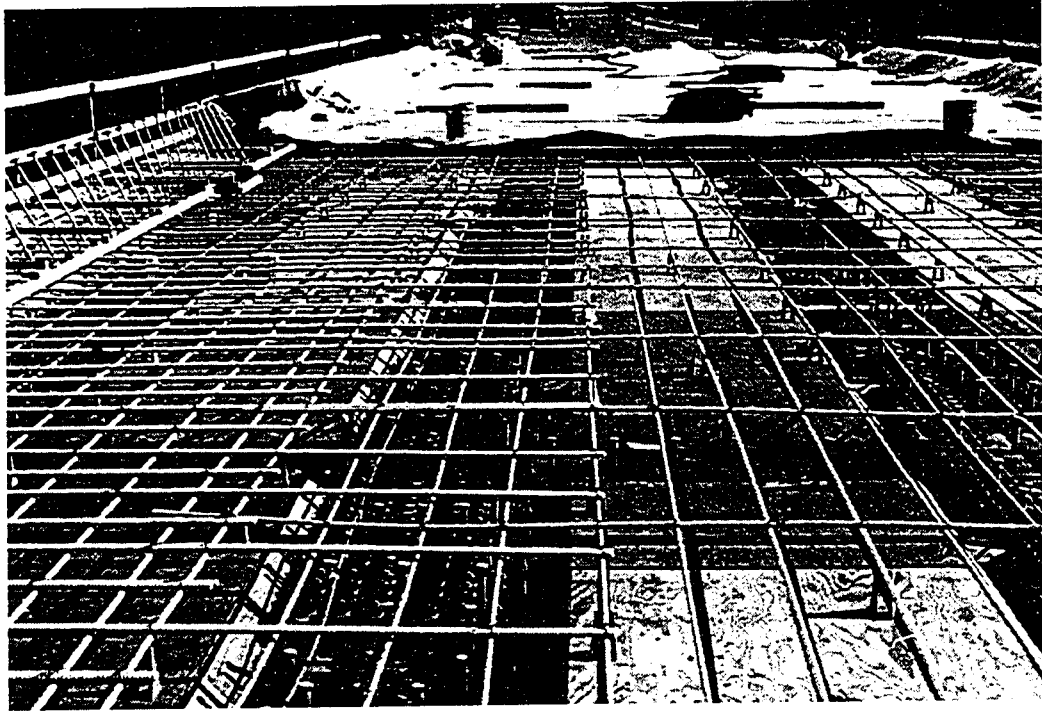


Photo 3.5: Reinforcement in Negative Moment Region

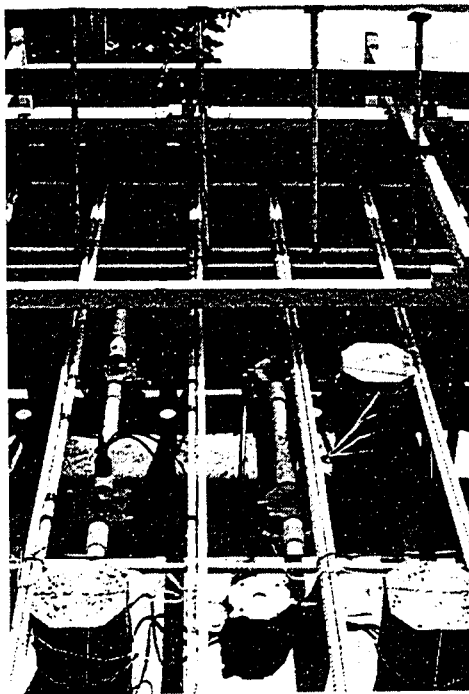


Photo 3.6: Reinforcement at Cantilever Ends

3.2.3 Steel Plate Girders

Built-up steel plate girders were used to replace the old prestressed concrete box girders. The flange, web thickness, and depth of the girders varied between the positive and the negative moment region. Figure 3.3 shows the top flange of the steel girders along the bridge and identifies the location of four different section types described in more detail in Table 3.1.

Table 3.1: Girder Type and Section Dimensions

BRIDGE GIRDER & PIER DIAPHRAGM SCHEDULE			
SECTION TYPE	TOP FLANGE	WEB (d – 2t)	BOTTOM FLANGE
1	18 x 350 mm	10 x 900 mm	30 x 550 mm
2	32 x 600 mm	12 x 900 mm	38 x 600 mm
3	18 x 350 mm	10 x 900 mm	25 x 500 mm
4 (PIER)	40 x 650 mm	28 x 860 mm	40 x 650 mm

Girder section type 1 is used in the positive moment regions of the first and last spans of the bridge. Girder section type 2 is used in the negative moment regions, over the piers. Girder section type 3 is used in the positive moment region of the middle span. The steel grade used for the steel plate girders is CSA-G40.21M 300W.

Steel straps and girders are made composite with the concrete slab by cold-finished carbon steel shear studs, grade 1020. The steel straps were attached to the concrete deck using three shear studs above each girder as depicted in Photo 3.7. Before the placement of the concrete deck, the steel straps were temporarily tied to the top of the girders with light gauge wire.

The five steel girders are braced with cross frames; four equally spaced within each span. Stiffened transverse girders over the two piers form transverse diaphragms between all five girders. Bridging between the superstructure and the foundation supports

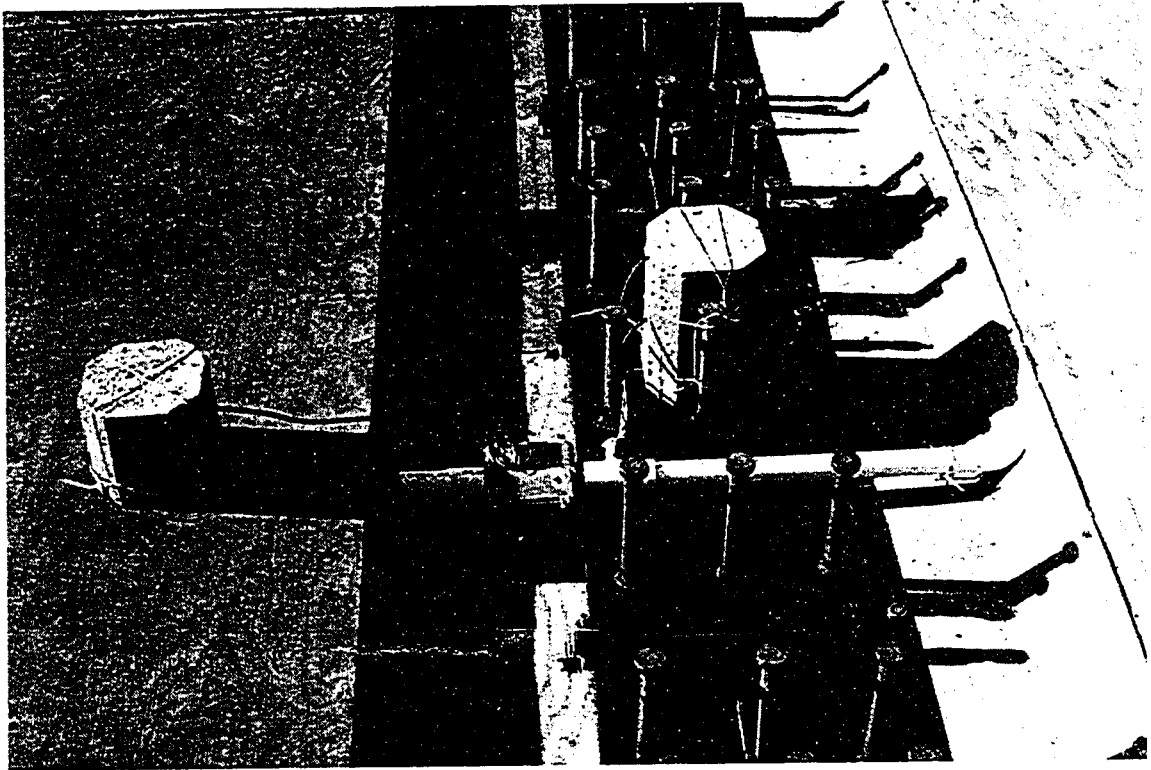


Photo 3.7: Steel Studs on Plate Girders and Steel Straps

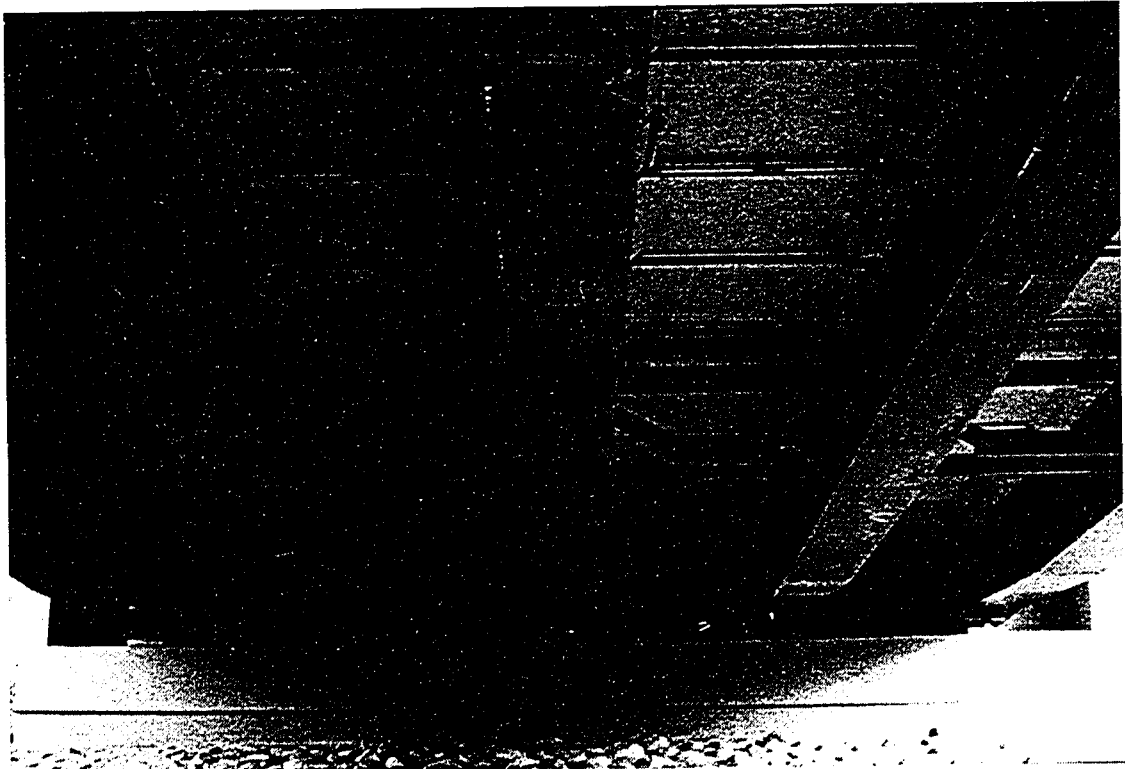


Photo 3.8: Supports at North Abutment

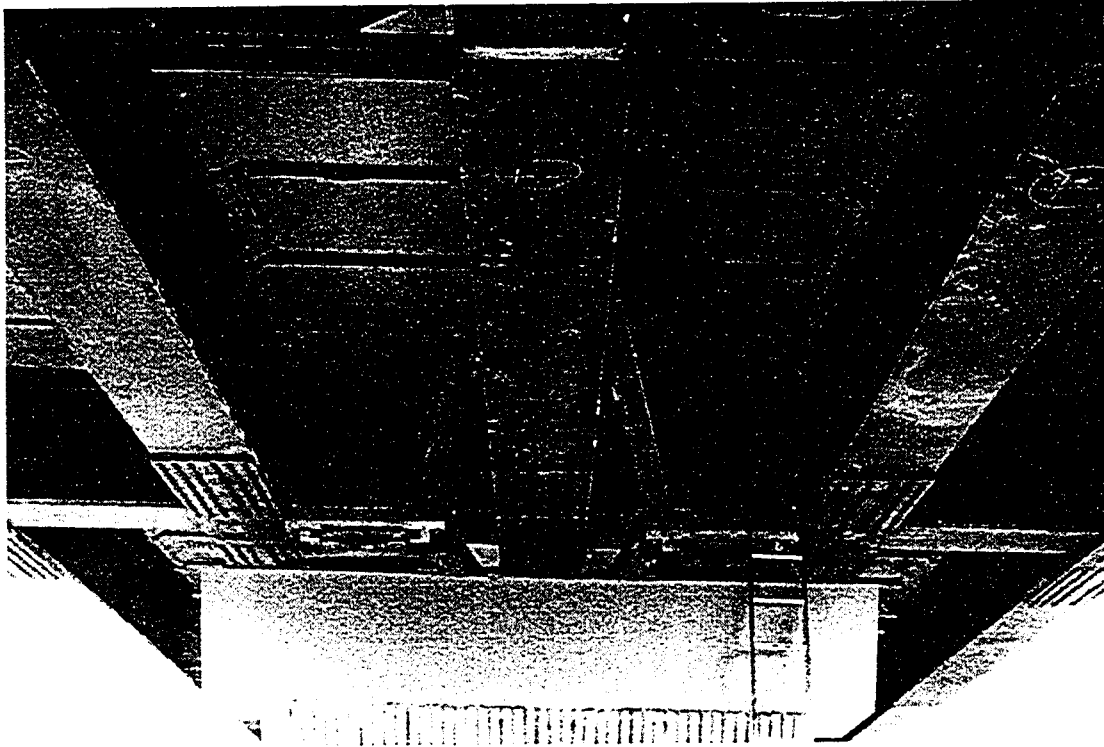


Photo 3.9: Supports at Pier No. 1 (Looking South)

3.3 Instrumentation

To better understand the behavior of the new superstructure of the bridge, a field instrumentation and monitoring program was developed at the University of Alberta in collaboration with ISIS Canada, City of Calgary, and SPECO Consultant. Of particular importance are the studies of static and dynamic behavior under service loading conditions.

3.3.1 Location of Gauges

In the last two weeks of July 1997, the University of Alberta has extensively instrumented the Crowchild Trail Bridge. The instrumentation installed on the Crowchild Trail Bridge consisted of 108 strain gauges and five thermistors. Among the 108 strain gauges, 86 of the strain gauges are 5 mm foil strain gauges, two are glued-on fiber optic strain gauges, three are embedded fiber optic strain sensors in GFRP bars (called smart

bars), and 17 are electrical resistance embedded concrete strain gauges (120 x 10 mm gauge length). Four of the five thermistors were embedded inside the concrete deck and one was used to measure the ambient air temperature near the bridge. Photo 3.10 shows a typical embedded concrete strain gauge, a thermistor and an electrical resistance strain gauge.

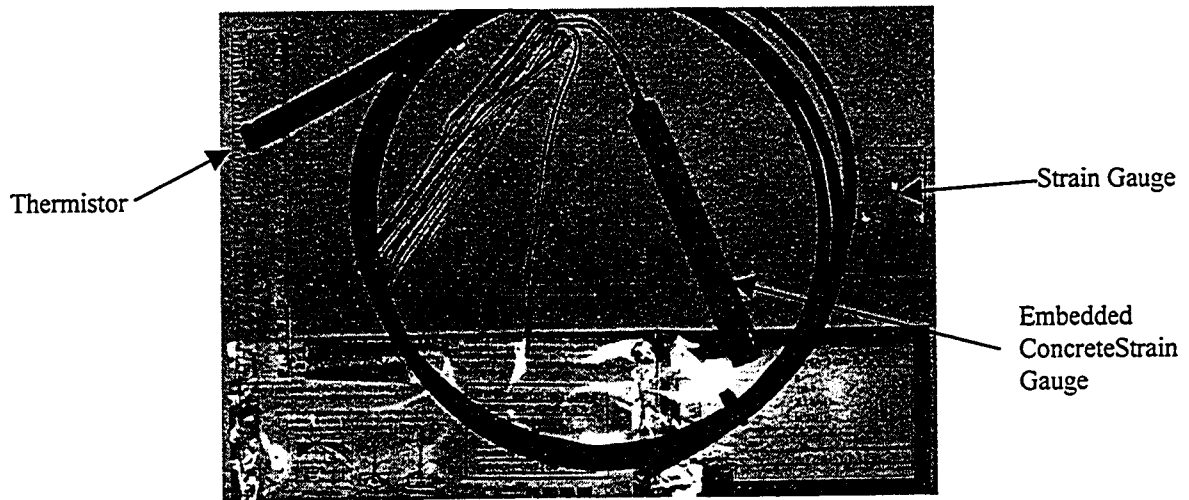


Photo 3.10: Gauging Instruments Used on Crowchild Bridge.

The 86 electrical resistance foil strain gauges were installed on the following structural members: 64 electrical resistance strain gauges on structural steel members, two on the NEFMAC grid, 17 on the GFRP bars, and three on smart bars. Smart bar is a 10 mm GFRP bar, with exterior sand coating, that comes with an embedded fiber optic sensor. TUNS manufactured the bars under an ISIS research project. The smart bars were used in conjunction with the three foil strain gauges for comparison with the fiber optic sensors. The two glued-on fiber optic strain gauges were installed opposite to the two foil strain gauges for comparison of their performance. The 17 electrical resistance concrete strain gauges were embedded inside five precast concrete blocks. Four of the five thermistors were also embedded inside two precast concrete blocks. All precast concrete blocks had higher sand and water content than the concrete mix for the deck, thereby giving the precast concrete blocks lower modulus of elasticity than the deck.

A summary of all the instrumentation used in Crowchild Trail Bridge is presented in Table 3.3. Included in this table are descriptions of the instrumentation, structural members on which the instruments were mounted, notations, descriptions, and quantities.

Table 3.3: Instrumentation

Notation	Structural Members Monitored	Quantities
<i>[I] Electrical resistance foil strain gauges (120Ω, 5 mm in length, F=2.12)</i>		
G	Built-Up Plate Girders	34
T	Steel Straps	18
S	Shear Studs	6
C	Cross Frame	4
N	NEFMAC grid and Stainless Steel Rods in the barriers	4
R	GFRP bars (On deck reinforcement)	15
RC	GFRP bars (Same location as glue-on fiber optic gauges)	2
RS	Smart bar (Same location as embedded fiber optic gauges)	3
<i>[II] Electrical resistance embedded strain gauges (120Ω, 120mm in length, F=2.0)</i>		
E	Embedded in precast concrete blocks	17
<i>[III] Fiber Optic Sensors</i>		
FC	GFRP @ RC gauge (Ser. No. N1001-441, -395)	2
FS	Smart bars @ RS gauge (Ser. No. N1001-163, -356, -186)	3
<i>[IV] Thermistors</i>		
TH	Four in precast concrete blocks and one in open air	5

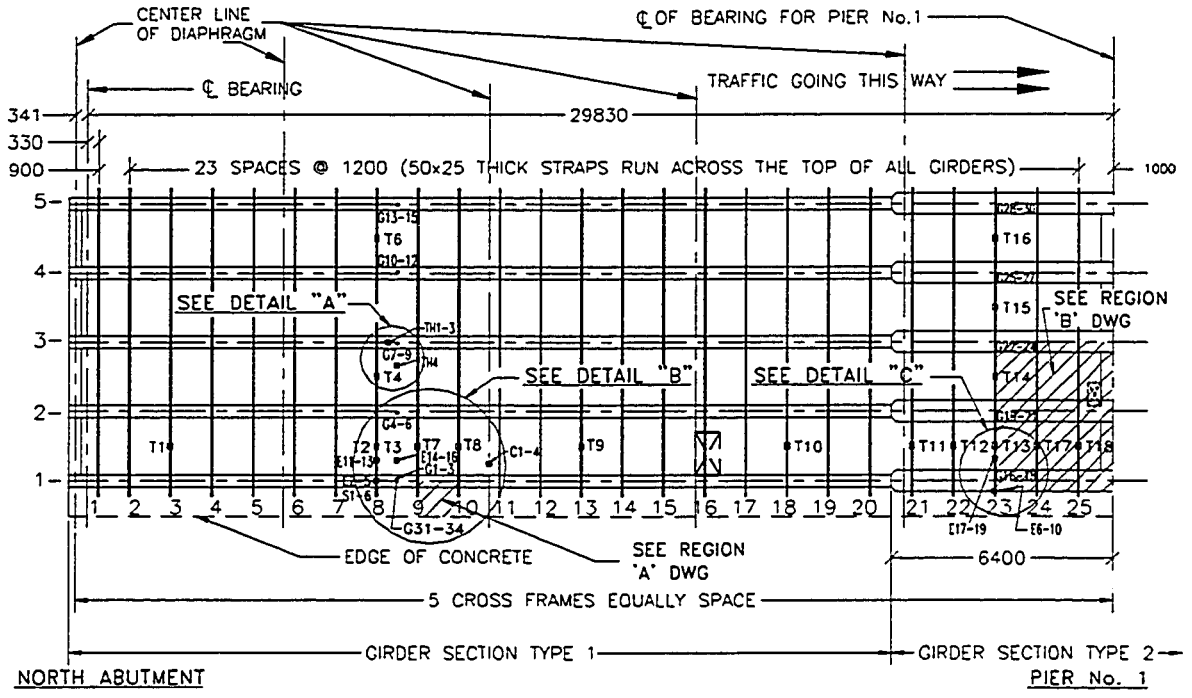
All the instrumentation was mounted in the North span of the bridge. The overall layout of all the instrumentation used in the Crowchild Trail Bridge is shown in Figure 3.4. The strain gauges placed on the girders are designated as the “G” series. The “T” series strain gauges shown in Figure 3.4 were mounted on the tension straps at mid-length. The “S” series strain gauges were mounted on the shear studs and the “C” series were mounted on the cross frame. The “N”, “R”, “F”, and “TH” series were mounted on

NEFMAC, the reinforcing bars, the fiber optic sensors, and the thermistors, respectively. The gauge notation summarized in Table 3.3 is used in all of the figures that follow.

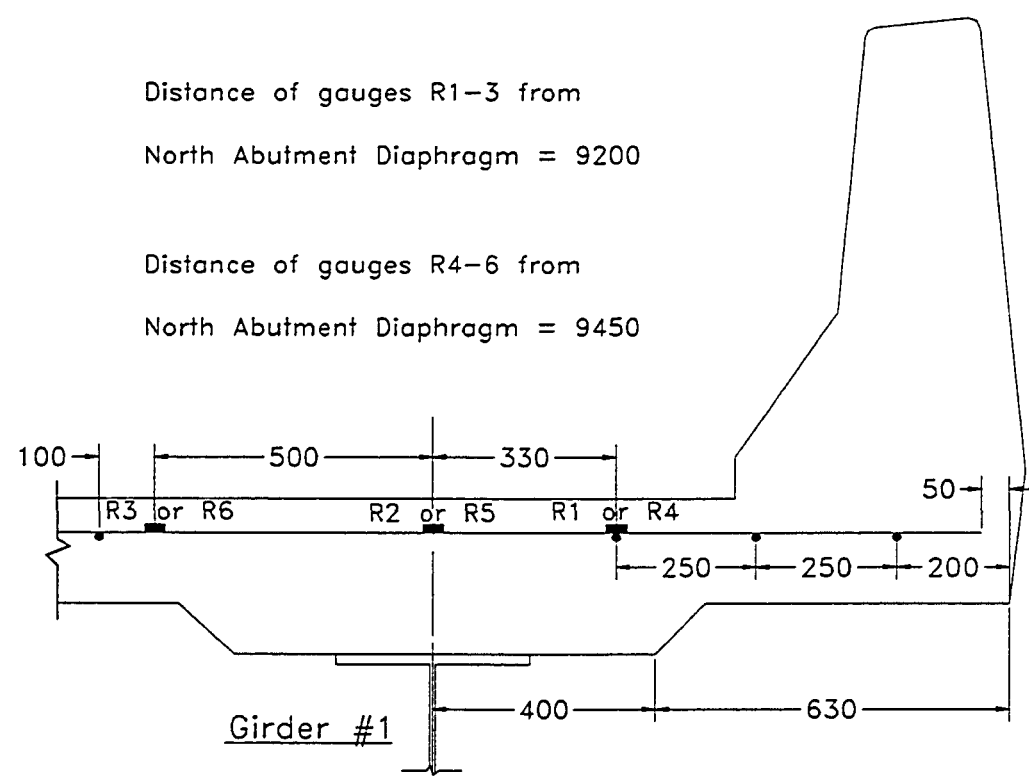
Detail *region* “B” in Figure 3.4 shows 14 strain gauges and the fiber optic sensors on the glass fiber reinforcement. The goal of *region* “B” instrumentation was to monitor the behavior of the deck in the negative moment region and to evaluate the use of fiber optic sensors. Two Fabry-Perot type of fiber optic sensors, manufactures by Rock Test Inc., were installed on the glass fibre reinforcement at the same location as conventional electrical resistance strain gauges to evaluate the performance of the fiber optic sensors. The fibre optic sensors were non-compensated for temperature, and were installed using the same epoxy as any other gauges (AE10 epoxy). More detail for drawing in *region* “B” can be found in Appendix A, drawing number T200006.

Details for *region* “A” drawing in Figure 3.4 shows the six strain gauges on the glass fiber reinforcements. The purpose of *region* “A” instrumentation was to monitor the behavior in the cantilevers. All the gauges on the glass fiber reinforcement were mounted in the laboratory before shipping out for field installation.

The numbers from 1 to 5 running vertically at the North Abutment shown in Figure 3.4 identify the girders. The numbers from 1 to 25 running across the bottom from North Abutment to Pier No. 1 identify the tension straps. Figure 3.4 depicts a rectangular box between girders 1 and 2 on strap number 16, used as the central box where all the wiring from all of the strain gauges converged. At the intersection of Pier No. 1 and girder number 2, there is another central box for all the fiber optic gauges. Figure 3.4 also shows the location of the six diaphragms between North Abutment and Pier No. 1. Two of the diaphragms, on top of Pier No. 1 and the North Abutment, are stiffened steel plate girders. The other four diaphragms are cross frames. The cross frames are made up of back-to-back angles. The cross frame next to strap number 11 was instrumented as shown in Figure 3.5. The instrumented cross frame is the third diaphragm from the North as shown in Figure 3.4.

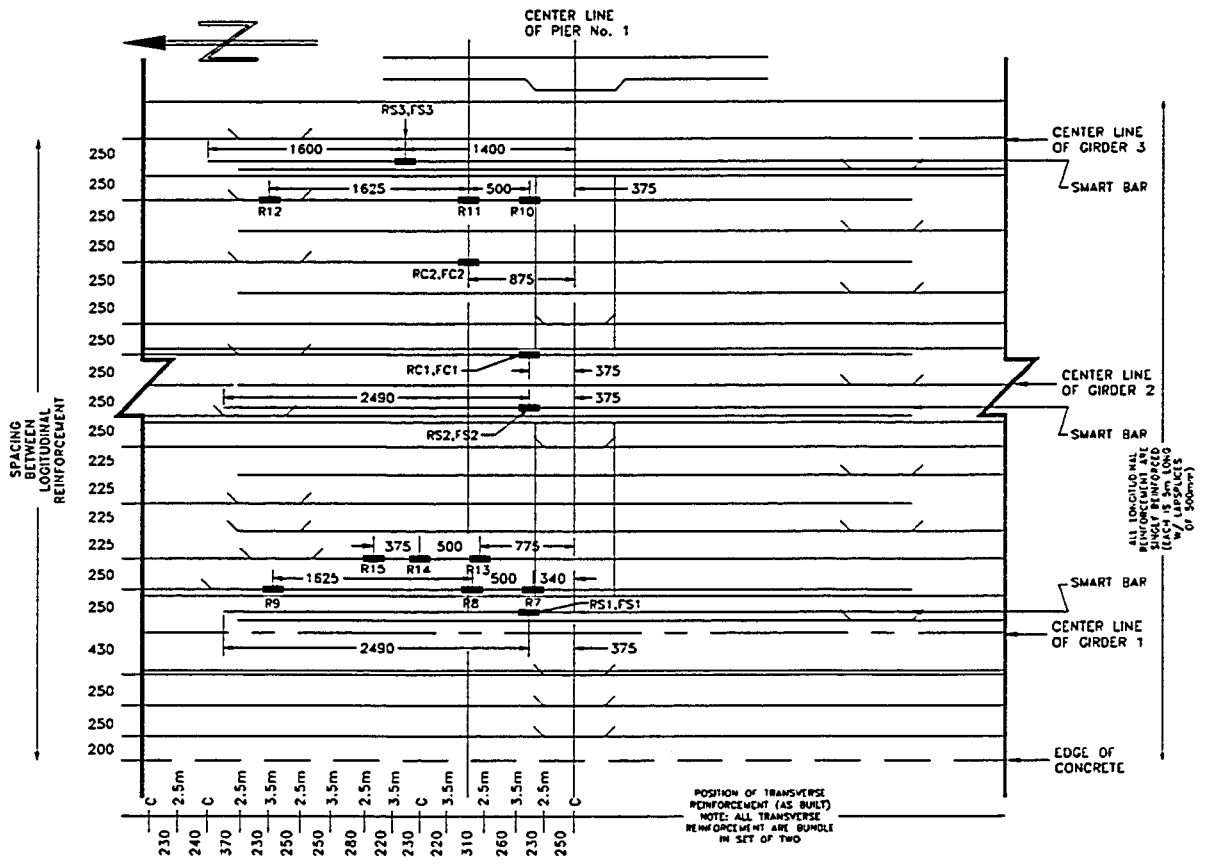


(a) Instrumentation in the North Span

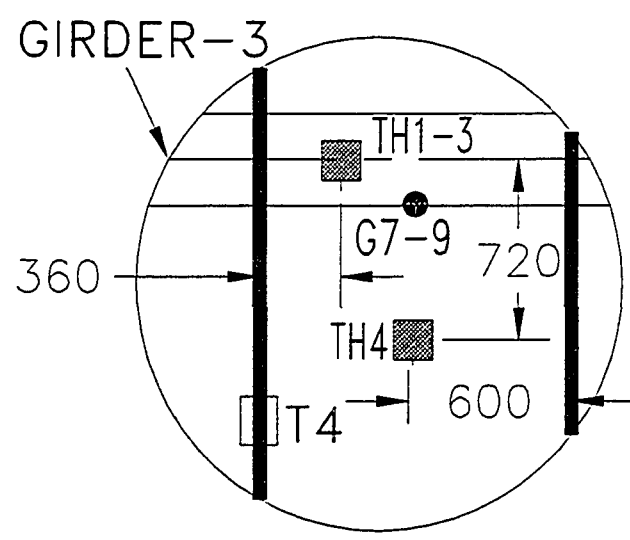


(b) Region "A"

Figure 3.4: Instrumentation Used in the Crowchild Bridge



(c) Region "B"



(d) Detail "A"

Figure 3.4: Instrumentation Used in the Crowchild Bridge (Cont'd)

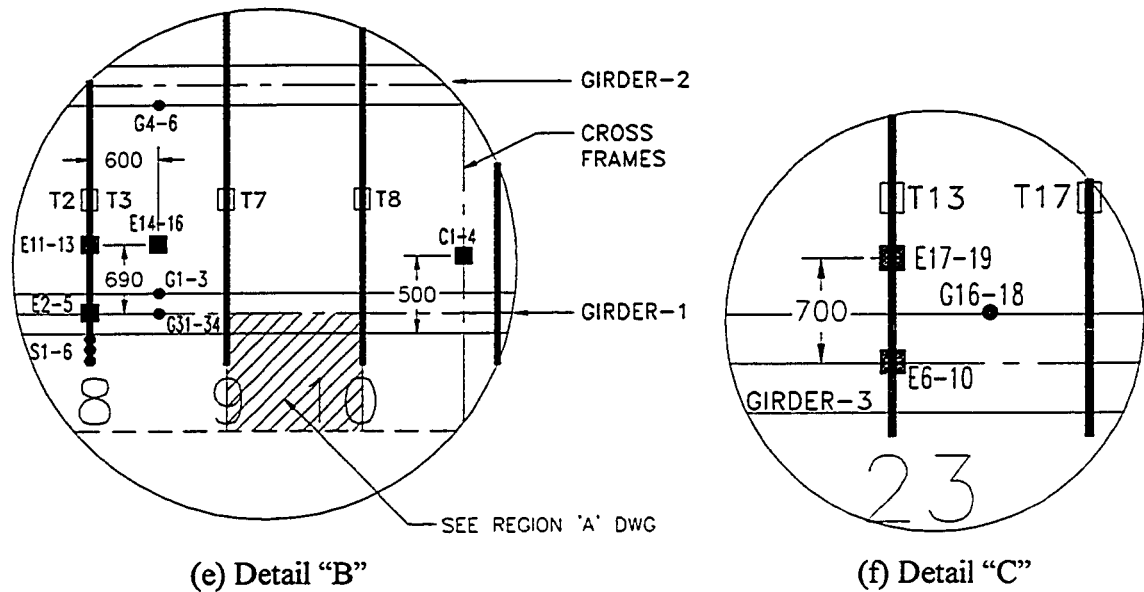


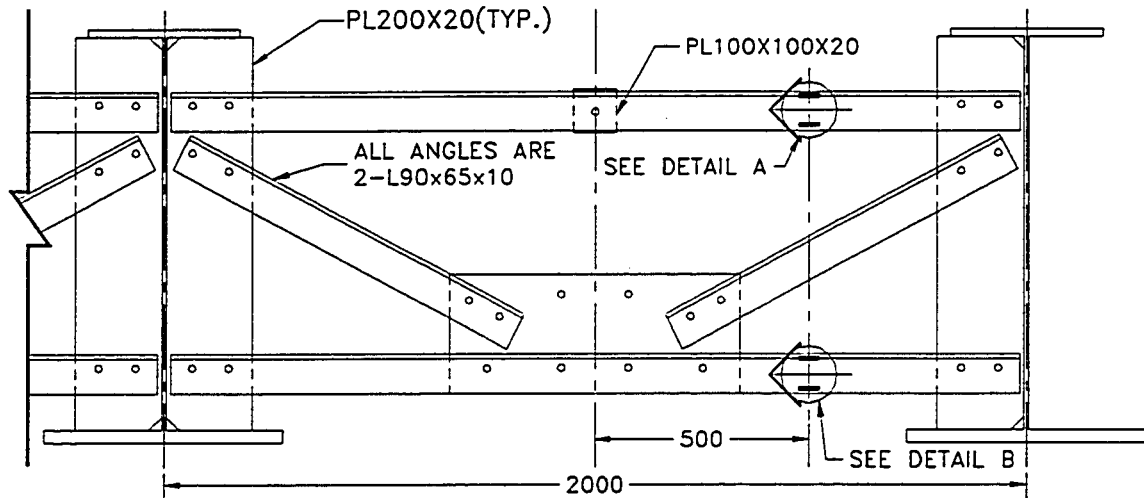
Figure 3.4: Instrumentation Used in the Crowchild Bridge (Cont'd)

Figure 3.5 shows the North elevation of the cross frame. All the strain gauges on the cross frame were located at one quarter of the distance between the two girders in order to stay away from the region of disturbance at mid-span. Photo 3.8 shows the completed cross frames on Crowchild Bridge.

Detail "A" in Figure 3.5 shows the location of the gauges on the top horizontal member of the cross frame. *Detail "B"* in Figure 3.5 shows the location of the gauges on the bottom horizontal member of the cross frame. Strain gauges C1 and C3 were used to evaluate the load sharing between the girders. Strain gauges C2 and C4 were placed as shown in Figure 3.5 to monitor the out of plane movement of the cross frame under heavy loading. The cross frame members consist of two L90 x 65 x 10 mm back-to-back. The typical space between the two back-to-back angles is 20 mm, as shown in *Detail "B"*. A 100 x 100 x 20 mm gusset plate is bolted between these two angles at the mid-span between the girders.

To control the alignment and position of the concrete strain gauges and the thermistors in the cast-in-place concrete deck, the thermistors and the concrete strain gauges were embedded in precast concrete blocks. The concrete blocks were sand blasted

to improve bond with the deck concrete. Photos 3.11 and 3.12 show the formwork used for the blocks of embedded concrete strain gauges and thermistors, respectively.



North Elevation View of Typical Cross Frame Layout

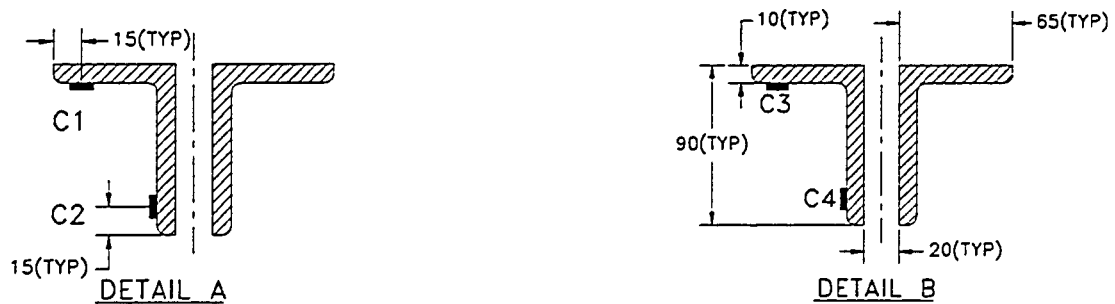


Figure 3.5: Instrumentation on Cross Frame

Photos 3.13 through 3.15 show the completed precast blocks, field placement of these precast blocks and the casting of concrete deck. Figure 3.6 shows the location of the gauges and the precast concrete blocks for the embedded concrete strain gauges. To monitor the arching action in the concrete deck, seventeen embedded concrete strain gauges were installed in five precast concrete blocks. Blocks 1 and 4 each had four strain gauges and blocks 2, 3, and 5 each had three strain gauges as shown in Figure 3.6.

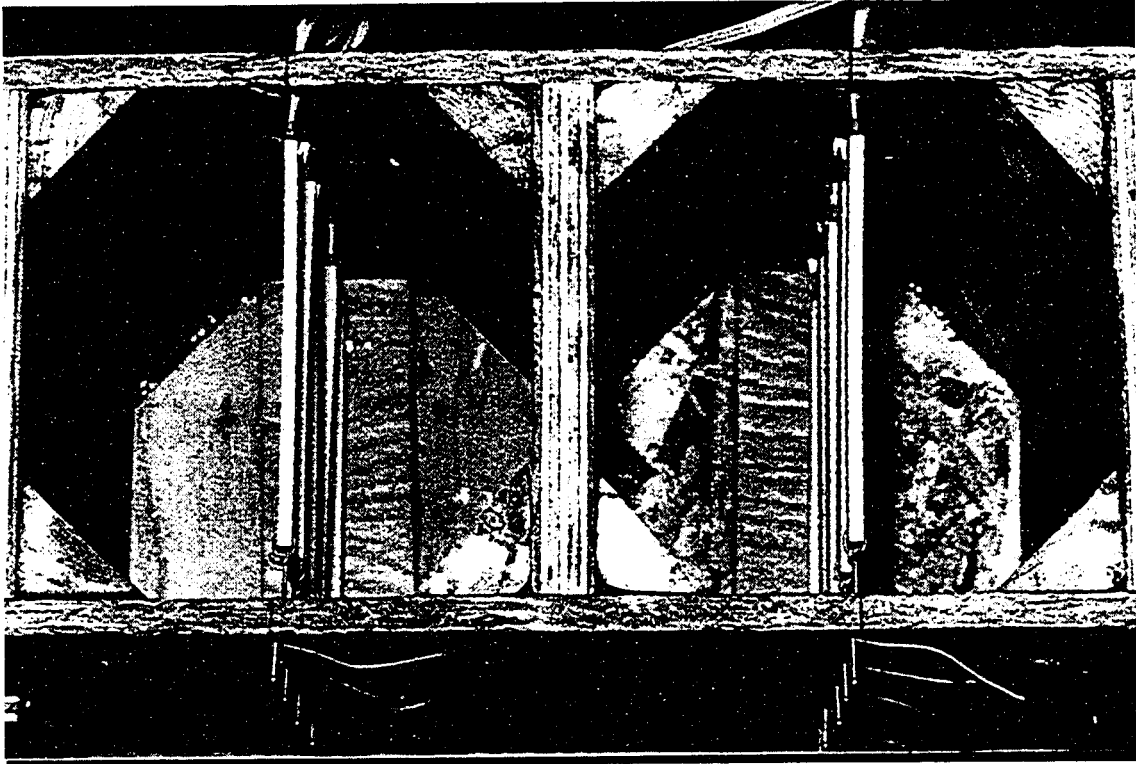


Photo 3.11: Formwork for the Embedded Concrete Strain Gauges

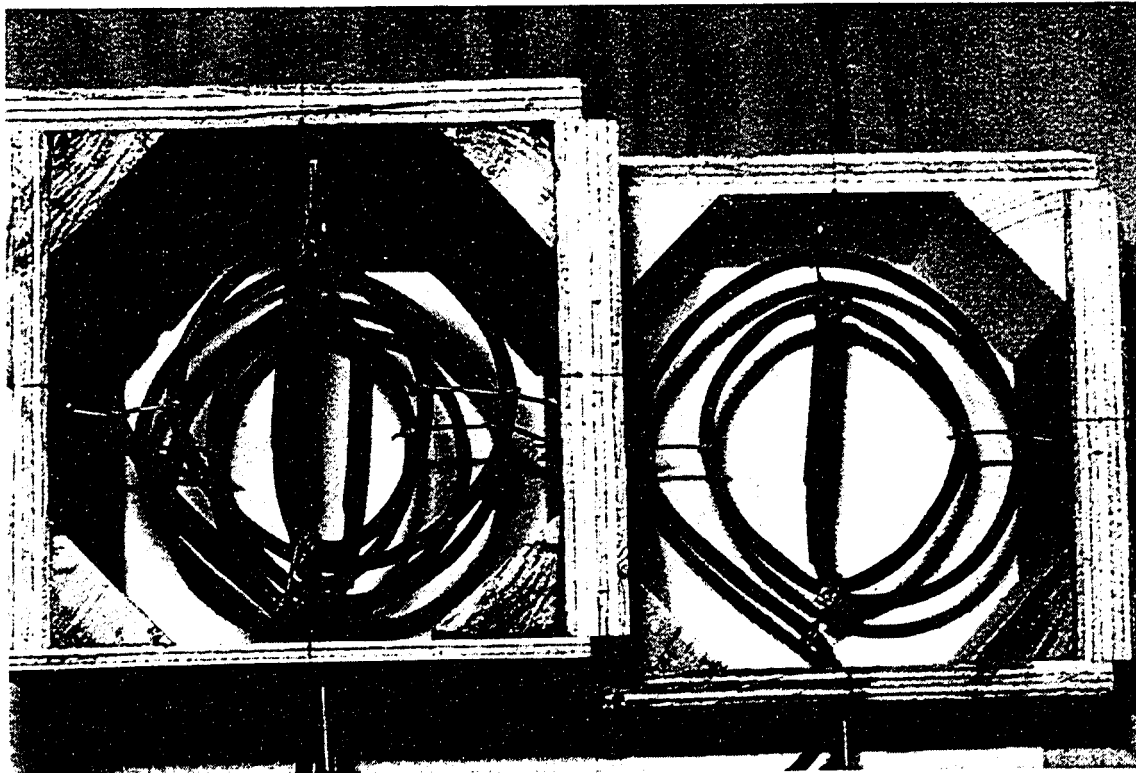


Photo 3.12: Formwork for the Embedded Thermistors



Photo 3.13: Precast Blocks for Embedded Instruments

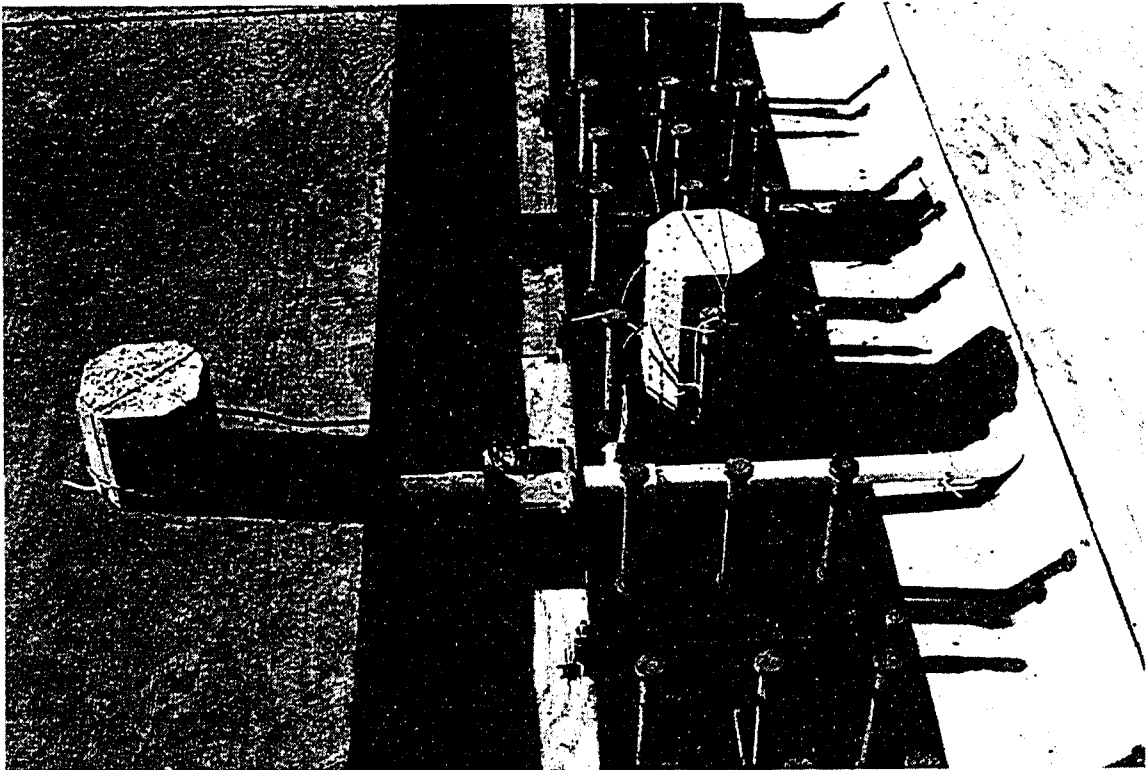


Photo 3.14: Precast Blocks for Embedded Thermistors (Field Placement)

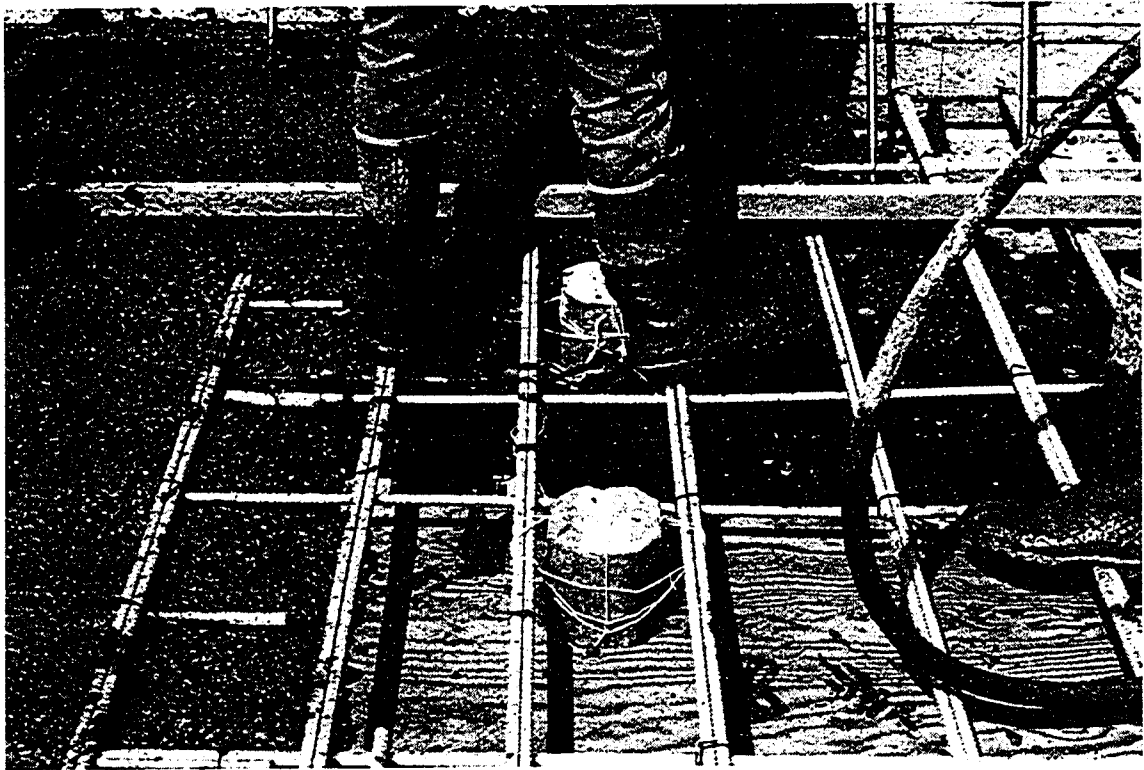


Photo 3.15: Precast Blocks for Embedded Concrete Strain Gauges (Field Placement and Concrete Casting)

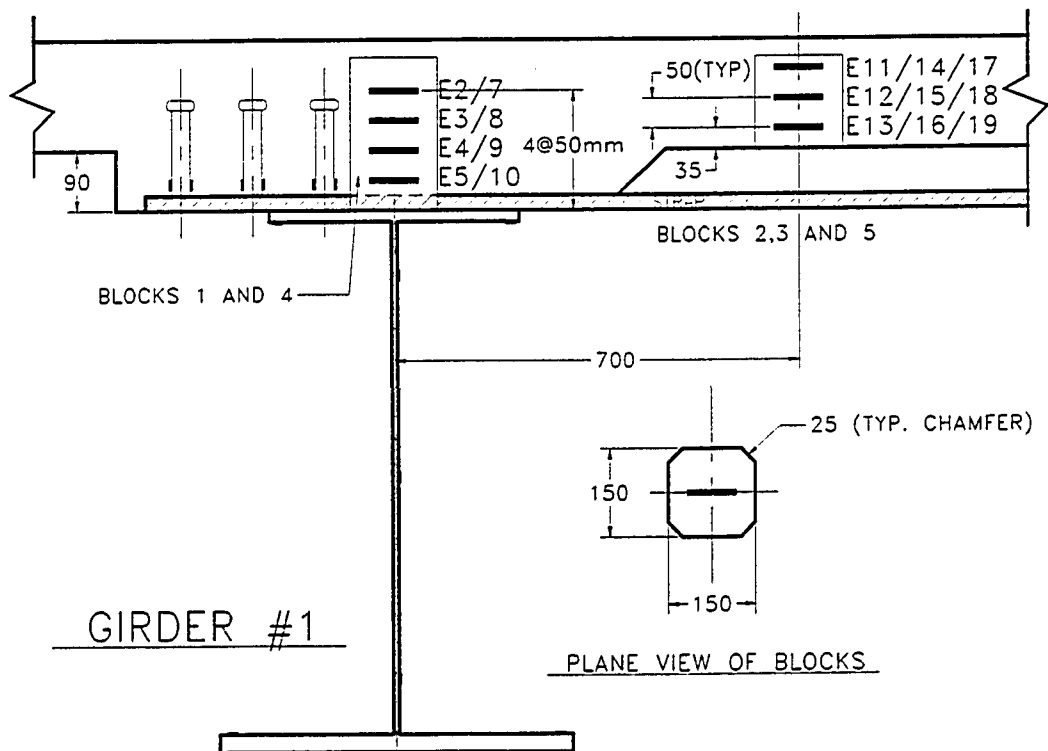


Figure 3.6: Embedded Concrete Strain Gauges

Locating on top of girder #1, as shown in Figure 3.6, Block 1 had gauges E2 to E5 and Block 4 had gauges E7 to E10. Blocks 2, 3 and 5 had gauges E11 to E13, E14 to E16, and E17 to E19 respectively. Blocks 1, 2, and 3 shown in Figure 3.6 were placed in the positive moment region. Blocks 1 and 2 were placed on the eighth strap, 8770 mm from the centreline of the North Abutment diaphragm as shown in the layout drawing *Detail "B"* in Figure 3.4. Block 3 was placed 600 mm South of the eighth strap between girders 1 and 2 as shown in *Detail "B"* of Figure 3.4. Photo 3.6 shows the field placement of blocks 1, 2 and 3.

Blocks 4 and 5 were placed in the negative moment region on top of strap number 23 at 3400 mm North of centerline of Pier No. 1 (see *Detail "C"* shown in Figure 3.4 and layout drawing number T200004A in Appendix A). These gauges have an overall length of 120 mm, a nominal gauge factor of 2.0, a resistance of 120 Ω , and are temperature compensated for concrete. The thermal output of these gauges is $\pm 1.8 \mu\epsilon/^{\circ}\text{C}$ between 0 $^{\circ}\text{C}$ and 60 $^{\circ}\text{C}$.

Four thermistors monitored the temperature profile in the deck and a fifth thermistor measured air temperature. The location of the embedded thermistors is shown in Figure 3.7. Three of the four embedded thermistors namely TH1, TH2 and TH4 were placed inside the concrete deck as shown and TH3 thermistor was placed on the boundary of the concrete deck and steel girder. A plan view of the blocks in Figure 3.7 shows the coil of the thermistors wrapped at least two revolutions inside the concrete block before extending out of the concrete. This precaution is taken to minimize effect of the temperature conductivity through the lead wires of the thermistors. Photos 3.12 and 3.13 show the formwork and completed precast blocks for the thermistors and Photo 3.14 shows the field placement of the blocks.

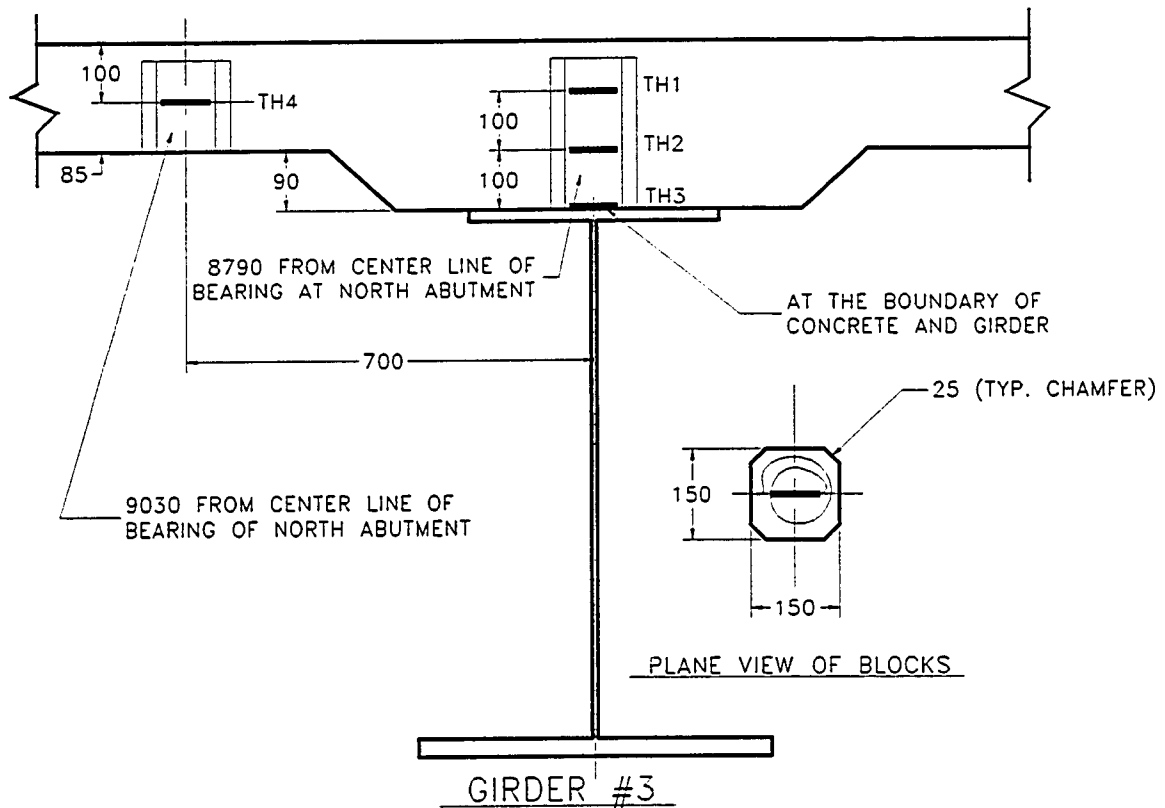


Figure 3.7: Embedded Thermistors

Eighteen strain gauges were used to monitor the performance of the steel straps. Twelve of the gauges, placed between girders 1 and 2, were used to examine the response of the straps along the length of the bridge. Straps close to the supports and cross frames are expected to carry less load than straps that are further away. The other six gauges were used to monitor strain distribution along one steel strap. Three strain gauges were placed on strap # 8 and the other three gauges on strap # 23 in the positive and negative moment region, respectively. Figure 3.8 shows a typical cross sectional view of the straps that were instrumented.



Figure 3.8: Gauges on Steel Straps

Six strain gauges were used to monitor strains in the end shear studs at 8430 mm from centerline of the North end bearing. Figure 3.9 shows the location of these strain gauges.

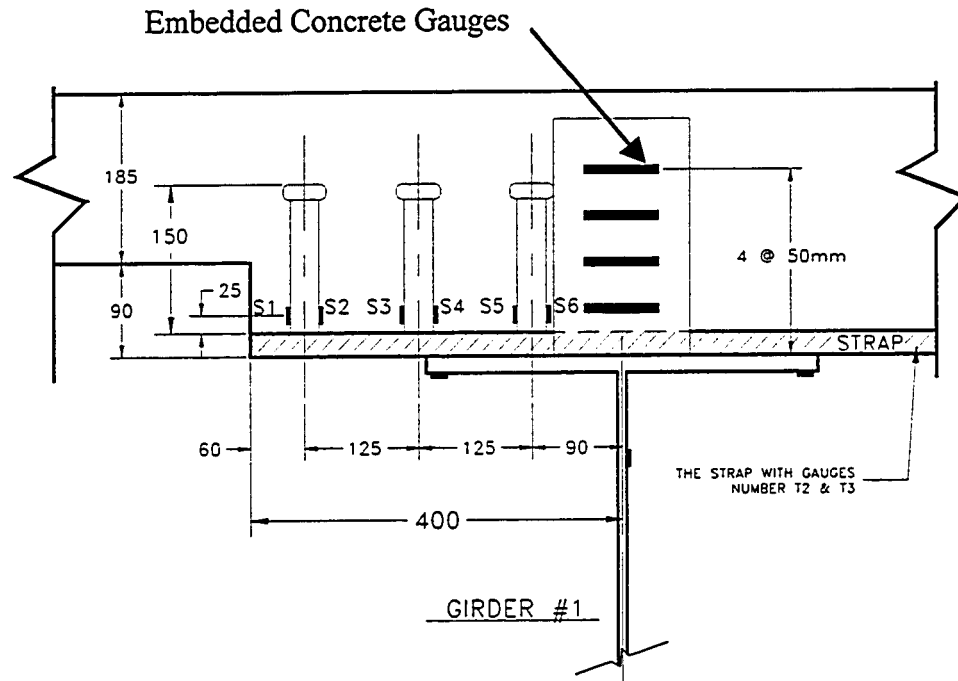
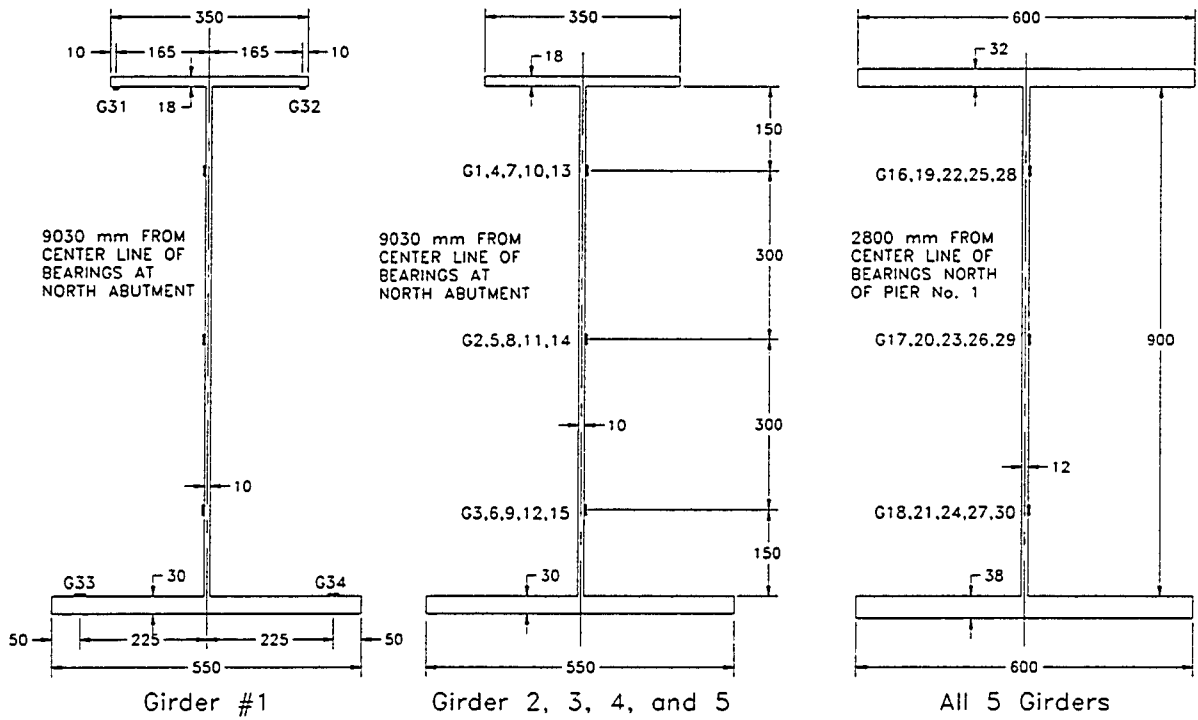


Figure 3.9: Gauges on Shear Studs

Thirty-four strain gauges were used to monitor strains in the steel girders. As shown in Figure 3.10, the webs of all five girders were instrumented with three gauges at both the positive and the negative moment regions to monitor load sharing among the girders and moment distributions along the girders. Furthermore, four gauges were also installed on the flanges of girder 1 to measure any warping of the girders and to better examine the strain distribution at a cross section. Figure 3.10 shows the location of the gauges on the girders.

At the side barriers, two strain gauges were installed on NEFMAC and two on a stainless steel bar. Figure 3.11 and Photo 3.6 show in detail the installed gauges on the NEFMAC and a stainless steel bar.



Sections at Positive Moment Region

Section At Negative Moment Region

Figure 3.10: Strain Gauges on Girders

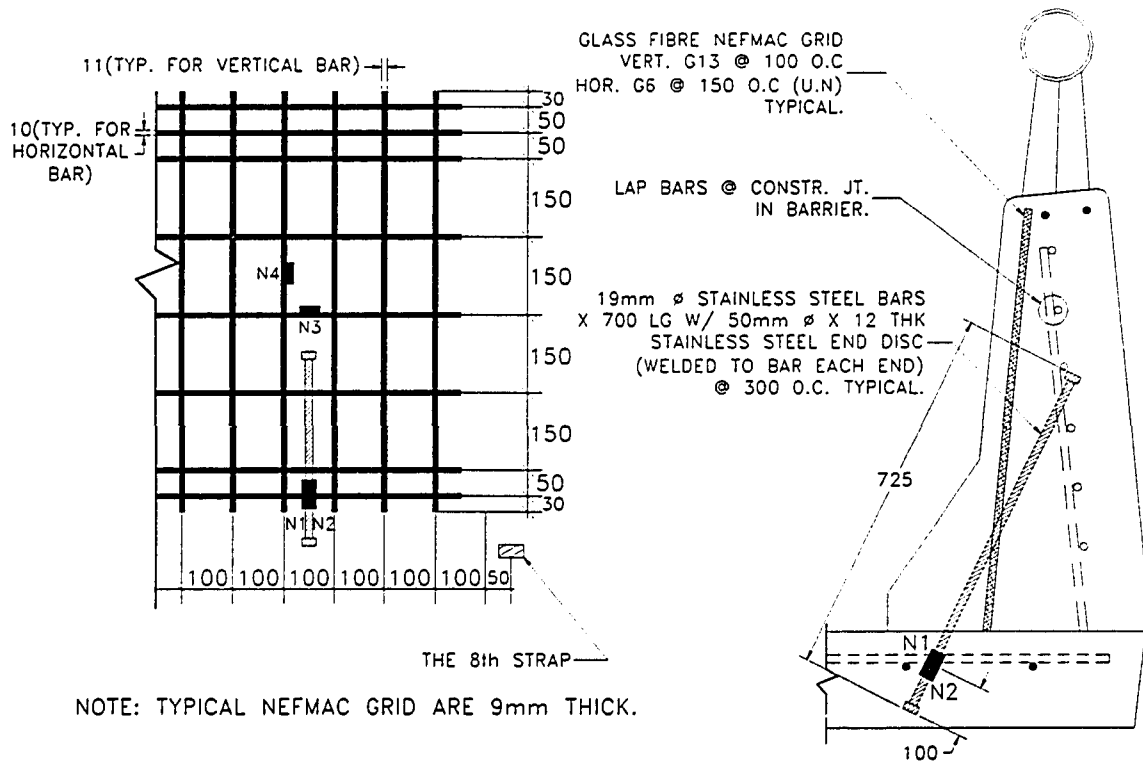


Figure 3.11: Gauges on NEFMAC and Stainless Steel Bar

The distance from the center line of the diaphragm at the North abutment is 9170 mm to the instrumented stainless steel bar or 400 mm South of strap number 8.

3.4 Field Testing

3.4.1 Tests Performed on Crowchild Trail Bridge

Since the superstructure of the Crowchild Bridge was replaced in 1997, five sets of tests have been conducted. All five different sets of tests done on the bridge up to August 1998 are summarized in Table 3.4. Tests in October 1997 and June 1998 were conducted with unknown axles load, speed, and location of load. Some investigation of the October 1997 data on the load sharing due to overall deflection is shown in Appendix B. Tests in October 1997 and June 1998 and the temperature investigation in September 1997 were detailed in the *Field Instrumentation and Monitoring of Crowchild Trail Bridge* report (Cheng and Afhami, 1999) and will not be covered here. Since tests in August 1997 and August 1998 were conducted with known axles load, these two tests are investigated in details as outlined in Chapter 4. Some comparison analysis of August 1997, October 1997 and August 1998 are shown in Chapter 5.

Table 3.4: Tests Performed on Crowchild Bridge

Test	Measurements	Comments
<i>I. August '97</i>		
Ambient Vibration	Acceleration	UBC performed the test before the Bridge was open to traffic
Field Survey	Deflections	Truck load was known accurately
Static Test	Strains	Truck load was known accurately
Mapping Cracks	Mapping Cracks	Mapping of crack patterns
<i>II. September '97</i>		
Temperature Test	Strains, and Temperatures	Test performed under known temperature changes
<i>III. October '97</i>		
Dynamic Test	Strains	Tests performed under unknown traffic loading
<i>IV. June '98</i>		
Dynamic Test	Strains	Tests performed under unknown traffic loading
<i>V. August '98</i>		
Ambient Vibration	Acceleration	U of A tested the bridge after it was in operation for one full year.
Dynamic Test	Strain, Deflection, and Acceleration	Truck load was known accurately
Static Test	Strain and Deflection	Truck load was known accurately
Mapping Cracks	Mapping Cracks	Mapping of crack patterns

4. EXPERIMENTAL RESULTS

4.1 Results of the August 1997 Test

In August 97, just prior to the first opening of the bridge to traffic, a research team from the University of British Columbia (UBC) performed an ambient vibration test on Crowchild Trail Bridge (Ventura *et al.*, 1997). Ambient vibration tests do not involve direct force excitation, but rather just forces from wind, surrounding traffic, human activities etc. Measurements from ambient vibration tests are typically taken over a longer period than for dynamic tests to ensure that all modes of interest have been excited. The peaks in the Averaged Normalized Power Spectral Density of ambient vibration measurements from different locations on the structures are then determined and used to estimate the natural frequencies of the structure. It is worth noting that dynamic properties of structures at low level of excitation may be slightly different from high level of excitation.

Prior to the ambient vibration tests, University of Alberta, the City of Calgary and Speco Consultants performed static tests. Two heavily loaded tractor-trailer trucks were used in the static test. Vertical deflection points were measured by surveying, and strain measurements were recorded using strain indicators. Finally, an initial crack pattern was mapped.

4.1.1 Ambient Vibration Results from UBC

Data acquisition systems used in the ambient vibration test on the Crowchild Trail Bridge by UBC are as follows (Ventura *et al.*, 1997):

- Forced-balanced accelerometers, kinematics model FBA-11 capable of measuring up to ± 0.5 g with a resolution of $0.2 \mu\text{g}$.

- Signal Conditioners, which used to remove undesired frequency contents and amplify the signals. All filter cards (Kinometrics AM3) were set to a cut-off frequency of 50 Hz.
- Analog to digital converter used was Keithly Model 575 AMM2 board.

Measurements were obtained when there was no traffic on the bridge, thus the only forces acting on the bridge during the ambient vibration tests were wind, human activity, traffic below and beside the overpass. Due to limited number of accelerometers available, 14 different setups were required. In 11 of the 14 setups two accelerometers were used as references and in the remaining three setups three accelerometers were used as references. In phase analysis, reference accelerometer is required to establish the relationships between the different setups. Eight accelerometers were used to monitor the acceleration at 46 locations. The acceleration was monitored at 44 different locations in the bridge deck, one near the base of Pier No.1 and one near the base of Pier No. 2. Locations of the accelerometers are listed in UBC report EQ97-005 (Ventura *et al.*, 1997). The temperature at the bridge site during the test was approximately 8°C with moderate to heavy rain for the majority of the test. The maximum recorded level of vibration was approximately 1.7 milli-g's.

In identifying natural frequencies, Ventura *et al.* (1997) used an average of 64 records in the vertical direction, 40 records in the transverse direction, and 7 records in the longitudinal direction. The most significant peaks between 0 and 20 Hz were identified. Ventura *et al.* (1997) suggested that the results were preliminary and needed to be complemented with results of finite element analyses. Furthermore, the resolution of higher vibration modes was not as good due to the limited number of measuring points. It was suggested that some modes are highly coupled and current techniques for ambient vibration data analysis have difficulty handling these situations.

The ambient vibration tests were performed by UBC on the Crowchild Trail Bridge on August 15, 1997, between 9:00 AM to 11:00 PM. The tests identified 13

natural frequencies between 0 and 20 Hz. A list of these natural frequencies is given in Table 4.1.

Table 4.1: Natural Frequencies Between 0 - 20 Hz.

<i>Peak</i>	<i>Frequency (Hz)</i>	<i>Mode Shape</i>
1	2.78	1 st Fundamental Vertical
2	3.13	1 st Fundamental Torsional
3	3.76	2 nd Vertical Mode
4	4.05	2 rd Torsional Mode
5	4.64	3 rd Vertical Mode
6	5.18	3 th Torsional Mode
7	7.13	4 th Torsional Mode
8	9.13	4 th Vertical Mode
9	10.94	6 th Torsional
10	12.99	6 th Fundamental Transverse
11	15.63	6 th Couple Torsional
12	17.87	5 th Vertical
13	19.24	7 th Torsional

4.1.2 Static Test Results

For the static tests, two trucks, each weighing approximately 357 kN, as shown in Figure 4.1, were used for nine different load cases, P1 to P9. The two trucks used in the tests; they had approximately the same axles load and spacing of the axles as illustrated in Figure 4.1. Figure 4.2 shows the locations of the truck on the North span of the bridge for the nine different load cases used in the static tests, P1 to P9. The trucks were facing north for all tests. The nine load points are shown by the 'X' marks running between girder 1 and girder 2. These 'X' marks are in reference to the front axial of the truck's left wheel. In all the tests, the trucks were moving from South to North. For six of the nine load cases, the two trucks were parked side by side at points P1 to P6 along the bridge as

shown in Figure 4.2. For load points P1 to P6, the layout positions of the two trucks in the transverse direction of the bridge are as follows: facing north, the truck on the West side; its' left wheel of the front axle is at midpoint between girder 1 and girder 2. Since the two trucks were parked side by side, the truck on the East side, its' right wheel of the front axle is at an approximate midpoint between girder 4 and girder 5. The bridge was therefore loaded symmetrically. For the last three load cases, P7 to P9, only one truck was used for the tests. The layout positions of the truck for load cases P7 to P9 in the transverse direction of the bridge are facing north; the truck's left wheel is at an approximate midpoint between girder 1 and girder 2.

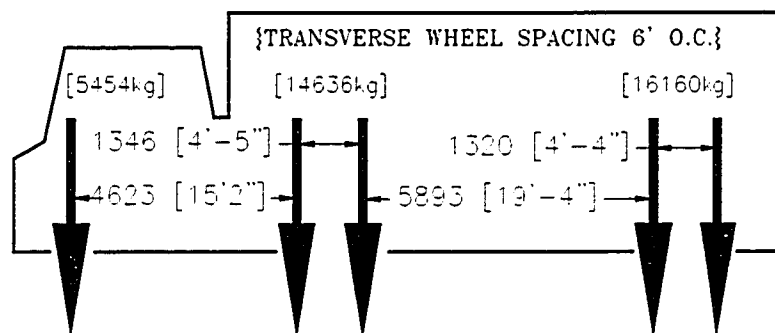


Figure 4.1: Trucks Use in August 97 Test

For all nine load cases, strain readings were recorded at the same time as the surveying measurements. For each loading condition, 25 deflection points were surveyed, namely, five points along each girder in the North span. The survey points are identified as A1-A5, B1-B5, C1-C5, D1-D5, and E1-E5 in Figure 4.2. The field survey results and their corresponding load points are shown in Table 4.2. All the corresponding strain gauge readings are presented in Appendix B.

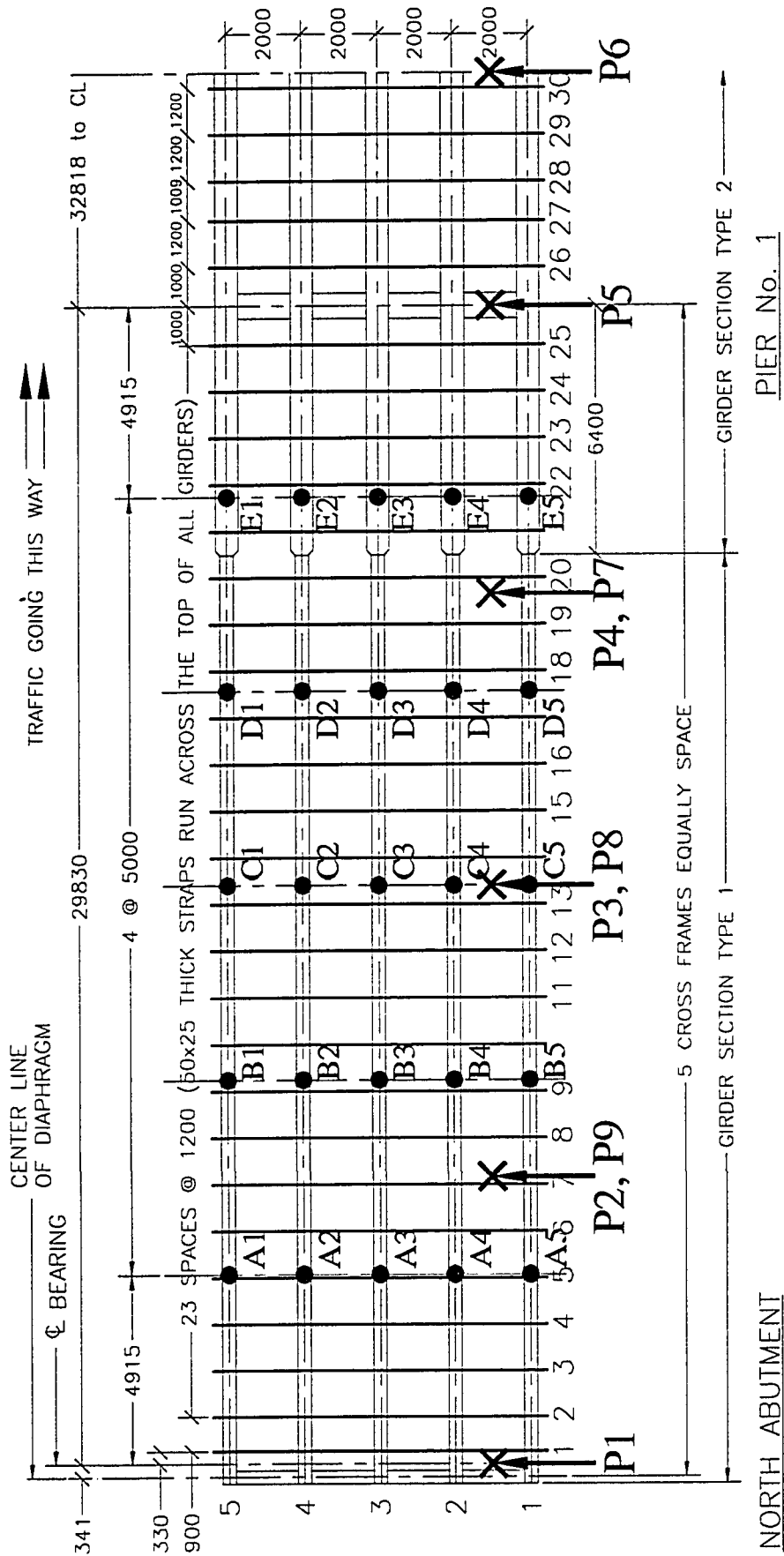


Figure 4.2: Load Points and Survey Points [August 1997]

Table 4.2: Static Tests-Survey Deflections Measurements, mm [August 1997]

	No truck	P1	P2	P3	P4	P5	P6	P7	P8	P9	No truck
A1	1	1	1	-1	-6	-8	-6	1	-1	-1	-1
A2	0	1	1	0	-5	-8	-5	0	-1	-2	0
A3	1	3	3	-1	-3	-6	-6	0	-1	-2	-1
A4	2	3	3	-2	-3	-7	-7	-1	-3	-5	-2
A5	1	2	2	1	-4	-7	-6	-1	-4	-7	-1
B1	2	3	3	-3	-8	-13	-12	-2	-2	-2	-2
B2	1	3	3	-2	-8	-12	-12	-1	-2	-3	-1
B3	2	3	3	-3	-9	-13	-13	-3	-6	-7	-2
B4	2	4	3	-3	-11	-14	-14	-4	-8	-11	-2
B5	1	5	4	-1	-8	-11	-10	-2	-9	-13	-1
C1	1	4	3	-5	-11	-15.0	-12	-1	-1.0	-1.0	-1
C2	2	4	3	-3	-12	-16.5	-14	-2	-3.5	-4.5	-2
C3	2	4	4	-3	-12	-14.5	-13	-2	-5.5	-7.5	-2
C4	2	5	5	-2	-10	-14.5	-12	-2	-7.5	-11.5	-2
C5	2	6.5	6	2	-8	-12.5	-13	-1	-9.5	-13.5	-2
D1	1	4	3	-5	-10	-12	-11	-1	-1	-1	-1
D2	1	6	4	-3	-9	-13	-10	-2	-3	-3	-1
D3	1	5	4	-2	-9	-13	-11	-1	-6	-6	-1
D4	1	6	6	-1	-9	-12	-10	-1	-7	-9	-1
D5	2	7.0	6	0	-7	-8	-8	-2	-8	-11	-2
E1	0	4	2	-2	-6	-8	-6	0	-1	-1	0
E2	1	3	2	-3	-6	-8	-6	0	-2	-3	-1
E3	1	5	4	-1	-7	-8	-7	-1	-4	-5	-1
E4	1	4	4	-1	-6	-6	-6	-1	-5	-6	-1
E5	2	5	4	-1	-5	-7	-5	-2	-7	-7	-2
Max	2	7	6	2	-3	-6	-5	1	-1	-1	0
Min	0	1	1	-5	-12	-17	-14	-4	-10	-14	-2

4.1.2.1 Survey Results

The maximum deflection in the North span was 17 mm downward at survey point C2, when the front axles of the two trucks were placed at load point P5. Figure 4.3 shows the deflections for the five girders at survey points C1 to C5 for this load case. In turns, these deflection measurements can be used to assess the level of load sharing between the girders.

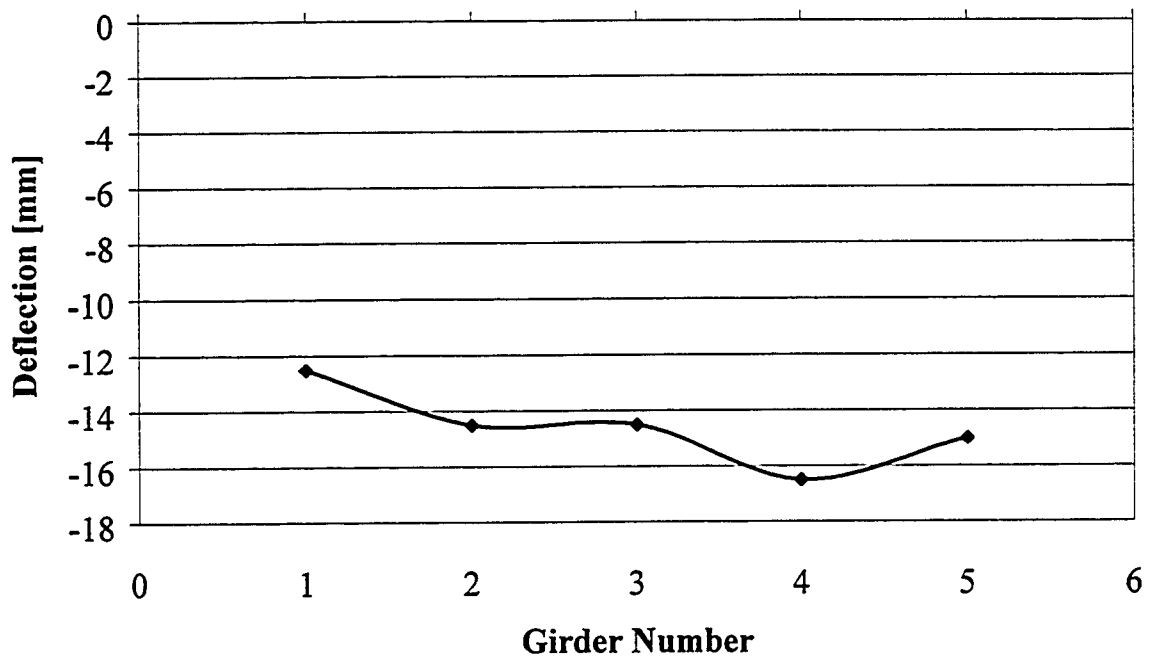


Figure 4.3: Deflection at C1 to C5 for Load Case P5

Figure 4.4 shows the deflection for all five girders at the measurement points C1 to C5 for load case P1. For this load case P1, the two trucks were on the middle span, the maximum deflection in the North span was 7 mm upward at C5 as shown in Figure 4.4. Although the bridge was loaded symmetrically, girder 1 shows the highest deflection of all five girders. Girder 4 in Figure 4.4 shows the least among of deflection among the five girders. Deflection results from August 1997 were done by surveying, thus its may scatter significantly.

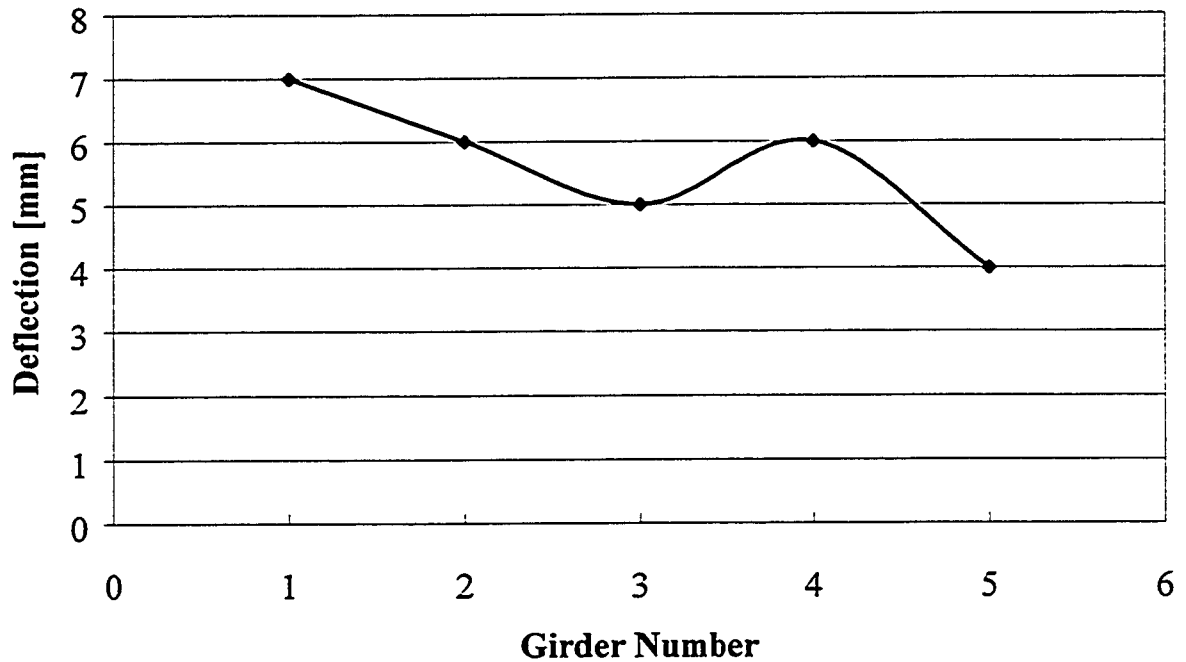


Figure 4.4: Deflection at C1 to C5 for Load Case P1

To impose an eccentric loading on the superstructure, the front axle of a truck is placed at load point P9. The resulting deflection measured in the girders is shown in Figure 4.5 below. The maximum deflection under the truck load is 13.5 mm at C1 for girder 1. At this time, the cross frame between the girders perform very well in redistributing its load among it neighboring girders. Note the slight non-linearity in load sharing among the girders for girder 2. This is expected because under tributary area, it is carrying twice the load as its neighboring girders under this loading condition.

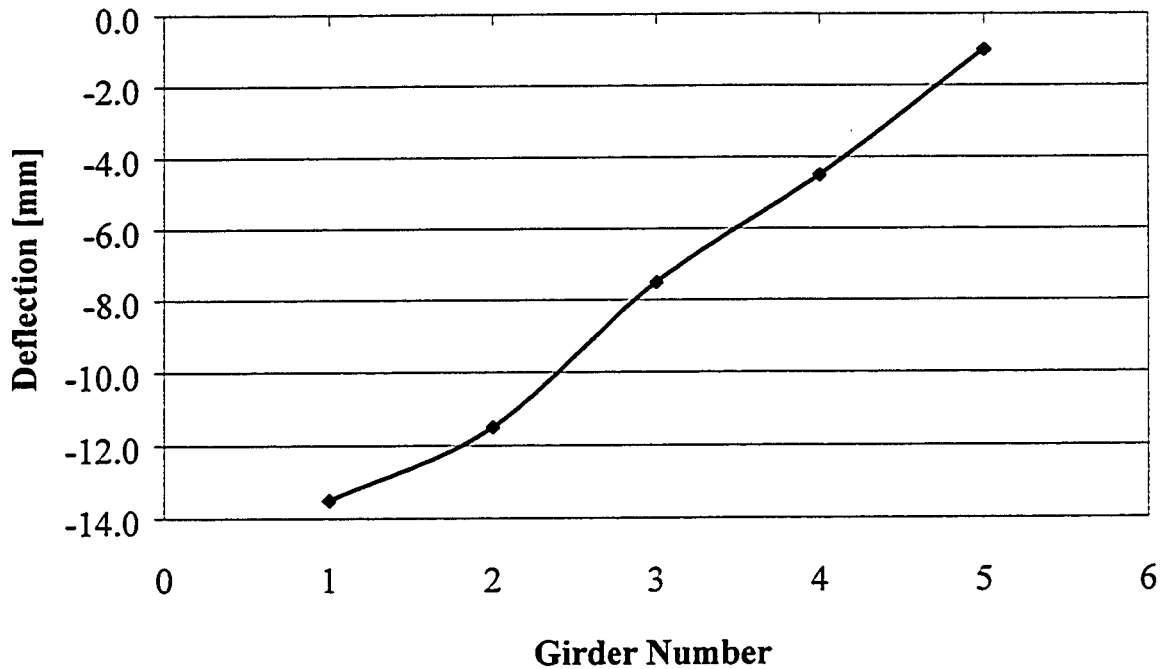


Figure 4.5: Deflection at C1 to C5 for Load Case P9

4.1.2.2 Results from Strain Measurements

A manual switch box was used to record the strains during the static test in August 1997. On August 11th, 1997, the first set of readings was taken at 6:30 a.m., just prior to placing asphalt. The air temperature at the time was 14°C. At 11:20 a.m. on the same day, a second reading was taken after the asphalt was placed and had cooled; the air temperature was 21°C. The strain gauge readings for before asphalt and after asphalt is placed are documented in Appendix B. In addition, strain gauge readings obtained for all the nine load cases are also presented in Appendix B. The strain gauge readings were used to find strain distribution in the cross section, the location of the neutral axis, assess the load sharing between girders, and compare the analysis results with the field test results. Furthermore, it provided the base structural characteristics of the bridge for future studies.

The strain distribution in girder 1 obtained from the measured strains is shown in Figure 4.6. With such loading configuration, the maximum measured strain is 103 $\mu\epsilon$ on

strain gauge G3. Although strain gauges G33 and G34 show smaller strain than G3, nonetheless, strain distribution in the cross section is still linear otherwise. Field investigation showed that strain gauges G33 and G34 had poor connections, hence they are unreliable. The small strains indicate that the bridge response was well within the elastic range. Note the neutral axis is at 54.1 mm below the bottom of the top flange.

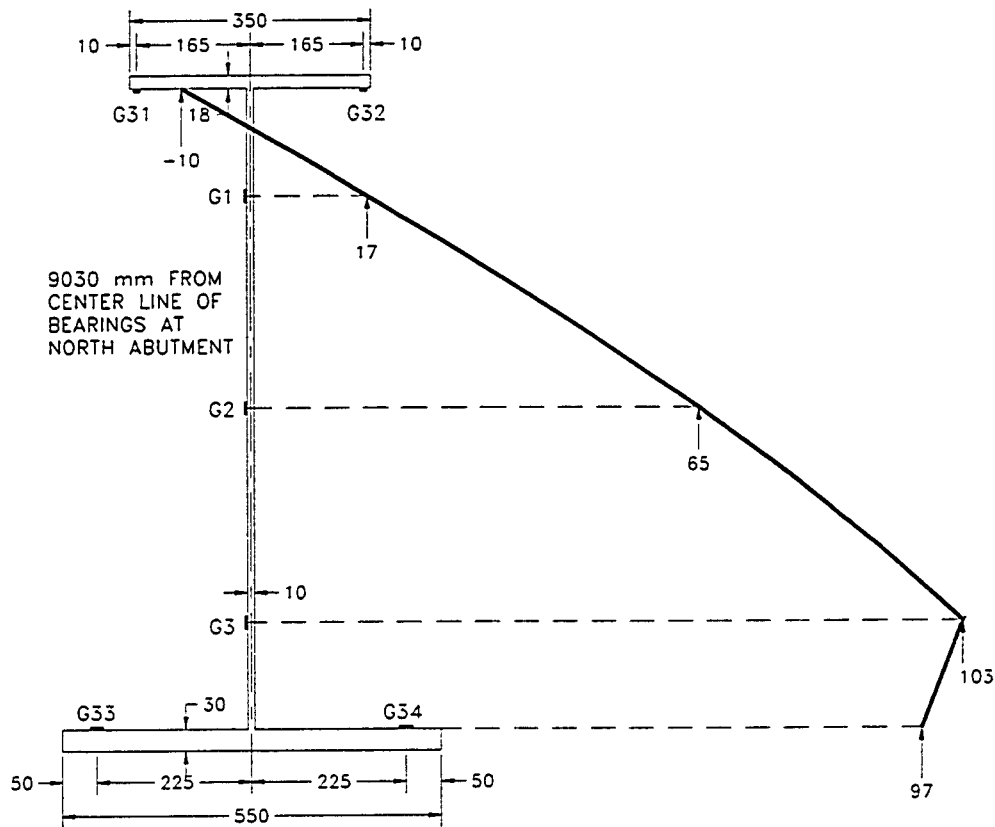


Figure 4.6: Positive Moment Region Strain Distribution in Girder #1

For the same load case P9, the strain distribution in the negative moment region is shown in Figure 4.7. Despite the slight non-linearity, the strain distribution is essentially linear. From extrapolation, the high compressive strain in the bottom flange is $30.7 \mu\epsilon$. The neutral axis is at 93 mm below the bottom side of the top flange. The change in the location of the neutral axis in the negative moment region reflects the change in composite action of the member.

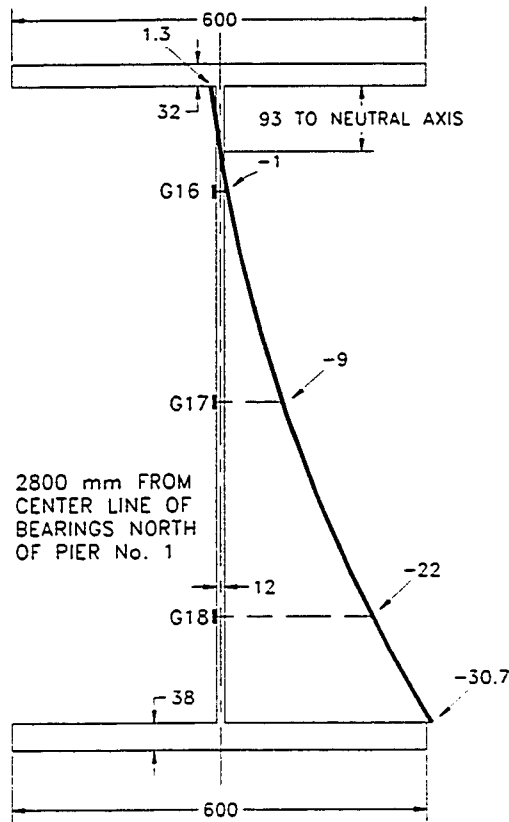


Figure 4.7: Negative Moment Region--Strain Distribution in Girder #1

Load sharing between girders is best examined by using the measured strains in the girders. On all web of the girders in positive and negative moment regions, there are longitudinal strain gauges at 150 mm from the topside of the bottom flanges. When one truck is loaded at load point P9, load sharing among the girders were based on strain gauge measurements as shown in Figure 4.8. The maximum strain under this loading condition is $103 \mu\epsilon$ on girder 1 in the positive moment region. In the negative moment region, the maximum compressive strain is $22 \mu\epsilon$ in girder 1 and girder 2. Note the strains on girders in the negative moment region; almost all have the same magnitude. This would indicate that the load distribution by the diaphragm over the pier is very effective in distributing the load.

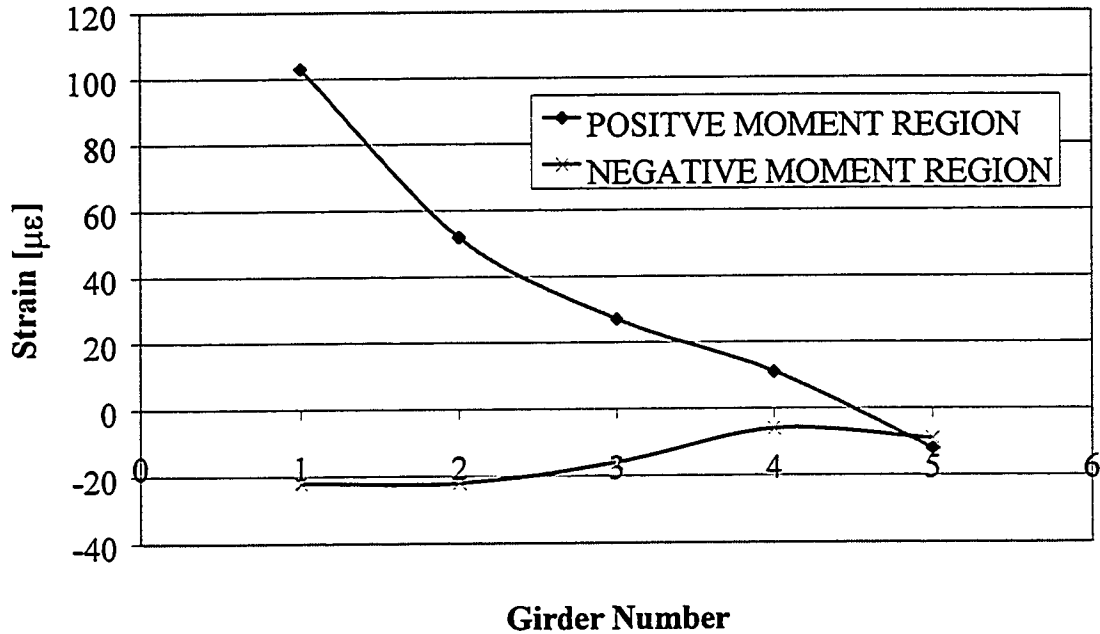


Figure 4.8: Strains in Positive and Negative Moment Regions for August 1997

4.1.3 Crack Pattern for August 1997

Crack patterns on the bottom side were mapped in August 1997 for the first time. The reader should recall that Crowchild Trail Bridge consists of three continuous spans. The South span was reinforced with both GFRP and steel reinforcement. The crack pattern detected in the south span as of August 1997 is shown in Figure 4.9. All cracks formed were transverse cracks. Most cracks at that stage were less than 0.5 mm in width. No longitudinal cracks were detected.

Figure 4.10 shows the crack pattern observed in the middle span, which is partially reinforced with GFRP bars and has no steel reinforcement. This appears to have more transverse cracks than the North or South span. The North span, reinforced only in the cantilever edge, has the least cracks as shown in Figure 4.11. All cracks width was approximately 0.5 mm. As of August 1997, there were no longitudinal cracks in any of the spans.

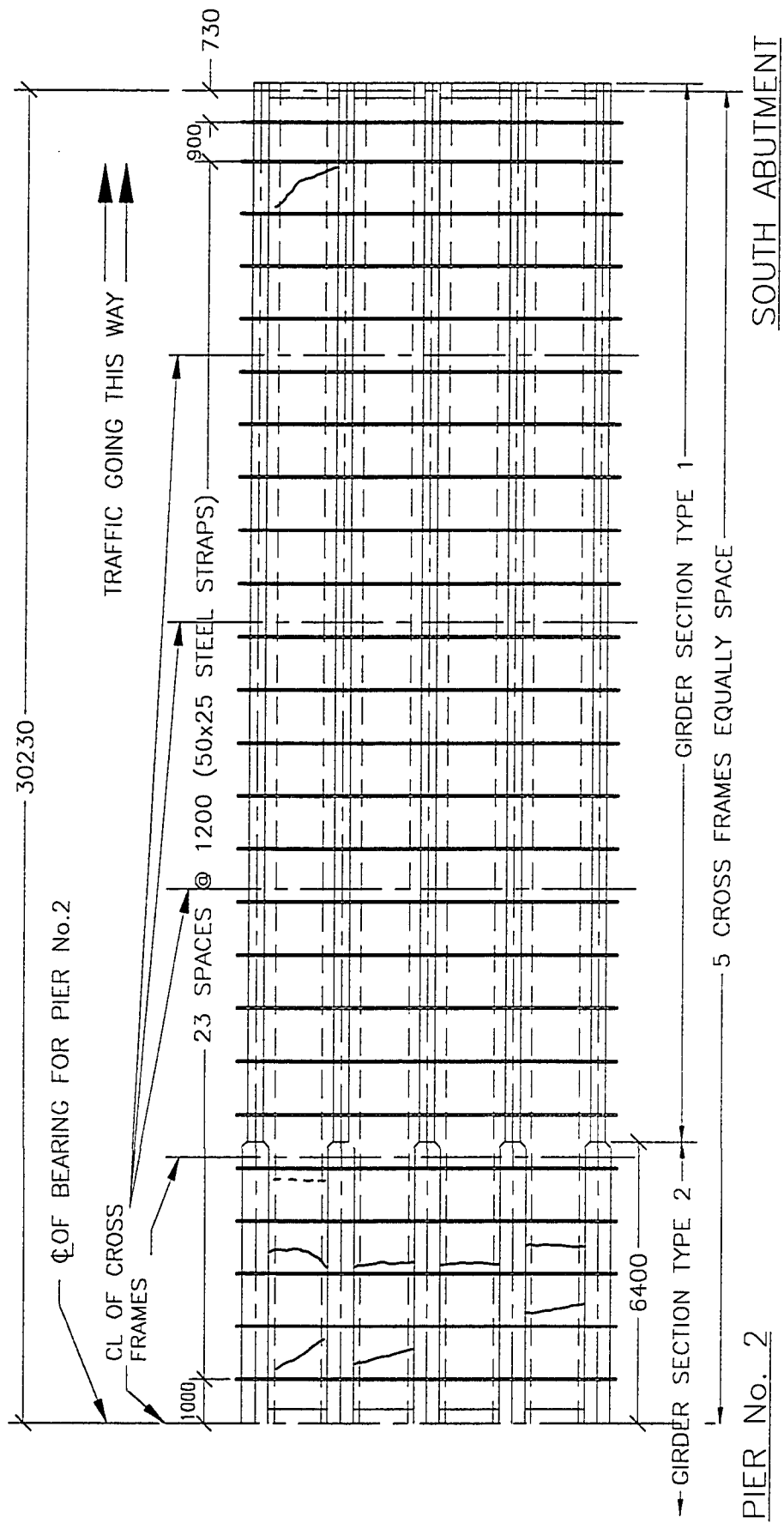


Figure 4.9: South Span Crack Pattern [August 1997]

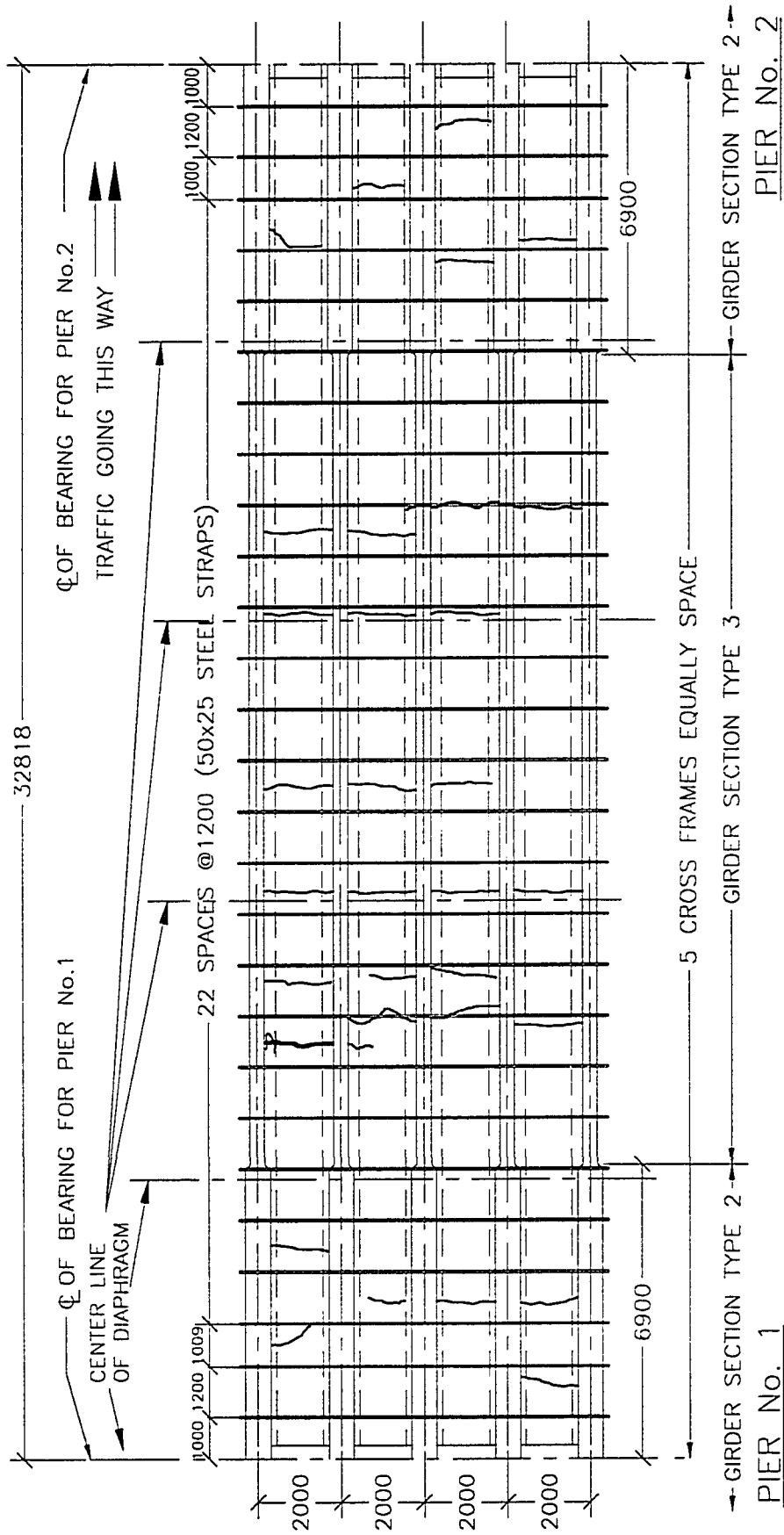


Figure 4.10: Middle Span Crack Pattern [August 1997]

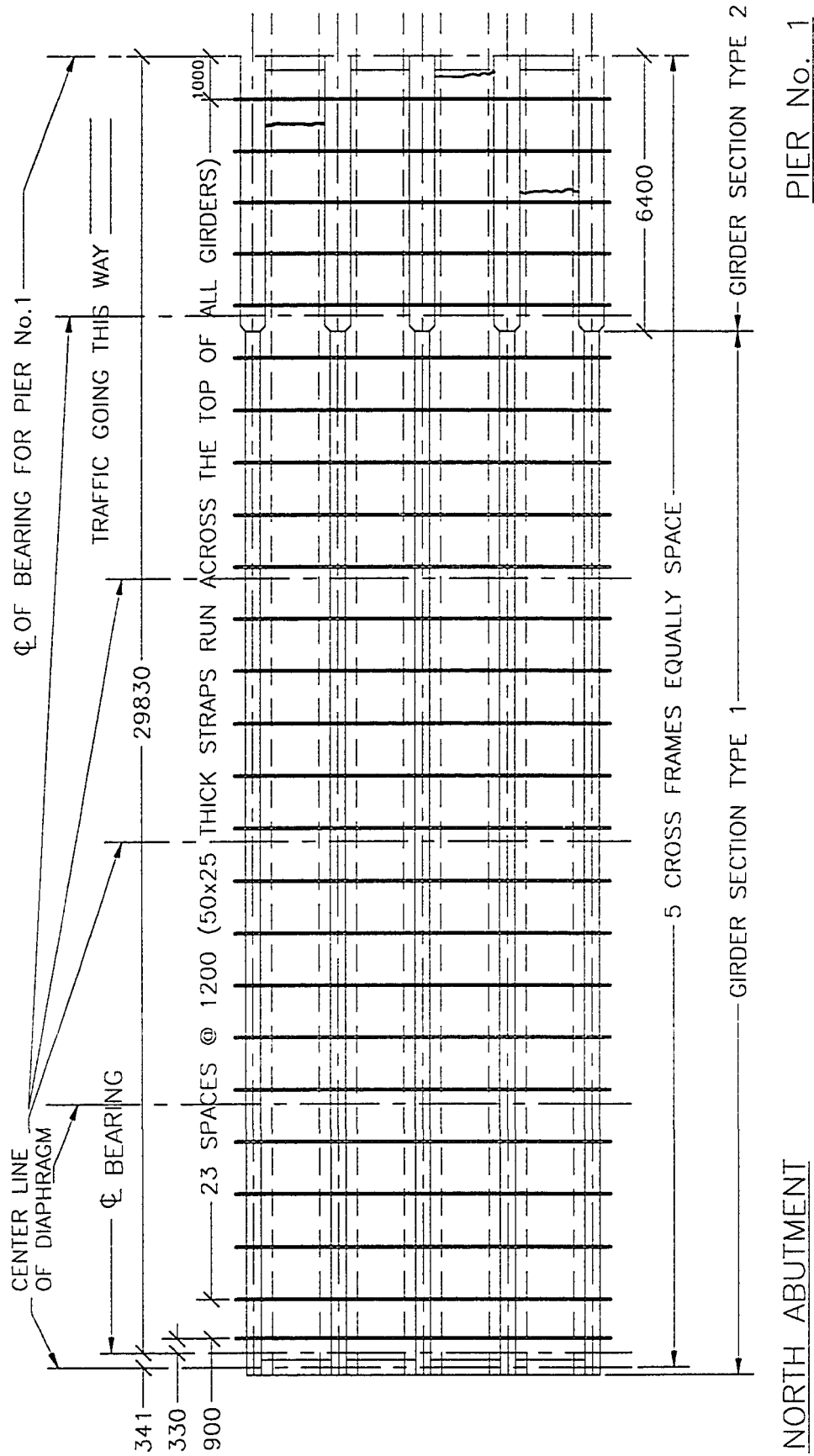


Figure 4.11: North Span Crack Pattern [August 1997]

4.2 Results of the August 1998 Test

By August 1998, Crowchild Trail Bridge had been in operation for one full year. Initial tests were carried out in August 1997, before the bridge was open to traffic, to establish base structural characteristics of the bridge. A second test was conducted in August 1998. The second test included static and dynamic load tests using truck with known axle loads and ran at various speeds. In addition to the electrical strain gauges installed in the first year, cable transducers and accelerometers were added in the second year test. Natural frequencies and mode shapes of the bridge were also determined by the ambient vibration test.

Results from the second test, such as load sharing between girders, dynamic load factor, bridge stiffness, natural frequencies and damping factor of the bridge, are presented. Where applicable, these results are compared to the base test results. In addition, the crack pattern of the concrete deck is mapped and compared to the pattern observed before the bridge was open to traffic. The changes in the bridge structural characteristics are used as an indication of the amount of deterioration of the Crowchild Trail Bridge during the first year of operation.

4.2.1 Ambient Vibration Tests

Field assessment of a full-scale real life structure in service was never an easy task. On August 1998, a second ambient vibration test was performed on the Crowchild Trail Bridge. The tests took less than two hours to perform with only one lane closed to traffic and the other closed only intermittently. The results from this second Ambient Vibration Tests are essential for comparison to the base structural characteristics of the bridge.

4.2.1.1 Objective and Problems

The objective is to use ambient vibration tests to determine the dynamic behavior [frequencies, mode shapes, stiffness, and torsional rigidity of the deck] of the Crowchild Trail Bridge. The selection of the proper tools and procedure was an important part of this investigation. During ambient vibration tests, the bridge is considered to be excited by various random low-level forces. Such random forces can be from wind, passing vehicle underneath the bridge and other human activities. Such random forces cannot be controlled, and the level of excitation is very low. Reliable results are possible, provided that:

1. Strains are small, and the system behaves linear elastically.
2. The level of excitation is such that the structure's mode shapes of interest are significantly excited. Thereby, it is identifiable in the power spectrum.
3. The system is lightly damped.

Thereby, the period of measurements in ambient vibration test is typically longer than in dynamic tests in order to capture all the mode shapes of interest.

4.2.1.2 Field Testing

Due to various limitations for field testing of such bridge in service, testing programs must be very carefully designed to take the least amount of time and create minimal interference to traffic flow. Ideally, 200 accelerometers or more are needed on a bridge this size, thus only one set of reading is needed. Accelerometer instrument is however very expensive, and therefore only four accelerometers were made available. Due to this limitation, the ambient vibration test was broken up into a series of ten sets of tests. Despite limited number of accelerometers available, ambient vibration tests performed in August 1998 took less than two hours. Only one of the two lanes was closed to traffic for the full two hours, where as the other lane was only closed

intermittently for each of the test. All four accelerometers were used in each of the ten sets of reading were taken. For each set of reading, the intermittent closing of the second lane was 3 minutes and 20 seconds. Eight of the ten sets of readings were taken for the vertical modes and two for the transverse modes behaviour of the bridge. In each set of test, the data was acquired for 200 seconds with a scan rate of 200 scans per second. This enabled the capture of frequencies up to 50 Hz with the corresponding mode shapes for a complete phase analysis. However, only frequencies below 10 Hz are of interest in this work and discussed in details.

For ambient vibration tests, all the accelerometers were placed as shown in Figure 4.12. In the transverse direction, the accelerometers were placed directly on top of either girder #1 or girder #2. For each set of reading, one of the four accelerometers was placed at the reference point (see Figure 4.12). This reference accelerometer was later used to normalize the other accelerometers with respect to the magnitude and direction of the vibration. By normalize all other accelerometers' magnitude with respect to the reference accelerometer for each set of test, it had the effect of canceling out the different levels of excitation forces in various sets of tests. In addition, reference accelerometer also serves a vital role in correlating all the different sets of tests for phase analysis to identify the mode shapes. Table 4.3 shows the test #, filename, accelerometer # and its' location on the bridge for each test performed (see Figure 4.12).

Table 4.3: Filenames and Accelerometer Locations

Test #	Filename	Accelerometer #	On Top of Girder #
1	A0825P0952.raw	10(Ref.)	1
		11	1
		12	1
		13	2
2	A0825P1001.raw	10(Ref.)	1
		11	1
		12	1
		13	2
3	A0825P1008.raw	10(Ref.)	1
		11	1
		12	1
		13	2
4	A0825P1019.raw	10(Ref.)	1
		11(Ref.)	1
		12(Ref.)	1
		13(Ref.)	1
5	A0825P1049.raw	10(Ref.)	1
		11	1
		12	1
		13	2
6	A0825P1057.raw	10(Ref.)	1
		11	1
		12	1
		13	2
7	A0825P1121.raw	10(Ref.)	1
		11	1
		12	1
		13	2
8	A0825P1131.raw	10(Ref.)	1
		11	1
		12	1
		13	2
9T	A0825P1041.raw	10(Ref.)	1
		11	1
		12	1
10T	A0825P1029.raw	13	1
		10(Ref.)	1
		11(Ref.)	1
		12(Ref.)	1
		13(Ref.)	1

The eight elliptical-circles shown in Figure 4.12 were referred to the eight sets of tests performed to determine the vertical characteristics of the bridge. These eight elliptical-circles shown from North to South respectively were directly corresponding to *Test #1* to *#8* as shown in Table 4.3. For example for *Test #1*, the three dots shown in the elliptical-circle on the North span were the locations of the accelerometers. The last column in Table 4.3 indicates the location in which the accelerometers were placed. *Tests #1* to *#8* are for vertical mode shapes. Note the Accelerometer # 10 was always placed between the 33rd and the 34th steel strap from the North, and it was not moved for any of the eight tests. Only three of the four accelerometers were moved for each of the test performed. For the transverse mode shapes, only two readings were taken, *Test #9T* and *#10T*. For *Test #9T*, the location of the accelerometers #10, #11, #12, and #13 were near the 17th, 30th, 33rd, and 43rd steel strap from the North abutment, respectively. For *Test #10T*, all accelerometers were placed between the 33rd and the 34th steel strap from the North. All accelerometers were monitored using LabVIEW in combination with a high-speed data acquisition system to obtain data shown in Table 4.3.

4.2.1.3 Data Reduction

Plot of raw data for accelerometer #10 in file A0825P0952.raw is shown in Figure 4.13. It shows the response of the accelerometer in mV as a function of time in second. The analog signal from the accelerometer was converted to digital signal and sampled at 200 scans per second for 200 seconds. Nyquist frequency rule dictates that the maximum frequency can be determined from any response is half of the sampling rates (McConnell, 1995). Consequently, for a sampling rate of 200 scans per second, the maximum frequency that can be determined is 100 Hz. Hence, the scan rate used was more than sufficient for the interested frequencies of 10 Hz and less.

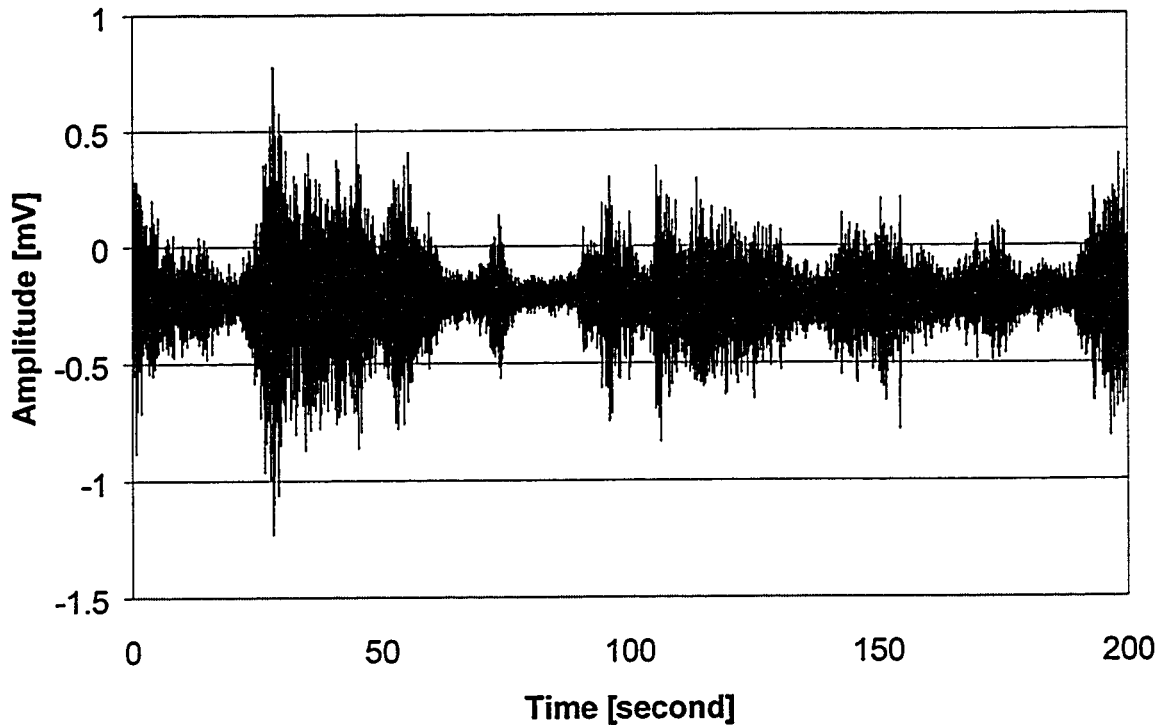


Figure 4.13 Accelerometer #10-- Raw Data

Before the tests begin, several sampling rates were trailed and tested for variation in frequencies response. At 200 scans per second, there was no variation in frequency response for this bridge. Hence, the Aliasing problem had been considered in collecting these data. An example of Aliasing error in data collecting is shown in Appendix B. Despite all precaution had been taken to eliminate all known errors, the background noise from the DC power source render such raw data are of little use. Fortunately, these noises were deterministic and periodic (typically they occurred at a multiple frequency of 20 Hz). Butterworth filter type was chosen to filter out such unwanted frequencies. This filter was chosen for its smooth response at all frequencies and a monotonic decrease from the specified cutoff frequency characteristics. Butterworth filter was applied to all raw data to obtain the final filtered data.

Figure 4.14 shows power spectrum plot of the raw file A0825P0952.raw. The power spectrum of the raw data was computed by applying Fourier Transforms to find the

frequencies of the function. The horizontal axis represents the frequency axis and the vertical axis is the square of the amplitude of the accelerometer response. Commercially available software such as LabVIEW was used to digitally apply Fast Fourier Transforms, FFT and Discrete Fourier Transforms, DFT and plot the power spectrum (National Instruments Corporation, 1996). Since only frequencies between 2 to 10 Hz are of interest, Figure 4.14 below only shows frequency between this range.

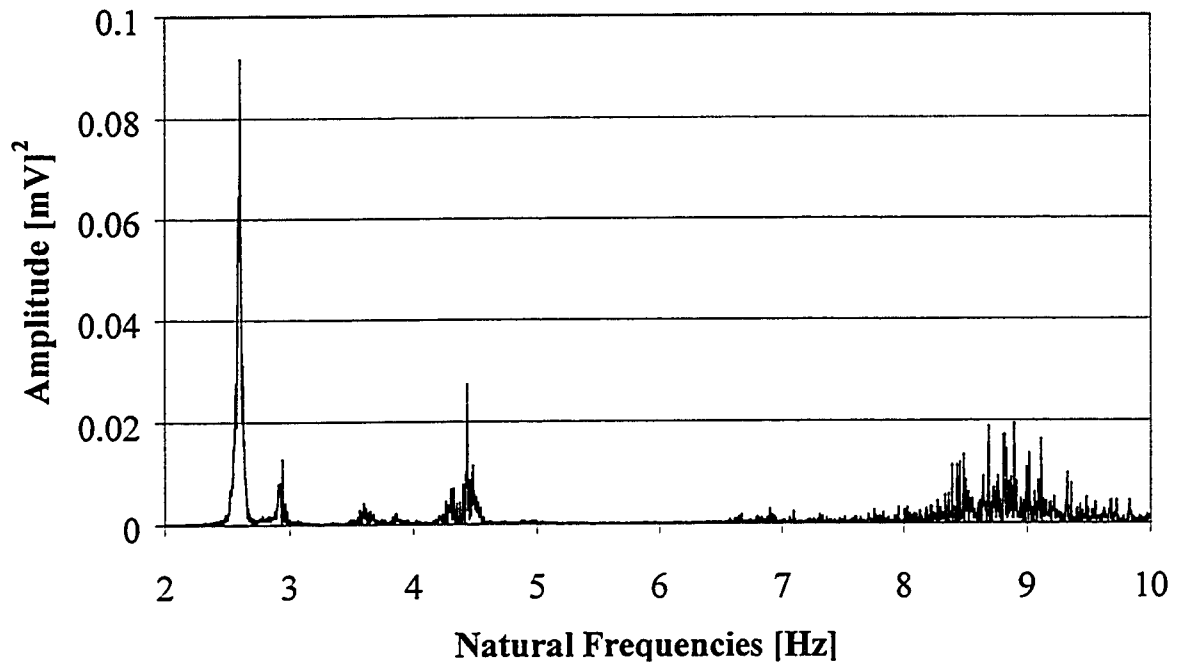


Figure 4.14 Power Spectrum for Accelerometer #10

The actual vibration modes of a structure may be highly coupled. Depending upon the location of the accelerometer placed on the structure, it may see higher magnitude of excitation for some frequencies and little or none of the others frequencies. For example, if an accelerometer is placed at mid-span on a simply supported beam, it may see maximum magnitude of vibration in the first mode and little or none in the second mode. Figure 4.15 is a plot of the accelerometer #11 from the same file as Figure 4.14, which is a plot of accelerometer #10. Note that the frequency of 2.60 Hz is very predominant in Figure 4.14, but very little is showing in Figure 4.15 despite the fact that all the accelerometers were calibrated to have the same output when subjected to the same level of excitation. The significantly lower magnitude of excitation for the 2.60 Hz

frequency shown in Figure 4.15 compared to Figure 4.14 is due to the location of the accelerometer and not the accelerometer itself. To determine the exact mode shape of each frequency, the following parameters are require: the level of excitation as a function of location on the bridge and the direction of excitation at an instant frame of time. Since the vertical axis of the power spectrum plot is amplitude squared, the directions are not known at that particular time frame.

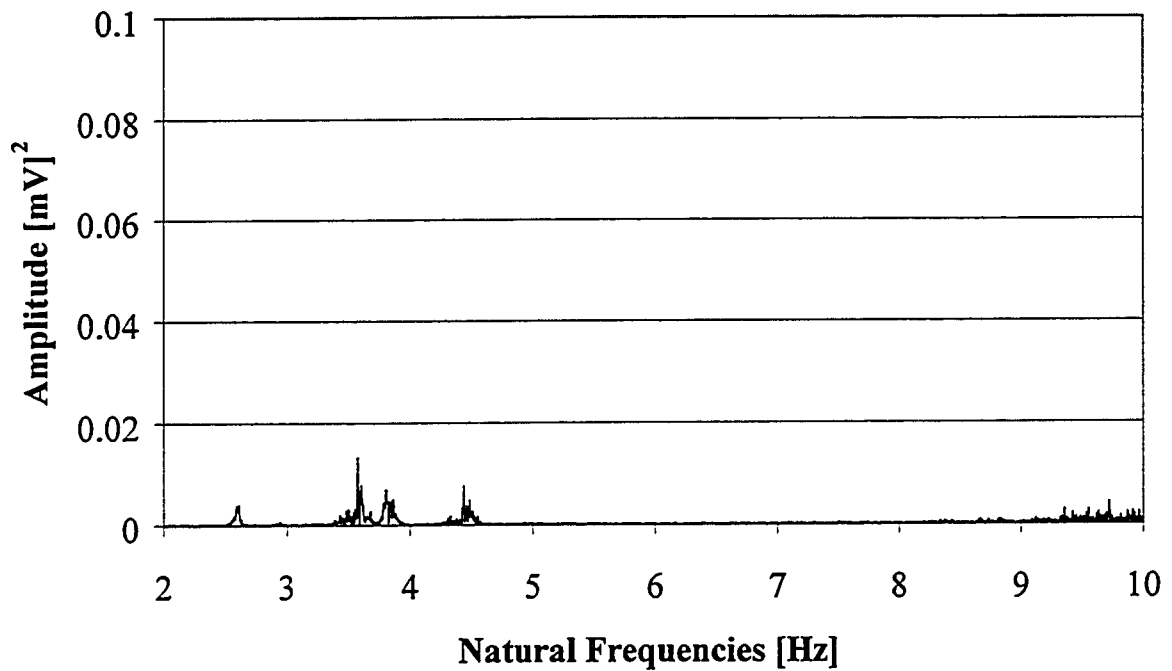


Figure 4.15: Power Spectrum for Accelerometer # 11

In order to determine the mode shape for a particular frequency the magnitude and direction of excitation at different points along the bridge must be known. The magnitude of excitation for each frequency can be found from the power spectrum analysis. The direction of excitation can be determined by comparing the phase of excitation to the reference accelerometer excitation. In raw data, the frequencies are highly coupled. In phase analysis, only one frequency can be examined at a time. Thus, a band-pass filter is used to isolate the frequency of interest. Each file is then filtered for all frequencies of interest in turn. Finally, the phase of each frequency can be compared to the reference accelerometer with the same frequency. Figure 4.16 shows the phase

analysis plots for 2.60 Hz frequency. Clearly for 2.60 Hz, accelerometers #11 to #13 are all moving in the opposite direction compared to the reference accelerometer #10.

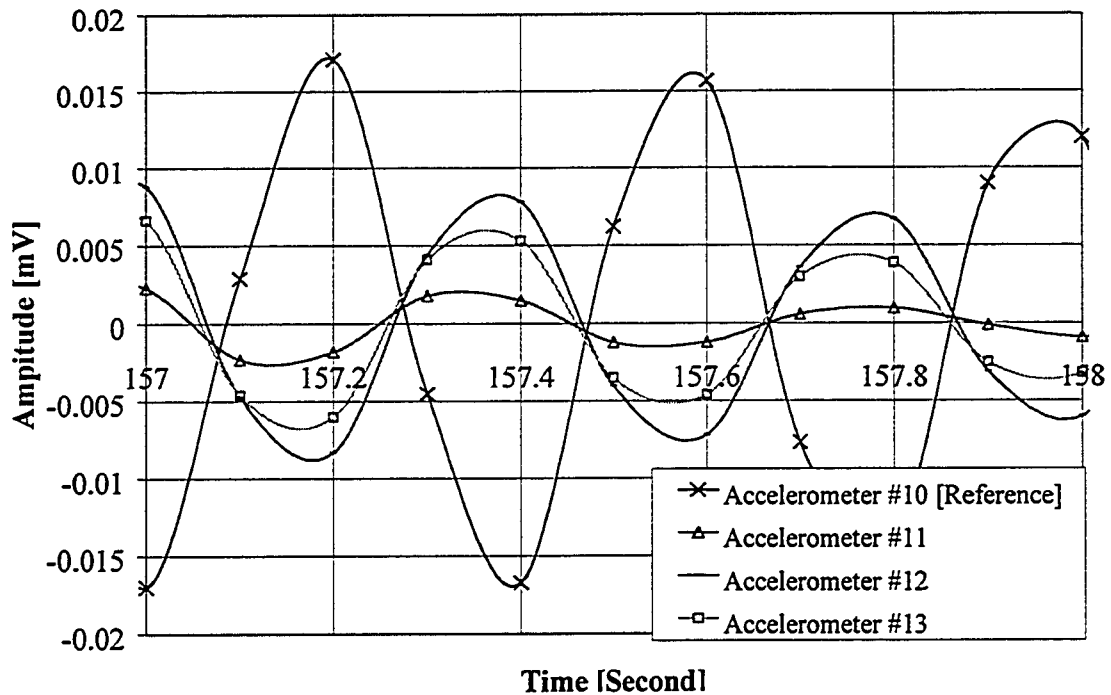


Figure 4.16: Phase Analysis for 2.60 Hz

In order to distinguish between the torsional and vertical mode shapes, the magnitude of excitation of girder #1 is compared to that of girder #2. If both accelerometers on girder #1 and girder #2 located at the same distance along the bridge show a very close magnitude of excitation, the mode of vibration is a vertical mode. Figure 4.17 shows such magnitude comparison. Likewise, if the difference between the magnitudes of excitation is always proportional to the distance between the accelerometers across the width of the bridge at a cross section, the mode of vibration is a torsional mode as shown in Figure 4.17. This method is based on the assumption that the bridge deck is rigid. An improvement in future testing would be to place an accelerometer on every girder, since the bridge deck may not be rigid. Another benefit of this modification is that it allows a closer examination of the stiffness of the individual girders, and the stiffness of the deck.

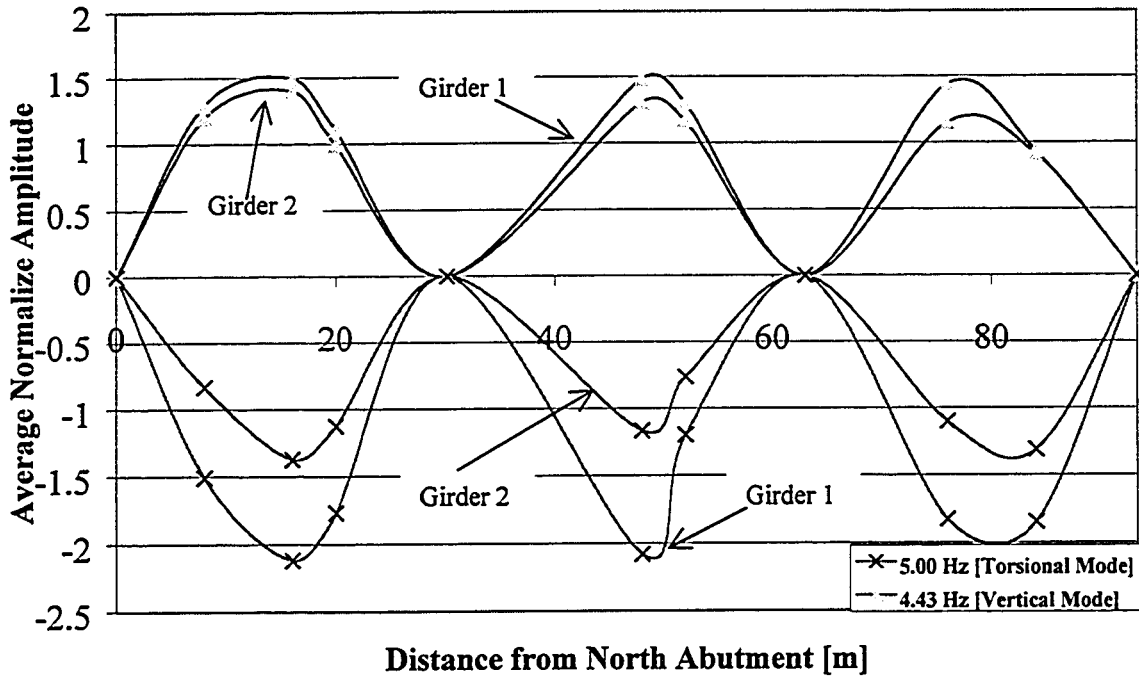


Figure 4.17: Distinguish between Vertical [4.43 Hz] / Torsional [5.00 Hz] Mode Shapes

4.2.1.4 Frequencies and Mode shapes

Due to the nature of mode shapes and the small number of accelerometers used on this bridge, some accelerometers may or may not capture some particular frequencies. For example, the power spectrum for Accelerometer #11 shown in Figure 4.15 practically did not captures the 2.90 Hz frequency, where as Accelerometer #10 shown in Figure 4.14 does. Again, this is due to the location of the accelerometer on the bridge, which determine the frequencies and magnitude of the frequencies captured. It is worth noting that eight different vertical vibration tests were performed, and each test was conducted with the accelerometers at different locations on the bridge. Consequently, if one accelerometer did not capture some particular frequencies, than chances are other accelerometers at other locations on the bridge will captures these missing frequencies. Therefore by summing all four accelerometers in each of the test, from eight different tests, it is possible to capture the majority of the lower modes of vibration without missing any modes. Likewise, if there were enough data gather from infinite number of points from the bridge, then there is no limits to the number of mode shapes in which it

can captures. The power spectrum of all eight files in the vertical mode are summed and plotted in Figure 4.18.

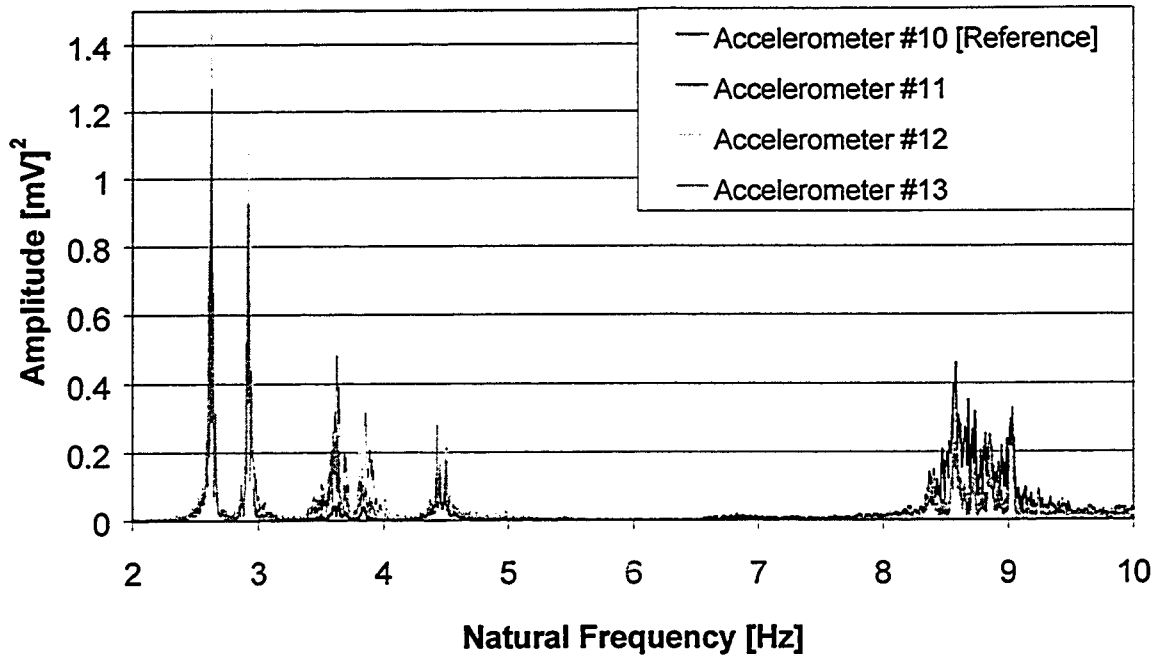


Figure 4.18: Power Spectrum for the Sum of All Accelerometers from Eight Files

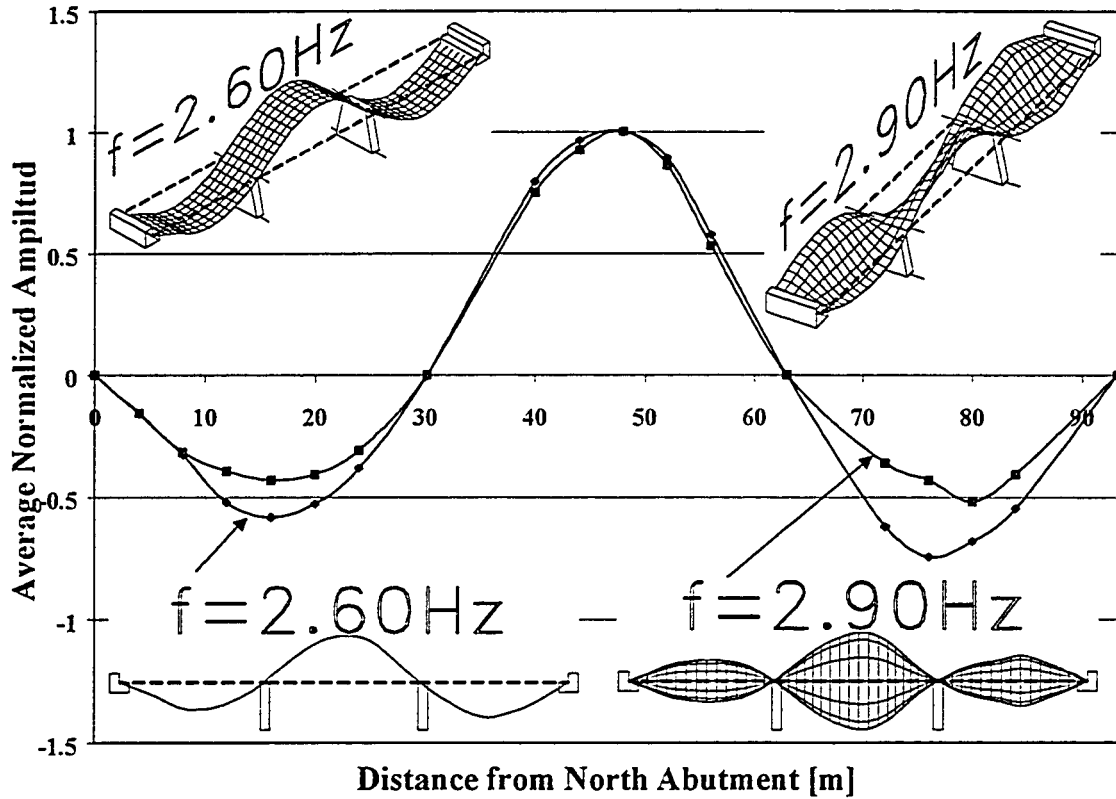
The power spectrum shown in Figure 4.18 identifies eight predominant frequencies below 10 Hz as outlined in Table 4.4. The resolution of these frequencies is ± 0.01 Hz. Table 4.4 shows the ambient vibration tests done by U of A and UBC yields very close results. In addition, the mode shapes found by both Universities were all matched. In general, the frequencies found in August 1998 were approximately 0.20 Hz lower than the frequencies found in September 1997. Since the mass of the bridge had not changed over the last one year of operation, thus the bridge stiffness could have been reduced.

Table 4.4: Vertical and Torsional Modes

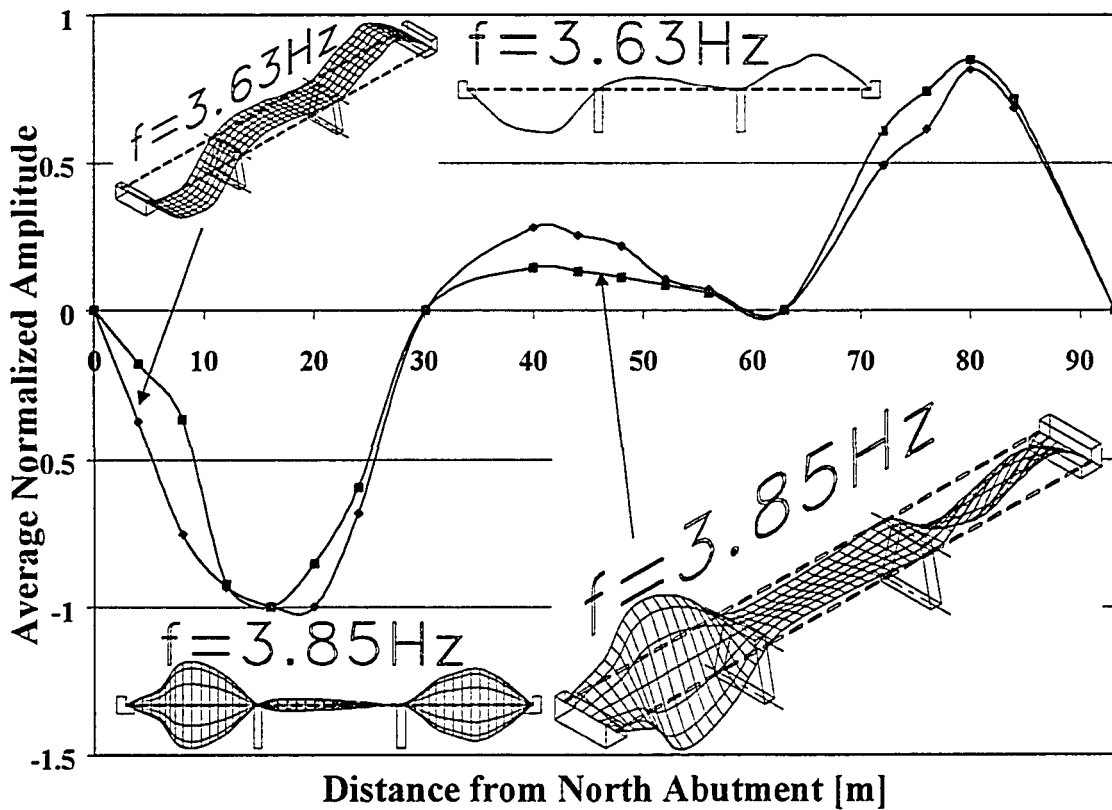
U of A (Aug '98)	UBC Report (Sept '97)	Description
2.60 Hz	2.78 Hz	1 st Fundamental Vertical Mode
2.90 Hz	3.13 Hz	1 st Fundamental Torsional Mode
3.63 Hz	3.76 Hz	2 nd Vertical Mode
3.85 Hz	4.05 Hz	2 nd Torsional Mode
4.43 Hz	4.64 Hz	3 rd Vertical Mode
5.00 Hz	5.18 Hz	3 rd Torsional Mode
6.85 Hz	7.13 Hz	4 th Torsional Mode
8.60 Hz	9.13 Hz	4 th Vertical Mode

The frequencies in Table 4.4 above and its corresponding mode shapes are shown in Figure 4.19. Both three-dimensional prospective view and the West elevation view of the each mode shape are shown in the figure. For each figure, it consisted of one vertical and one torsional mode shapes. For all figures shown in Figure 4.19, the horizontal axis is the distance along the bridge, and the vertical axis is the average normalized magnitude of excitation for each mode shape. For each frequency list in Table 4.4 above, the corresponding mode shapes are shown in Figure 4.19 as follows:

1. Figure 4.19 (a) 1st fundamental vertical and torsional mode shapes.
2. Figure 4.19 (b) 2nd fundamental vertical and torsional mode shapes.
3. Figure 4.19 (c) 3rd fundamental vertical and torsional mode shapes.
4. Figure 4.19 (d) 4th fundamental vertical and torsional mode shapes.



(a) 1st Fundamental Vertical and Torsional Mode Shapes



(b) 2nd Vertical and Torsional Mode Shapes

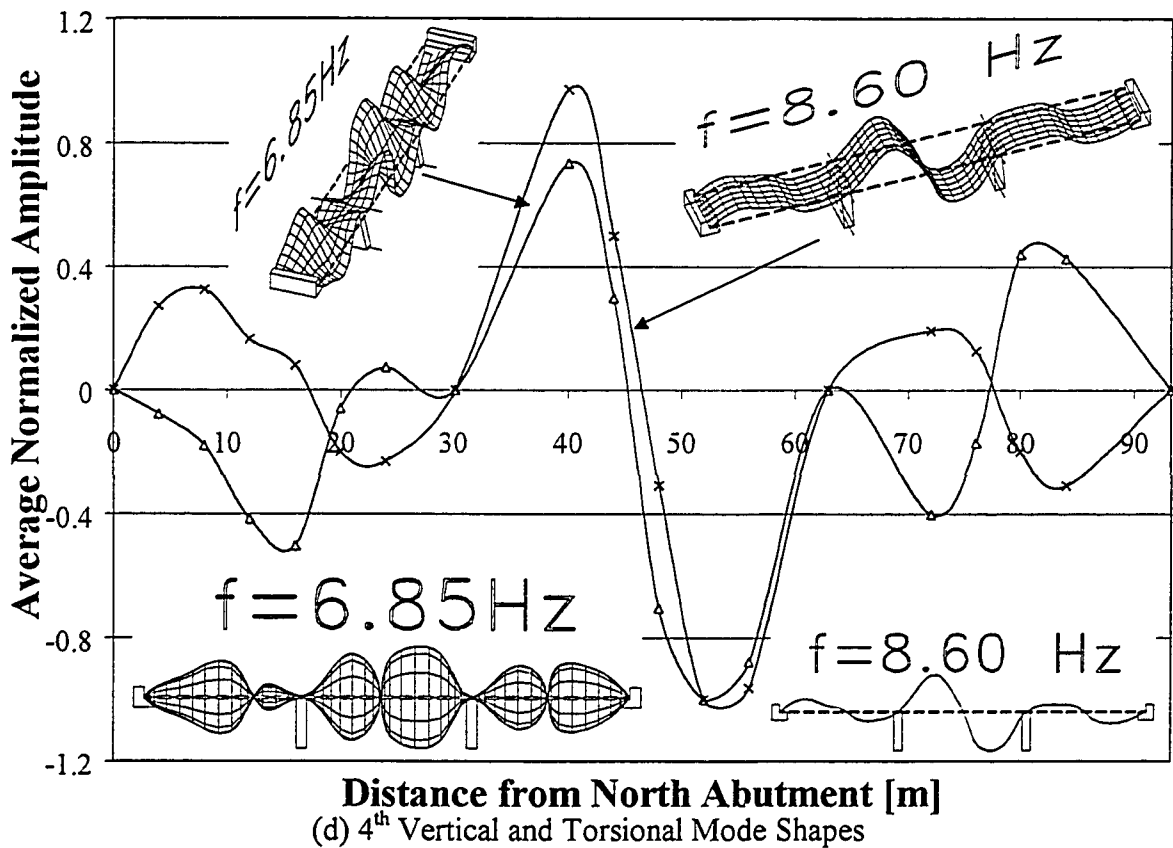
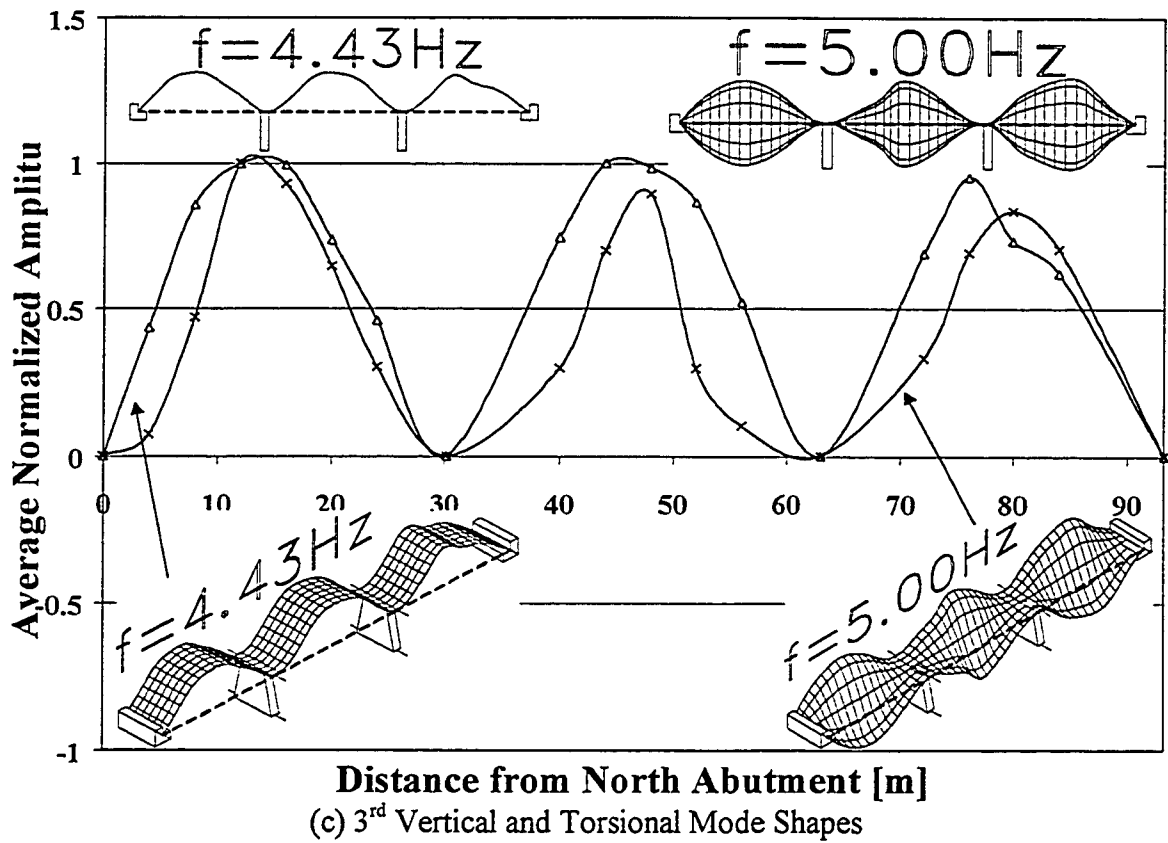


Figure 4.19: Frequencies and Mode Shapes

4.2.2 Static Test Results

To establish the static behaviour of the bridge under service load, a truck with known axles load was used in the tests. The static test results in August 1998 were used to monitor the change in the bridge structural characteristics by comparing it to the static test results obtained in August 1997. Subsequently, the results were also used to compare to the dynamic test results in August 1998. The truck had a total gross weight of 395 kN with 42 kN on the front axle, and 154 kN and 199 kN on the second and third tandem axles as shown in Figure 4.20. For all the tests performed in August 1998, the truck was moving from North to South as shown in Figure 4.21. Figure 4.21 shows the position of the right wheel of the front axle along the bridge for each of the static tests. All load points were located at midpoint between girders #1 and #2 as indicated in Figure 4.21.

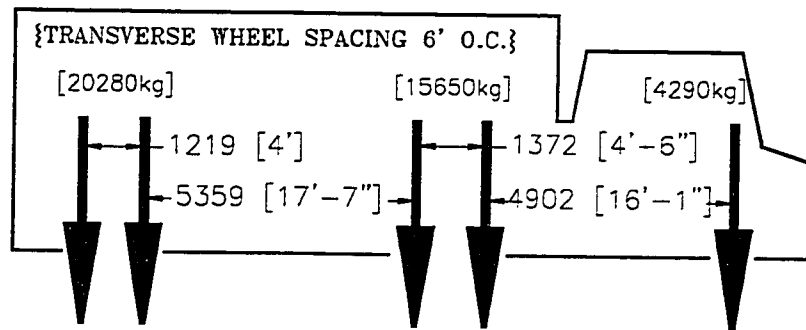


Figure 4.20: Truck Used for August 1998 Static Tests

Initial zero readings were obtained before the test truck moved onto the bridge. Strain gauges and cable transducers were recorded for each load position indicated in Figure 4.21. It takes approximately 1-2 minutes to complete each set of reading for one load point. After every four to five readings, the truck was moved off the bridge to re-establish zero readings for all the instrumentation to account for possible temperature effects.

The high-speed data acquisition system available was limited to read 50 channels at a time. Due to this limitation, all static and dynamic tests were repeated three times for each load point of interest. Over 100 strain gauges, 10 cable transducers, and four

accelerometers were used for the August 1998 tests. Due to high number of strain gauge channels needed for each load point, these strain gauge channels were divided into three separate sets as follows:

Strain Gauges Set 1 Strain gauges G1 to G34 and T4

Strain Gauges Set 2 Strain gauges T1 to T18, R1 to R15, RC1 and RC2

Strain Gauges Set 3 Strain gauges E2 to E19, N1 to N4, T4, S1 to S6, C1 to C4,
and RS1 to RS3

Consequently, each test had to be repeated three times in order to record the three sets of strain gauges. For each test run, the high-speed data acquisition channels were set up to log the following readings:

1. Channels 0 to 34 are for 35 strain gauges (either Set 1, Set 2, or Set 3 was connected for Static and Dynamic tests).
2. Channels 35 is for the one standard strain gauge (Connected at all times for Static and Dynamic tests).
3. Channels 36 to 45 are for the 10 cable transducers (Connected at all times for Static and Dynamic tests).
4. Channels 46 to 49 are for the four accelerometers (These channels were connected for Dynamic test only).

Since all test runs were repeated three times for each load point, data for the ten cable transducers, one standard strain gauge, one *T4* strain gauge and four accelerometers were logged redundantly three times each. Hence, these triplicate sets of data were used to check the consistency of test results. Due to high volume of strain gauge channels needed for each load point, *Strain Gauges Set #1, Set #2, and Set #3*, were logged only once for each test run. Unfortunately, for *Set #3* in the static test, the truck was not positioned on every load point due to time limitation.

4.2.2.1 Data Obtained from the Cable Transducers

Cable transducers # 1 to #5 measured the vertical displacement at strap #13 for girders #1 to #5, respectively (see Figure 4.22). Strap numbering system is shown in Figure 4.22 below. Cable transducers #6 to #9 were mounted on girders #1 to #4, respectively at strap # 21. Cable transducer #10 was used to measure the vertical displacement of girder #5 at strap #35, in the middle span.

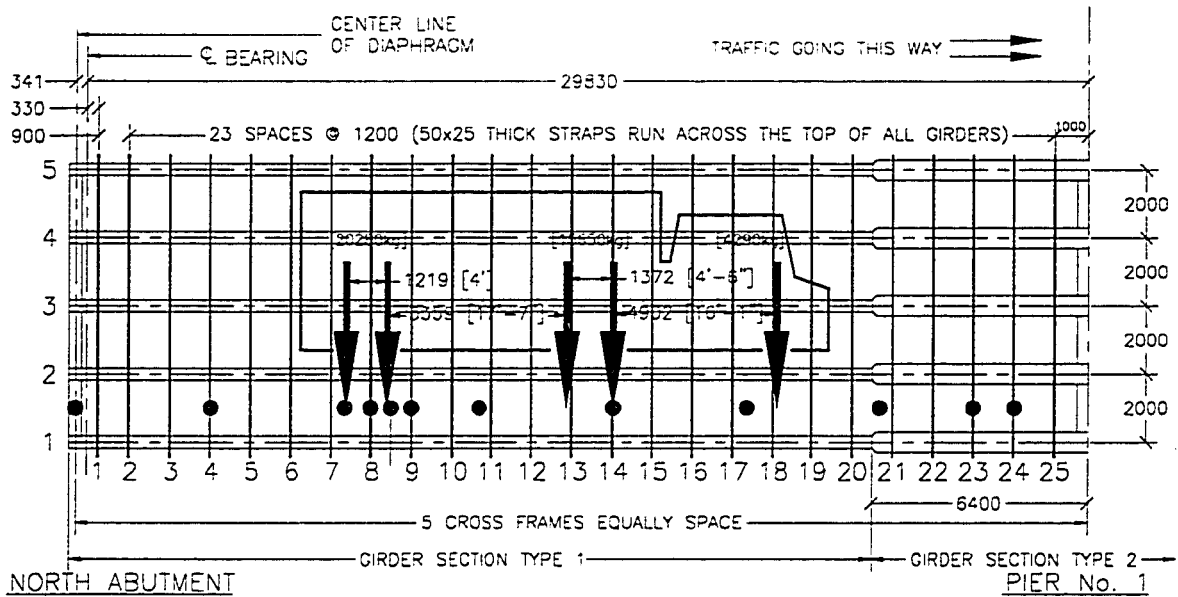


Figure 4.22: North Span Loading Configuration and Strap Numbering.

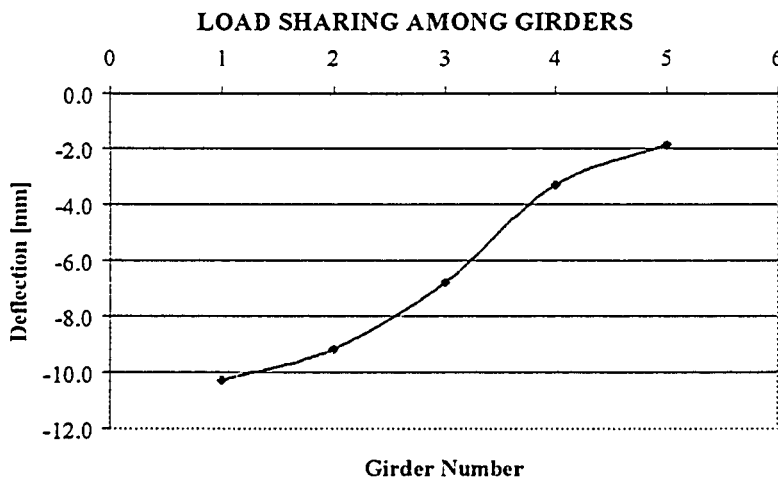


Figure 4.23: Cable Transducers at Strap #13

Load sharing between the girders can be assessed from the cable transducer data collected at Strap #13. As shown in Figure 4.23 the maximum deflection under this one truckload was 10.28 mm for girder #1.

The bridge influence line can be shown from the cable transducer results at strap #13, as shown in Figure 4.24. The locations of the cable transducers at strap #13 is shown in Figure 4.24 by a single vertical line labeled *Cable T*. The vertical axis shows the deflection in millimeters for girders G1 to G5 for different positions of the front axle of the test truck from the North end of the bridge, plotted along the horizontal axis. The horizontal axis is the distance in meters along the bridge from North to South. In addition, the two vertical lines labeled *Pier No.1* and *Pier No.2* indicate the location of the two interior piers with respect to the overall length of the bridge. For the North span, the maximum deflection recorded was 10.3 mm when the truck front axle was 15.90 m from the North abutment (at Strap #14). Assuming the bridge to be a continuous beam, the maximum deflection is expected at strap #14. However, the middle span had a maximum deflection of 4.46 mm when the truck front axel reaches 9.85 meter South of Pier No.1. This was not expected based on Maxwell's reciprocal theorem. Because for a continuous 3 equal spans bridge, assuming the bridge has the same stiffness all along its length, the maximum deflection is expected to be at the midspan. A maximum deflection at 9.85 meter South of Pier No.1 is merely one-third the length of the middle span. This may suggested that the stiffness at this point is lower than its neighboring part. Whereby the same loads at this point had a larger influence effects on the overall structure than its counter part.

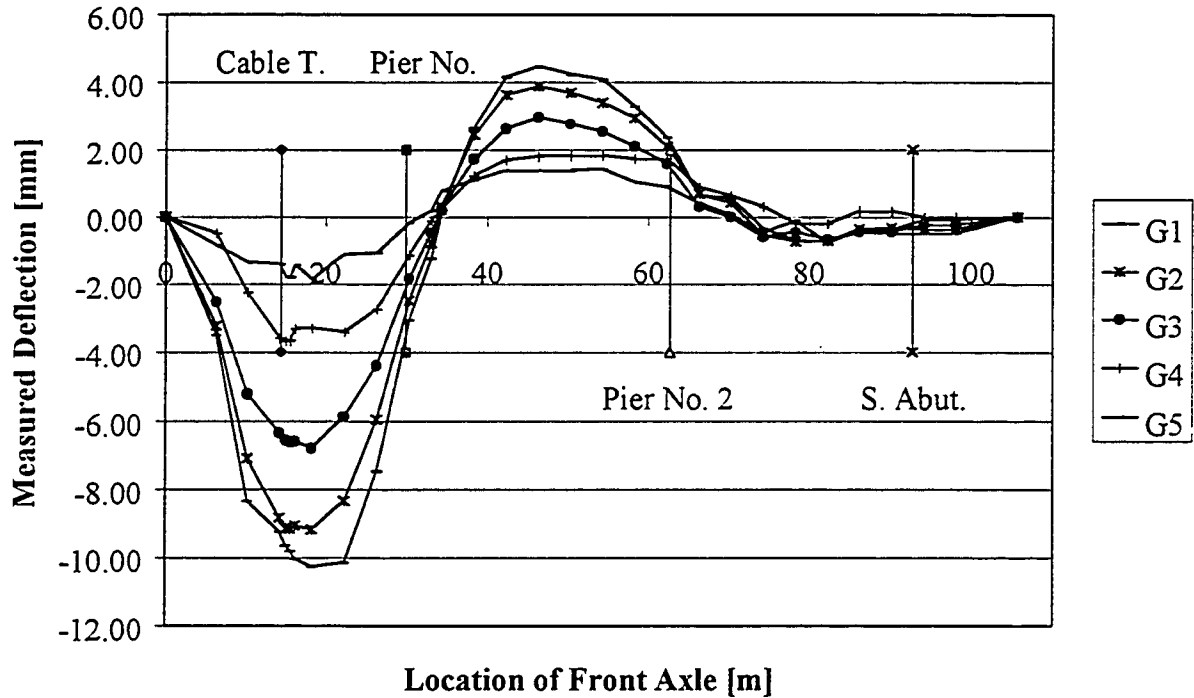


Figure 4.24: Influence Lines from Cable Transducers at Strap #13

4.2.2.2 Results from Strain Measurements

On the bottom side of the strap #8, there were two strain gauges mounted at midpoint between girder #1 and #2, side by side on the strap. This was used to monitor the deviation in the strain gauges readings and arching action in the deck. Results show the maximum difference in the two strain gauges readings on strap #8 was $2 \mu\epsilon$. This indicated that the variation in the any of the strain gauge readings were quite small. Secondly, when the centerline of the second axel was offset to the South of strap #8 by 1.027 mm, the steel strap #8 gives a maximum strain reading of $85 \mu\epsilon$ and it cycles between -15 to $85 \mu\epsilon$ as the truck move across the entire length of the bridge. With such low strain cycle on the steel straps, fatigue is not a concern.

The cross sectional views of the girders *type 1* and *type 2* that was indicated in Figure 4.22 are shown in Figure 4.25. The strain gauges location on all steel girders and its distances from the North Abutment were also detailed as shown below.

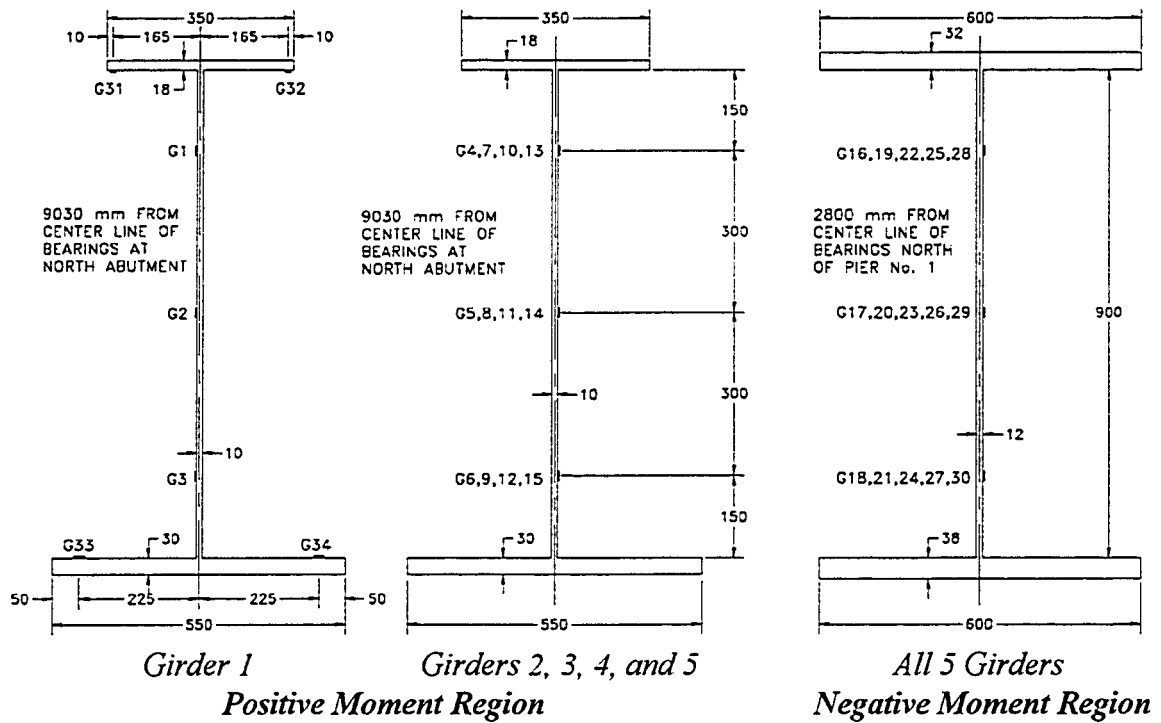


Figure 4.25: The Three Girder Type Used and Strain Gauges Layout

Strain gauges G1 to G3 were mounted on the web of girder 1 and gauges G31 to G34 were mounted on the flange of girder 1 as shown in Figure 4.25. The strain gauges were mounted at 9.03 m from North abutment. When the front axle of the truck reaches 15.05 m from North abutment, the cross sectional strain from top to bottom of the cross section are -10, 18.6, 65.1, 97.1, and 104 $\mu\epsilon$ respectively for August 1998. These recorded strain distribution in girder 1 is shown in Figure 4.26. The location of the neutral axis is 52 mm below the bottom face of the top flange. With such loading configuration, the maximum measured strain is 104 $\mu\epsilon$ on strain gauges G33 and G34. A close examination of the strain gauges indicated strain gauges G33 and G34 had a poor connection, hence their readings were unreliable. Despite the slight non-linearity observed in the strain distribution due to strain gauges G33 and G34, the cross section is linear otherwise. The small strains indicate that the bridge response was well within the elastic range.

Comparison of the cross sectional strain distribution for girder #1 between August 1997 and August 1998 shows practically no change in the location of neutral axis for the positive moment region. The difference between the neutral axes was 2 mm closer to the top flange for August 1998. These results suggested that there is no change in composite action for the positive moment region. Furthermore a shift of 2 mm up closer to the concrete deck may be from the gain in concrete strength over the last one year of curing process or simply instrumentation errors.

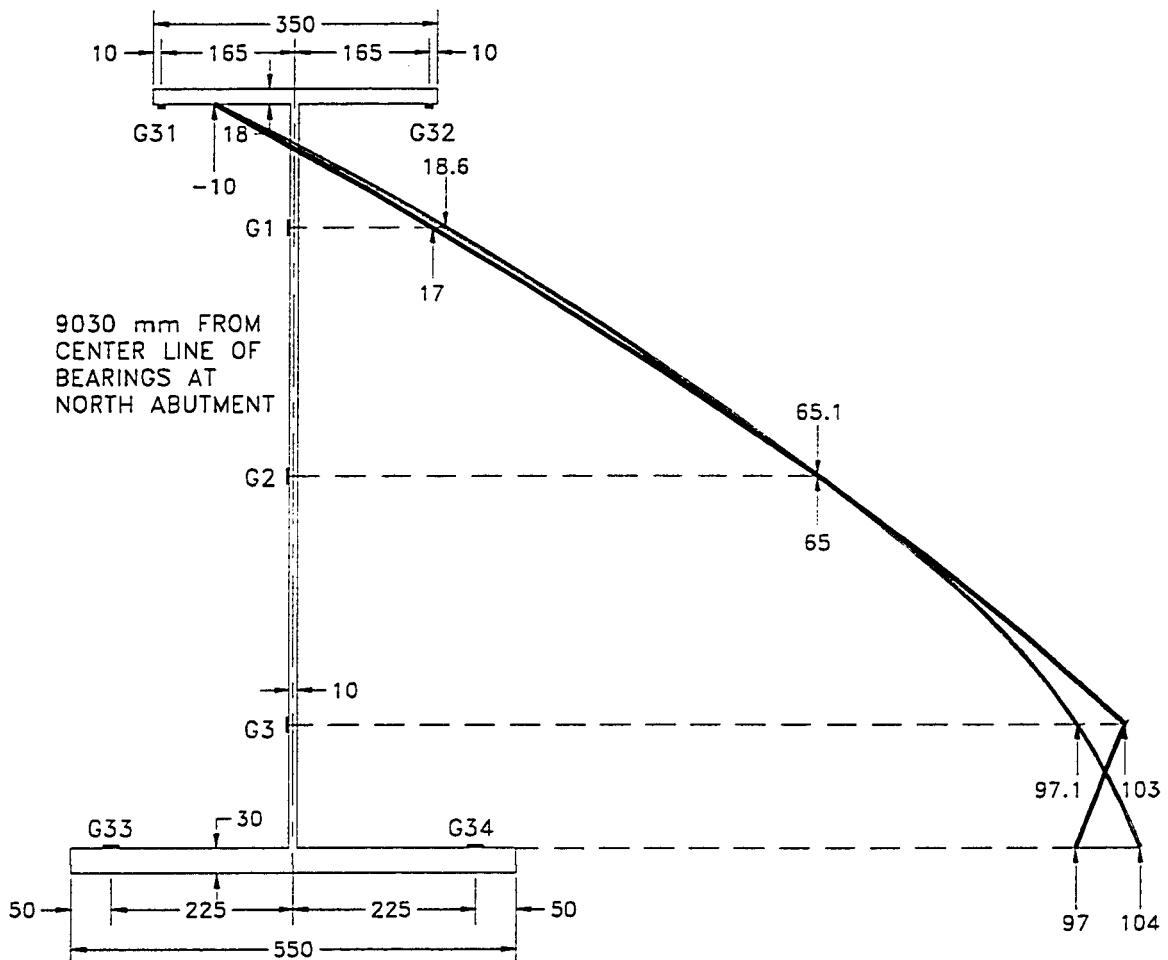


Figure 4.26: Strain Distribution for Aug. '97 and Aug. '98 in Positive Moment Region

For the same load case, the strain distribution in the negative moment region is shown in Figure 4.27. The instrumented section in the negative moment region is 2.8 m North of Pier No.1. As expected, the strain distribution in the cross-section is almost

linear. From extrapolation, the maximum compressive strain in the bottom flange is $14.8 \mu\epsilon$. The neutral axis is at 191 mm below the bottom face of the top flange. The change in location of the neutral can be interpreted as a measure of the change in composite action of the member. Figure 4.27 clearly shows that the neutral axis had moved from 93 mm to 191 mm between August 1997 and August 1998 respectively. This 98 mm shift in neutral axis suggests that there was a partial loss of composite action in the negative moment region. It should be recalled that the tests performed in August 1997 were done before the bridge was open to traffic. Comparison of the crack patterns between August 1997 and August 1998 (see Figure 4.48) shows a lot of new transverse and longitudinal cracks in the bridge deck in the negative moment region.

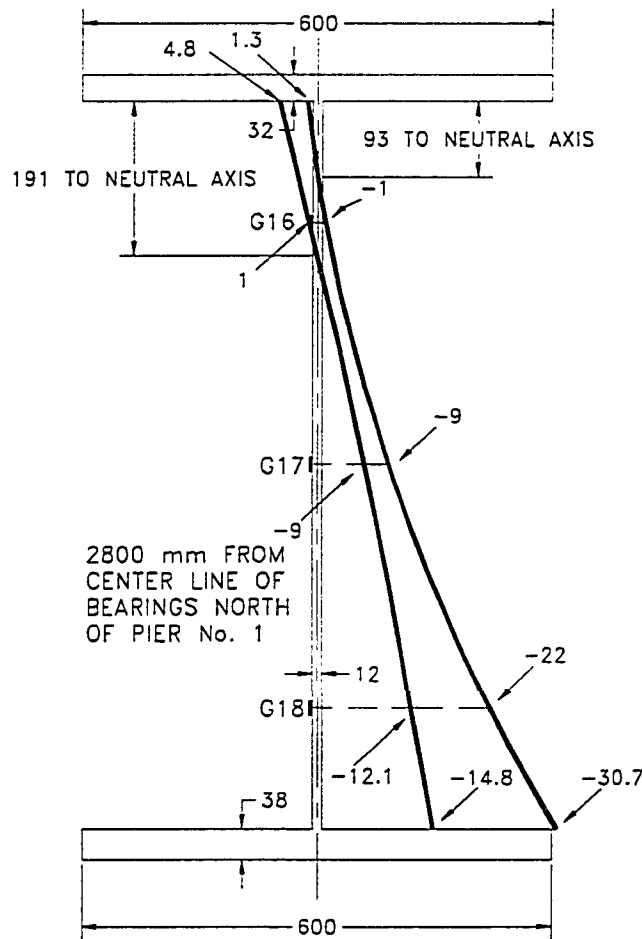


Figure 4.27: Strain Distribution for Aug. '97 and Aug. '98
in the Negative Moment Region

Load sharing between the girders is best examined through strain gauges. On all the girders' web in positive and negative moment region, there is a longitudinal gauge at 150 mm from the topside of the bottom flange. With the truck front axle loaded at 15.05 meter from the North Abutment, load sharing among the girders from strain gauges is shown in Figure 4.28. The maximum strain under this loading condition is 97.1 $\mu\epsilon$ for gauge G3 on girder #1 in the positive moment region. In the negative moment region, the maximum compressive strain is 25.3 $\mu\epsilon$ for gauge G21 on girder #2. Note that the strains in the negative moment region have almost the same magnitude. This would indicate that the load sharing and the load redistribution by the diaphragm over the pier were very effective in redistributing the load.

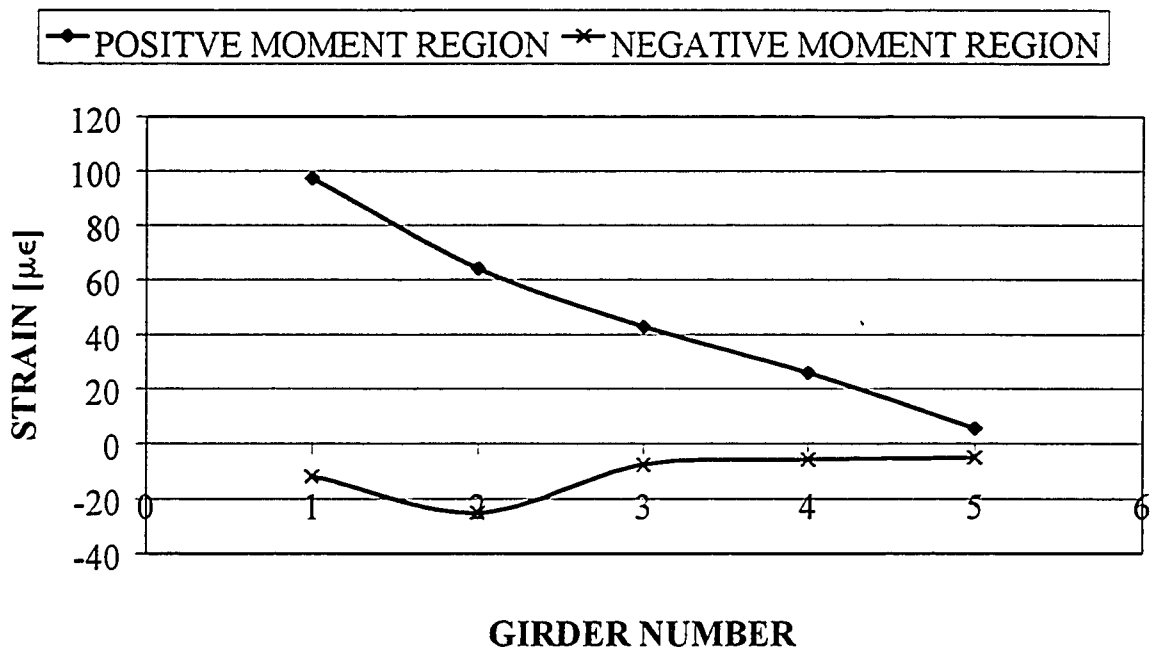


Figure 4.28: Strain Distribution for Positive and Negative Regions in August 1998

4.2.2.3 Influence Line

The bridge influence line under static load test in August 1998 is shown in Figure 4.29. The vertical axis is the strain measurement, and the horizontal axis is the distance in meters along the bridge from North to South. This figure shows the locations of the North and South abutment, Pier No1 and Pier No.2, and the location of the Strain

gauge G3. Clearly, the maximum strain is $97.1 \mu\epsilon$, when the truck front axle is at 15.05 meters. Although the influence line is slightly jagged in shape, but this is quite acceptable for a static test.

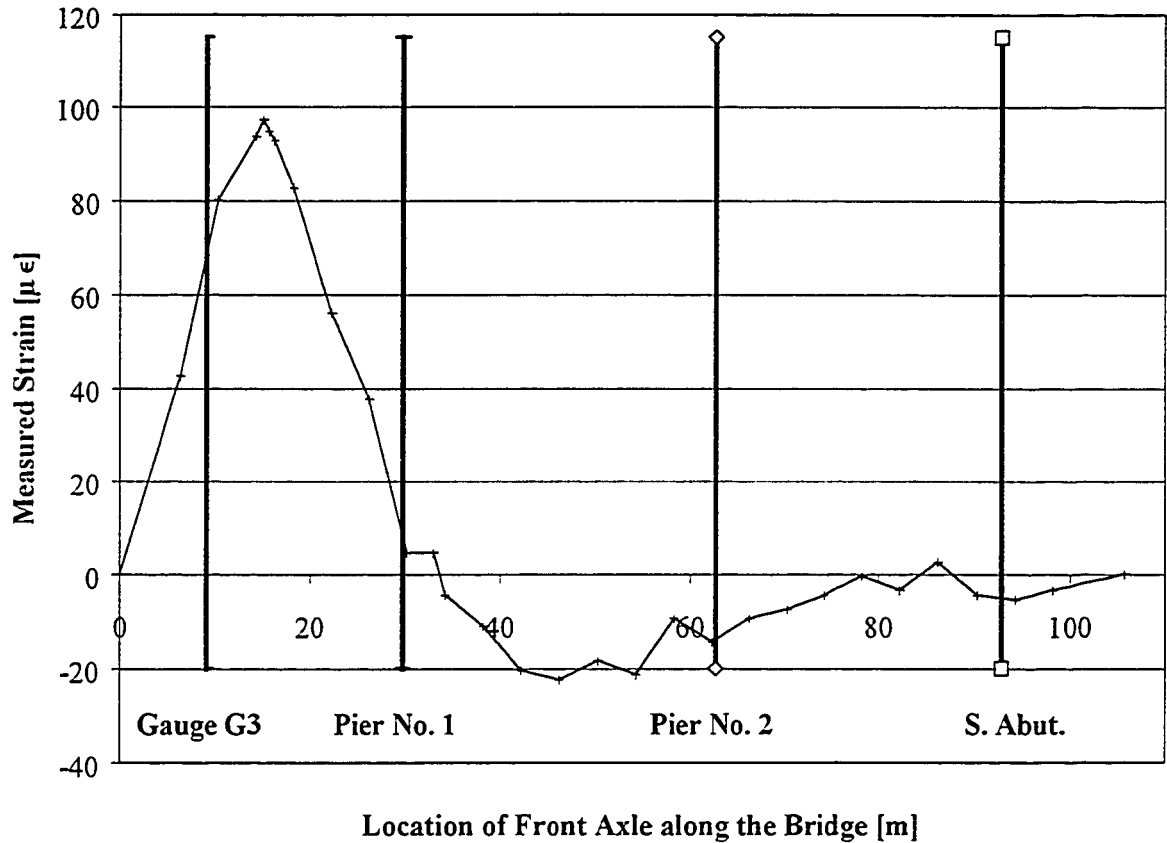


Figure 4.29: Influence Line for Strain Gauge G3

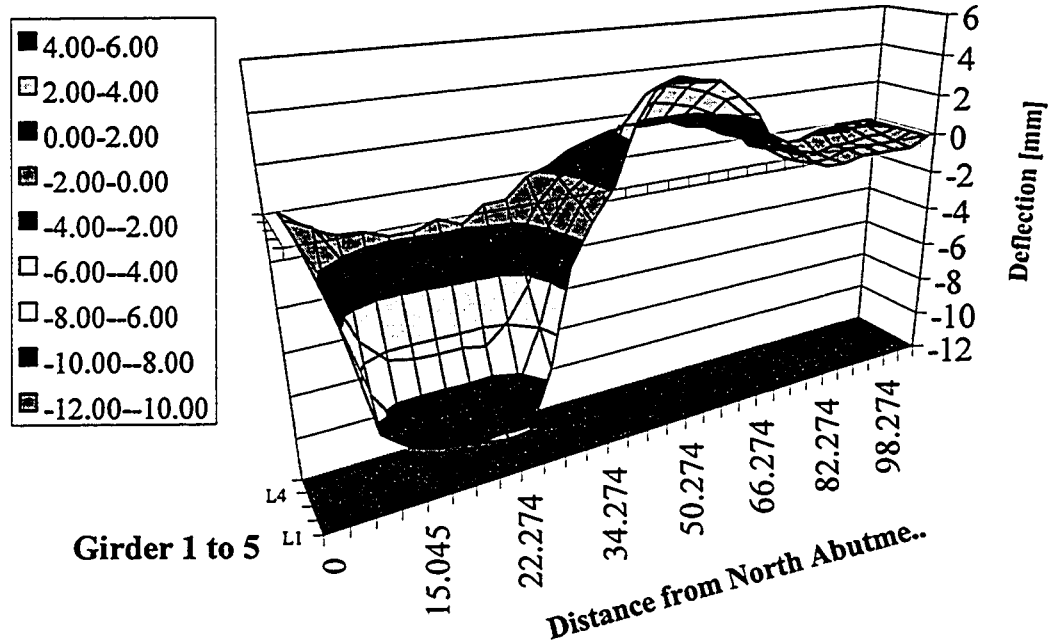


Figure 4.30: 3D Influence Surface for the Bridge from Cable Transducer at Strap #13

Figure 4.30 shows a 3D-influence surface for the entire length and width of the bridge. The vertical axis is the deflection of the girders in millimeters, the horizontal axis is the distance along the length of the bridge in meter, and the third axis is the width of the bridge. The ‘*Girder 1 to 5*’ axis is representing girder #1 to girder #5 in the transverse direction. The ‘*Distance from North Abutment*’ axis represents the location of the front axle of the truck. The legend on the left indicates different ranges of deflection.

4.2.3 Dynamic Tests

It is very important to determine the similarities and differences in the behaviour of the bridge under static and dynamic loading. If there are enough similarities can be established between static and dynamic results; the static test can be eliminated all together. Static test takes almost a full day to perform where as dynamic test takes less than a half-hour. The same truck is use in dynamic test as in static test. Loading conditions are identical, thereby; the results can be monitored and compared between all the tests. Four different speeds were investigated: 15, 30, 40, and 55 km/hr. The longest

test lasted no more than 25 seconds. Hence, the temperature effects can be neglected. Before the truck came onto the bridge, two seconds or more of zero readings were taken. Second zero readings were taken, where scan continued for approximately three or more seconds after the truck had completely move off the bridge.

Dynamic field-testing was done in three stages. Ten cable transducers, four accelerometers, strain gauge T4, and the standard strain gauge are presented in all three stages of the tests. Stages 1 – 3 contain strain gauge sets 1 – 3 as outlined in Section 4.2.2. Table 4.5 shows the three stages, its corresponding filename, speed of the truck, and the size of the file in seconds.

Table 4.5: Filenames, Test Speed and Stage Number
[All files are scanned at 500 scans per second]

Stage	Filename	Speed of Truck [km/hr]	File Size [sec.]
1	C10825P0027.raw	15	30
	C10825P0003.raw	30	20
	C10825P0010.raw	40	20
	C10825P0020.raw	55	20
2	C20825P0207.raw	15	30
	C20825P0210.raw	30	20
	C20825P0216.raw	40	20
	C20825P0223.raw	55	20
3	C30825P0312.raw	15	30
	C30825P0316.raw	30	20
	C30825P0324.raw	40	20
	C30825P0344.raw	55	20

4.2.3.1 Data Reduction

All measurements were recorded by a high-speed data acquisition system. Dynamic data were all scanned at 500 readings per second. Depending upon the location of the strain gauge, the length of the lead wires and the power sources, the environmental noises on raw data can be as high as $400 \mu\epsilon$ in magnitude. The major sources of noises were power supply and long lead wires. Long lead wire acted as antennas in the system and generated the noises. Figure 4.31 shows the raw data for strain gauges G3. The response is buried in these noises due to small input/output voltage. Fortunately, most of these noises were deterministic and periodic; thereby filtration for the actual response is possible. Figure 4.32 is a plot of the filtered data with a low pass Butterworth filter of 10 Hz. Since frequencies above 10 Hz have very little effect upon the influence line response of the bridge, a low pass filtered limit of 10 Hz was used.

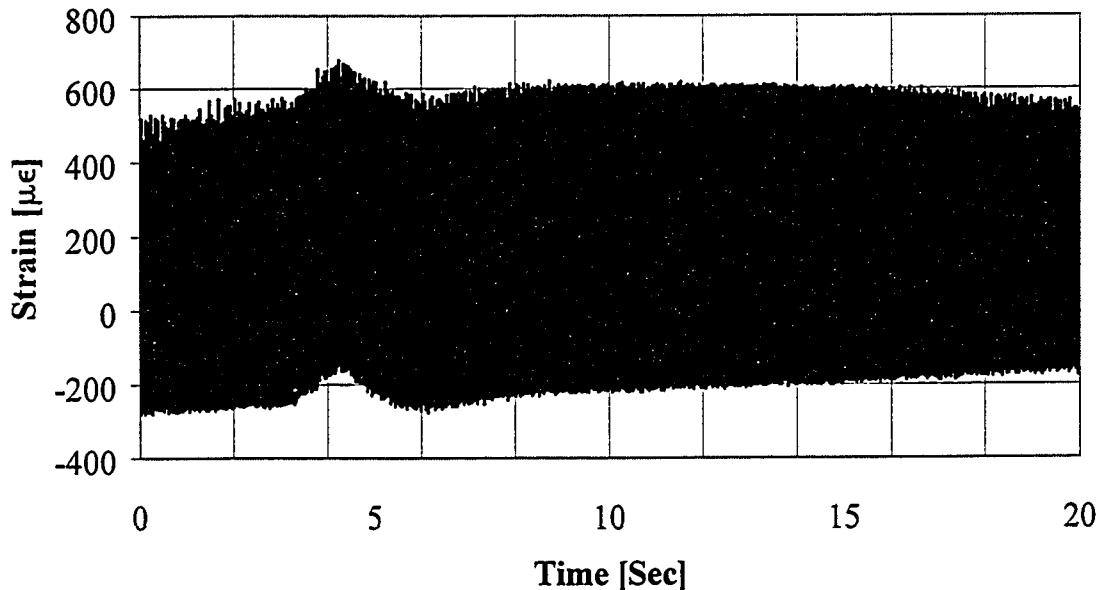


Figure 4.31: Raw Data for Strain Gauges G3 in 55 km/hr test on August 1998

For each test run, raw data were scanned at 500 Hz for 30 second long; render each file size in the magnitude of five megabytes. Although a scan rate of 500 Hz may capture frequency and mode shape as high as 125 Hz, only frequencies up to 10 Hz are of interest. With this frequency range of interest and a file that was scanned at 500 Hz, the

original file size can be reduced by 13 times and still capture up to a 10 Hz frequency. This row averaging of the raw data will not only reduce the file size by 13 times, but also improve the resolution of the amplitude of the 10 Hz frequency over the 125 Hz frequency by a factor of 13 times.

Due to various system limitations, the response drifted over time as shown in Figure 4.32. This drift was a random phenomenon; however, it manifested itself in a very low cycle drift characteristic. Theoretically, a band stop on the low cycle drift is possible thereby leaving the final responses of the gauges. In practice, a digital filtration on one of the two frequencies that are so very close to each other shall have an effect on the magnitude of the response of the other frequency. Consequently, this phenomenon is best corrected with second order polynomial as shown in Figure 4.32. With this specific truck ran at 55 km/hr, Figure 4.33 shows the final dynamic response for all frequencies under 10 Hz in strain gauge G3.

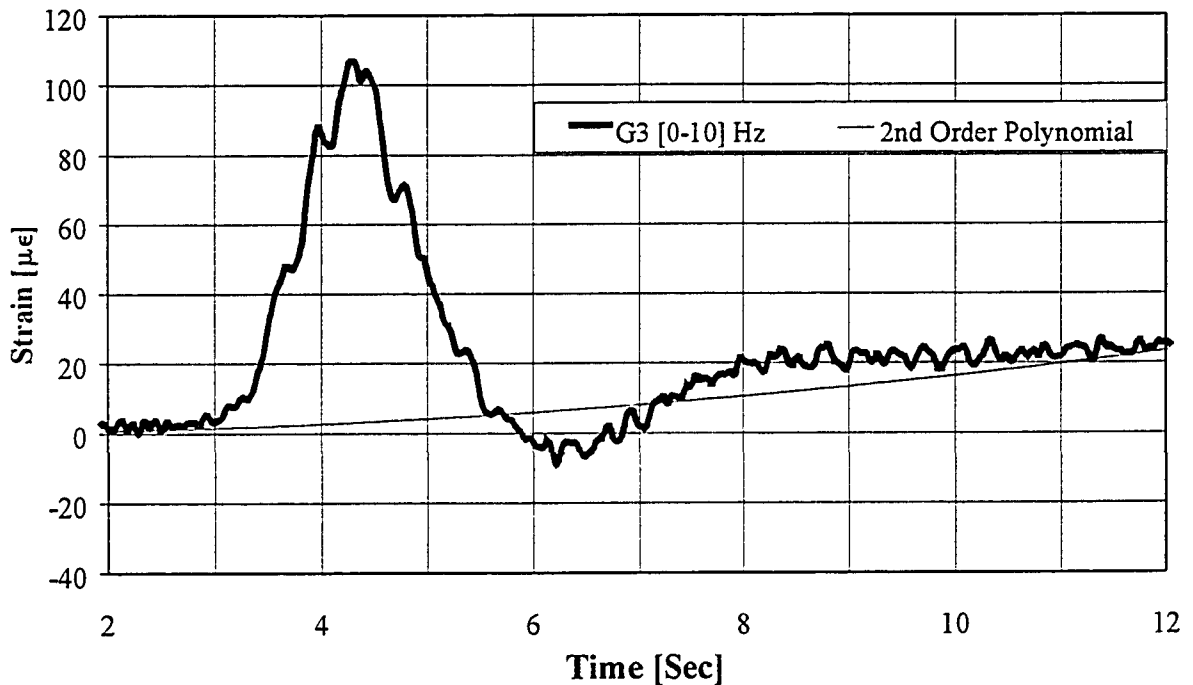


Figure 4.32: Low Pass Filtered Data of 10 Hz for Gauge G3 [Before correcting for drift]

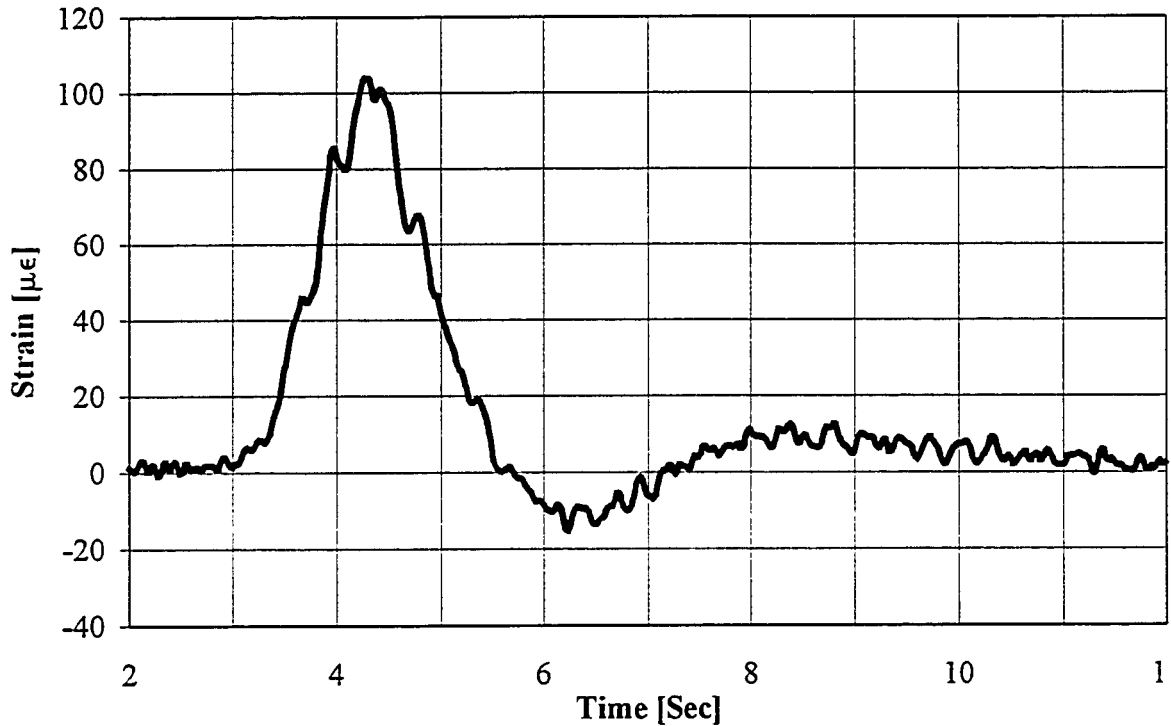


Figure 4.33: Final Filtered Response for Strain Gauge G3 [After corrected for drift]

Similar filtering processes and drift correction were applied to the standard strain gauge. The standard strain gauge, ST is mounted on the small 10 x 10 x 100 mm steel bar. This bar was subjected to similar environmental noises as the gauges on the superstructure. The data from standard strain gauge was log simultaneously in correspondence with all the other strain gauges. The only difference is that the small steel bar was not subjected to any load as opposed to other strain gauges on the structure. After applying the same filtering process as the strain gauge G3, the strain gauge ST final response is shown in Figure 4.34.

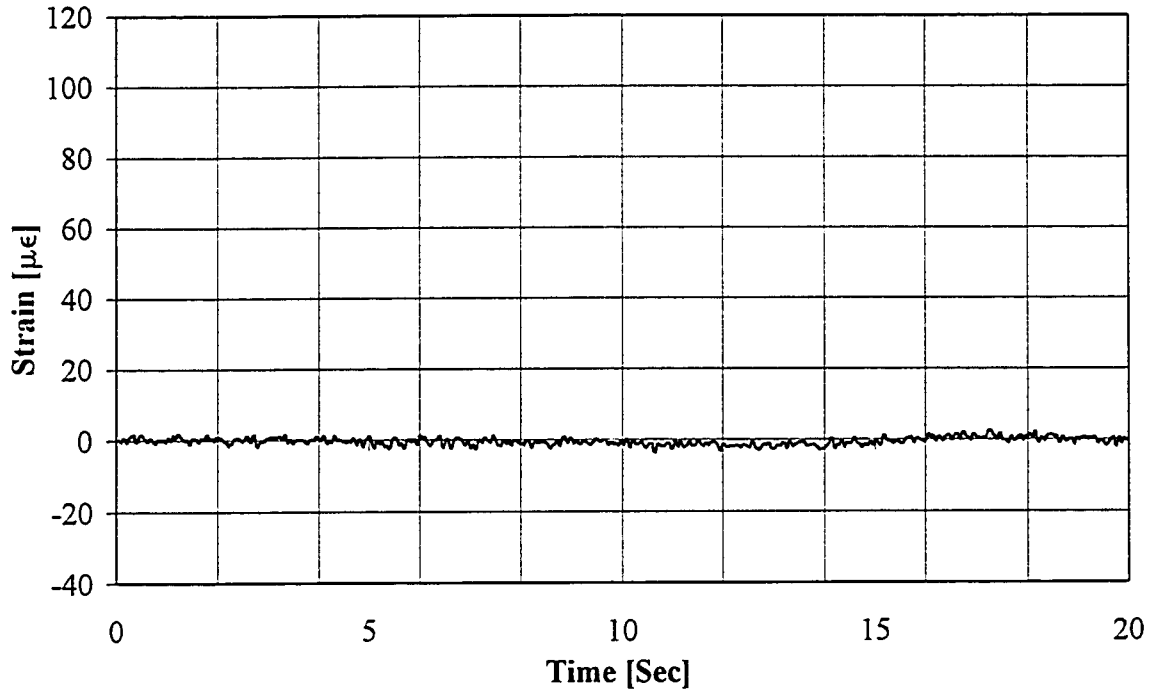


Figure 4.34 Final Filtered Response for Strain Gauge ST

Clearly, the filtering processes do not add any response to the final results. As expected, the standard strain gauge shows practically zero strain. Hence, the response in Figure 4.33 is the actual response due to the truck load only, and not noises or effect of the filter.

Figure 4.33 shows the dynamic response of the bridge for strain gauges G3 between 0 and 10 Hz. In order to compare this dynamic response to the static response, the dynamic response needs to be decoupled into *static component* and *dynamic component*. Commercial software such as LabVIEW can be used to digitally filter out the *dynamic component* thereby leaving the *static component*. However, before this decoupling process can begin, frequency limit needs to be established between the static and dynamic components. The lowest frequency limit is used to set a low pass filter in the LabVIEW program, therefore, any frequencies that pass under this filter will be the static response. Likewise, any frequency that is above this limit is the dynamic response. To establish the lowest frequency limit for the static component, speed of the vehicle that is moving over the bridge, length of the bridge, and number of spans must be known. The

Crowchild Trail Bridge has approximately three equal spans, and the overall length is 92.878 meters. A sum of the first two spans is 62.648 meters. According to influence line behaviour, the first two spans will form one full cycle in the response of the bridge. By knowing the speed of the truck, the time it takes for the truck to pass the first two spans is the approximate period of one cycle for the passing truck.

$$\text{Period, } T = \frac{\text{Distance}}{\text{Speed}} = \frac{62.648m}{15.2778m/\text{sec.}} = 4.101\text{sec.}$$

$$\text{Frequency } \therefore f = \frac{1}{T} = \frac{1}{4.101\text{sec.}} = 0.244\text{Hz} \quad [\text{for } 55 \text{ km/hr}]$$

$$\text{Frequency } \therefore f = \frac{1}{T} = \frac{1}{15.036\text{sec.}} = 0.0665\text{Hz} \quad [\text{for } 15 \text{ km/hr}]$$

For the 15 km/hr and the 55 km/hr, the influence line's frequency of the passing truck over the Crowchild Trail Bridge was 0.0665 Hz and 0.244 Hz respectively. Thus, the highest frequency of the passing truck over the Crowchild Bridge is 0.244 Hz for all the test-speed investigated. Consequently, a low-pass filter of 0.8 Hz will not affect the influence line even at 150 km/hr [0.665 Hz] on this bridge. Since all the speed ranges investigated have a maximum frequency of 0.244 Hz, a band-pass filter between 0 to 0.8 Hz will not affect the static influence line of the truck being investigated here. For the 55 km/hr test speed, the response of strain gauge G3 shown in Figure 4.35 yields identical influence line as in static test (Figure 4.29).

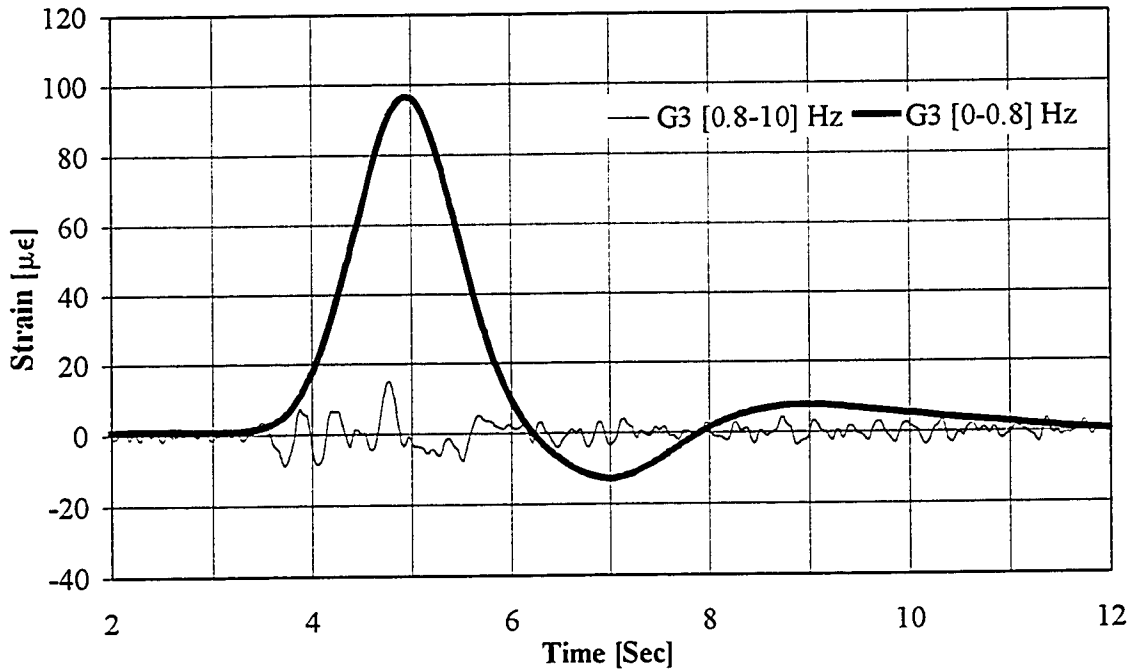


Figure 4.35: Filtered Data with Low Pass of 0.8 Hz and Band Pass of [0.8-10] Hz

Since the truck passes over the bridge at a much lower cycle than 0.8 Hz, a low-pass filtered below this frequency gives the influence line of the structure as shown. The influence line is plotted for strain versus time. This is the static response of the bridge. Final dynamic response of strain gauge G3 from 55 km/hr test is also shown in Figure 4.35. The maximum strain due to the dynamic component is $14.9 \mu\epsilon$. Clearly, dynamic test results can be filtered and reduced to obtain the static test results. In less than one minute, influence line, strains, length of each span, dynamic amplification factor, static/dynamic behaviour of the bridge can be determined with one truck and one strain gauge.

Cable transducer results from the same dynamic test had much less noises than strain gauge results. This is a result of the input/output voltage ratio that is much smaller in cable transducer than in strain gauge. Figure 4.36 shows the filtered and unfiltered data for the cable transducer. Note the Butterworth filter cause a slight shift in the filtered data of 0.696 second. As shown in Figure 4.37, the filtered data can easily be corrected for the shift of 0.696 second. Clearly, the result in Figure 4.37 shows that Butterworth filtered

has neither effect the shape nor the magnitude of the responses. The raw data shows the jagged curve, and the filtered data shows the smooth curve.

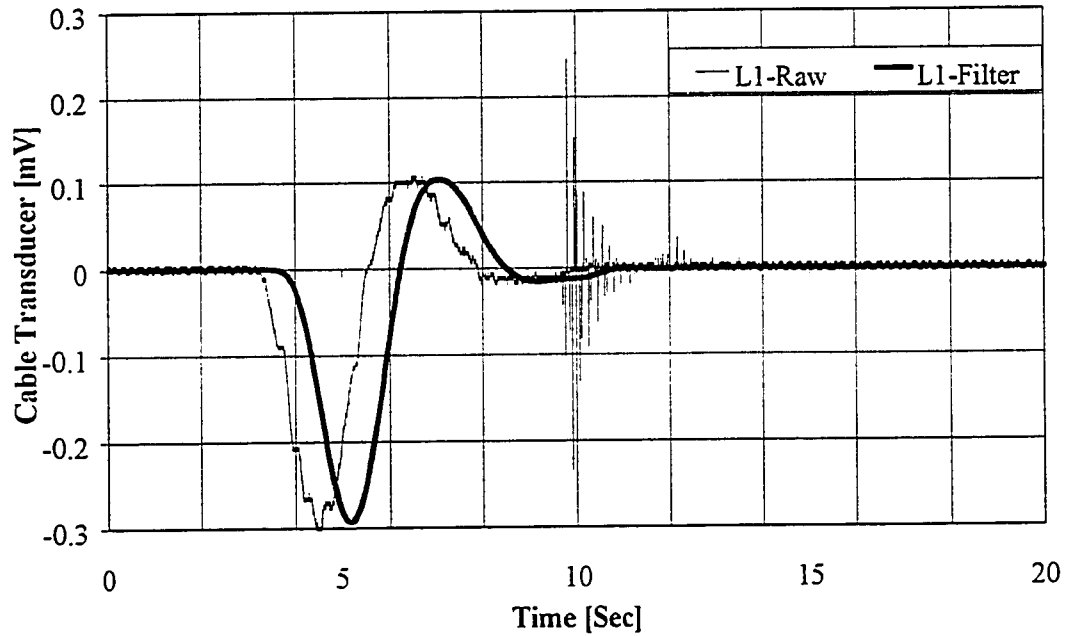


Figure 4.36: Cable Transducer Raw/Filtered Data *[Before Corrected for Shift]*

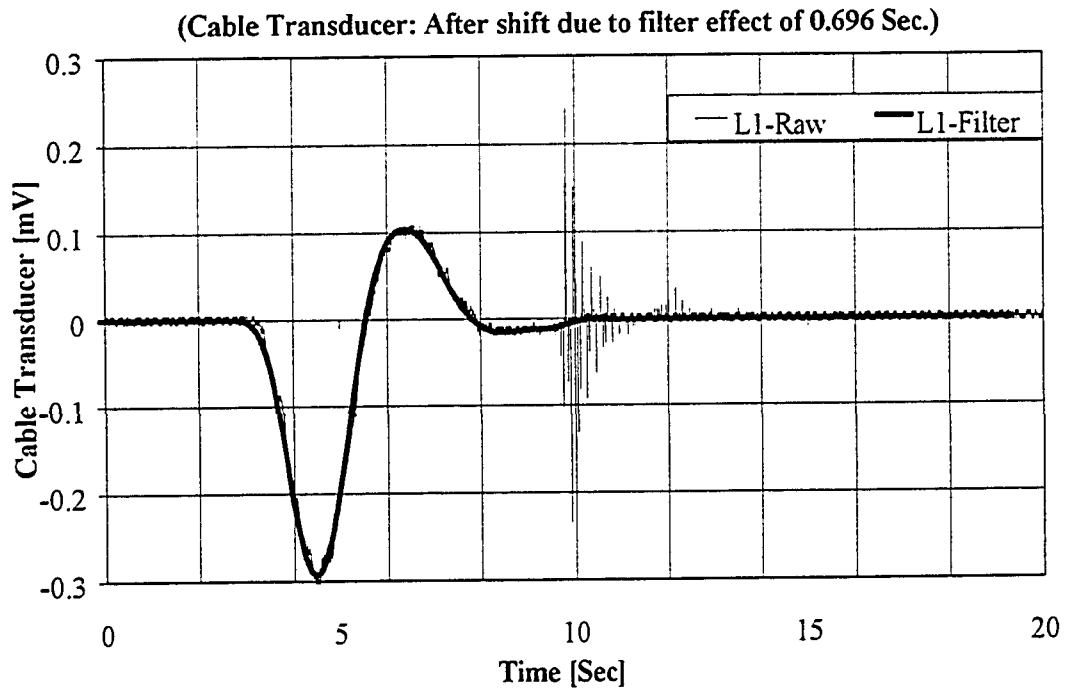


Figure 4.37: Cable Transducer Raw/Filtered Data *[After Corrected for Shift]*

Since the low-speed dynamic results can always be filtered for static results, future static tests can be eliminated altogether for the Crowchild Trail Bridge. Furthermore, results in Figure 4.35 seem to support that dynamic amplification factor can be found without the use of static test. The advantage of this implication translates into a tremendous saving in future field testing, little or no obstruction to traffic flow, hence more structures can be assess and evaluate in a very short time.

4.2.3.2 Damping Coefficient

Damping ratio of the bridge can be found by the decay of the free vibration motion. From the influence line, it is possible to determine the time when the truck comes onto the bridge and the time when the truck has completely left the bridge. Since accelerometer data were taken at the same time as the cable transducer, the free vibration period can easily be determined. Figure 4.38 shows the accelerometer data superimposed on cable transducer data. When the cable transducer data shows approximately zero reading, this would indicated that the truck had completely left the bridge. Thus, free vibration period can be determined. In turn, damping ratio of the structure can be determined. As of August 98, Crowchild Trail Bridge shows a damping ratio of 1.20 percent for the governing vibrating frequency was 3.40 Hz. The closest vertical mode found in ambient vibration test was 3.63 Hz. Figure 4.39 shows a close-up of the free vibration portion of Figure 4.38 and the damping curves for the structure. Damping curves plot in this figure was for accelerometer #48, and it was confirmed with all other accelerometers at the same speed.

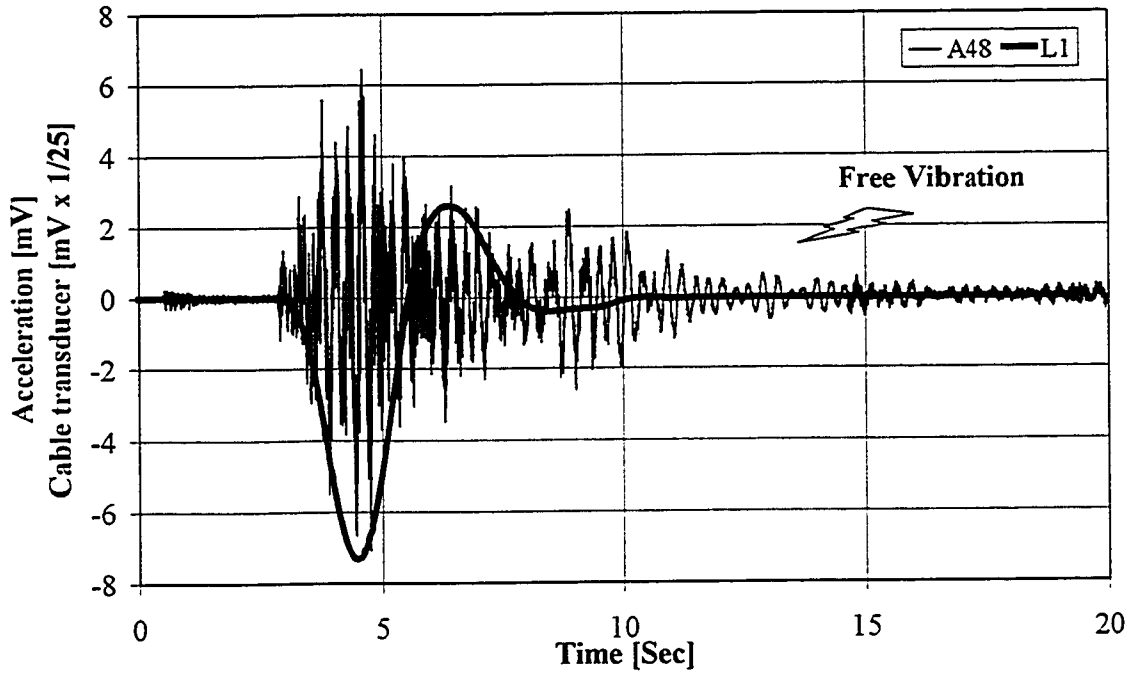


Figure 4.38: Superimposition of Cable Transducer and Accelerometer Data

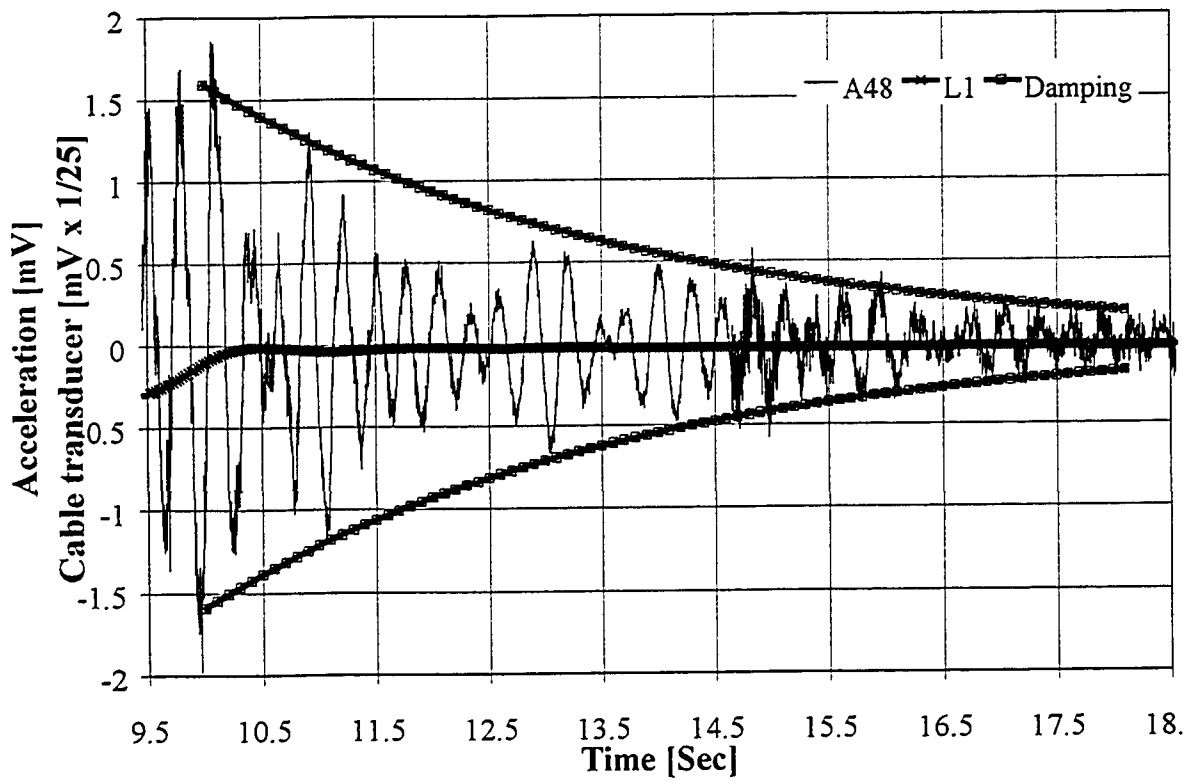


Figure 4.39: Accelerometer and Cable Transducer--Damping Curve

4.2.3.3 Dynamic Amplification Factor

Two approaches can be used to find the dynamic amplification factor. The first approach is to run static and dynamic tests on the structure and measured its responses. To find the dynamic amplification factor, takes the ratio of the maximum dynamic response to maximum static response for the structure. In which case, there must be enough dynamic test runs to ensure that the maximum dynamic effect is in phase with the maximum static response. If they are out of phase, then the maximum dynamic response could be less than the maximum static response. Thus, a true dynamic amplification factor cannot be calculated. However, to ensure that the maximum dynamic effect is in phase with the maximum static response is very time consuming and could be difficult to achieve in actual field-testing. An alternative method to find the dynamic amplification factor is to decouple the dynamic and the static responses. Thereby leaving the dynamic response completely independent of the location along the bridge. Hence, the maximum magnitude in the dynamic response portion is the dynamic amplification factor. With the latter method, only one test run is needed, and it has proved to provide a very reliable result. This method is used throughout all the analysis.

Dynamic amplification factor can be determined from either strain gauge or cable transducer test results. For the dynamic test of 15, 30, 40, and 55 km/hr, both results were used to calculate the dynamic amplification factor and compare it with each other, for all the various speeds tested. Results from the Crowchild Trail Bridge have clearly demonstrated that the dynamic amplification factor can be broken down into two components: the overall vertical deflection component and the local strain component in the bridge members.

4.2.3.3.1 Dynamic Amplification Factor: Local Strain Component

For running speed of 55 km/hr, Figure 4.40(a) shows the maximum strain due to static and dynamic affect are $96.4 \mu\epsilon$ and $14.9 \mu\epsilon$ respectively. Thereby giving a dynamic

amplification factor of 1.15. For the 40, 30, and 15 km/hr, the decoupled static/dynamic responses are shown in Figure 4.40(b), (c), and (d) respectively.

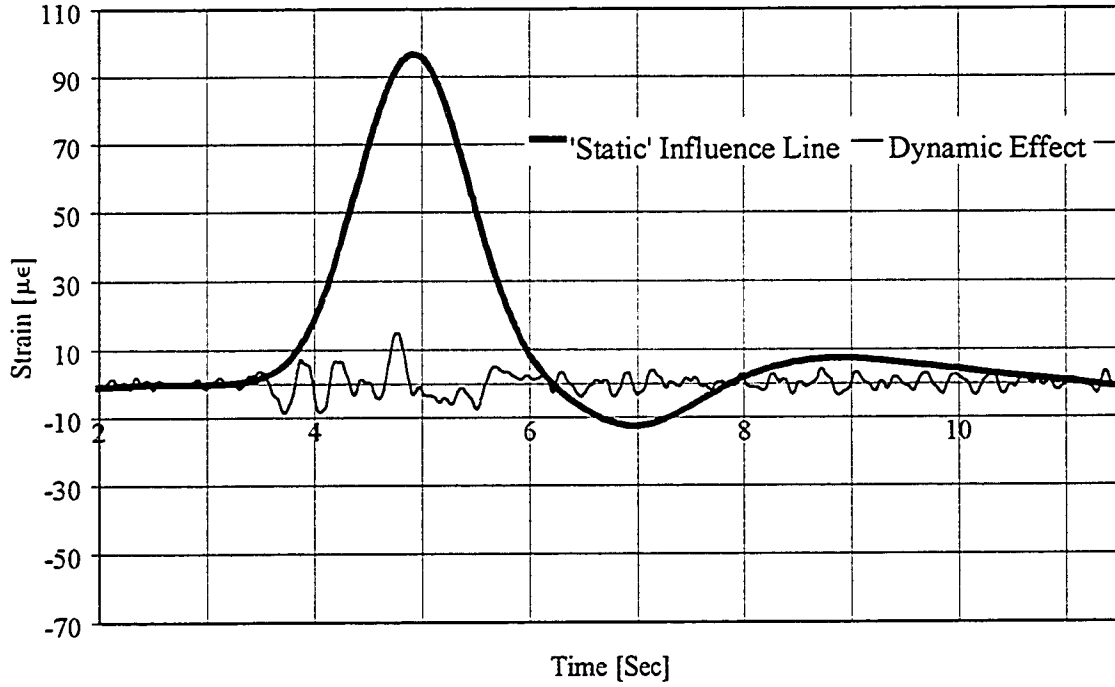


Figure 4.40(a): Decouple Response in Strain Gauges G3 for 55 km/hr Test

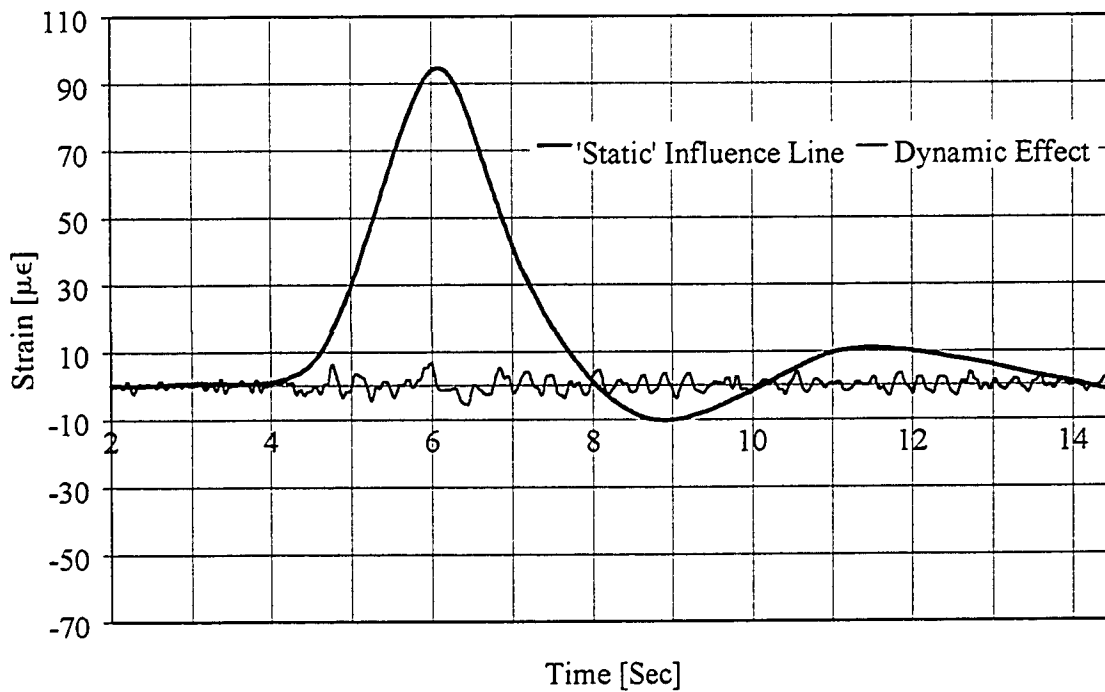


Figure 4.40(b): Decouple Response in Strain Gauges G3 for 40 km/hr Test

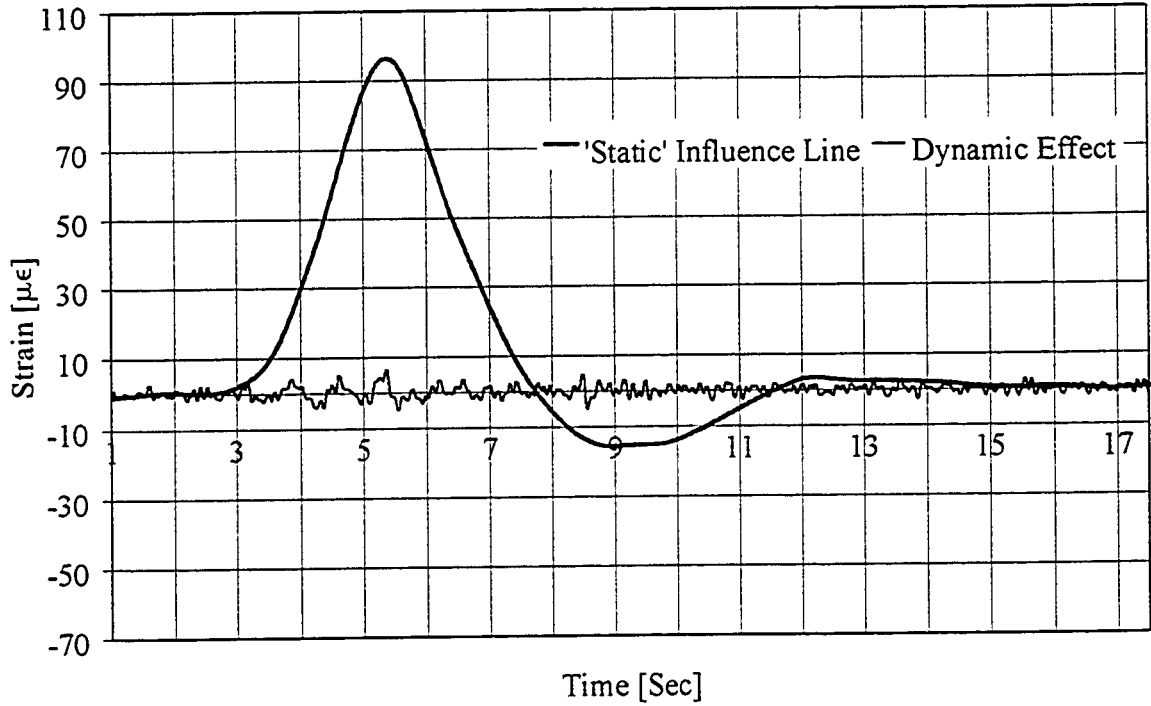


Figure 4.40(c) Decouple Response in Strain Gauges G3 for 30 km/hr Test

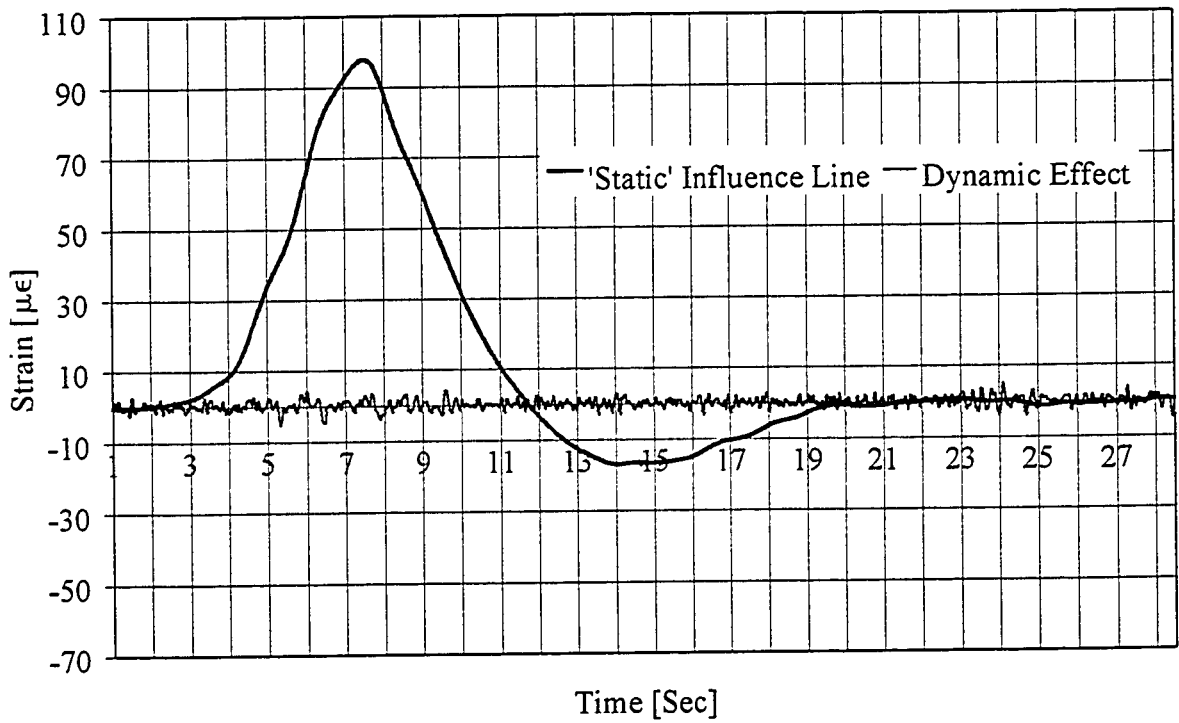


Figure 4.40(d) Decouple Response in Strain Gauges G3 for 15 km/hr Test

These figures suggest that the dynamic amplification factors vary nonlinearly with respect to speed. Table 4.6 shows a summary of the static response, dynamic response, and its' corresponding dynamic amplification factors for the strain gauge G3, G6, G33, and G34.

Dynamic Amplification Factor, DAF, due to local strain effects can be shown to vary with respect to speed in Figure 4.41. For 15 km/hr, the DAF is 5.5% with a variation of less than 0.07% for all the strain gauges investigated. Largest scatters were for 30 and 40 km/hr test speed with a 2.5% and 1.6% variation respectively. Finally, for the 55 km/hr, the maximum spreads for all the strain gauges were 0.7 % as shown in Figure 4.41 below.

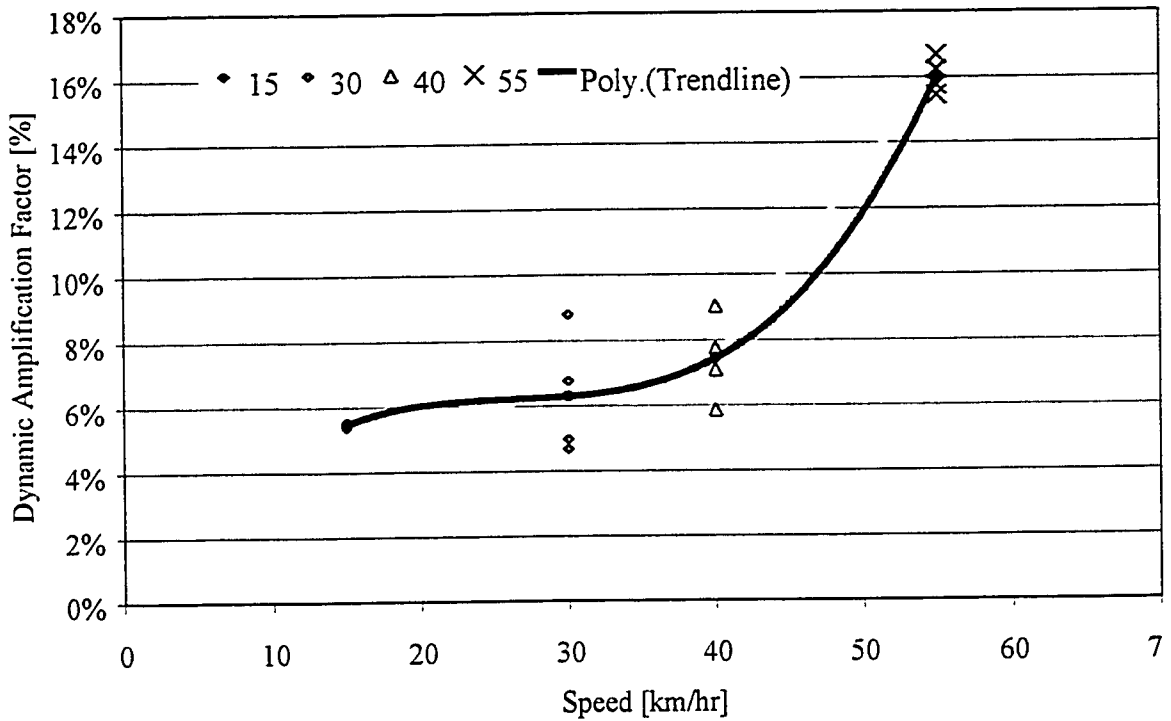


Figure 4.41: Dynamic Amplification Factor – Local Effect

Table 4.6: Dynamic Amplification Factor: Local Strain Effects for [Set 1]

Static Maximum Strain for Gauge G3 = 97.1 $\mu\epsilon$

G3

Speed	Static Response [$\mu\epsilon$]	Dynamic Response [$\mu\epsilon$]	DAF wrt Static	DAF wrt Filtered Response
15	97.83	5.4	6.3%	5.5%
30	96.23	6.5	5.8%	6.8%
40	94.44	6.7	4.1%	7.1%
55	96.51	14.9	14.7%	15.4%

Static Maximum Strain for Gauge G33 = 100.5 $\mu\epsilon$

G33

Speed	Static Response [$\mu\epsilon$]	Dynamic Response [$\mu\epsilon$]	DAF wrt Static	DAF wrt Filtered Response
15	98.8	5.3	3.5%	5.4%
30	106.8	5.3	11.5%	5.0%
40	96.9	7.5	3.8%	7.7%
55	101.5	16.9	17.8%	16.7%

Static Maximum Strain for Gauge G34 = 108.7 $\mu\epsilon$

G34

Speed	Static Response [$\mu\epsilon$]	Dynamic Response [$\mu\epsilon$]	DAF wrt Static	DAF wrt Filtered Response
15	104.8	5.8	1.8%	5.5%
30	117.8	5.5	13.5%	4.7%
40	104.3	6.1	1.6%	5.8%
55	109.2	17.7	16.8%	16.2%

Static Maximum Strain for Gauge G6 = 64.4 $\mu\epsilon$

G6

Speed	Static Response [$\mu\epsilon$]	Dynamic Response [$\mu\epsilon$]	DAF wrt Static	DAF wrt Filtered Response
15				
30	61.5	5.4	3.9%	8.8%
40	63.07	5.7	6.8%	9.0%
55	64.85	10.2	16.5%	15.7%

4.2.3.3.2 Dynamic Amplification Factor: Overall Deflection Component

Second method of examining the dynamic amplification factor is through the overall deflection of the structural components. The bridge was tested three times for each of the four speeds investigated. In set #1, for the 55 km/hr test, readings from cable transducer at the same location as the strain gauge G3 is plotted in Figure 4.42. The Deflections due to static and dynamic response were 11.5 mm and 0.94 mm respectively. Subsequently, the dynamic amplification factor is 1.08. The factor found from cable transducer is slightly lower than that of the suggested by strain gauge results. [However, the maximum response in the filtered data for the cable transducer was a little higher than from the static test. This relationship between the dynamic test and the static test will not be further investigated. Since cars were still allowed to pass in the other lane during the dynamic test, therefore the loads were slightly different in dynamic test as oppose to static.]

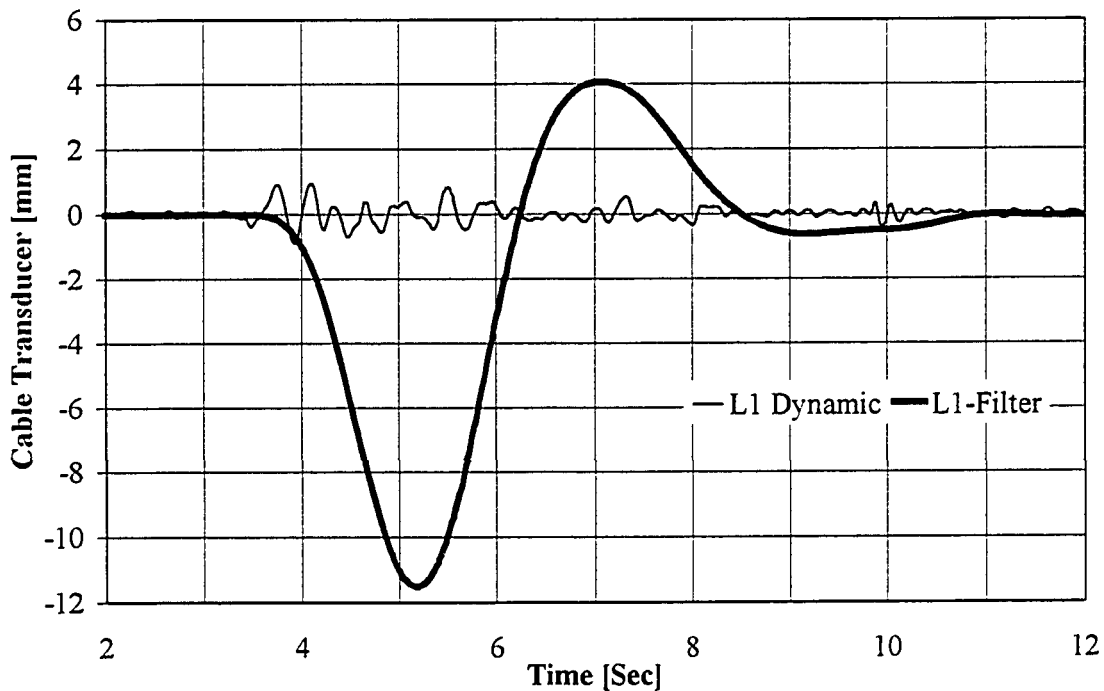


Figure 4.42: Cable Transducer #1 for 55 km/hr Test

Cable transducer plots of all different speeds for all three sets are in Appendix B. Table 4.7 below shows the decoupled responses of the cable transducers tested. It details the static and dynamic responses, and its' corresponding DAF for all the tests.

Table 4.7: Dynamic Amplificaiton Factor: Overall Deflection

$$\text{Static Maximum Deflection} = 10.28 \text{ mm}$$

Set 1				
	Static	Dynamic	DAF wrt	DAF wrt
Speed	Response [mm]	Response [mm]	Static	Filtered Response
15	10.02	0.48	2.2%	4.8%
30	10.23	0.61	5.5%	6.0%
40	10.36	0.77	8.3%	7.4%
55	11.49	0.94	21.0%	8.2%

Set 2				
	Static	Dynamic	DAF wrt	DAF wrt
Speed	Response [mm]	Response [mm]	Static	Filtered Response
15	10.61	0.57	8.8%	5.4%
30	10.77	0.57	10.3%	5.3%
40	10.10	0.79	6.0%	7.8%
55	11.30	0.86	18.3%	7.6%

Set 3				
	Static	Dynamic	DAF wrt	DAF wrt
Speed	Response [mm]	Response [mm]	Static	Filtered Response
15	10.26	0.51	4.8%	5.0%
30	12.09	0.93	26.7%	7.7%
40	11.56	0.84	20.7%	7.3%
55	12.04	1.34	30.2%	11.2%

From the above table, the dynamic amplification factor due to overall deflection effects can be shown to vary with respect to speed, as shown in Figure 4.43 below. The overall trend for the DAF as a function of speed seems to be linear. For 15 km/hr test speed, the DAF from the deflection is 5.1%, comparing to the strain gauge of 5.5%. The DAF results from cable transducer and strain gauge give very close results for a low speed of 15 km/hr. In the 30 km/hr and 40 km/hr, the DAF are 6.3% and 7.5% respectively. For the 55 km/hr, the DAF is 9.0%. The overall trend of the DAF obtains from the cable

transducer and strain gauge gives quite vastly different behaviour. The trend from the cable transducers gives a linear relationship with respect to the speed; however, the strain gauge gives a nonlinear relationship that increases exponentially for all the speeds tested. This suggests that the local strain effects are much more severe under dynamic load than that of the overall deflection effects. This implies a ‘lag effect’ in load distribution under dynamic loading. The differences between the DAF from the overall deflection and the strain gauge clearly show a large portion of DAF that the designer may never have considered in the design.

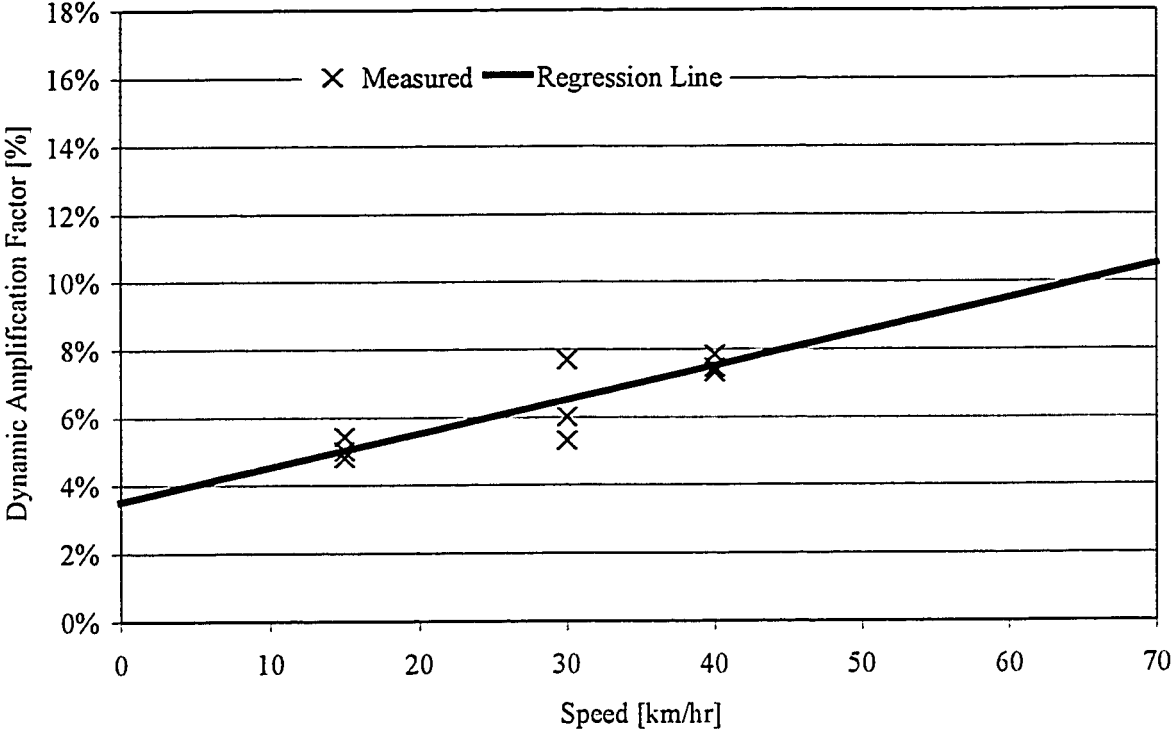


Figure 4.43: Dynamic Amplification Factor – Overall Deflection Effect

4.2.3.4 Load Sharing

Load sharing among girders can be examined through the strain gauges or by cable transducers that were mounted on the superstructure. Comparison of the cable transducer results between static and dynamic tests are shown in Figure 4.44 below. It is important to note that the difference of the sum at a cross section for the deflection measurements in

static and dynamic tests was only 0.7 percent. Hence, the bridge does not overall deflected more in dynamic test than static test; rather it absorbed the energy in a torsional mode as opposed to the vertical mode.

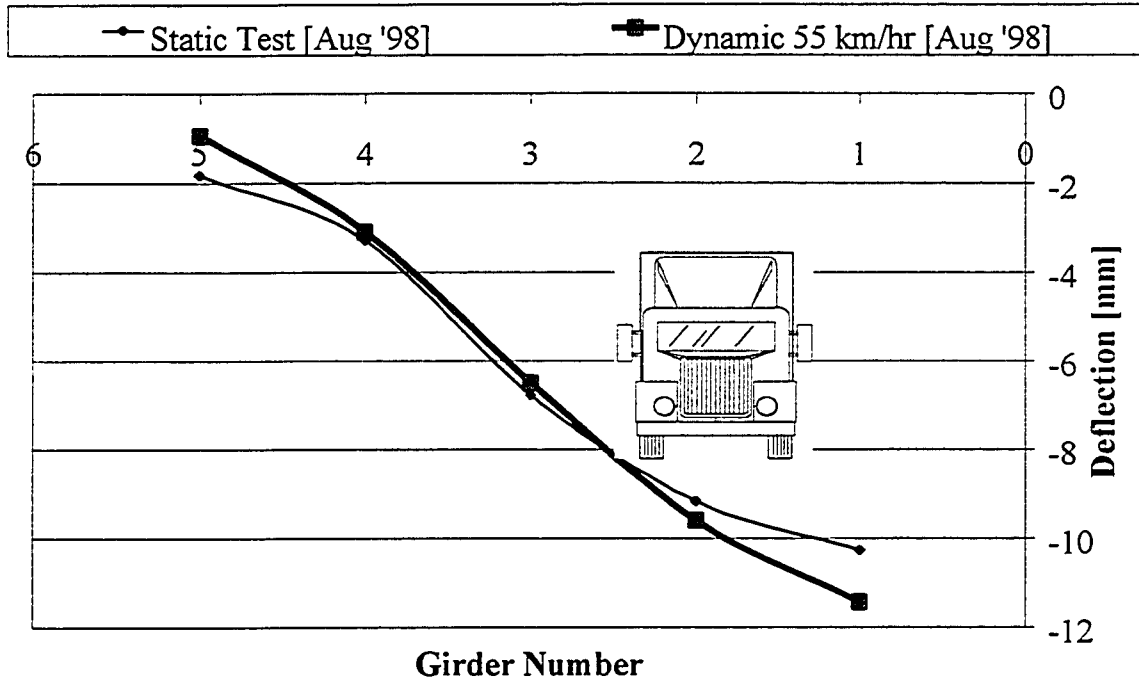


Figure 4.44: Overall Deflection Among Girders

The torsional excitation characteristics manifest itself again in the three-dimensional influence surface plots in Figure 4.45. Figure 45(a) and Figure 45(b) are plots for the static test and the 55 km/hr dynamic test, respectively. The purpose of these plots is for visual aid in the behaviour of the bridge under vertical loads in the transverse as well as longitudinal directions along the bridge. Comparison between the static and the dynamic results shows that they are almost identical. The static curve is more jagged in shape, and it has slightly smaller maximum deflection than that of the dynamic test. Likewise, it has bigger minimum deflection than that of the dynamic test. These facts have further reinforced the torsional excitation in the 55 km/hr test speed.

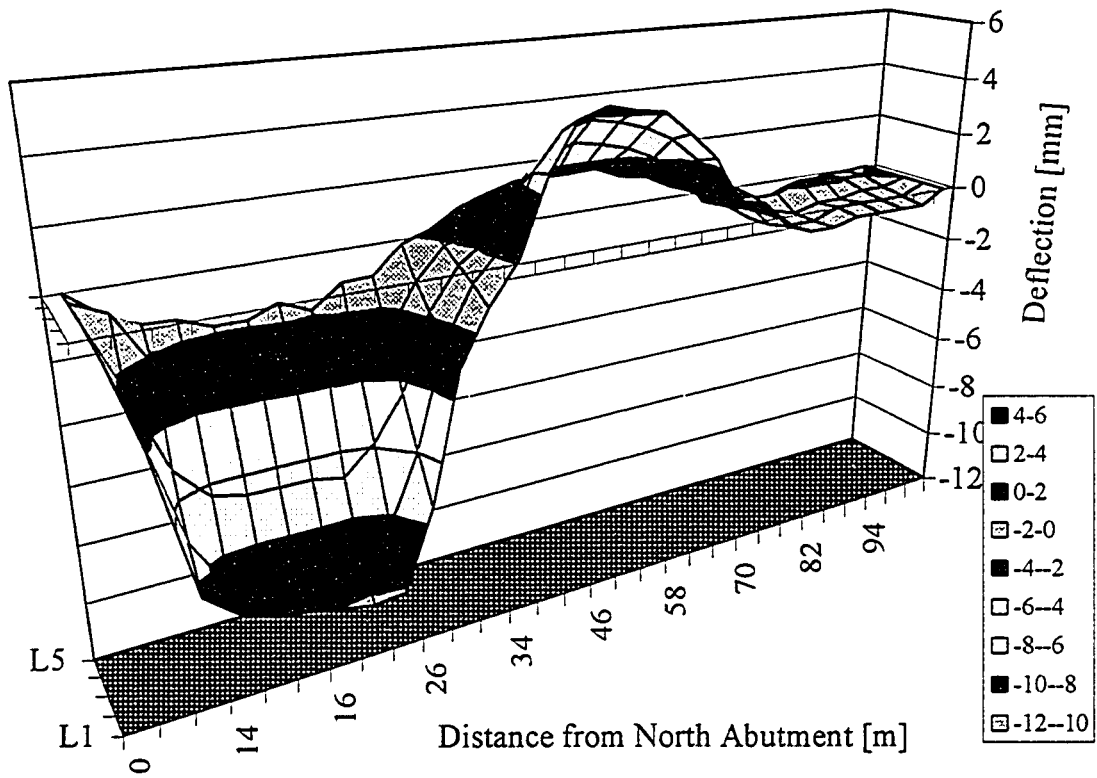


Figure 4.45(a): 3D Influence Surface – Static Test Results

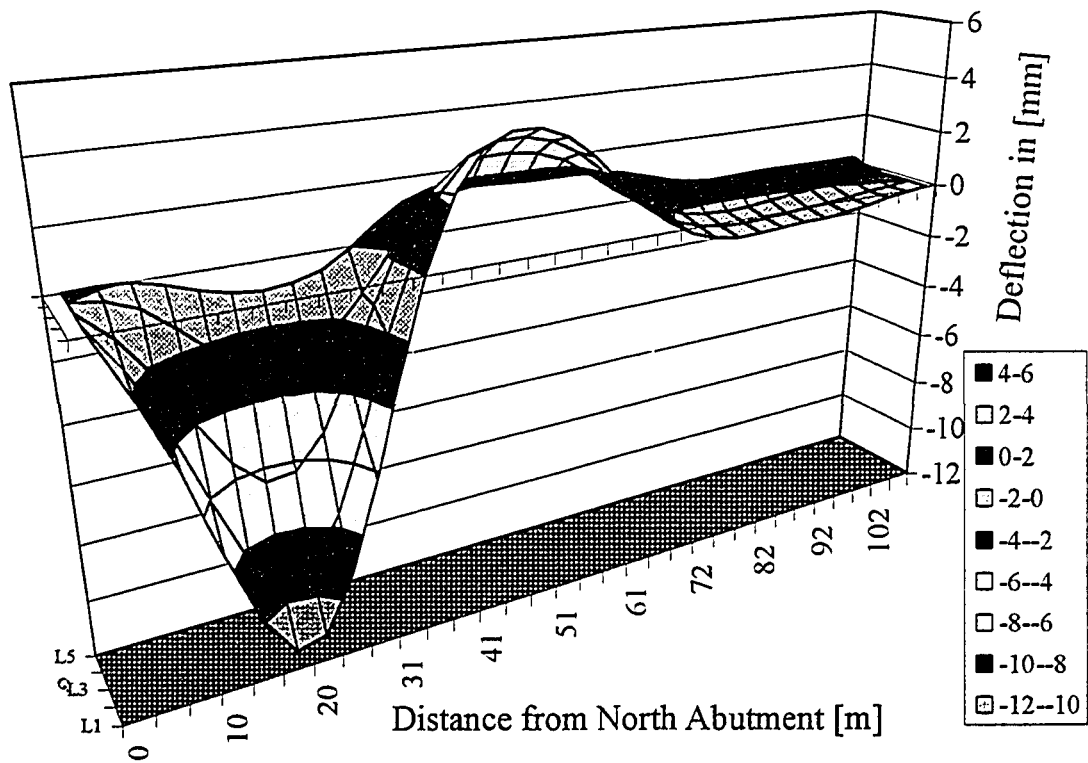


Figure 4.45(b): 3D Influence Surface – Dynamic Test Results

4.2.4 Crack Pattern for August 1998

The first crack patterns were mapped in August 1997. Crowchild Trail Bridge consisted of three continuous spans. The South span was reinforced with both GFRP and steel reinforcement. Crack pattern for the South span to the North span as of August 1997 is shown in Figures 4.9 to 4.11. All cracks were in the transverse direction. Most cracks were approximately 0.5 mm in width. As of August 1997, there was no longitudinal crack.

After one full year of operation, a second crack pattern was mapped in August 1998. Crack pattern for the South span, Middle span and North span are shown in Figures 4.46 to 4.48 respectively. The cracks that were there already from August 1997 seem to have grown twice wider by August 1998. As of August 1998, there were quite a few new cracks had formed on the underside of the bridge. In addition to many new transverse cracks formed, there were quite a few longitudinal beginning to appear. Most longitudinal cracks were formed right at the transition point between the flat part of the deck and the taper part. However, a few longitudinal cracks formed at midway between the two supporting girders in the South span.

Overall, there are quite a few new cracks pattern formed over the last one year of operation. Most of the cracks formed were 0.5 mm and less in width. Cracks that were there already since August 1997 are now a little wider and there existed water stain marks. There appeared to be more transverse cracks in the Middle and the South spans. North span, which was reinforced only in the cantilever edge, now had longitudinal cracks in the sophist and at midway in between the two girders as shown in Figure 4.48.

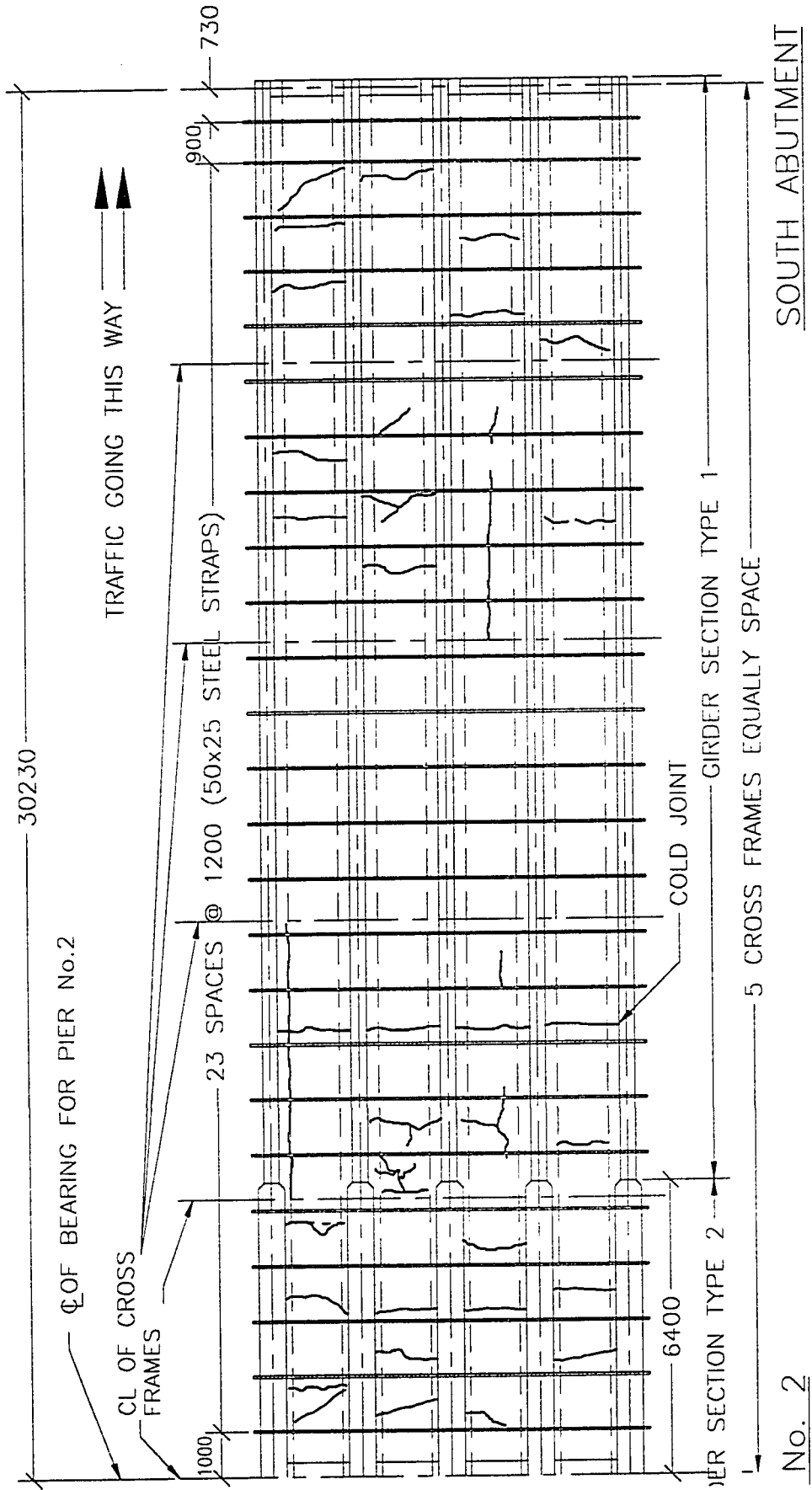


Figure 4.46: South Span Crack Pattern [August 1998]

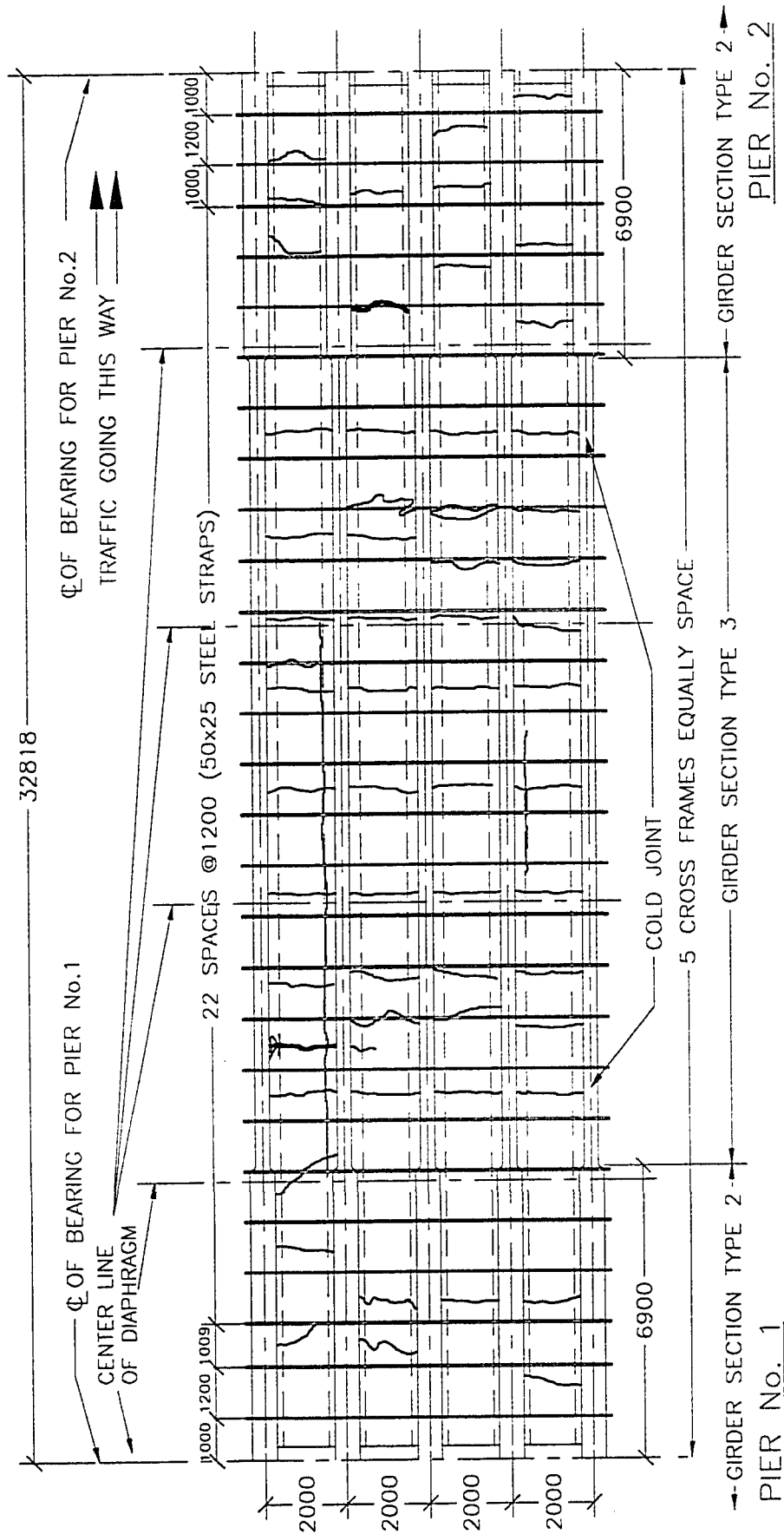


Figure 4.47: Middle Span Crack Pattern [August 1998]

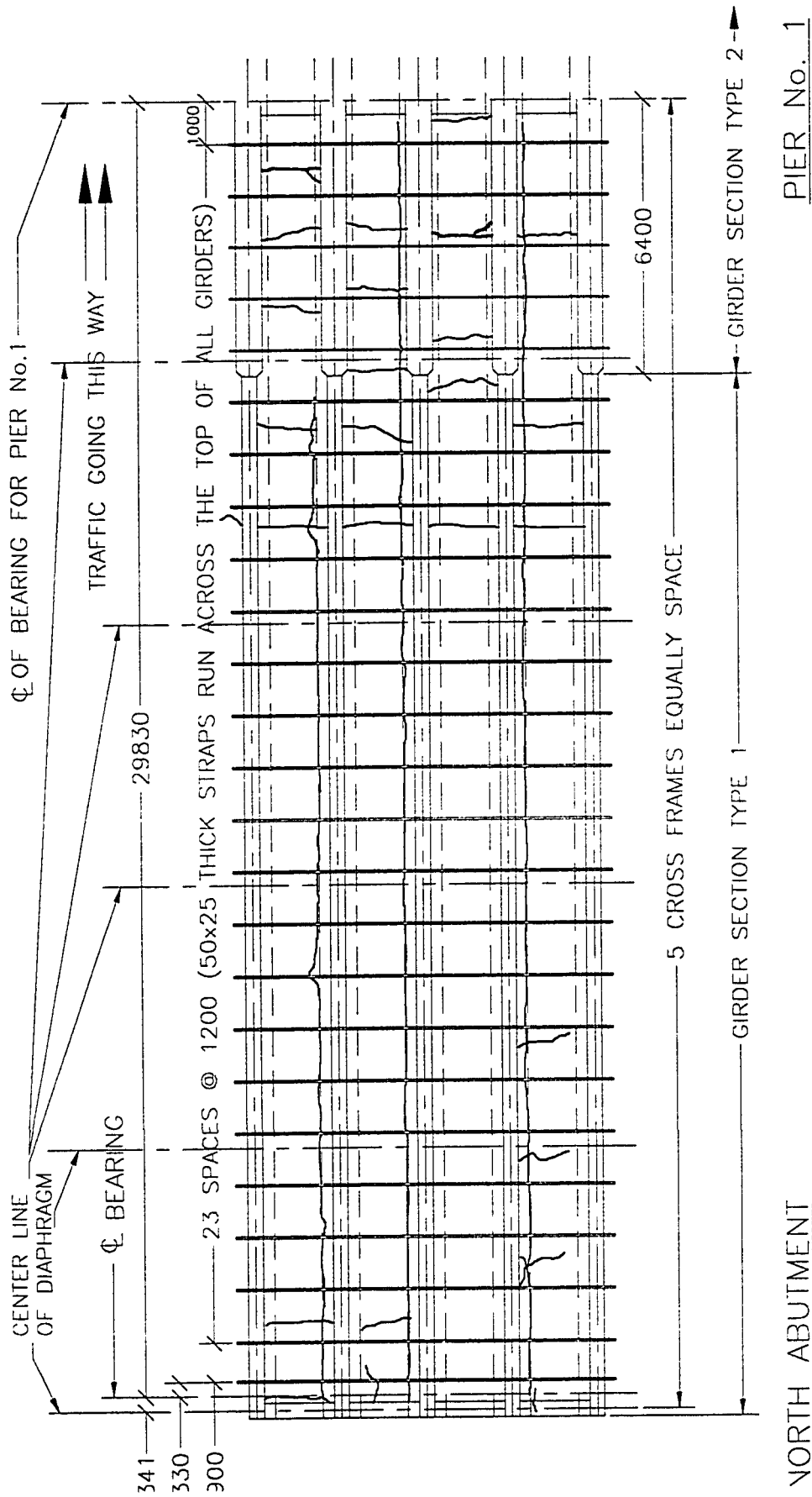


Figure 4.48: North Span Crack Pattern [August 1998]

5. ANALYSIS AND COMPARISON

5.1 Dynamic Behaviour of Crowchild Trail Bridge

5.1.1 Theoretical Background

Structural dynamic problems are often difficult to visualize, design for, and anticipate. Exact modeling of structural dynamic problems is either impossible or impractical. Thus, dynamics problems are idealize and visualize in three pure components. Figure 5.1 below shows the idealized components of a dynamic problem.

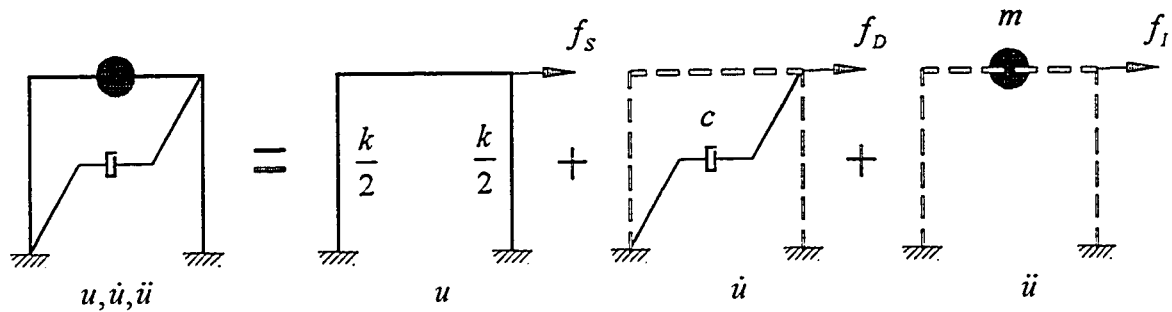


Figure 5.1: Idealized Components

For the force $P(t)$ acting on the idealized system above, the governing equation of motion become

$$\begin{aligned}
 f_I + f_D + f_s &= P(t) \\
 m\ddot{u} + c\dot{u} + ku &= P(t) && \text{for Elastic Systems} \\
 m\ddot{u} + c\dot{u} + f_s(u, \dot{u}) &= P(t) && \text{for Inelastic Systems}
 \end{aligned}
 \tag{5.1}$$

<i>where</i>	<i>u</i> Displacement	<i>f_I</i> Inertia Force
	<i>u</i> Velocity	<i>m</i> Mass
	<i>u</i> Acceleration	<i>k</i> Stiffness
	<i>f_s</i> Stiffness Force	<i>c</i> Damping Coefficient
	<i>f_D</i> Damping Force	<i>P(t)</i> Force as a function of time, <i>t</i>

Equation (5.1) can be solved by four methods: closed form solution, Duhamel's Integral, Transform methods, and Numerical Integration. However, the closed form solution can be very complex and sometimes no solution to the differential equation can

be found. Duhamel's Integral and Transform method are designed to solve for linear differential equations. Only the numerical time-stepping integration method is a practical approach in solving the equation of motion in inelastic systems.

For a damped, free vibration system, and forcing function $P(t) = 0$, the governing second order, linear, homogeneous differential equation of motion with constant coefficients is:

$$m\ddot{u} + c\dot{u} + ku = 0 \quad (5.2)$$

Let $u = Ge^{rt}$, where G and r are constants that depend on initial conditions. Equation (5.2) becomes

$$Ge^{rt}(mr^2 + cr + k) = 0$$

Therefore $mr^2 + cr + k = 0 \quad (5.3)$

(a) For Undamped System

The solution of equation (5.3) for undamped systems, $c = 0$, is

$$r^2 = \frac{-k}{m} \quad (5.4)$$

Letting $i = \sqrt{-1}$ and $w_n = \sqrt{\frac{k}{m}}$, equation (5.4) becomes

$$r = \pm iw_n \quad (5.5)$$

where w_n is the natural frequency of the undamped systems.

Therefore, $u = G_1e^{-iw_nt} + G_2e^{iw_nt} \quad (5.6)$

$$= A \sin(w_nt) + B \cos(w_nt) \quad \text{by Euler's Identity} \quad (5.7)$$

$$= \frac{\dot{u}_o}{w_n} \sin(w_nt) + u_o \cos(w_nt) \quad \text{after initial conditions, } u(0) = u_o$$

and $\dot{u}(0) = \dot{u}_o$ are applied (5.8)

where A, B constants \ddot{u}_o Initial Acceleration
 \dot{u}_o Initial Velocity t time

(b) For Damped System

The solution of equation (5.3) for damped system is

$$\begin{aligned} r &= \frac{-c}{2m} \pm \frac{\sqrt{c^2 - 4km}}{2m} \\ &= \frac{-c}{2m} \pm \sqrt{\left(\frac{c}{2m}\right)^2 - \left(\frac{k}{m}\right)} \end{aligned} \quad (5.9)$$

(i) For critically damped systems,

$$\left(\frac{c}{2m}\right)^2 = \left(\frac{k}{m}\right)$$

$$\text{Thus, } c_{cr} = 2mw_n \quad (5.10)$$

where c_{cr} is the critical damping coefficient.

(ii) For Heavily damped systems,

$$\left(\frac{c}{2m}\right)^2 > \left(\frac{k}{m}\right) \quad (5.11)$$

(iii) Lightly damped systems,

$$\left(\frac{c}{2m}\right)^2 < \left(\frac{k}{m}\right) \quad (5.12)$$

Letting $\xi = \frac{c}{c_{cr}} = \frac{c}{2mw_n}$, equation (5.9) becomes

$$\begin{aligned} r &= -w_n\xi \pm \sqrt{(w_n\xi)^2 - w_n^2} \\ &= -w_n\xi \pm iw_n\sqrt{1 - \xi^2} \end{aligned} \quad (5.13)$$

where ξ is the damping ratio.

Letting $w_D = w_n\sqrt{1 - \xi^2}$, equation (5.13) can be simplified as

$$r = -w_n\xi \pm iw_D \quad (5.14)$$

where w_D is the natural frequency of the damped systems.

$$\begin{aligned} \text{Therefore } u &= G_1 e^{(-w_n\xi + iw_D)t} + G_2 e^{(-w_n\xi - iw_D)t} \\ &= e^{-w_n\xi t} (G_1 e^{iw_D t} + G_2 e^{-iw_D t}) \end{aligned} \quad (5.15)$$

$$= e^{-w_n\xi t} (A \sin w_D t + B \cos w_D t) \quad \text{by Euler's Identity} \quad (5.16)$$

Applying Initial Conditions, $u(0) = u_o$ and $\dot{u}(0) = \dot{u}_o$

$$u(t) = e^{-\xi w_n t} \left[u(0) \cos w_n t + \left(\frac{\dot{u}(0) + w_n \xi u(0)}{w_D} \right) \sin w_n t \right] \quad (5.17)$$

Finally, $u(t) = \rho \cos(w_D t - \theta) e^{-\xi w_n t} \quad (5.18)$

where $\rho = \sqrt{\left(\frac{\dot{u}_o + u_o w_n \xi}{w_D} \right)^2 + u_o^2}$

$$\theta = \tan^{-1} \left[\frac{(\dot{u}_o + u_o w_n \xi)}{w_D u_o} \right]$$

(c) Damping Coefficient

Equation (5.17) shows that the ratio of the amplitude between each successive peak is defined as follow (Chopra, 1995):

$$\frac{u(t)}{u(t + T_D)} = e^{\frac{2\pi\xi}{\sqrt{1-\xi^2}}} \quad (5.19)$$

Similarly, the ratio for the acceleration between each successive peak is,

$$\frac{\ddot{u}(t)}{\ddot{u}(t + T_D)} = e^{\frac{2\pi\xi}{\sqrt{1-\xi^2}}} \quad (5.20)$$

Solving for the damping ratio, ξ

$$\ln \left(\frac{\ddot{u}(t)}{\ddot{u}(t + T_D)} \right) = \frac{2\pi\xi}{\sqrt{1-\xi^2}}$$

$$\xi = \pm \frac{\ln \left(\frac{\ddot{u}(t)}{\ddot{u}(t + T_D)} \right)}{\sqrt{\left[\ln \left(\frac{\ddot{u}(t)}{\ddot{u}(t + T_D)} \right) \right]^2 + 4\pi^2}} \quad (5.21)$$

However, it is more accurate to select multiple peaks, such that the amplitude has decreased at least 50%. Similarly, for multiple successive peaks, we can derive the relationship as follow:

$$\frac{u(t)}{u(t+mT_D)} = e^{\frac{2\pi m\xi}{\sqrt{1-\xi^2}}} \quad (5.22)$$

$$\xi = \pm \frac{\ln\left(\frac{u(t)}{u(t+mT_D)}\right)}{\sqrt{\left[\ln\left(\frac{u(t)}{u(t+mT_D)}\right)\right]^2 + 4\pi^2 m^2}} \quad (5.23)$$

(d) *Simply Supported Beams*

A simply supported beam is shown in Figure 5.2. The first three frequencies and mode shapes of this free simply supported beam are shown in Table 5.1. Obviously, Table 5.1 is valid only for free vibration with zero initial velocity and an initial displacement (Chopra, 1995).

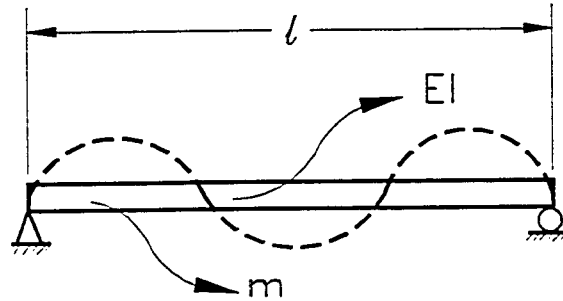


Figure 5.2: Simply Supported Beam

Table 5.1: Frequency of Single Span and Simply Supported

Mode	Mode Shape	Angular Velocity, ω	Period, T	Frequency
1		$\omega_1 = \frac{\pi^2}{l^2} \sqrt{\frac{EI}{m}}$	$\frac{2\pi}{\omega_1}$	$\frac{\omega_1}{2\pi}$
2		$\omega_2 = \frac{4\pi^2}{l^2} \sqrt{\frac{EI}{m}}$	$\frac{2\pi}{\omega_2}$	$\frac{\omega_2}{2\pi}$
3		$\omega_3 = \frac{9\pi^2}{l^2} \sqrt{\frac{EI}{m}}$	$\frac{2\pi}{\omega_3}$	$\frac{\omega_3}{2\pi}$

(e) Continuous Beams

Unlike a simply supported beam shown above, the dynamic analysis of continuous beams is more cumbersome. Due to the complexity of its' mode shapes, derivation of a mathematical equivalent is not an easy task. Take the case of three continuous span, simply supported as shown in Figure 5.3. Assuming three identical spans, the first three vertical-fundamental mode shapes of the beam are shown in Table 5.2 (Biggs, 1964).

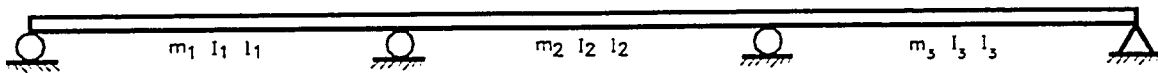


Figure 5.3: Three Continuous Span

Table 5.2: Frequency of Three Continuous Span and Simply Supported

Mode	Mode Shape	Angular Velocity, ω	Period, T	Frequency
1		$\omega_1^2 = \frac{EI\pi^4}{ml^4}$	$\frac{2\pi}{\omega_1}$	$\frac{\omega_1}{2\pi}$
2		$\omega_2^2 = \frac{EI(3.55)^4}{ml^4}$	$\frac{2\pi}{\omega_2}$	$\frac{\omega_2}{2\pi}$
3		$\omega_3^2 = \frac{EI(4.30)^4}{ml^4}$	$\frac{2\pi}{\omega_3}$	$\frac{\omega_3}{2\pi}$

5.1.2 Natural Frequencies and Mode Shapes of the Crowchild Trail Bridge

To analyze the Crowchild Trail Bridge, the following assumptions are made:

1. All five girders have the same stiffness;
2. Barrier rail and asphalt have no contribution to the stiffness;
3. Each girder has the same stiffness along the length and is continuous in all three spans;
4. All three spans are equal, with span length = 30 230 mm;
5. Small deformation and elastic behaviour are assumed;
6. Shear deformation is ignored;
7. Rotational inertia of masses is considered to be negligible;

8. Damping is negligible;
9. Full composite action is assumed;
10. Steel Strength, $F_y = 350MPa$ is used;

Table 5.3: Crowchild Trail Bridge Concrete Mix Properties

CONCRETE MIXES (for 1 m ³)	
Specified Strength, $f_c'_{28} = 35$ MPa	Fine Aggregates = 680 kg
Water = 155 kg	Air Entrainment = 50 ml / 100 kg
Cement = 430 kg	Superplastizer = 290 ml / 100 kg
Coarse Aggregates = 1080 kg	Polypropylene Fibers = 4.5 kg (0.45% by volume)

From Table 5.3 above, the concrete density is determined to be $\gamma_c = 2350 \frac{kg}{m^3}$.

Based on the second modulus, the elastic modulus of concrete can be determined by

$$E_c = (3300\sqrt{f'_c} + 6900) \left(\frac{\gamma_c}{2300} \right)^{1.5} = 27290MPa$$

$$n = \frac{E_c}{E_s} = \frac{27290}{207000} = 0.131836$$

Figure 5.4 shows a simplified model of the Crowchild Trail Bridge. The diagram shown on the left in Figure 5.4 shows the section before conversion to steel equivalent, and the diagram shown on the right is the steel equivalent after conversion. The distance from the bottom side of the bottom flange to the neutral axis is at 916 mm. Moment of inertia is $I_x = 24489.3 \times 10^6 mm^4$. Assuming the density of concrete, steel, and asphalt are 2350, 7850, and 2293 kg/m³ respectively. Thus, the simplified model to the left has a mass of 1864 kg/m.

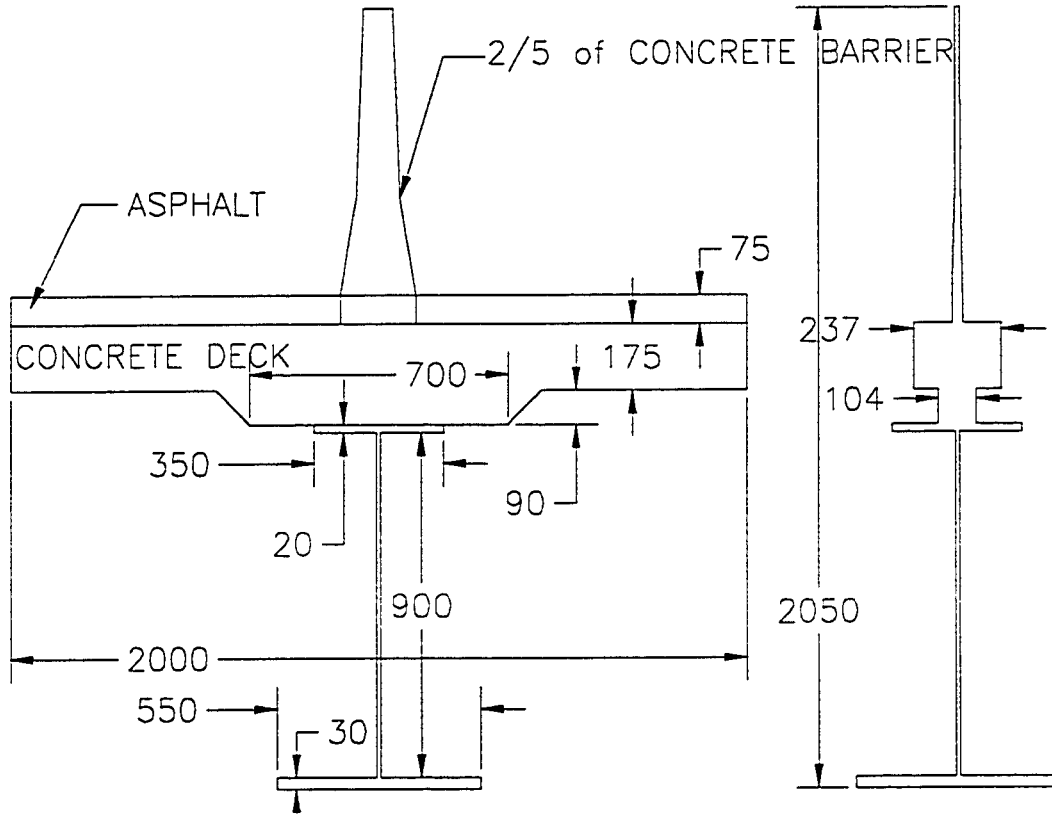


Figure 5.4: Simplified Model of Bridge Deck

Natural frequencies of the above simplify model is calculated with the following variables substituted into the equations in Table 5.2:

$$E_s = 207000 \text{MPa}, \quad I_x = 24489.3 \times 10^6 \text{mm}^4,$$

$$l = 30.23 \text{m}, \quad m = 1864 \frac{\text{kg}}{\text{m}}$$

Therefore,

$$\omega_1 = 17.84 \frac{\text{rad}}{\text{s}} \quad \text{and} \quad f_1 = 2.83 \text{Hz}$$

$$\omega_2 = 22.74 \frac{\text{rad}}{\text{s}} \quad \text{and} \quad f_2 = 3.62 \text{Hz}$$

$$\omega_3 = 33.37 \frac{\text{rad}}{\text{s}} \quad \text{and} \quad f_3 = 5.31 \text{Hz}$$

Comparing the results of the ambient vibration tests done by the University of Alberta in 1998 and University of British Columbia in 1997 with the theoretical solutions shows very good agreement, as indicated in Table 5.4.

Table 5.4: Comparison of Natural Frequencies Results

U of A [August '98]	UBC Report [September '97]	Analysis [Section Properties]	Description
2.60 Hz	2.78 Hz	2.83 Hz	1 st Vertical Mode
3.63 Hz	3.76 Hz	3.62 Hz	2 nd Vertical Mode
4.43 Hz	4.64 Hz	5.31 Hz	3 rd Vertical Mode

5.1.3 Damping of the Crowchild Trail Bridge

The damping curve shown in Figure 5.5, along with the test curves, is derived from equation (5.22). It can be seen that the two curves agree with the free vibration portion of the test curve very well. [The conversion factors for the accelerometer, A48, and the cable transducer, L1 are 1 V = 10 mg and 1 V = 1.57 mm, respectively.]

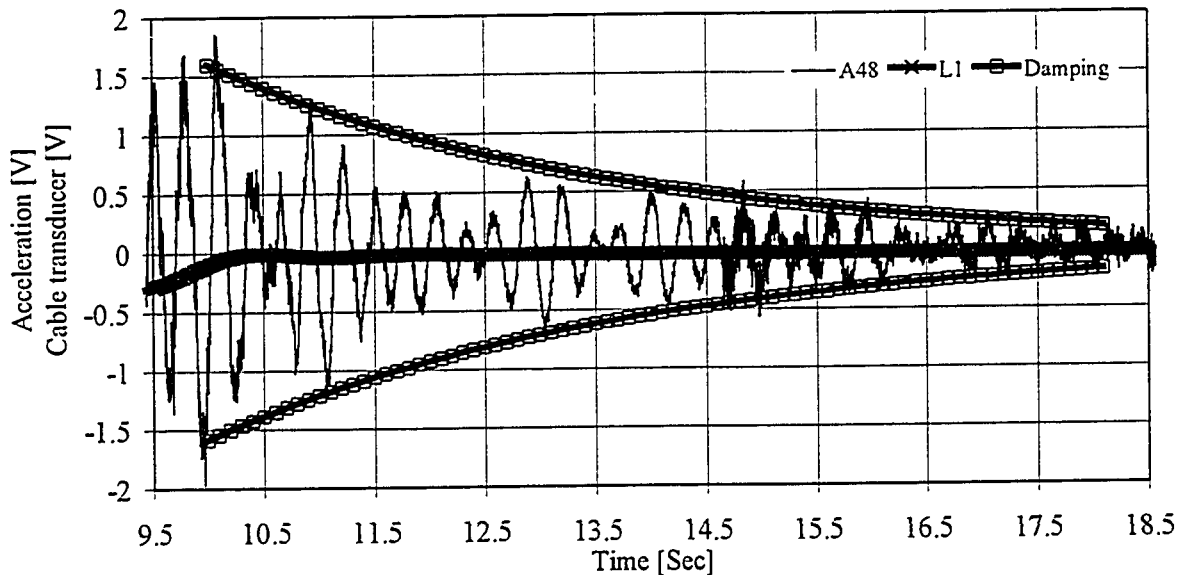


Figure 5.5: Damping Curve

Damping in real structures is from internal friction as solids deformed, friction at connection, open and close of micro-cracks in concrete, etc. It is impossible to identify and describe mathematically every individual energy dissipation mechanisms. Even for system that is vibrating within linear elastic range the damping coefficient 'c' can still

vary with respect to amplitude of deformation. The effects of damping will reduce the natural frequency of an undamped system, w_n to a damped system, w_D . Likewise, period of an undamped system, T_n is increased to period of a damped system, T_D . However, the effects are negligible for a damping ratio of $\xi \leq 20\%$, a range that includes most of

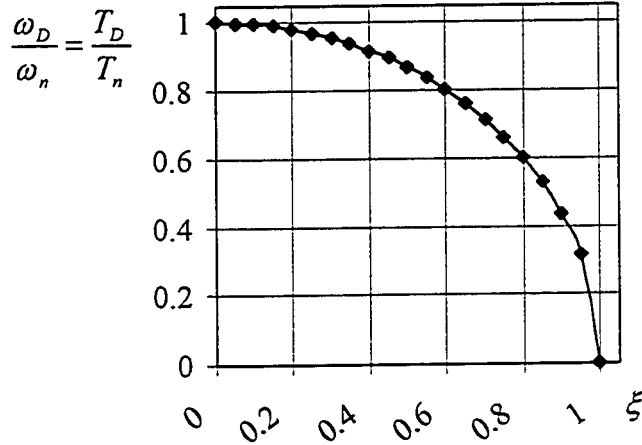


Figure 5.6: Effect of Damping

structures. A plot the relationship of $w_D = w_n \sqrt{1 - \xi^2}$ in equation (5.16) is shown in Figure 5.6. Clearly, for low damping ratio, neglecting damping effects are quite acceptable, such as a structure with $\xi \leq 20\%$ produces only a 2% error in frequencies if the damping is neglected. To determine the damping ratio analytically is either

impossible or impractical. On the other hand, a simple force vibration test can not only easily determine the damping ratio, but also the stiffness, and the natural frequency of the structures.

5.2 Static Behaviour of Crowchild Trail Bridge

Four issues of static behaviour of Crowchild Trail Bridge are being discussed in this section: 1) shear transfer inside the concrete deck in the transverse direction, 2) rigidity of the deck and load sharing among the girders, 3) composite action between the concrete deck and the steel girders in the longitudinal direction, and 4) change in the stiffness of the bridge.

5.2.1 Shear Transfer in the Transverse Direction

In a one way flexural member, shear is the gradient of bending moment along the length of the member, and consists of two components: beam action and arching action. Shear resulting from a gradient in tensile force acting on a constant moment arm is

referred to as beam action. Beam action is a characteristic of slender flexural members. Shear resulting from a constant tensile force acting on a varying moment arm is called arching action. It requires only remote anchorage of the reinforcement and, unlike beam action, the transfer of shear flow will not be prevented by the inclined cracks. Shear transfer by means of arching action is usually associated with deep beams and regions adjacent to discontinuities or disturbances in either the loading or the geometry of the member.

The concrete deck of the Crowchild Bridge is designed so that, at ultimate load, shear is mainly transferred by the arching action. As illustrated in Figure 5.7, near the ultimate load, the concrete cracks at the mid-span. Hence, the applied load is transferred to the supporting girders by means of compressive struts. The horizontal component of the compressive arch is resisted partly by the tension ties (i.e. steel straps) and partly by the restraints provided by the lateral stiffness of the girders. At service loads, however, shear is transferred by a combination of beam action and arching action. Beam action is the governing mechanism before cracking of the concrete deck, as it is the stiffer mechanism of the two.

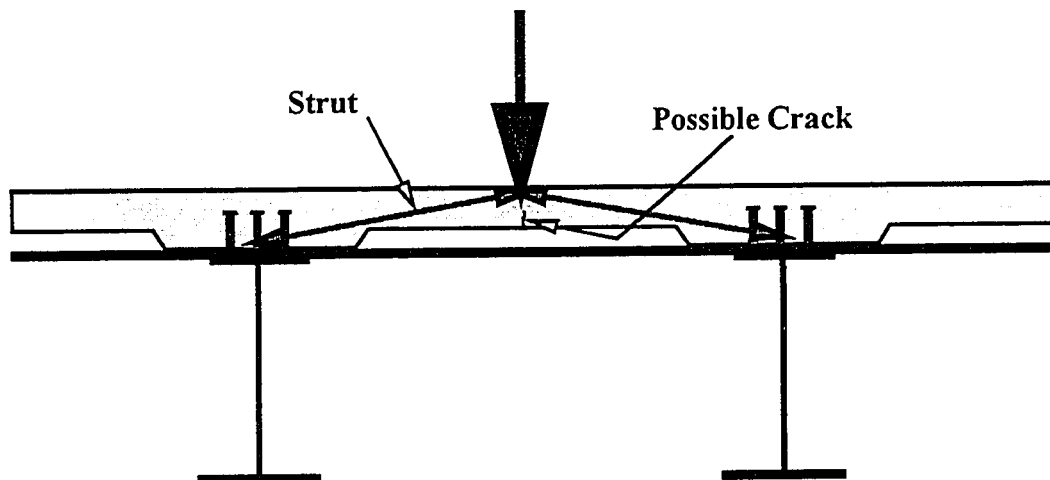


Figure 5.7: Shear Transfer in the Concrete Deck

In 1997 tests and measurements, the largest measured strain for the straps was $40 \mu\epsilon$. Recalled the steel straps had a rectangular cross section of 25 mm x 50 mm; therefore the steel strap carried an axial load of 10 kN. Recalled from chapter 3, the heaviest tandem axle was 160 kN; each wheel set weighted 80 kN per side. Assuming only one strap was carrying the applied load by arching action alone, the strap must carried 144 kN. Since the strap only carried 10 kN as measured under the applied load, arching action was obviously not the sole load carrying mechanism in the system. In addition, no longitudinal crack was visible on the bottom surface of the deck. It is then concluded that as of late October 97, the shear transfer inside the concrete deck in the transverse direction was mainly by the beam action.

Strains in the straps, however, had increased to about $80 \mu\epsilon$ in 1998. The increased strain, together with the existence of the longitudinal cracks, suggests that the contribution of tensile concrete in transferring shear has reduced in the second year.

5.2.2 Rigidity of the Deck and Load Sharing between Girders

The stiffness of the bridge deck in the transverse direction (or the rigidity of the deck) is the most important factor controlling the load sharing between the girders. Load sharing between the girders is of great importance since it illustrates the contribution of the girders that are not directly loaded. It is impractical to quantify any of these two terms. Consequently, any discussion in this regard is subject to engineering judgment.

The deflection measurements in the 1997 static tests with two trucks sides by side was used to evaluate the rigidity of the bridge deck. Neglecting the small transverse slope of the bridge, the centerline of the middle girder becomes an axis of symmetry. In the extreme case of a rigid deck, any symmetric load about this axis results in equal deflections for all the girders. This is not necessarily the case with poor stiffness of the deck in the transverse direction. As shown in Figure 4.3, the deflection of the girders in cases with two side by side trucks is almost uniform, suggesting a good stiffness in the transverse direction. Note that in Figure 4.3 the deflection of girder 5 was slightly higher

than the deflection of girder 1. This may be a result of the misalignment of the two trucks.

The case of asymmetric loading, such as a single truck in one lane, can be replaced by a concentric load and a torque. Often, torque caused by the eccentricity of the load results in additional downward movements in girders on one side and uplift on the other side. With a rigid deck, the deflected shape remains very close to a straight line. In a deck with poor stiffness, however, the deflection of the girders that are not directly loaded is close to zero.

Any significant change in the stiffness of the superstructure with time, therefore, can be detected by plotting the load sharing between girders for similar truck positions. Figure 5.8 shows the load sharing between girders based on the deflection measurements for 1997 and 1998. Similarity, the two figures suggest that the load sharing between the girders has not changed. Note that the truck specifications as well as its eccentricity from centerline of torsion (Girder #3) were slightly different in each year.

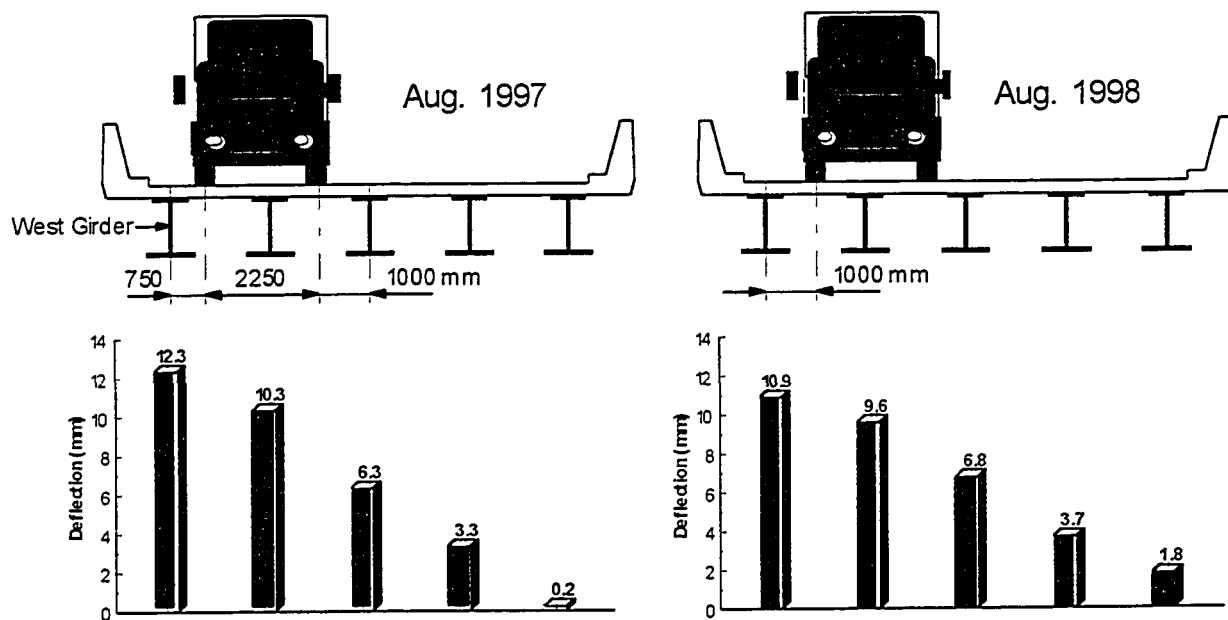


Figure 5.8: Load Sharing between Girders Based on the Deflection Measurements

5.2.3 Composite Action in the Longitudinal Direction

Composite action between the concrete deck and the steel girders in the longitudinal direction is being studied for two regions in the North span, namely the positive moment region where the concrete is mostly in compression and the negative moment region where the concrete is mostly in tension. The contribution of the concrete to the stiffness and load carrying can be evaluated based on the measured location of the neutral axis in each region.

Figure 5.9 illustrates the location of the neutral axis for Girder #1 in the positive moment region. To investigate any changes in the location of the neutral axis with time, four load cases were considered: August 1997, October 1997, June 1998, and August 1998. Note that the specification of the trucks was different from one load case to another, with the August 98 truck being the heaviest. As a result, the maximum strain in each load case is different. However, the location of the neutral axis is approximately 50 mm from the bottom face of the top flange. For all four tests conducted up to the end of August 1998, the composite action between the concrete deck and the steel girders in the longitudinal direction has not deteriorated significantly in the positive moment region.

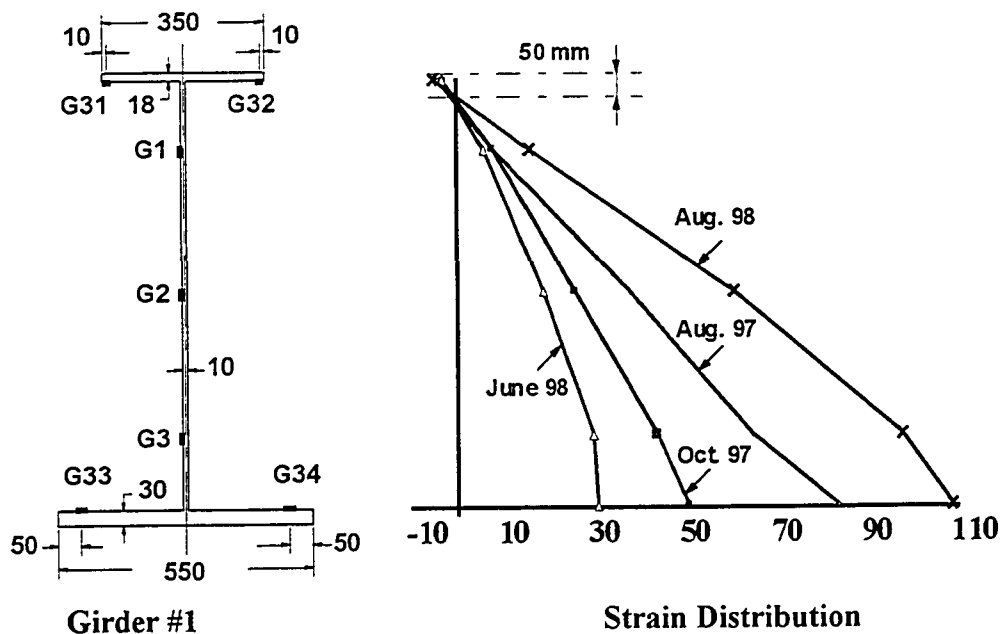


Figure 5.9 Location of the Neutral Axis in the Positive Moment Region

Figure 5.10 illustrates the location of the neutral axis for girder 1 in the negative moment region for the four load cases. Note that the accuracy in determining the location of the neutral axis is lower compared to the positive moment region, due to the magnitude of the strain were much smaller. In addition, there were no strain measurements on the flanges. The neutral axis has moved from 93 mm in 1997 to 191 mm in 1998 with reference to the bottom face of the top flange. The 98 mm shift in the location of neutral axis indicates a loss in the composite action between the concrete deck and the steel girders in the negative moment region.

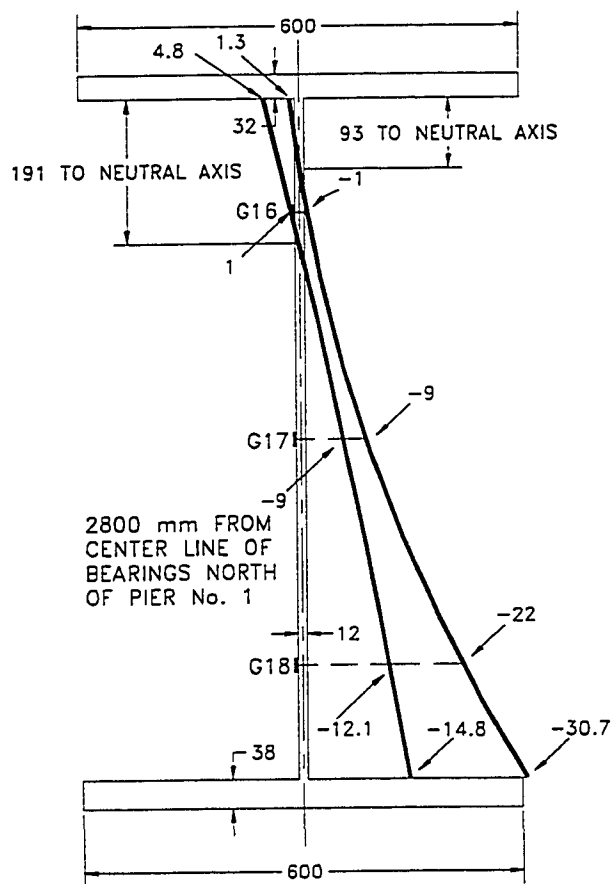


Figure 5.10 Location of the Neutral Axis in the Negative Moment Region

5.2.4 Change in the Stiffness of the Bridge

Any losses in the composite action of the concrete deck and the steel girders in the negative moment region associates with a reduced moment of inertia in that region.

Consequently, the stiffness of the bridge in the longitudinal direction is affected. To evaluate the change in the stiffness with time, the bridge has been modeled as a continuous beam. A primary concern with any analytical model is to model the contribution of the concrete, especially at the negative moment region where the transverse cracks propagate with time. To overcome this problem, the cross sectional properties were determined based on the measured location of the neutral axis for each year. The thickness of the concrete deck was assumed 200 mm. The equivalent contributing width of concrete for segment types 1 and 2 were determined so that the calculated location of the neutral axis matches those based on the strain measurements. The width of the concrete for segment type 3 is assumed equal to that for type 1. Cross sectional properties obtained are presented in Table 5.5.

Segment type 1 is used at the positive moment regions of the exterior spans. Segment type 2 is used at the negative moment regions of both piers, and extends 6.4m and 6.9m from the centerline of the piers into the exterior and middle spans, respectively. Segment type 3 is used at the positive moment regions of the middle span.

Three cases are studied using a simple two-dimensional beam analysis: 1) beam and truck of 1997, 2) beam and truck of 1998, and 3) beam of 1997 but truck of 1998. Deflections in the first two cases can be compared directly to the test results. As the model is only a two-dimensional analysis, the average of the deflection of all the girders is used (6.5mm and 6.56mm for the years 1997 and 1998, respectively as shown in Figure 5.8). Comparison of the last two cases, however, demonstrates the change in the stiffness of the bridge with time.

Table 5.5: Section Properties of the Girders

Segment	Component	b (mm)	h (mm)	Neutral Axis (mm)	A (mm ² × 10 ³)	I (mm ⁴ × 10 ⁶)
Type 1 Aug. 97 & 98	Concrete & GFRP	521	200			
	Top flange	350	18	50	136	17700
	Web	10	900			
	Bottom flange	550	30			
Type 2 Aug. 97	Concrete & GFRP	380	200			
	Top flange	600	32	120	129	21900
	Web	12	900			
Type 2 Aug. 98	Concrete & GFRP	140	200			
	Top flange	600	32	270	80.8	16870
	Web	12	900			
Type 3 Aug. 97 & 98	Concrete & GFRP	521	200			
	Top flange	350	18	23.5	132	14560
	Web	10	900			
	Bottom flange	500	25			

The calculated deflections (at the locations where measurements were conducted for each year) were 6.69, 6.91, and 6.67 mm respectively for the 3 cases. The calculated deflections in the first two cases are in good agreement with their corresponding measured deflections. Comparison of the last two cases suggests that the stiffness of the bridge has reduced approximately 3.5% from 1997 to 1998.

6. SUMMARY AND CONCLUSIONS

6.1 Summary

The Crowchild Trail Bridge is an experimental bridge located at the intersection of Crowchild Trail and University Drive in Calgary, Alberta. It is a three-span, two-lane, one-way traffic overpass. It is spanning 92.878 meters with two interior supports. This bridge was built using the innovative steel free – fibre reinforced concrete deck design. This is the first of its kind in the world to utilize this innovative approach over the positive and negative moment regions. Field assessment of the Crowchild Trail Bridge focused on two main issues: performance under serviceability conditions and long-term durability. University of Alberta had extensively developed field instrumentation and monitoring program on this bridge. To assess its performance, static and dynamic tests were carried out using trucks with known axle loads. Based on the results of tests, the bridge fundamental structural characteristics, both static and dynamic, were determined under such service load conditions. For long-term durability study, the bridge is then monitored at various time intervals. The bridge fundamental structural characteristics are then re-evaluated and compared to the time before it was put into service. The scope of this thesis is the field assessment of the Crowchild Trail Bridge over the first years of its operation.

Since the superstructure of the Crowchild Trail Bridge was replaced in August 1997, two major phases of testing were completed by the end of August 1998. Tests consisted of ambient vibration, field survey, static load test, dynamic load test, and mapping of crack patterns. Strains, deflections and acceleration behaviour were measured. In August 1998, static and dynamic tests were performed using a truck with known axle loads and ran at various speeds. Natural frequencies and mode shapes of the bridge were determined by ambient vibration tests. Load sharing between girders, the dynamic load factor, stiffness, natural frequencies and damping factor of the bridge, were analyzed.

Comparison of the neutral axis in the positive moment region between August 1997 and August 1998 shows no change in the neutral axis. This result suggested no changes in composite action for the positive moment region. In the negative moment region, there was a 98 mm shift in the neutral axis, which suggested a partial loss in the composite action.

In August 1997, field survey indicated a maximum deflection of 17 mm in the North span, when two 357 kN trucks was loaded symmetrically in the North span. For asymmetric loading, one 357 kN truck was used, the maximum deflection was 13.5 mm. The steel strap had a maximum strain reading of 85 $\mu\epsilon$ and it varied between -15 to 85 $\mu\epsilon$ as the truck moved along the entire length of the bridge. With a maximum strain of 104 $\mu\epsilon$ in the girder and 85 $\mu\epsilon$ in the straps, the bridge clearly was behaving well within linear elastic range.

University of British Columbia performed an ambient vibration test on Crowchild Trail Bridge in September 1997. After it had been in operation for one full year, the University of Alberta did a second ambient vibration test at the end of August 1998. In the ambient vibration tests, eight predominant frequencies below 10 Hz were found. Comparison of the field-testing done by the University of Alberta and the University of British Columbia with the theoretical closed form solution shows very good agreement. Result comparison between UBC and U of A results shows that all the natural frequencies found have been reduce by approximately 0.20 Hz. The resolution of the measured frequency is ± 0.01 Hz.

Both static and dynamic tests were conducted on the Crowchild Trail Bridge in August 1998. The same truck was used in both tests. Four different speeds, 15, 30, 40, and 55 km/hr, of truck were investigated in the dynamic tests. Results show that the dynamic test results can be filtered and reduced to obtain the identical static test results. The advantages of this implication translate into tremendous saving in future field testing

since little or no obstruction to traffic flow due to the dynamic testing; hence more structures can be assess and evaluate in a very short time.

Damping ratio of the bridge can be found by the decay of the free vibration motion. Since accelerometer data are taken at the same time as the cable transducer, the free vibration period can easily be determined. As of August 98, the Crowchild Trail Bridge had a damping ratio of approximately 1.20 percent.

Dynamic amplification factor can be determined from either strain gauges or cable transducers test results. The results from Crowchild Trail bridge have clearly demonstrated that there are two distinct dynamic amplification factors: the *overall vertical deflection component* and the *local strain component* in the bridge members. For the 55 km/hr test, the maximum strain components due to static and dynamic are 96.5 $\mu\epsilon$ and 14.9 $\mu\epsilon$ respectively. Thereby giving the dynamic amplification factor of 1.16 with a scatter of 0.7% for all the strain gauges investigated. Dynamic amplification factor due to the local strain effects varies non-linearly with respect to speed. For the *overall deflection component* in the 55 km/hr test, the deflections due to static and dynamic response are 11.5 mm and 0.94 mm, respectively. This gives a dynamic amplification factor of 1.08. The factor found from cable transducer is lower than that suggested by the strain gauge results. The overall trend of the DAF obtains from cable transducer and the strain gauge give quite vastly different behaviour. The dynamic amplification factors from the cable transducers give a linear relationship with respect to the speed; however, the strain gauges give a nonlinear relationship that increases exponentially for the speed tested. This suggested that the local strain effects are much more severe under dynamic load than that of the overall deflection component.

Good load sharing among girders was found from both deflection and strain gauge results. The deflected shapes of the girders were close to a straight line. No deterioration with time has been observed for the load sharing among the girders.

The first crack patterns were mapped at the end of August 1997 after removal of concrete formwork. All cracks were running in transverse direction, and were approximately 0.5 mm in width. No longitudinal crack in any of the three spans was found. After one full year of operation, a second crack patterns were mapped in August 1998. Those cracks existed from August 1997 seem to become twice wider by August 1998. As of August 1998, there were quite a few new cracks formed on the underside of the bridge. In addition to many new transverse cracks formed, there were quite a few longitudinal cracks developed. Most longitudinal cracks are formed right at the transition point between the flat part of the deck and the taper part. However, a couple longitudinal cracks were formed at midway between the two supporting girders in the South span.

6.2 Conclusions

The following conclusions and major observations are found based on ambient vibration, static, and dynamic tests carried out on Crowchild Trail Bridge in August 1997, before the bridge was open to traffic, and August 1998, after the bridge has been in operation for one full year,

1. Composite Action in the positive moment region has not changed during this period, while in the negative moment region there is a shift of 98 mm in the neutral axis due to the cracking of the concrete deck. According to a simple beam analysis, this loss of composite action in the negative moment region associates with almost 3.5% decrease in the overall stiffness of the bridge.
2. As of August 1998, wheel loads are transferred inside the concrete deck to the steel girders mainly by means of beam action. The share of arching action in the transfer of shear, however, has almost doubled in 1998 compared to that in 1997. Under 80,000 lbs triple axle truck load, the tension strap has a strain cycled between 85 and $-15 \mu\epsilon$. At this low strain cycle, fatigue would not be a concern.

3. All the natural frequencies and mode shapes investigated show good correlation between both fields testing results and theoretical closed form solutions. The field ambient vibration tests show that all the natural frequencies investigated have been reduced by approximately 0.20 Hz after the bridge has been in service for one year. Since the mass of the structure has not changed, this may indicate stiffness of the bridge has reduced.
4. Based on the dynamic test results, the damping ratio and dynamic amplification factor can be obtained from both strain gauges and deflection data. The local strain gauge data yielded higher dynamic amplification factors than the ones based on the overall deflection results. Furthermore, dynamic test results can be filtered for static results, thus future static tests can be eliminated for the Crowchild Trail Bridge.
5. At a transverse section, the deflected shape of the girders has been very close to a straight line. This suggests a relatively stiff deck in the transverse direction, and hence, a good load sharing among the girders. No deterioration with time has been observed for the load sharing among the girders.
6. Overall, there are quite a few new cracks pattern formed over the one year of operation. Most cracks formed are 0.5 mm and less in width. Only few transverse cracks were observed in August 1997 while some longitudinal cracks with more transverse cracks were detected in August 1998. As of August 1998, cracks visible on the bottom surface of the bridge deck show no serviceability concern.

6.3 Recommendations for Future Research

It is recommended to conduct a yearly inspection and testing of the Crowchild Trail Bridge. The tests should include both ambient vibration test and dynamic load test. This ongoing periodic monitoring of the superstructure will eventually lead to a better

understanding of the performance of the bridge over time, which in turn lead to more effective maintenance and repair techniques.

A continuous monitoring of the performance of the bridge will enable engineers to a better understanding of the effects of truck load, temperature variations, and crack propagation on the long term performance of the bridge on a daily basis. Therefore, it is recommended to install a wireless remote monitoring system on the bridge to monitor a few selected key sensors in the bridge.

Recommendation for future ambient vibration testing is to place the accelerometers on every girder, since the bridge deck may not be rigid. Figure 6.1 shows the propose location of accelerometer for future testing. With such testing configuration, it minimizes the work and time of testing and maximizes the results. The results from the ambient vibration tests allow for closer examination of the changes in stiffness of individual girders, rigidity of the deck, and capture most of the important frequencies and mode shapes. These changes of the characteristics of the bridge will provide the health status of the bridge over time.

REFERENCES

1. Afhami, S., Alexander, S.D.B., and Cheng, J.J.R., 1998. "Field Instrumentation and Monitoring of Crowchild Bridge in Calgary, Alberta". Proceedings, CSCE Annual Conference held in Calgary, Alberta, Canada.
2. Aly, A., Bakht, B., and Schafer, J., 1997. "Design and Construction of a Steel-Free Deck Slab in Ontario". Proceedings, CSCE Annual Conference held in Sherbrooke, Canada, Vol. 6, pp. 81-90.
3. Barker, R.M., and Puckett, J.A., 1997. *Design of Highway Bridges*. John Wiley & Sons, Inc., New York.
4. Biggs, J.M., 1964. *Introduction to Structural Dynamics*. McGraw-Hill, Inc., New York.
5. Black, C., Tsai, P., and Ventura, C.E., 1997. "Ambient Vibration Measurements of the University Drive/Crowchild Trail Bridge in Calgary, Alberta". UBC Earthquake Engineering Research, Project number EQ 97-005, October.
6. Buckland, P.G., and Barlett, M.F., 1992. "Canadian Highway Bridge Evaluation: A General Overview of Clause 12 of CSA Standard CAN/CSA-S6-88". CAN. J. CIV. ENG. Vol. 19, pp. 981 – 936.
7. Canadian Institute of Steel Construction, 1999. *Handbook of Steel Construction*, 7th Edition, Willowdale, Ontario.
8. Cheng, J.J.R., and Afhami, S., 1999. "Field Instrumentation and Monitoring of Crowchild Trail Bridge in Calgary, Alberta". University of Alberta report for the City of Calgary, July.
9. Chopra, A.K., 1995. *Dynamics of Structures: Theory and Applications to Earthquake Engineering*. Prentice-Hall, Inc., New Jersey.
10. Clough, R.W. and Penzien, J., 1993. *Dynamics of Structures*. Second Edition, McGraw-Hill, Inc., New York.
11. Dimarogonas, A., 1996. *Vibration for Engineers*. Second Edition, Prentice Hall Inc, New Jersey.
12. Doncaster, A., Newhook, J., and Mufti, A.A., 1996. "An Evaluation of Fiber Optic Sensors". Concrete International, Vol.18, No. 6, pp. 215 – 226.
13. Dorey, A.B., Newhook, J.P., and Mufti, A.A., 1996. "The Behaviour of a Reinforcing Steel-Free Bridge Deck Under Negative Moment". Concrete International, V.18, No. 6.

14. McConnell, K.G., 1995. *Vibration Testing: Theory and Practice*. John Wiley & Sons, Inc., New York.
15. Ministry of Transportation, Ontario, 1991. *Ontario Highway Bridge Design Code*, 3rd Edition. MTO Quality and Standard Division.
16. National Instruments Corporation, 1996. *LabVIEW: Analysis VI Reference Manual*.
17. Newhook, J.P., Mufti, A.A., and Wegner, L.D., 1995. "Fibre Reinforced Concrete Deck Slabs Without Steel Reinforcement". Nova Scotia CAD/CAM Centre, Research Report No. 1-1995, February.
18. Newhook, J. P., and Mufti, A. A., 1996. "A Reinforcing Steel-Free Concrete Deck Slab for the Salmon River Bridge". *Concrete International*, Vol.18, No. 6, pp. 30 – 34. June.
19. Newhook, J.P., and Mufti, A.A., 1996. "Steel -Free Concrete Bridge Deck- the Salmon River Project: Experimental Verification". *Concrete International*, V.18, No. 6, pp. 123 – 134. June.
20. Newhook, J.P., Mufti, A.A., Jaeger, L.G., MacDonnell, R., and Hamilton, D., 1996. "Steel-Free Concrete Bridge Deck-the Salmon River Project: Design and Construction". *Concrete International*, V. 18, No. 6, pp. 203 – 214. June.
21. Taing, K.K., Cheng, J.J.R., and Afhami, S., 1999. "Field Assessment of Crowchild Bridge in Calgary, Alberta". Proceedings, CSCE Annual Conference held in Regina, Saskatchewan, Canada.
22. Tartaglione, L. C., 1991. *Structural Analysis*. McGraw-Hill Inc., New York.

Appendix A

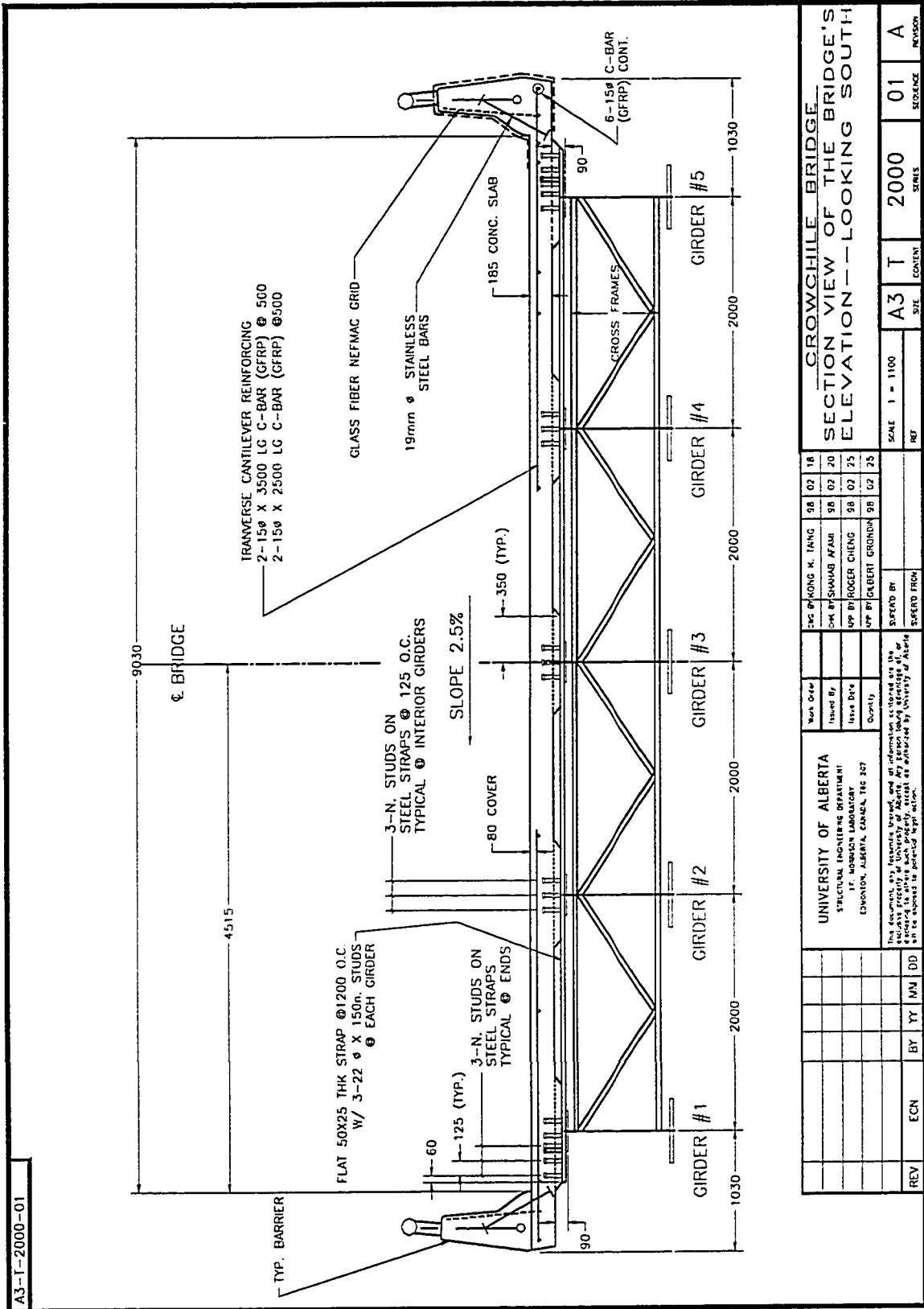


Figure A1: Cross Sectional View of the Crowchild Bridge

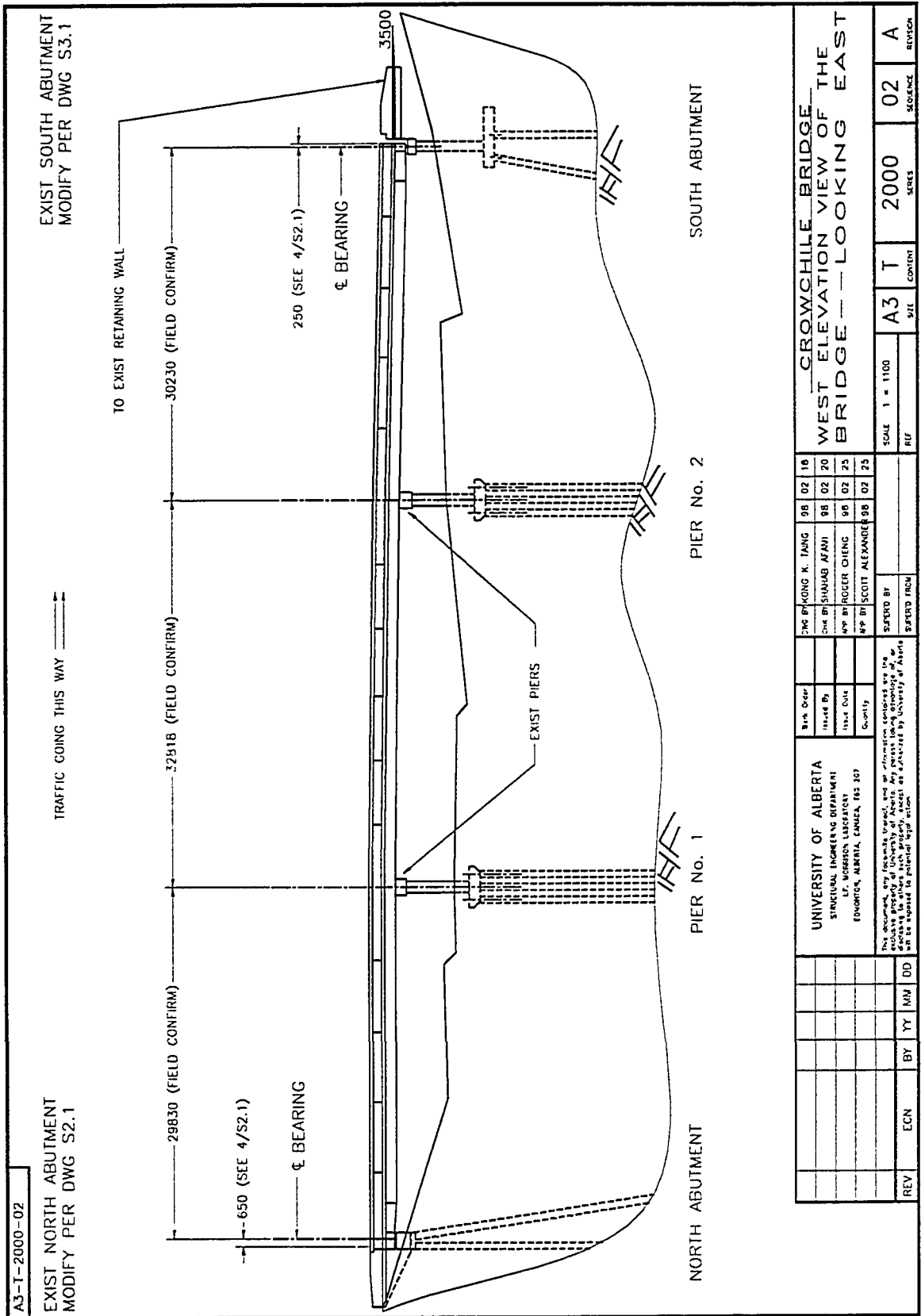


Figure A2: West Elevation View of the Crowchild Bridge

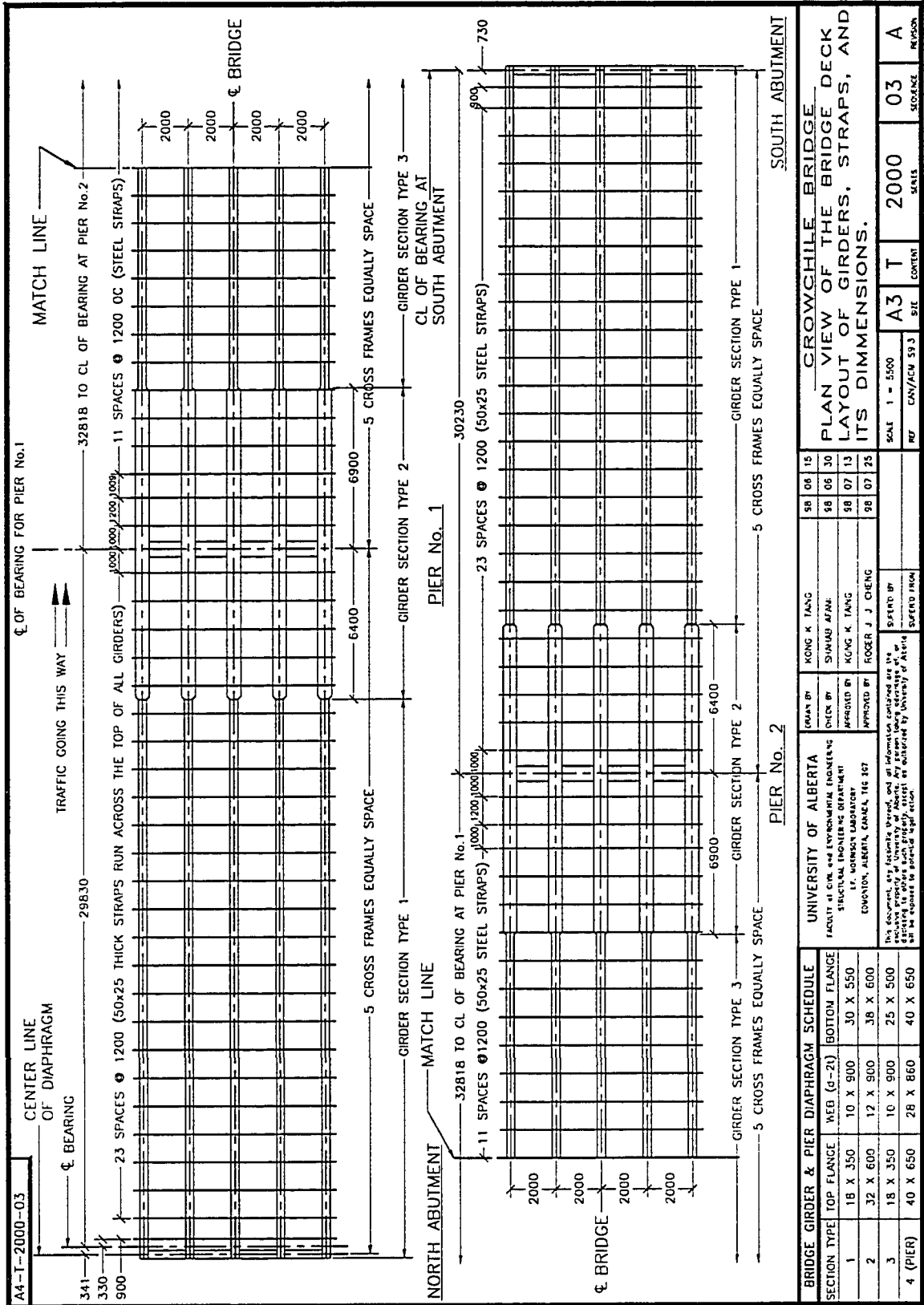


Figure A3: Plan View Layout of the Girders and Straps

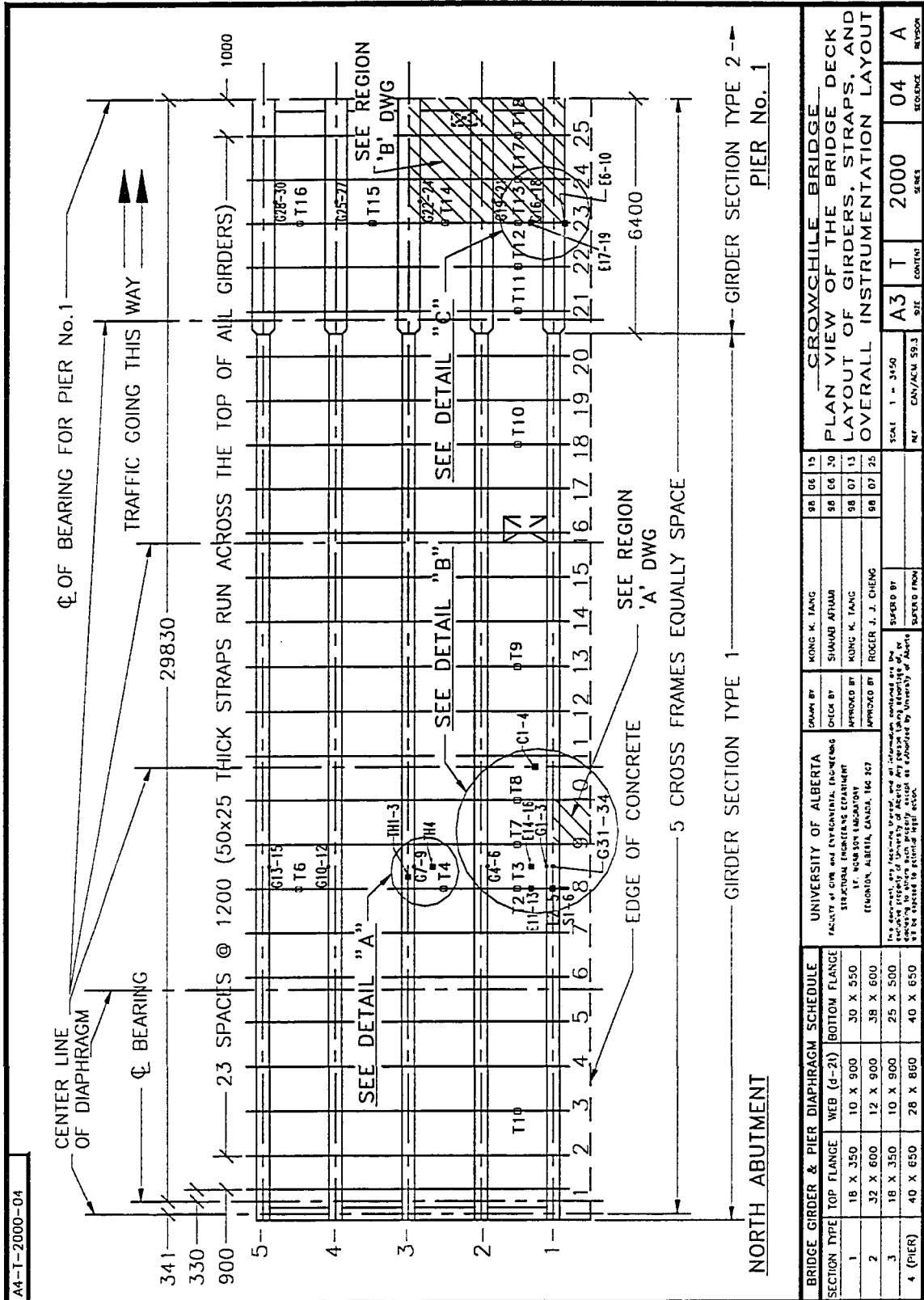
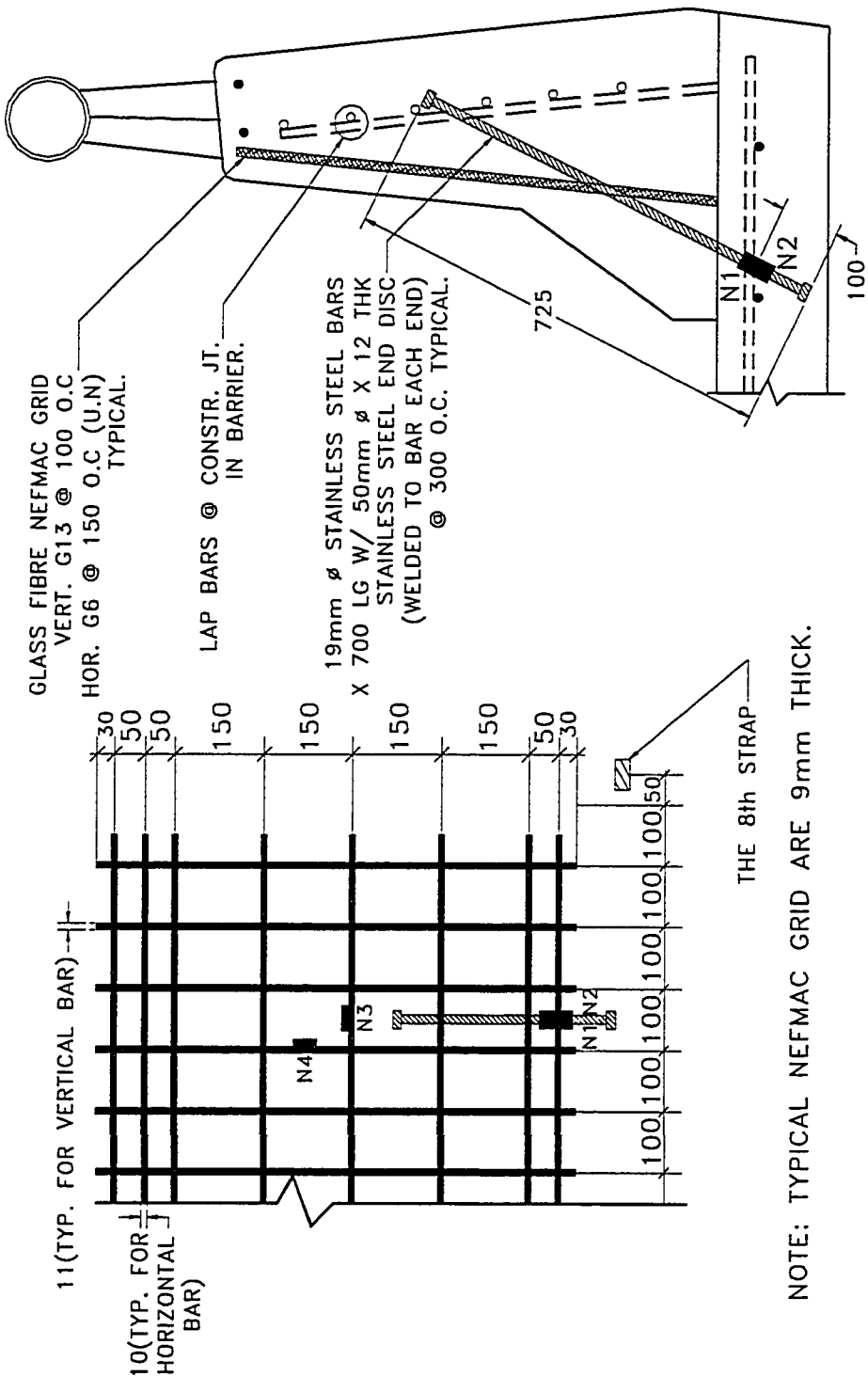


Figure A4: Overall Instrumentation Layout

A4-T-2000-05



GLASS FIBRE NEFMAC GRID
VERT. G13 @ 100 O.C
HOR. G6 @ 150 O.C (U.N)
TYPICAL.

LAP BARS @ CONSTR. JT.
IN BARRIER.

19mm ϕ STAINLESS STEEL BARS
X 700 LG W/ 50mm ϕ X 12 THK
STAINLESS STEEL END DISC
(WELDED TO BAR EACH END)
@ 300 O.C. TYPICAL.

11(TYP. FOR VERTICAL BAR)
10(TYP. FOR HORIZONTAL BAR)

THE 8th STRAP

NOTE: TYPICAL NEFMAC GRID ARE 9mm THICK.

BRIDGE GIRDER & PIER DIAPHRAGM SCHEDULE		UNIVERSITY OF ALBERTA		DESIGN BY		DRAWN BY		CHECK BY		APPROVED BY		SUPERVISED BY	
SECTION TYPE	TOP FLANGE	WEB (d-Z)	BOTTOM FLANGE	FACULTY OF CIVIL AND ENVIRONMENTAL ENGINEERING	STRUCTURAL ENGINEERING DEPARTMENT	17, NOBSON LABORATORY	EDMONTON, ALBERTA, CANADA, T6G 2G7	KONG K. TANG	SUNJAB AHMAD	KONG K. TANG	ROGER J. J. CHENG	SCALE	NO.
1	18 X 350	10 X 900	30 X 550					98 06 15	98 06 30	98 07 13	98 07 23	1 = 250	A3 T
2	32 X 600	12 X 900	38 X 600										2000
3	18 X 350	10 X 900	25 X 500										05
4 (PIER)	40 X 650	28 X 860	40 X 650										A

CROWCHILE BRIDGE
PLAN VIEW OF THE BRIDGE DECK BARRIER
LAYOUT OF NEFMAC, STAINLESS STEEL
BAR, AND IT'S DETAIL DIMENSIONS

SCALE 1 = 250
NO. CAN/ACI 59.3
SITE CONTIN

This document, by its title, and all information contained hereon, is the property of the University of Alberta. It is to be used only for the project for which it was prepared. It is not to be reproduced, stored in a retrieval system, or transmitted in any form or by any means, electronic, mechanical, photocopying, recording, or by any information storage and retrieval system, without the prior written permission of the University of Alberta.

Figure A5: Bridge Deck Barrier

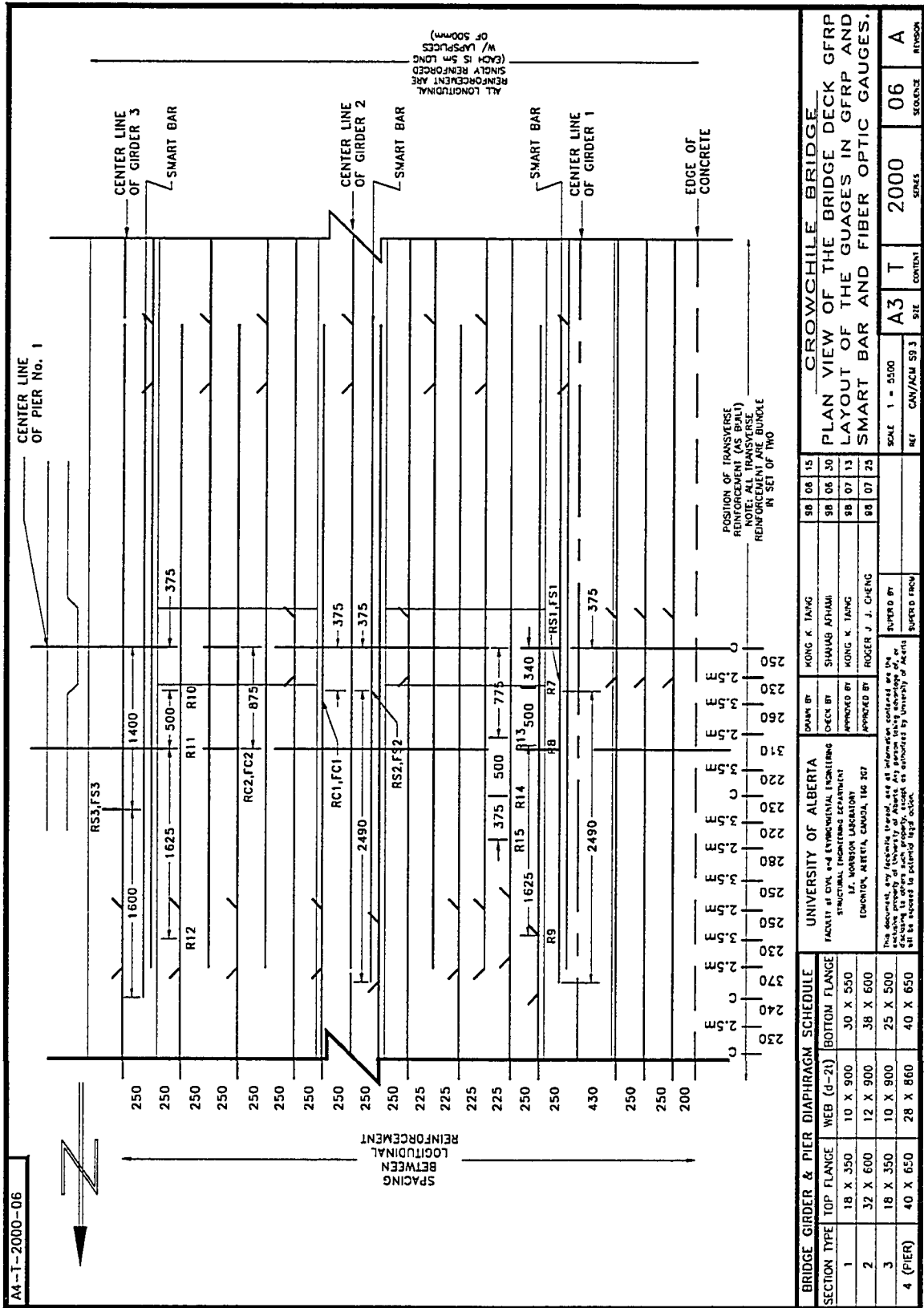


Figure A6: Layout of Gauges that are Embedded in Concrete

APPENDIX B

Table B1: Static Test of August '97, Strain Gauge Reading – by multiplexer

Date	truck positio		1		2		3		4		5		6		7		8		9		
	Aug. 11, 97	Aug. 13, 97	Aug. 14, 97																		
Standard Temperature	42	14	31	21	-10	-14	-15	-19	-22	-22	-12	-15	-18	-18	-18	-18	-18	-18	-18	-18	
At the Beginning:	6: 30 am	11: 20 am	9: 40 am	10: 05 am	10: 35 am	11: 00 am	11: 25 am	12: 00	1: 20 pm	1: 45 pm	2: 00 pm	2: 25 pm	2: 50 pm	3: 25 pm	4: 00 pm	4: 35 pm	5: 10 pm	5: 45 pm	6: 20 pm	6: 55 pm	
TH1			19.7	18.9	19.3	20.1	21.6	22.7	22.7	22.7	22.7	22.8	22.9	22.9	22.8	22.7	22.8	22.8	22.8	22.9	23.6
TH2			17.9	18.2	18.4	18.6	19.1	19.9	19.9	19.9	21.4	21.5	21.6	21.6	21.5	21.4	21.5	21.5	21.5	21.6	21.8
TH3			17.8	18.2	18.4	18.8	19.4	19.8	19.8	20.8	20.8	21	21.1	21.1	21	20.8	21	21.1	21.1	21.1	21.5
TH4			17.9	17.9	18.2	18.8	20.1	21.3	21.3	22.7	22.7	22.8	22.9	22.9	22.8	22.7	22.8	22.9	22.9	22.9	23.4
TH5			21.3	19.4	20.9	22.5	24.4	24.8	24.8	22.8	22.8	23.2	23.8	23.8	23.2	22.8	23.2	23.8	23.8	23.8	25
G1	-94	-126	-146	-136	-136	-136	-126	-112	-112	-101	-101	-105	-96	-96	-113	-113	-113	-113	-113	-113	-113
G2	-371	-443	-450	-439	-440	-421	-397	-381	-381	-393	-393	-374	-350	-350	-415	-415	-415	-415	-415	-415	-415
G3	-601	-655	-639	-680	-667	-636	-601	-599	-599	-663	-663	-628	-579	-579	-682	-682	-682	-682	-682	-682	-682
G4	-312	-313	-320	-312	-314	-304	-296	-285	-285	-286	-286	-284	-285	-285	-287	-287	-287	-287	-287	-287	-287
G5	-425	-424	-450	-445	-439	-421	-402	-388	-388	-408	-408	-400	-387	-387	-415	-415	-415	-415	-415	-415	-415
G6	-220	-203	-222	-213	-189	-159	-117	-107	-107	-170	-170	-150	-120	-120	-172	-172	-172	-172	-172	-172	-172
G7	-930	-932	-936	-929	-926	-920	-914	-901	-901	-896	-896	-898	-898	-898	-893	-893	-893	-893	-893	-893	-893
G8	-636	-635	-640	-635	-631	-614	-599	-586	-586	-614	-614	-602	-595	-595	-608	-608	-608	-608	-608	-608	-608
G9	-435	-435	-439	-432	-419	-381	-340	-333	-333	-395	-395	-379	-361	-361	-388	-388	-388	-388	-388	-388	-388
G10	-118	-147	-153	-146	-142	-132	-122	-113	-113	-112	-112	-116	-116	-116	-110	-110	-110	-110	-110	-110	-110
G11	325	314	300	306	319	341	368	375	375	341	341	345	343	343	340	340	340	340	340	340	340
G12	538	561	524	526	558	594	632	636	636	568	568	569	576	576	565	565	565	565	565	565	565
G13	247	228	227	221	232	244	249	258	258	269	269	262	258	258	270	270	270	270	270	270	270
G14	745	732	672	697	715	732	743	737	737	739	739	738	739	739	719	719	719	719	719	719	719
G15	471	443	355	394	359	467	511	521	521	492	492	485	484	484	496	496	496	496	496	496	496
G16	-1127	-1141	-1140	-1139	-1144	-1148	-1151	-1135	-1135	-1112	-1112	-1123	-1124	-1124	-1123	-1123	-1123	-1123	-1123	-1123	-1123
G17	-432	-484	-486	-480	-472	-475	-491	-475	-475	-443	-443	-448	-461	-461	-452	-452	-452	-452	-452	-452	-452
G18	-188	-244	-274	-264	-240	-231	-247	-237	-237	-210	-210	-213	-237	-237	-215	-215	-215	-215	-215	-215	-215
G19	-662	-666	-637	-634	-636	-637	-636	-626	-626	-615	-615	-623	-620	-620	-616	-616	-616	-616	-616	-616	-616
G20	-369	-400	-408	-405	-391	-389	-402	-391	-391	-363	-363	-371	-377	-377	-365	-365	-365	-365	-365	-365	-365
G21	140	106	68	75	108	122	103	114	114	138	138	135	123	123	145	145	145	145	145	145	145
G22	370	373	380	380	385	392	393	397	397	417	417	406	410	410	422	422	422	422	422	422	422

Table B1 Cont'd

G23	-442	-453	-478	-475	-458	-447	-461	-455	-433	-438	-437	-432
G24	-450	-538	-576	-572	-535	-512	-540	-533	-510	-511	-512	-496
G25		281	283	287	284	295	283	286	289	288	290	272
G26	532	507	501	505	521	529	519	530	550	546	545	547
G27	285	264	214	222	253	267	248	254	280	277	278	284
G28	306	296	306	312	314	324	324	339	351	343	342	344
G29	482	420	347	399	421	444	442	466	489	482	484	479
G30	206	127	23	60	48	125	131	148	188	184	187	196
G31	-41	-25	178	185	192	202	192	189	191	175	167	187
G32						146	144	144	155	143	161	160
G33						290	329	324	261	348	348	254
G34						917	-890	-890	-957	-917	-851	-948
T4	-1027	-1014	-1035	-1004	-984	-917	-890	-890	-957	-917	-851	-948
	-468	-532	-562	-562	-545	-526	-509	-504	-525	-526	-531	-514
T1	214	274	245	248	255	269	279	299	286	279	274	302
T2	-392	-305	-321	-317	-308	-282	-251	-235	-270	-276	-253	-268
T3	-1115	-1036	-1063	-1060	-1056	-1037	-1006	-999	-1052	-1042	-1013	-1056
T4	-551	-562	-585	-583	-571	-543	-521	-510	-541	-544	-537	-527
T5	133	217	202	208	217	242	267	281	241	231	231	264
T6	155	243	219	227	232	245	275	283	233	232	219	269
T7	-1333	-1230	-1251	-1241	-1233	-1199	-1161	-1150	-1196	-1197	-1165	-1192
T8	-849	-772	-787	-782	-772	-740	-706	-697	-746	-743	-710	-738
T9	-1644	-1556	-1573	-1568	-1558	-1516	-1494	-1502	-1538	-1517	-1493	-1526
T10	-1306	-1254	-1274	-1269	-1250	-1209	-1208	-1232	-1233	-1199	-1191	-1225
T11	-977	-907	-932	-924	-901	-886	-901	-904	-888	-890	-899	-875
T12	-1044	-950	-1004	-997	-970	-955	-979	-975	-947	-951	-968	-955
T13	-352	-298	-321	-315	-286	-271	-299	-292	-260	-264	-288	-271
T14	1580	1650						1616	1614	1605	1592	1592
T15	-174	-103	-117	-114	-117	-107	-112	-111	-92	-115	-102	-91
T16	3700	3847						3842	3872	3854	3814	3903
T17	-620	-558	-583	-573	-547	-545	-566	-557	-522	-526	-550	-536
T18	-43	30	-5	12	17	21	25	29	38	28	23	41
R12	1493	1489	1474	1487	1462	1465	1484	1471	1472	1472	1464	1468
R13	1446	1477	1459	1452	1459	1469	1473	1462	1473	1466	1474	1460
R14	-305	-281	-299	-306	-307	-303	-286	-289	-284	-292	-282	-283
R15	669	700	696	698	694	703	711	707	714	706	715	718
R1	19	82	0	11	23	36	40	38	28	30	33	42
R2	-305	-292	-310	-300	-293	-283	-280	-280	-273	-276	-275	-273

Table BI Cont'd

R3	199	205	164	177	187	187	184	187	174	193	197	180
R4	268	302	273	284	293	306	308	305	299	306	304	316
R5	-410	-384	-417	-401	-393	-387	-385	-386	-380	-380	-369	-370
R6 not reliable	3389	3274	3278	3277	3265	3265	3250	3237	3235	3239	3239	3250
R7	1857	1900	1907	1912	1912	1926	1929	1920	1929	1926	1941	1915
R8	855	886	887	902	898	906	912	907	895	901	912	899
R9	-437	-398	-396	-388	-396	-392	-381	-377	-382	-395	-373	-376
R10 TRBL	1222	1336	1332					1345	1328			1333
R11 TRBL	660	691	672					684	679			680
RC1	164	264	266	308	313	338	274	278	258	244	205	218
RC2	-468	-514	-465	-527	-516	-513	-530	-535	-540	-536	-553	-517
E2	51	81	52	54	75	81	86	86	85	139	92	113
E3	-1411	-1388	-1409	-1405	-1384	-1375	-1370	-1363	-1363	-1341	-1355	-1335
E4	-2714	-2657	-2697	-2691	-2675	-2663	-2673	-2659	-2659	-2630	-2670	-2656
E5	-669	-652	-664	-660	-647	-640	-633	-632	-621	-604	-615	-611
E7	-1875	-1802	-1843	-1839	-1820	-1811	-1817	-1810	-1789	-1772	-1788	-1780
E8	-2215	-2206	-2224	-2221	-2202	-2192	-2192	-2159	-2194	-2171	-2194	-2180
E9	-2144	-2135	-2157	-2155	-2129	-2116	-2122	-2119	-2109	-2085	-2111	-2096
E10	673	681	658	663	684	689	690	690	706	724	704	717
E11	-1166	-1060	-1099	-1094	-1064	-1057	-1046	-1042	-1044	-1023	-1038	-1027
E12	-1538	-1519	-1533	-1532	-1507	-1501	-1499	-1497	-1496	-1473	-1488	-1482
E13	-857	-858	-882	-879	-854	-846	-828	-827	-809	-783	-795	-792
E14	-1498	-1411	-1453	-1445	-1422	-1415	-1402	-1398	-1393	-1399	-1394	-1380
E15	-2342	-2286	-2323	-2313	-2285	-2276	-2249	-2245	-2234	-2239	-2231	-2219
E16	-2801	-2794	-2838	-2829	-2810	-2801	-2782	-2786	-2768	-2757	-2756	-2757
E17	-1032	-922	-948	-943	-934	-934	-909	-907	-895	-896	-889	-876
E18	-2738	-2675	-2706	-2699	-2685	-2678	-2674	-2672	-2664	-2667	-2664	-2651
E19	-2199	-2187	-2209	-2196	-2163	-2166	-2168	-2163	-2144	-2144	-2147	-2128
N1	6362	6588	6709	6707	6731	6741	6748	6752	6772	6772	6783	6782
N2	568	757	813	818	837	844	856	858	882	879	884	895
N3	911	914	909	906	914	893	868	873	937	916	891	953
N4	3117	3133	3125	3128	3156	3161	3156	3152	3159	3154	3160	3166
T4	-441	-426	-458	-453	-431	-415	-374	-376	-405	-402	-393	-386
S1	-519	-529	-545	-540	-541	-533	-532	-529	-520	-527	-522	-514
S2	-58	-66	-71	-63	-66	-54	-49	-46	-38	-42	-35	-28
S3	-462	-478	-494	-491	-493	-485	-488	-495	-476	-501	-491	-476

Table B1 Cont'd

S4	138	134	132	135	133	142	145	150	162	157	159	156
S5	-679	-694	-690	-690	-690	-683	-681	-681	-665	-669	-670	-664
S6	-648	-651	-652	-643	-644	-637	-636	-633	-626	-627	-624	-619
C1	-657	-641	-640	-631	-629	-606	-585	-582	-599	-601	-593	-595
C2	-173	-171	-180	-171	-175	-182	-200	-202	-156	-162	-165	-152
C3	-1114	-1118	-1120	-1114	-1115	-1110	-1108	-1110	-1097	-1101	-1100	-1094
C4	-911	-937	-942	-930	-934	-947	-977	-976	-920	-928	-938	-913
RS1	3450	3520	3541	3548	3545	3556	3575	3564	3580	3573	3577	3569
RS2	3062	3143	3155	3149	3170	3194	3186	3174	3192	3182	3188	3183
RS3	2517	2511	2545	2467	2450	2475	2472	2451	2467	2463	2444	2486
At the end :												
Time	7 : 30 am	12 : 10 pm	10 : 00 am	10 : 30 am	10 : 55 am	11 : 20 am	11 : 50 am	12 : 30 pm	1 : 40 pm	2 : 00 pm	2 : 20 pm	2 : 50 pm
Standard	1	-22	-10	29	-15	-19	-22	-19	-15	-18	-18	22
Temperature	15	22.5	21	21	23.5	25	24	23	22	23	24	25
TH1		21.1	18.8	19.3	20.1	21.3	22.6	22.9	22.7	22.9	23.3	24.1
TH2		18.6	18.2	18.4	18.6	19	19.8	20.3	21.4	21.6	21.7	22
TH3		18.5	18.2	18.4	18.8	19.3	19.8	20	20.8	21.1	21.3	21.6
TH4		19.1	17.7	18.2	18.8	19.9	21.2	21.9	22.8	22.9	23.2	23.7
TH5		22.9	19.2	20.7	22.5	24	25	24	23	23.8	24.8	25.2

Fiber optics		9:40 am	10:27	10:53	11:20	11:30	11:50	1:15 pm	1:45	2:00	2:25
9:15	491	568	568	589	603	609	594	599	607	606	582
	422	435	442	448	454	462	469	478	476	481	488
	-91	-14	-14	7	21	27	12	17	25	24	0
	-66	-53	-46	-40	-34	-26	-19	-10	-12	-7	0
	0	77	77	98	112	118	103	108	116	115	91
	0	13	20	26	32	40	47	56	54	59	66
	-45.5	31.5	31.5	52.5	66.5	72.5	57.5	62.5	70.5	69.5	45.5
	-33	-20	-13	-7	-1	7	14	23	21	26	33

Table B2: Strain Gauge Reading for Static Test, August '97—Before and After Asphalt

No Asphalt No Truck No Truck				Thermal effect	Date	Aug. 11, 97	Aug. 13	Aug. 14, 97
Date								
At the Beginning :								
Time	6 : 30 am	11 : 20 am	2 : 25 pm		Avg Temp.	14.75	21.75	24.75
Standard	42	31	-18					
Temperature	14.5	21	24.5					
TH1		19.7	23.6					
TH2		17.9	21.8					
TH3		17.8	21.5					
TH4		17.9	23.4					
TH5		21.3	25					
G1	-94	-126	-113					
G2	-371	-443	-415					
G3	-601	-655	-682					
G4	-312	-313	-287					
G5	-425	-424	-415					
G6	-220	-203	-172					
G7	-930	-932	-893					
G8	-636		-608					
G9	-435	-423	-388					
G10	-118	-147	-110					
G11	325	314	340					
G12	538	561	565					
G13	247	228	270					
G14	745	732	719					
G15	471	443	496					
G16	-1127	-1141	-1123					
G17	-432	-484	-452					
G18	-188	-244	-215					
G19	-662	-666	-616					
G20	-369	-400	-365					
G21	140	106	145					
G22	370	373	422					
G23	-442	-453	-432					
G24	-450	-538	-496					
G25		281	272					
G26	532	507	547					
G27	285	264	284					
G28	306	296	344					
G29	482	420	479					
G30	206	127	196					
G31	-41	-25	187					
G32			160					
G33			254					
G34	-1027	-1014	-948					
T4	-468	-532	-514					
T1	214	274	302					
T2	-392	-305	-268					
T3	-1115	-1036	-1056					
T4	-551	-562	-527					
T5	133	217	264					
T6	155	243	269					
T7	-1333	-1230	-1192					

Asphalt & Temp.			Asphalt only	
With respect to				
Aug. 13, 97			Aug. 14, 97	
$\Delta T =$	$\Delta T =$	$\Delta T =$		
3	7	10		
13	-32	-19	G1	-62
28	-72	-44	G2	-137
-27	-54	-81	G3	9
26	-1	25	G4	-62
9	1	10	G5	-20
31	17	48	G6	-55
39	-2	37	G7	-93
		28	G8	
		47	G9	-70
35	12	8	G10	-115
37	-29	15	G11	-72
26	-11	27	G12	14
4	23	23	G13	-117
42	-19	25	G14	17
-13	-13	-26	G15	-152
53	-28	4	G16	-56
18	-14	-20	G17	-127
32	-52	-27	G18	-124
29	-56	46	G19	-121
50	-4	4	G20	-113
35	-31	5	G21	-125
39	-34	52	G22	-111
49	3	10	G23	-60
21	-11	-46	G24	-186
42	-88		G25	
-9		15	G26	-118
40	-25	-1	G27	-68
20	-21	38	G28	-122
48	-10	-3	G29	-200
59	-62	-10	G30	-240
69	-79		G31	-479
212	16	228	G32	
			G33	
66	13	79	G34	-141
18	-64	-46	T4	-106
				0
28	60	88	T1	-5
37	87	124	T2	1
-20	79	59	T3	126
35	-11	24	T4	-93
47	84	131	T5	-26
26	88	114	T6	27
38	103	141	T7	14

Table B2 Cont'd

T8	-849	-772	-738	34	77	111	T8	-2
T9	-1644	-1556	-1526	30	88	118	T9	18
T10	-1306	-1254	-1225	29	52	81	T10	-16
T11	-977	-907	-875	32	70	102	T11	-5
T12	-1044	-950	-955	-5	94	89	T12	106
T13	-352	-298	-271	27	54	81	T13	-9
T14	1580	1650	1592	-58	70	12	T14	205
T15	-174	-103	-91	12	71	83	T15	43
T16	3700	3847	3903	56	147	203	T16	16
T17	-620	-558	-536	22	62	84	T17	11
T18	-43	30	41	11	73	84	T18	47
R12	1493	1489	1468	-21	-4	-25	R12	45
R13	1446	1477	1460	-17	31	14	R13	71
R14	-305	-281	-283	-2	24	22	R14	29
R15	669	700	718	18	31	49	R15	-11
R1	19	82	42	-40	63	23	R1	156
R2	-305	-292	-273	19	13	32	R2	-31
R3	199	205	180	-25	6	-19	R3	64
R4	268	302	316	14	34	48	R4	1
R5	-410	-384	-370	14	26	40	R5	-7
R6 not reliable		3389	3250	-139			R6 not reliable	
R7	1857	1900	1915	15	43	58	R7	8
R8	855	886	899	13	31	44	R8	1
R9	-437	-398	-376	22	39	61	R9	-12
R10	1222	1336	1333	-3	114	111	R10	121
R11	660	691	680	-11	31	20	R11	57
RC1	164	264	218	-46	100	54	RC1	207
RC2	-468	-514	-517	-3	-46	-49	RC2	-39
E2	51	81	113	32	30	62	E2	-45
E3	-1411	-1388	-1335	53	23	76	E3	-101
E4	-2714	-2657	-2656	1	57	58	E4	55
E5	-669	-652	-611	41	17	58	E5	-79
E7	-1875	-1802	-1780	22	73	95	E7	22
E8	-2215	-2206			9		E8	
E9	-2144	-2135	-2096	39	9	48	E9	-82
E10	673	681	717	36	8	44	E10	-76
E11	-1166	-1060	-1027	33	106	139	E11	29
E12	-1538	-1519	-1482	37	19	56	E12	-67
E13	-857	-858	-792	66	-1	65	E13	-155
E14	-1498	-1411	-1380	31	87	118	E14	15
E15	-2342	-2286	-2219	67	56	123	E15	-100
E16	-2801	-2794	-2757	37	7	44	E16	-79
E17	-1032	-922	-876	46	110	156	E17	3
E18	-2738	-2675	-2651	24	63	87	E18	7
E19	-2199	-2187	-2128	59	12	71	E19	-126
N1	6362	6588	6782	194	226	426	N1	-227
N2	568	757	895	138	189	327	N2	-133
N3	911	914	953	39	3	42	N3	-88
N4	3117	3133	3166	33	16	49	N4	-61
T4	-441	-426	-386	40	15	55	T4	-78
S1	-519	-529	-514	15	-10	5	S1	-45
S2	-58	-66	-28	38	-8	30	S2	-97
S3	-462	-478	-476	2	-16	-14	S3	-21
S4	138	134	156	22	-4	18	S4	-55
S5	-679	-678	-664	14	1	15	S5	-32

Table B2 Cont'd

S6	-648	-651	-619	32	-3	29	S6	-78
C1	-657	-641	-595	46	16	62	C1	-91
C2	-173	-171	-152	19	2	21	C2	-42
C3	-1114	-1118	-1094	24	-4	20	C3	-60
C4	-911	-937	-913	24	-26	-2	C4	-82
RS1	3450	3520	3569	49	70	119	RS1	-44
RS2	3062	3143	3183	40	81	121	RS2	-12
RS3	2517	2511	2486	-25	-6	-31	RS3	52
At the end :				23.63918				
Time	7 : 30 am	12 : 10 pm	2 : 50 pm					
Standard	1	-22	22					
Temperature	15	22.5	25					
TH1		21.1	24.1					
TH2		18.6	22					
TH3		18.5	21.6					
TH4		19.1	23.7					
TH5		22.9	25.2					

Table B3: Static Test, August '97, Survey Reading—Raw Data

	No truck	P1	P2	P3	P4	P5	P6	P7	P8	P9	No truck
a1	1068	1068	1068	1067	1062	1060	1062	1068	1067	1067	1067
a2	1012	1013	1013	1012	1007	1004	1007	1012	1011	1010	1012
a3	955	957	957	953	951	948	948	954	953	952	953
a4	911	912	912	908	907	903	903	909	907	905	908
a5	847	848	848	847	842	839	840	845	842	839	845
b1	2501	2502	2502	2497	2492	2487	2488	2498	2498	2498	2498
b2	2440	2442	2442	2437	2431	2427	2427	2438	2437	2436	2438
b3	2382	2383	2383	2378	2372	2368	2368	2378	2375	2374	2379
b4	2330	2332	2331	2326	2318	2315	2315	2325	2321	2318	2327
b5	2268	2272	2271	2266	2259	2256	2257	2265	2258	2254	2266
c1	2474	2477	2476	2468	2462	2458	2461	2472	2472	2472	2472
c2	2411	2413	2412	2407	2398	2393	2396	2408	2406	2405	2408
c3	2351	2353	2353	2347	2338	2335	2337	2348	2344	2342	2348
c4	2295	2298	2298	2292	2284	2279	2282	2292	2286	2282	2292
c5	2232	2237	2236	2232	2223	2218	2218	2230	2221	2217	2229
d1	2444	2447	2446	2438	2433	2431	2432	2442	2442	2442	2442
d2	2382	2387	2385	2378	2372	2368	2371	2379	2378	2378	2380
d3	2320	2324	2323	2317	2310	2306	2308	2318	2313	2313	2318
d4	2263	2268	2268	2261	2253	2250	2252	2261	2255	2253	2261
d5	2202	2207	2206	2200	2193	2192	2192	2198	2192	2189	2198
e1	2393	2397	2395	2391	2387	2385	2387	2393	2392	2392	2393
e2	2337	2339	2338	2333	2330	2328	2330	2336	2334	2333	2335
e3	2273	2277	2276	2272	2266	2265	2266	2272	2269	2268	2272
e4	2219	2222	2222	2217	2212	2212	2212	2217	2213	2212	2217
e5	2156	2159	2158	2154	2150	2148	2150	2153	2148	2148	2153

Table B4: Static Test, August '97, Reduce Survey Data

	No truck	P1	P2	P3	P4	P5	P6	P7	P8	P9	No truck
A1	1	1	1	-1	-6	-8	-6	1	-1	-1	-1
A2	0	1	1	0	-5	-8	-5	0	-1	-2	0
A3	1	3	3	-1	-3	-6	-6	0	-1	-2	-1
A4	2	3	3	-2	-3	-7	-7	-1	-3	-5	-2
A5	1	2	1	1	-4	-7	-6	-1	-4	-7	-1
B1	2	3	3	-3	-8	-13	-12	-2	-2	-2	-2
B2	1	3	3	-2	-8	-12	-12	-1	-2	-3	-1
B3	2	3	3	-3	-9	-13	-13	-3	-6	-7	-2
B4	2	4	3	-3	-11	-14	-14	-4	-8	-11	-2
B5	1	5	4	-1	-8	-11	-10	-2	-9	-13	-1
C1	1	4	3	-5	-11	-15.0	-12	-1	-1.0	-1.0	-1
C2	2	4	3	-3	-12	-16.5	-14	-2	-3.5	-4.5	-2
C3	2	4	4	-3	-12	-14.5	-13	-2	-5.5	-7.5	-2
C4	2	5	5	-2	-10	-14.5	-12	-2	-7.5	-11.5	-2
C5	2	6.5	6	2	-8	-12.5	-13	-1	-9.5	-13.5	-2
D1	1	4	3	-5	-10	-12	-11	-1	-1	-1	-1
D2	1	6	4	-3	-9	-13	-10	-2	-3	-3	-1
D3	1	5	4	-2	-9	-13	-11	-1	-6	-6	-1
D4	1	6	6	-1	-9	-12	-10	-1	-7	-9	-1
D5	2	7.0	6	0	-7	-8	-8	-2	-8	-11	-2
E1	0	4	2	-2	-6	-8	-6	0	-1	-1	0
E2	1	3	2	-3	-6	-8	-6	0	-2	-3	-1
E3	1	5	4	-1	-7	-8	-7	-1	-4	-5	-1
E4	1	4	4	-1	-6	-6	-6	-1	-5	-6	-1
E5	2	5	4	-1	-5	-7	-5	-2	-7	-7	-2
Max	2	7	6	2	-3	-6	-5	1	-1	-1	0
Min	0	1	1	-5	-12	-17	-14	-4	-10	-14	-2

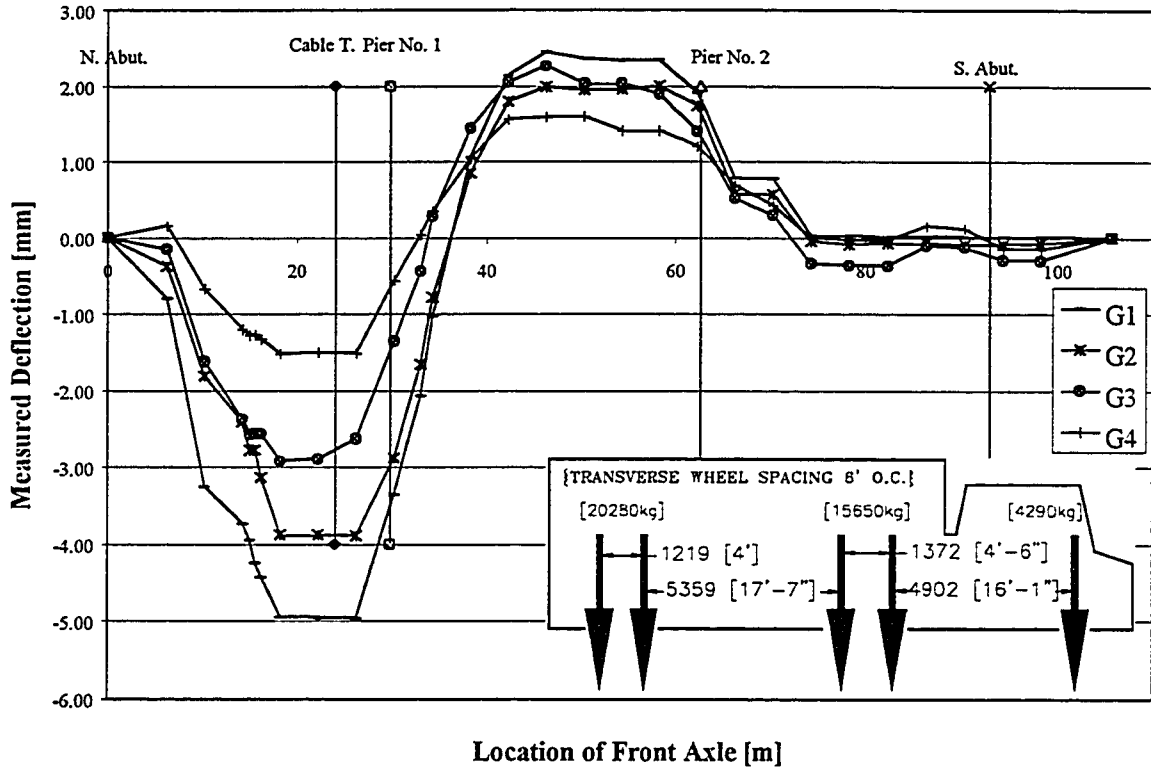


Figure B1: Static Load Test, August '98 for Cable Transducer at Strap #21

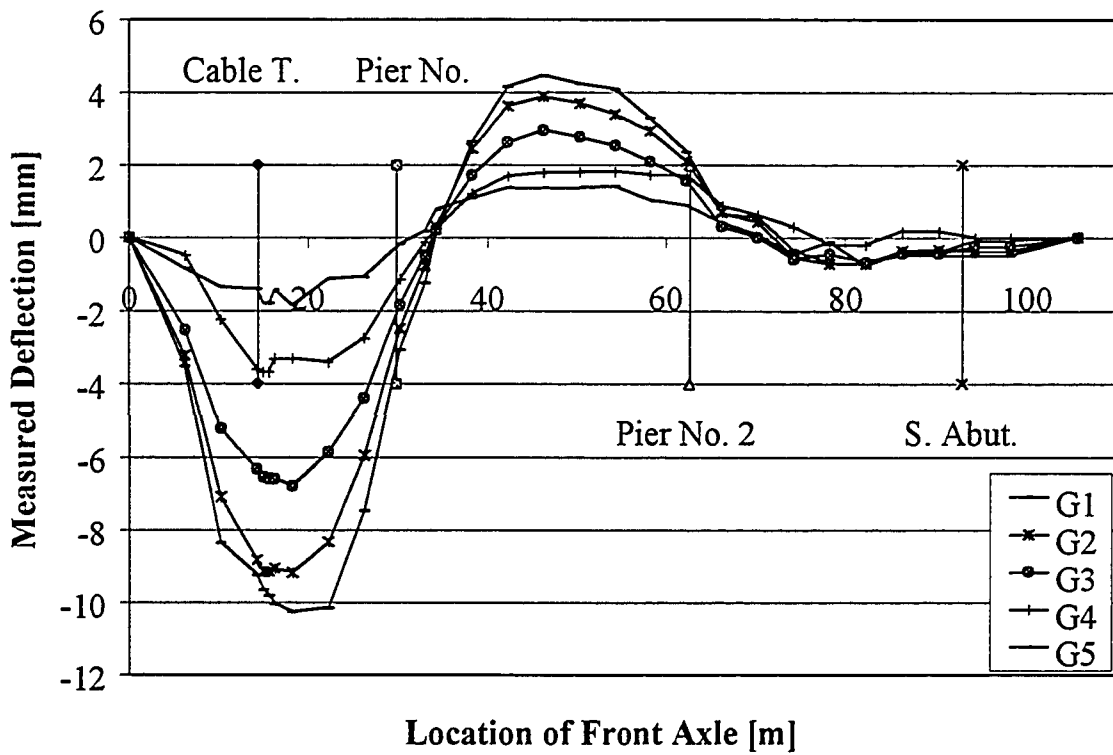


Figure B2: Static Load Test, August '98 for Cable Transducer at Strap #13

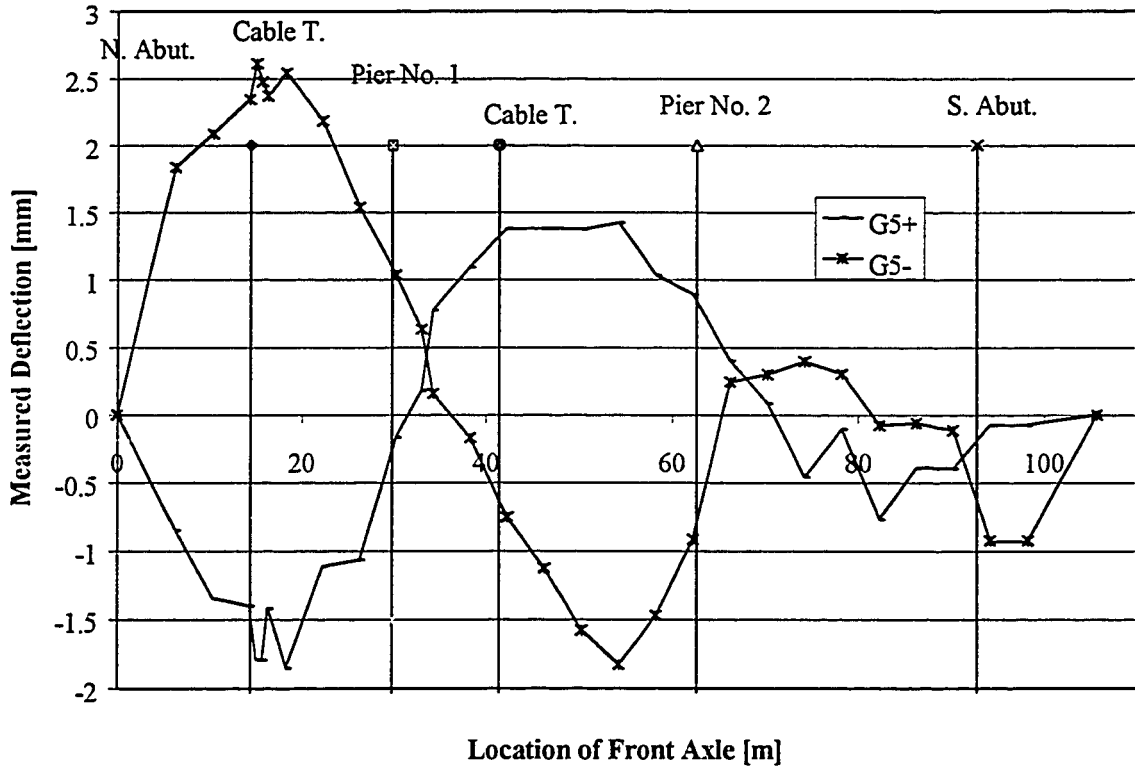


Figure B3: Static Load Test, August '98 for Two Cable Transducers for Girder 5 in the Positive and Negative Moment Region.

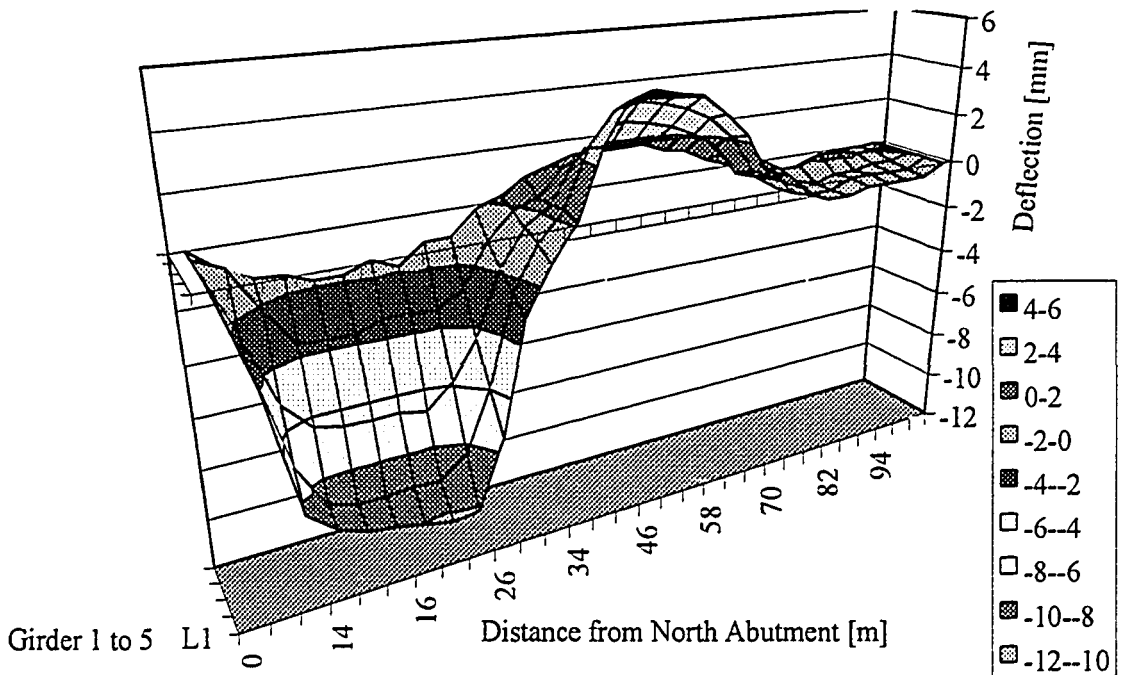


Figure B4: Static Load Test, August '98 from Cable Transducers at Strap #13—3D Plot

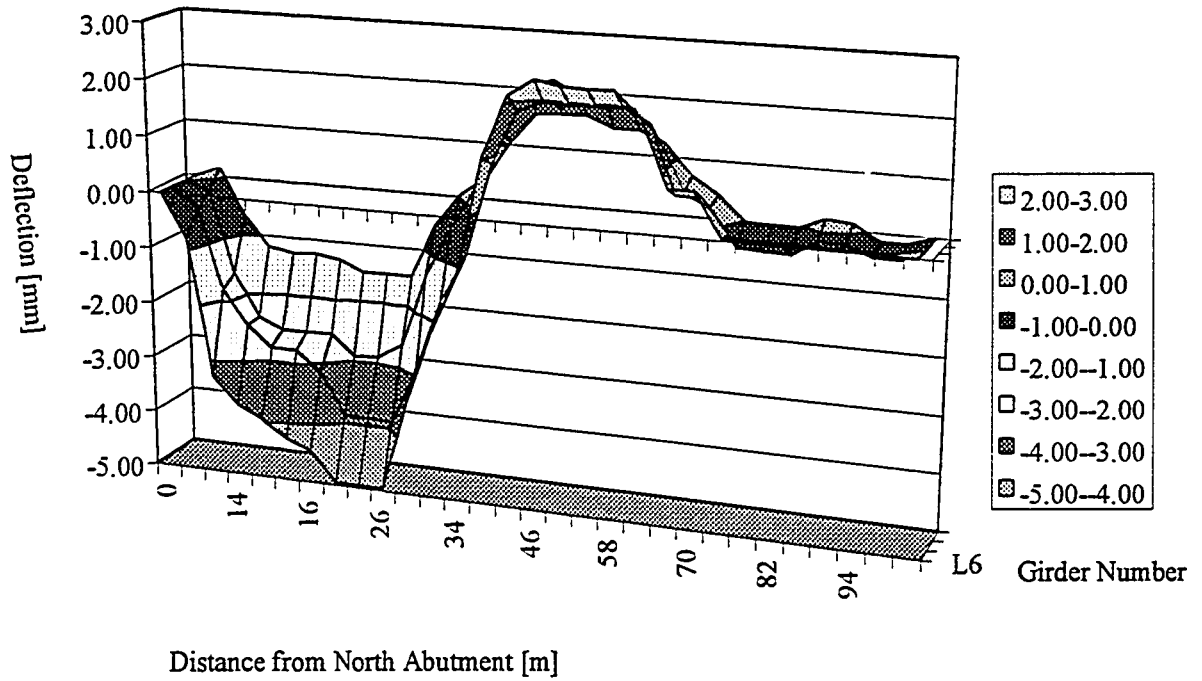


Figure B5: Static Load Test, August '98 from Cable Transducers at Strap #21—3D Plot

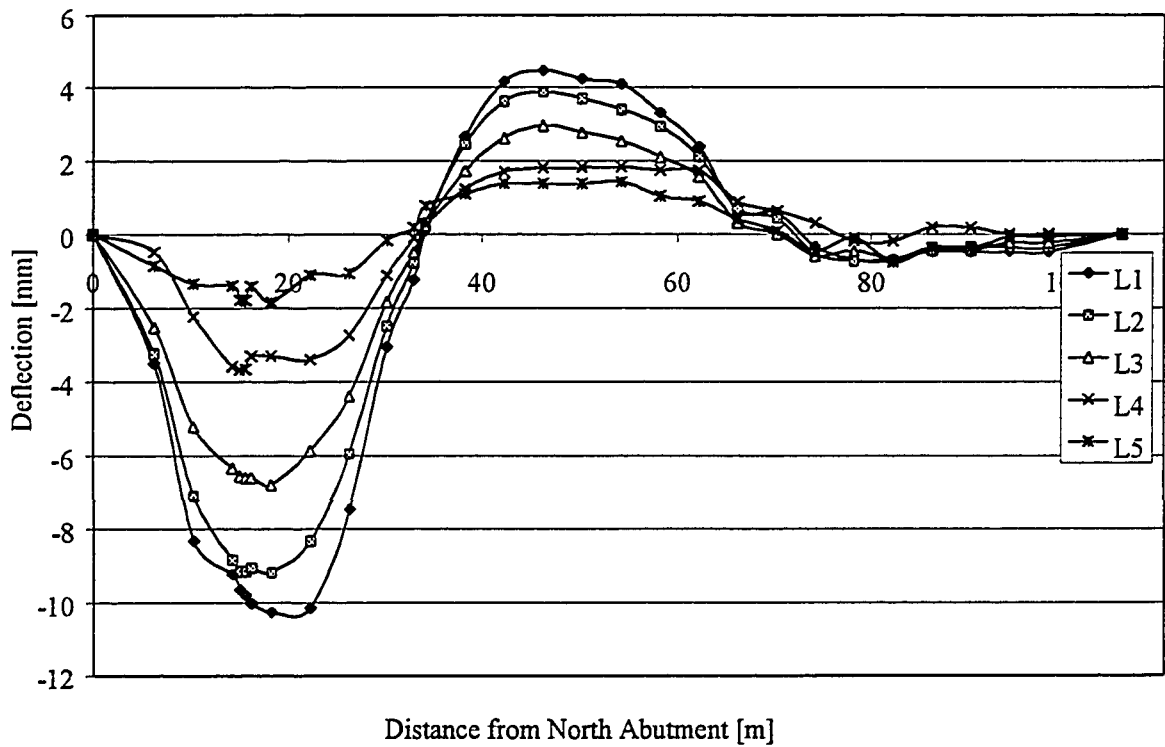


Figure B6: Static Load Test, August '98 from Cable Transducers at Strap #13

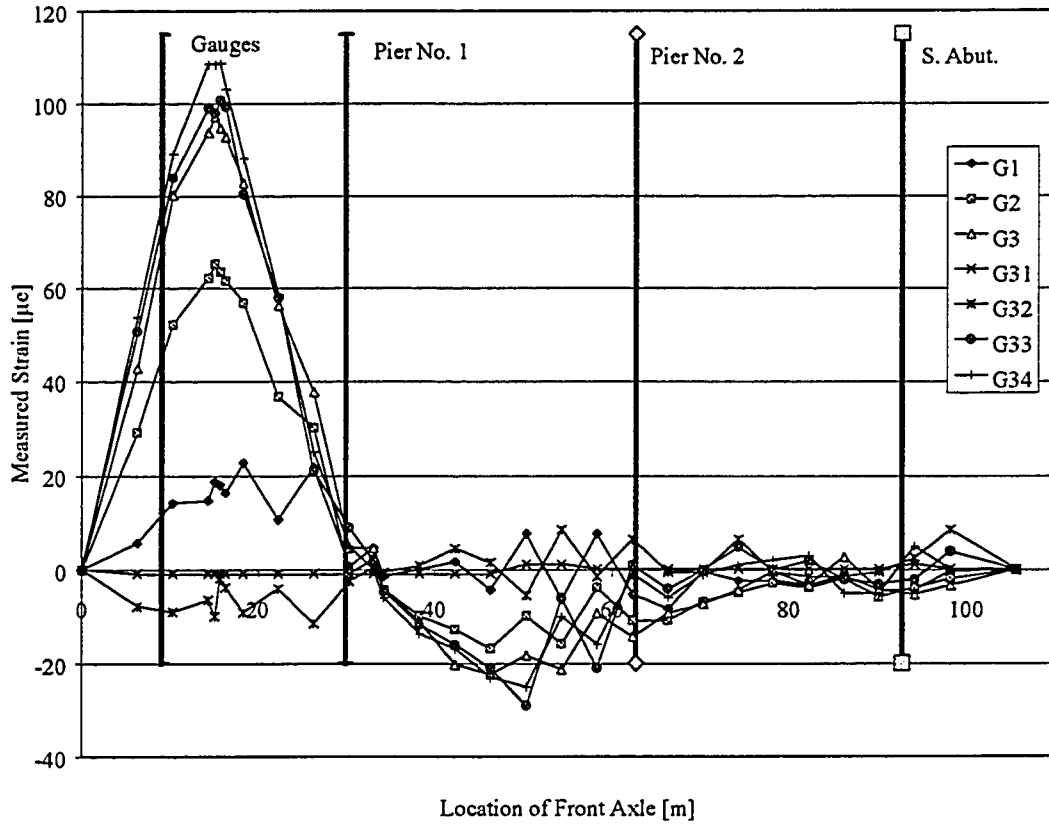


Figure B7: Static Load Test, August '98 for Girder 1 in Positive Moment Region



Figure B8: Static Load Test, August '98 for Girder 2 in Positive Moment Region

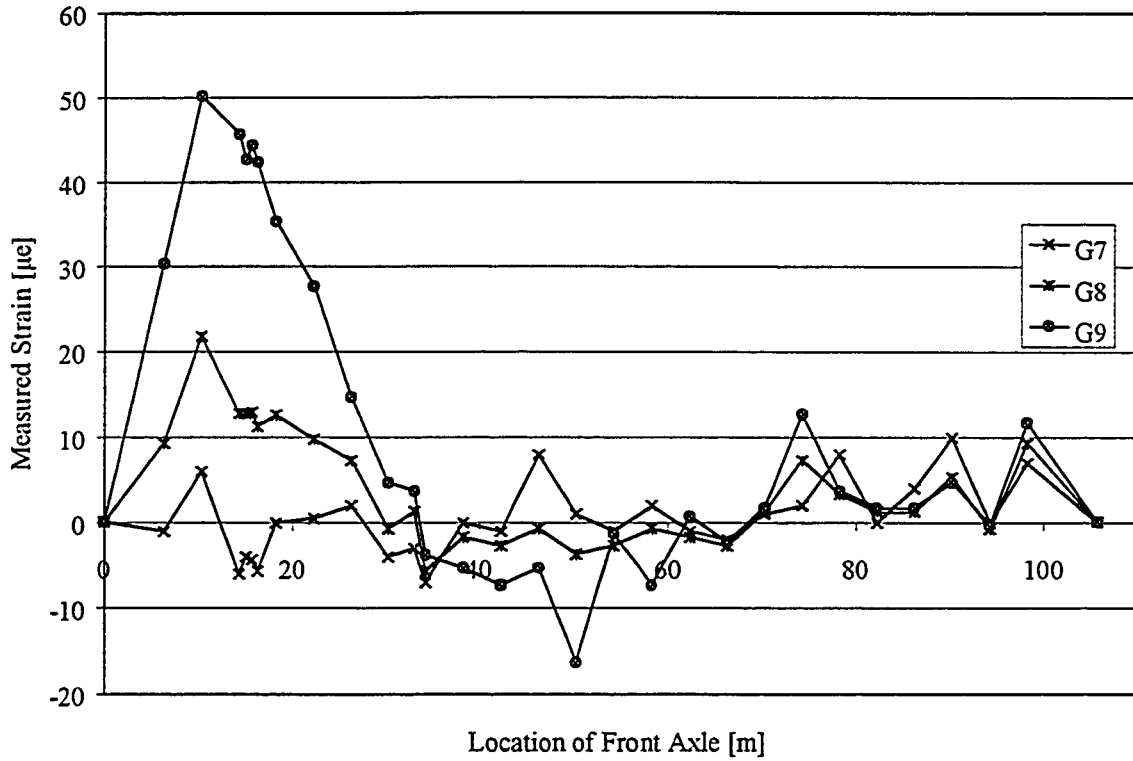


Figure B9: Static Load Test, August '98 for Girder 3 in Positive Moment Region

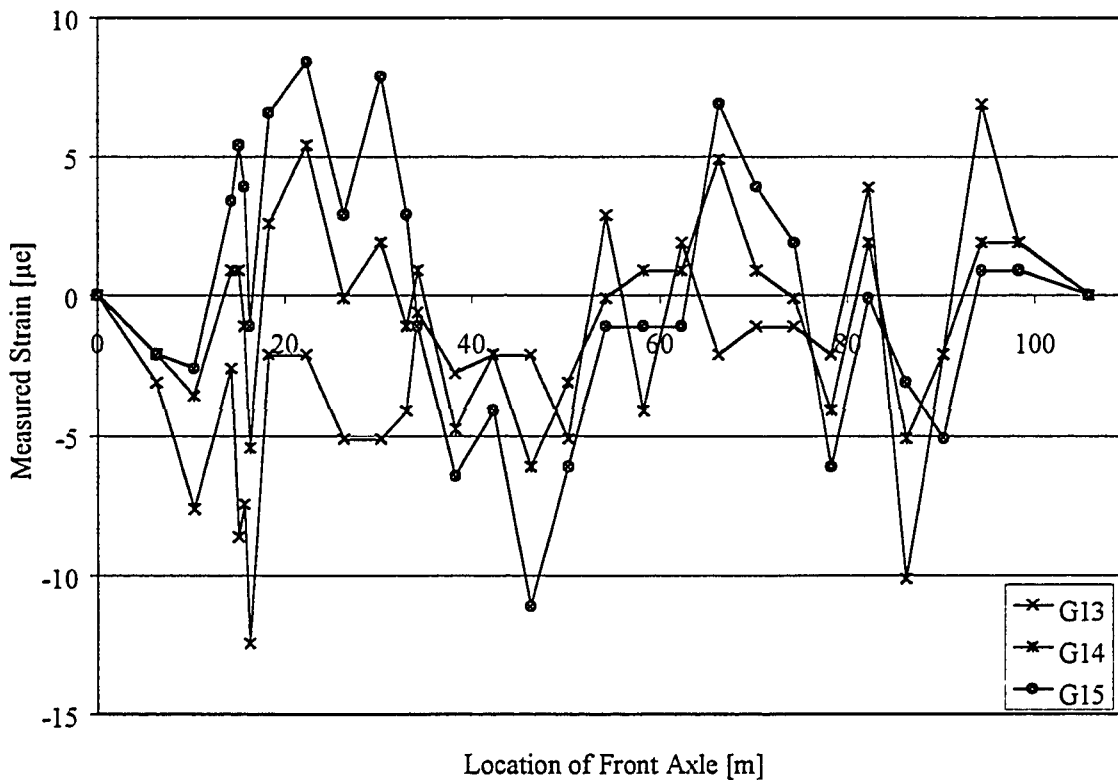


Figure B10: Static Load Test, August '98 for Girder 5 in Positive Moment Region



Figure B11: Static Load Test, August '98 for Girder 4 in Positive Moment Region

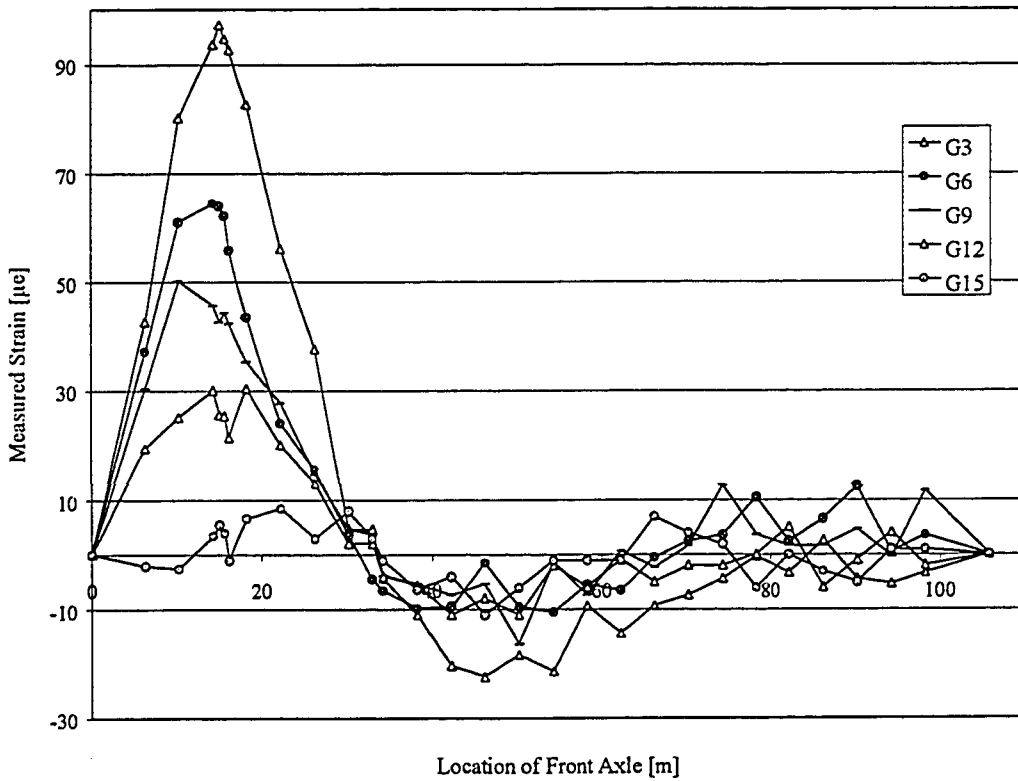


Figure B12: Static Load Test, August '98 for all Bottom Gauges in Positive Moment Region

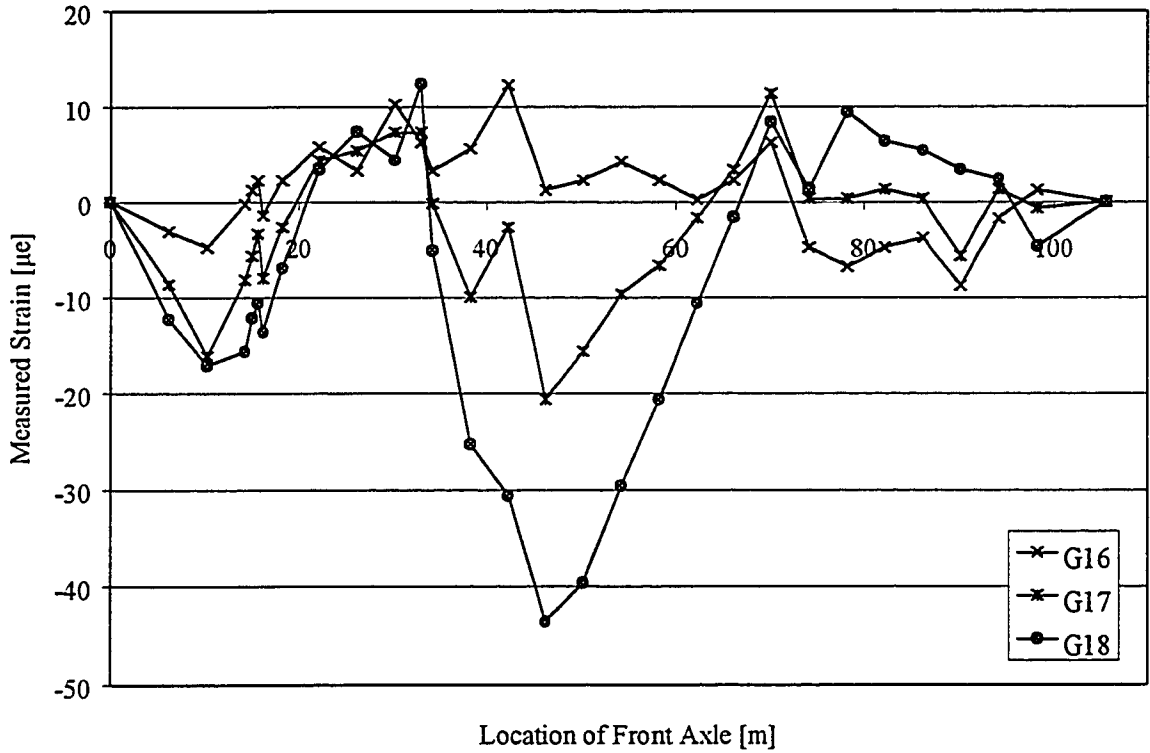


Figure B13: Static Load Test, August '98 for Girder 1 in Negative Moment Region

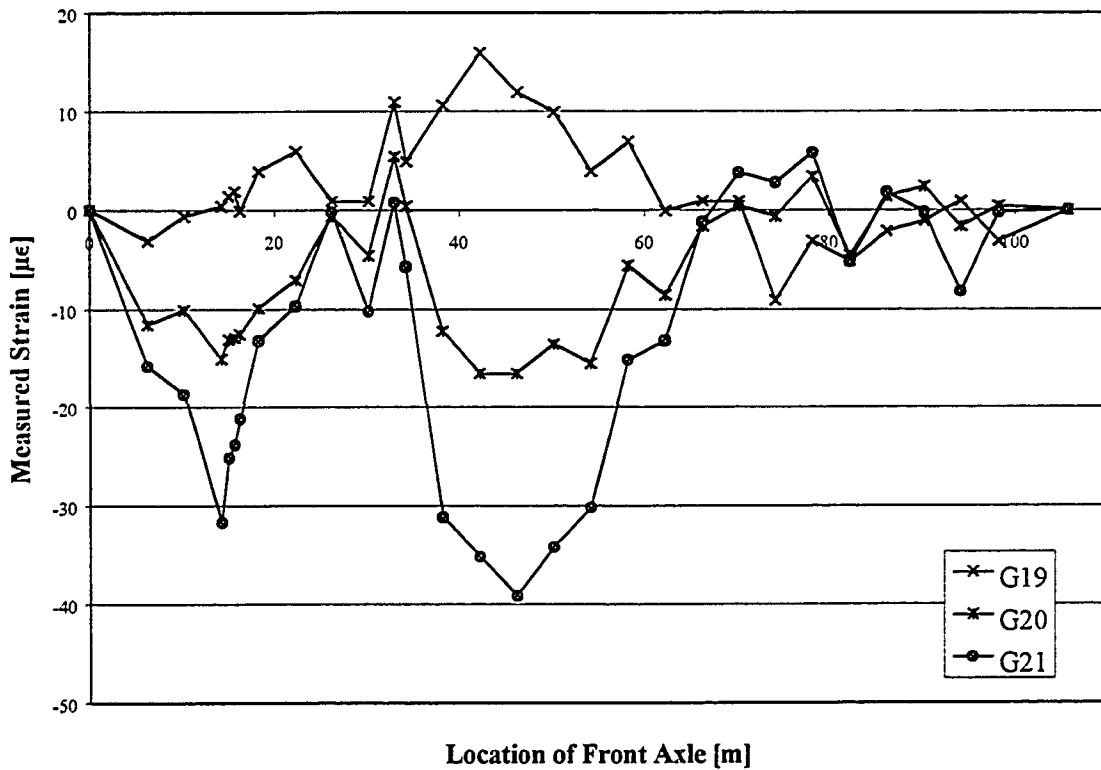


Figure B14: Static Load Test, August '98 for Girder 2 in Negative Moment Region

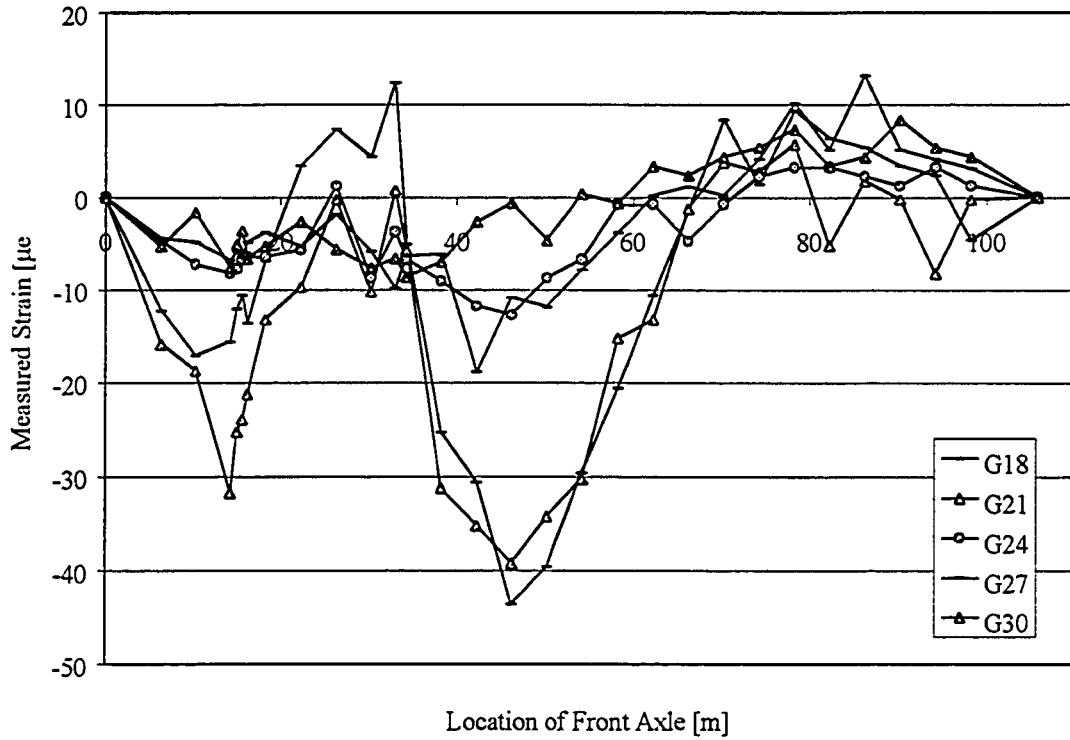


Figure B15: Static Load Test, August '98 for all Bottom Gauges in Negative Moment Region

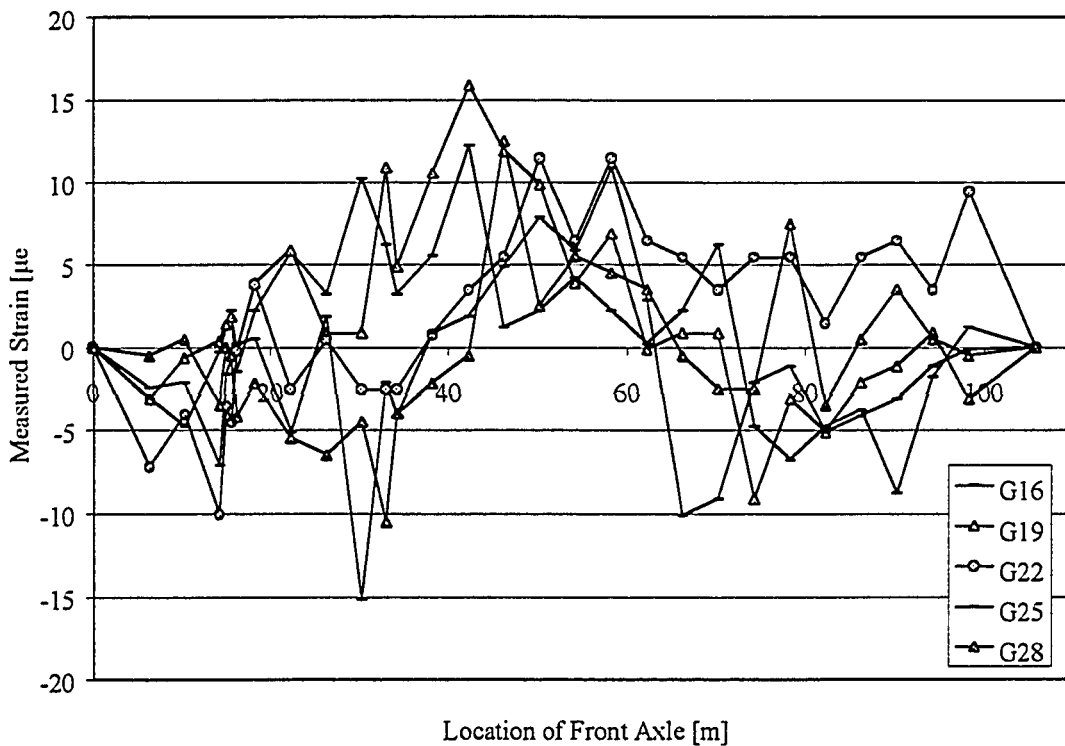


Figure B16: Static Load Test, August '98 for Top Gauges in Negative Moment Region

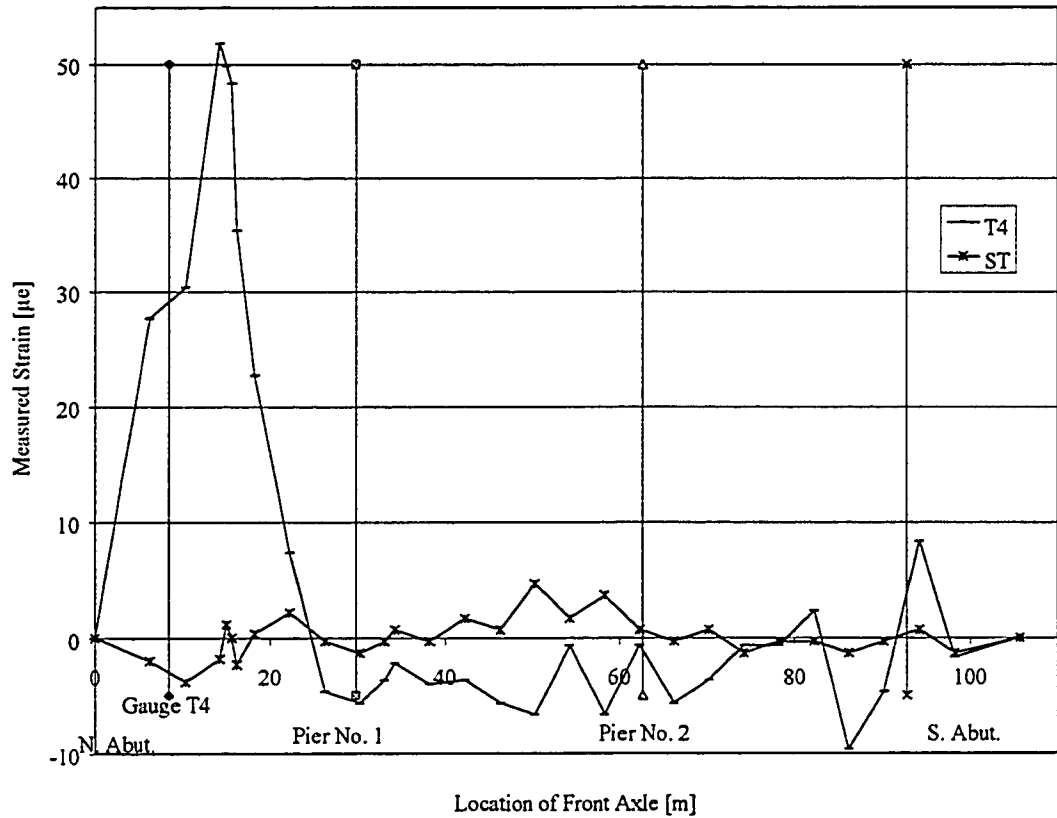


Figure B17: Static Load Test, August '98 for T4 & ST Gauges

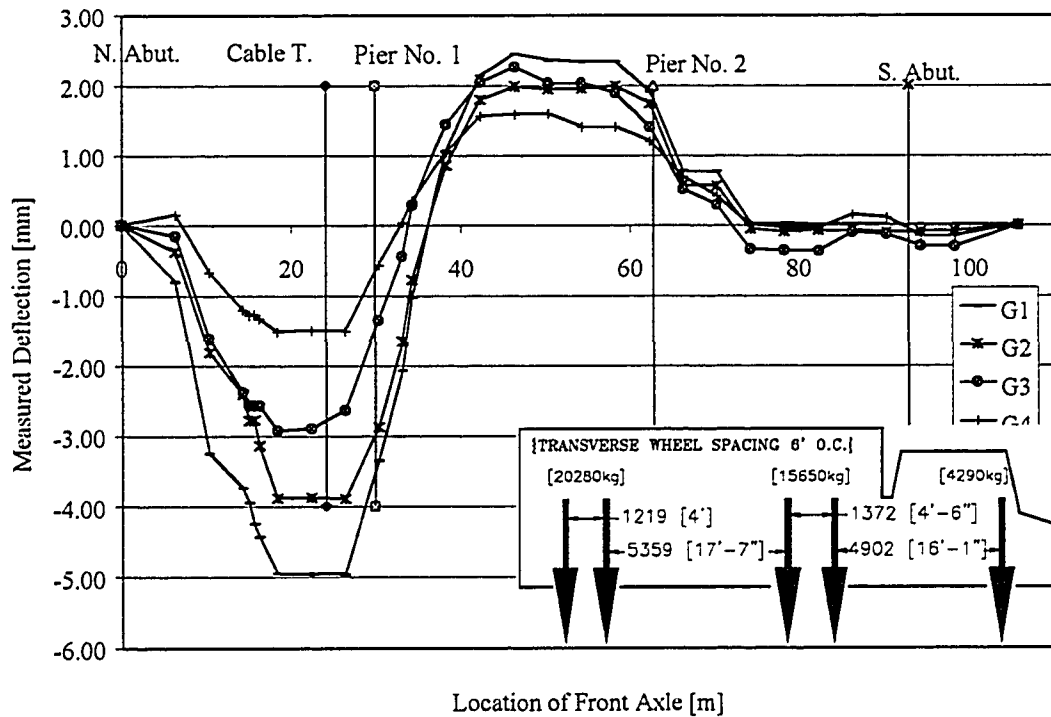


Figure B18: Static Load Test, August '98 for All Cable Transducers at Strap #21

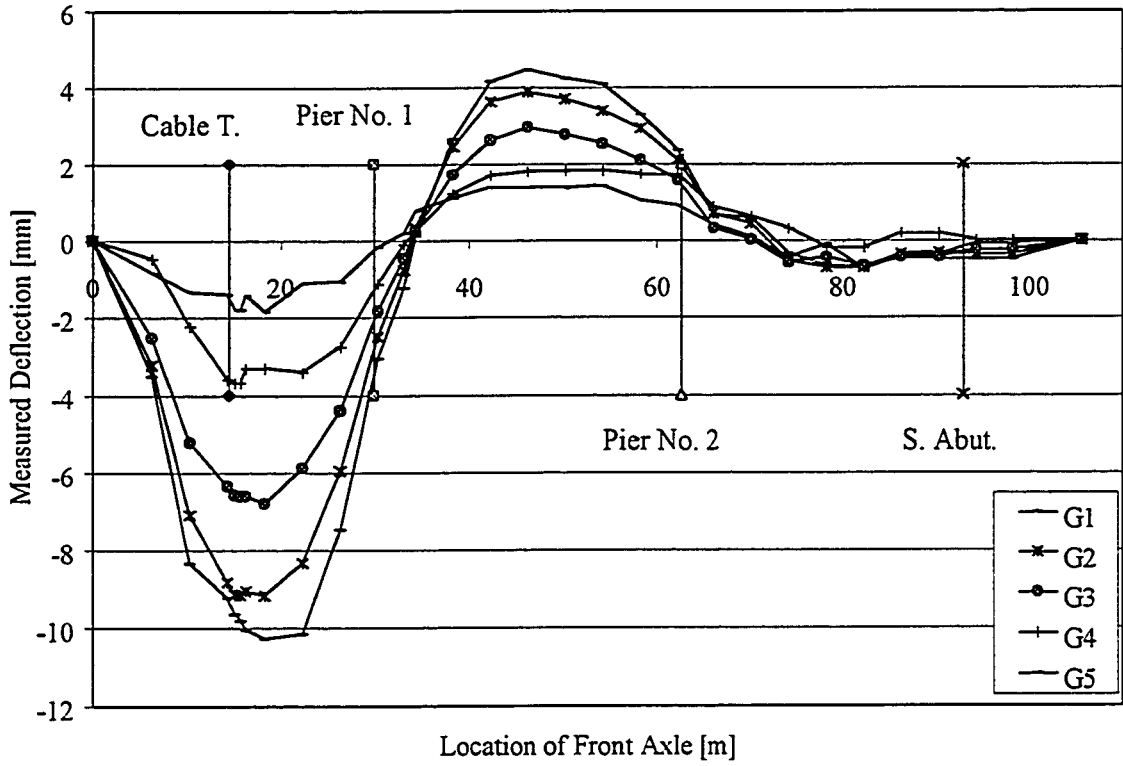


Figure B19: Static Load Test, August '98 for Cable Transducers at Strap #13

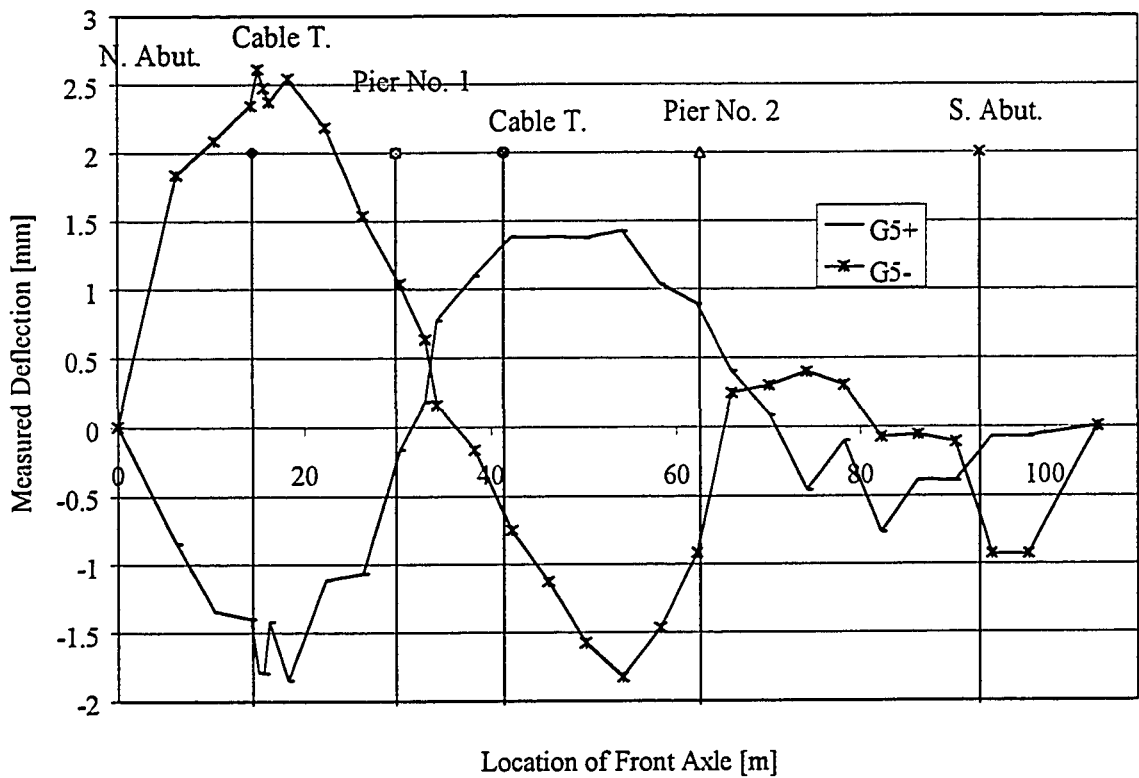


Figure B20: Static Load Test, August '98 for Cable Transducers on Girder 5

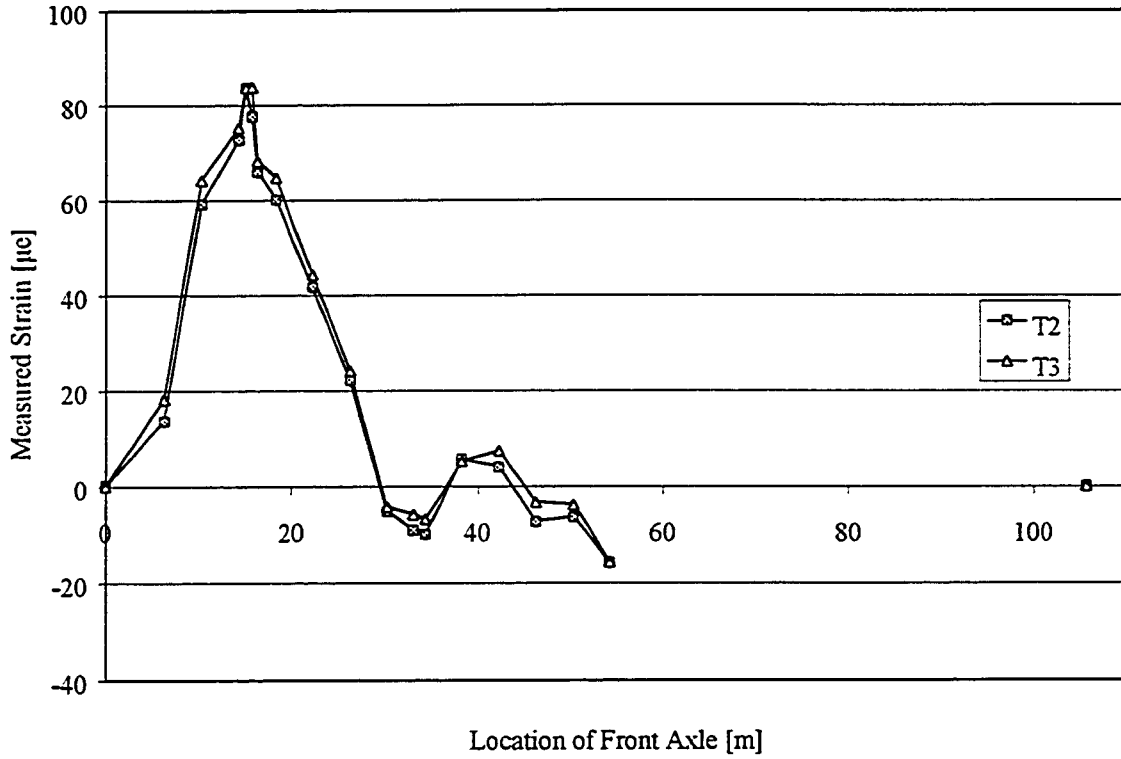


Figure B21: Static Load Test, August '98 for Strap #8 in Positive Moment Region

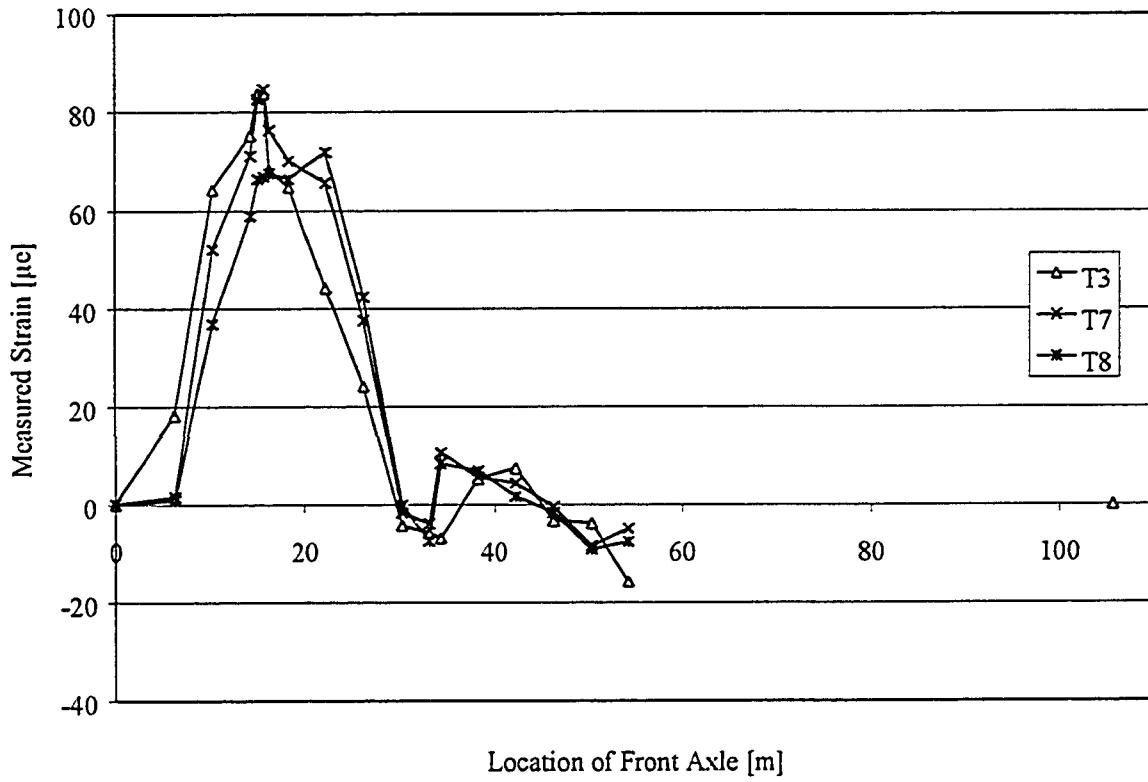


Figure B22: Static Load Test, August '98 for Straps #9, 10, 11 in Positive Moment

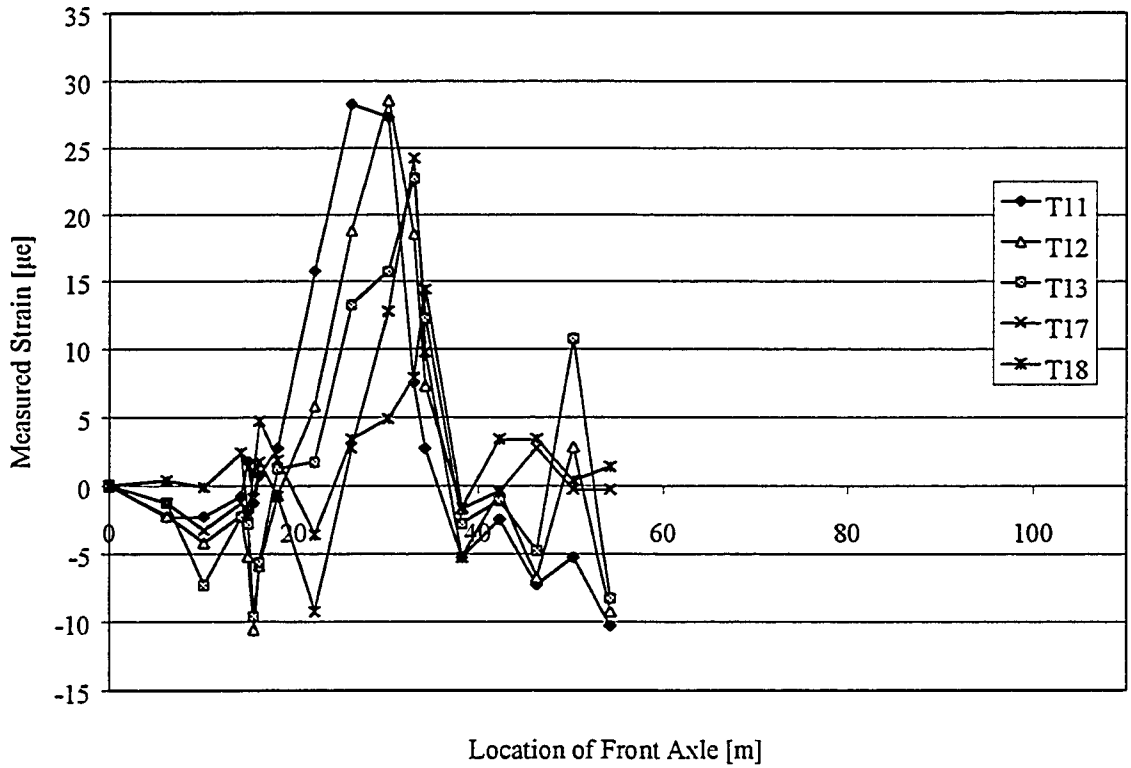


Figure B23: Static Load Test, August '98 for Straps in Positive Moment Region

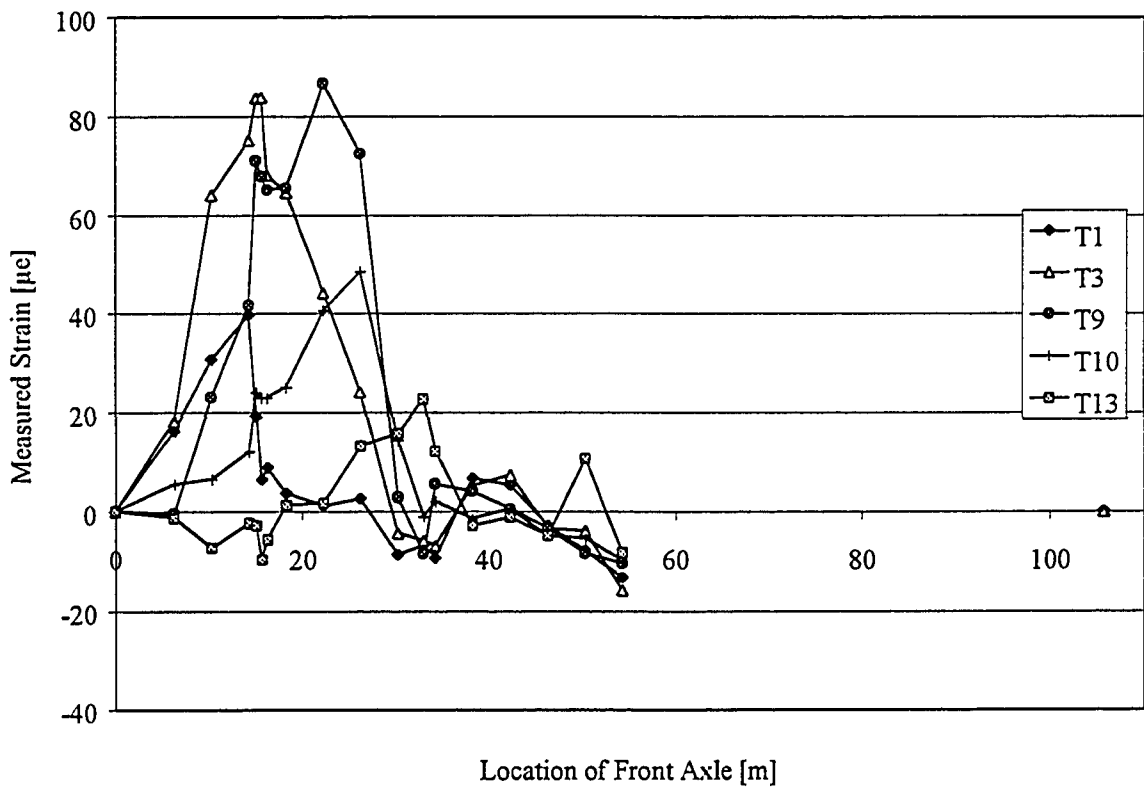


Figure B24: Static Load Test, August '98 for Straps in Positive Moment Region

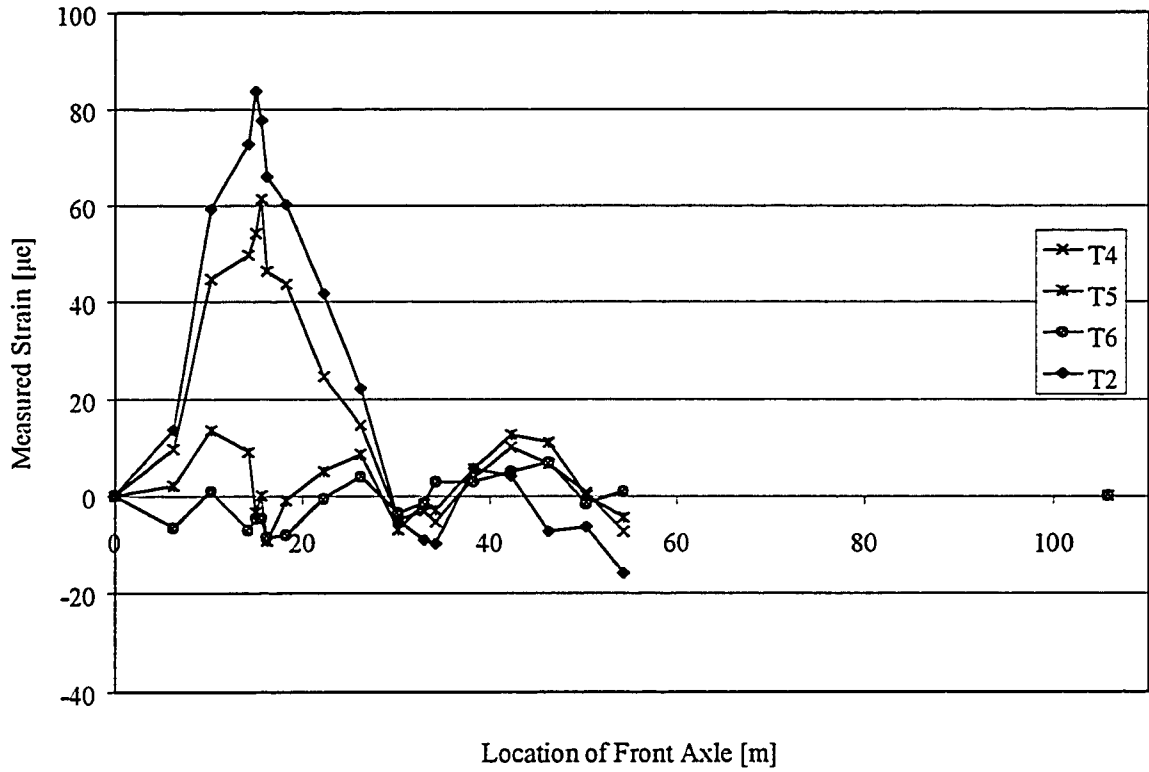


Figure B25: Static Load Test, August '98 for Strap #8 in Positive Moment Region

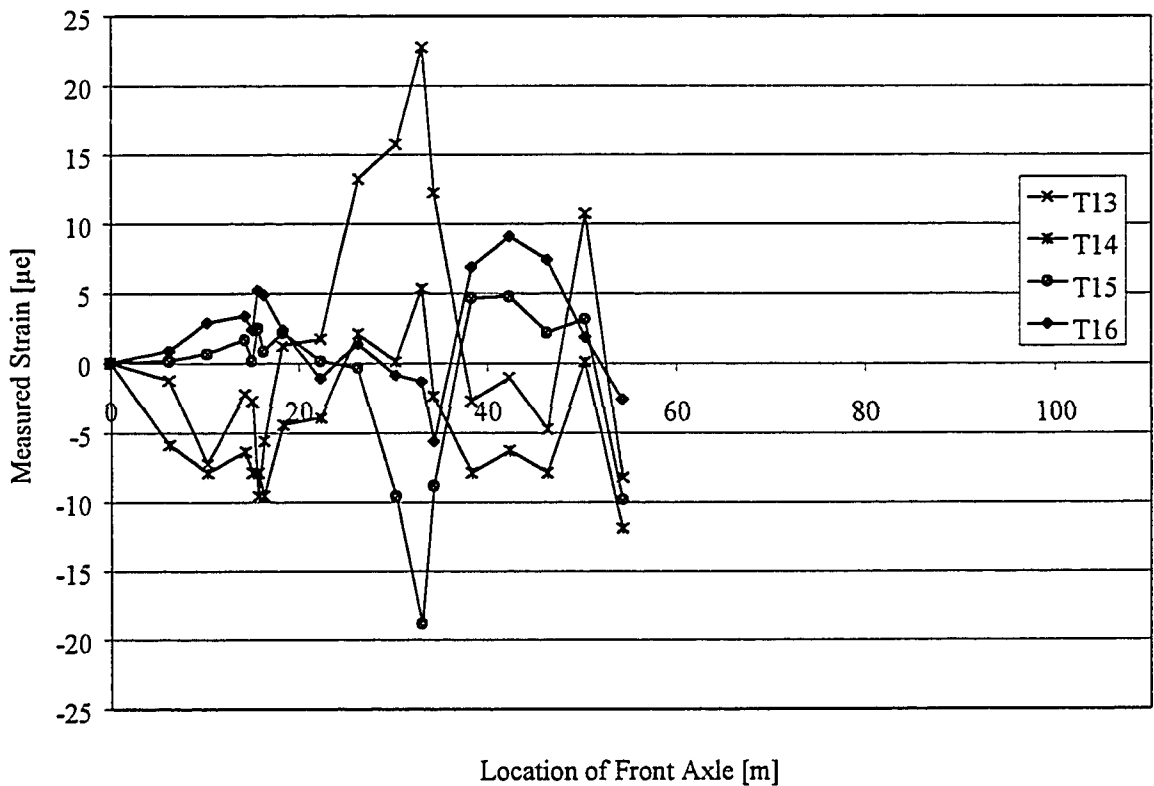


Figure B26: Static Load Test, August '98 for Strap #23 in Positive Moment Region

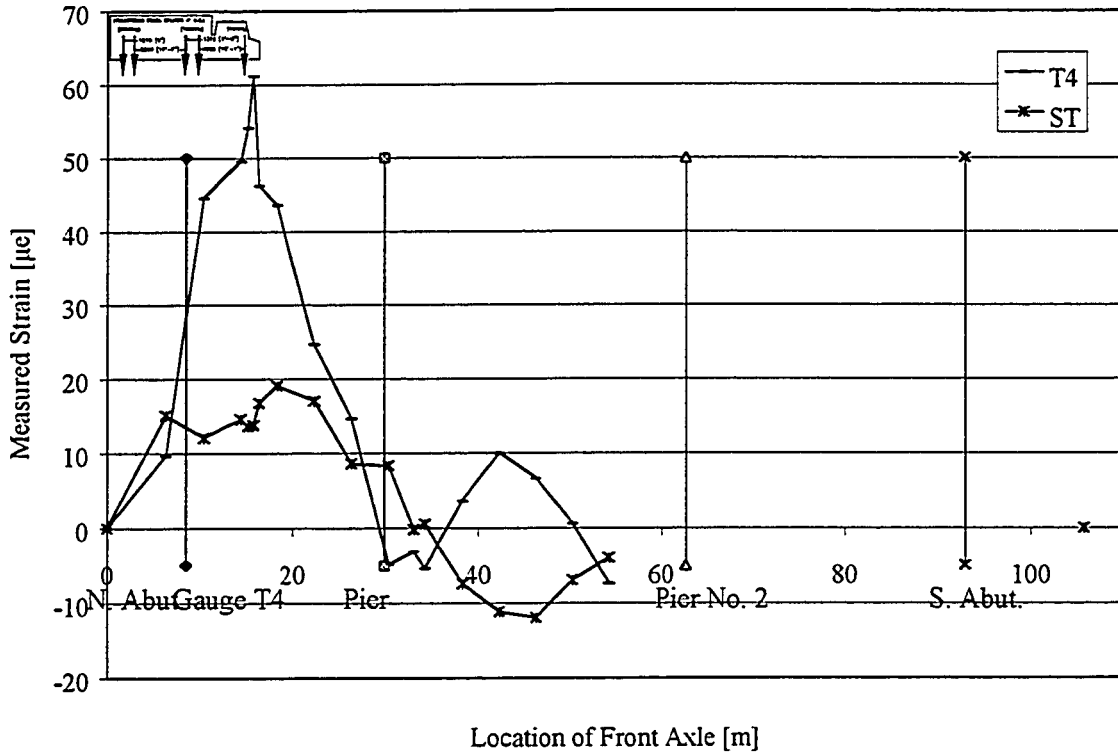


Figure B27: Static Load Test, August '98 for T4 & Standard Gauges

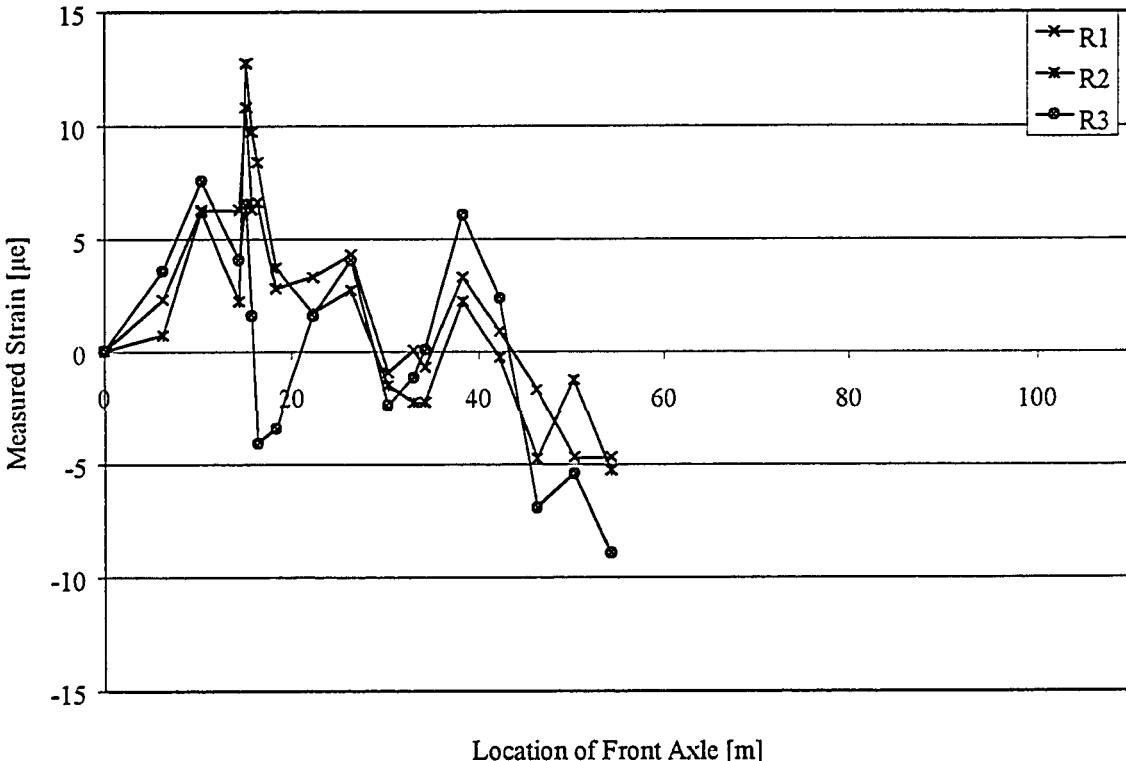


Figure B28: Static Load Test, August '98 for C-Bar at Cantilever

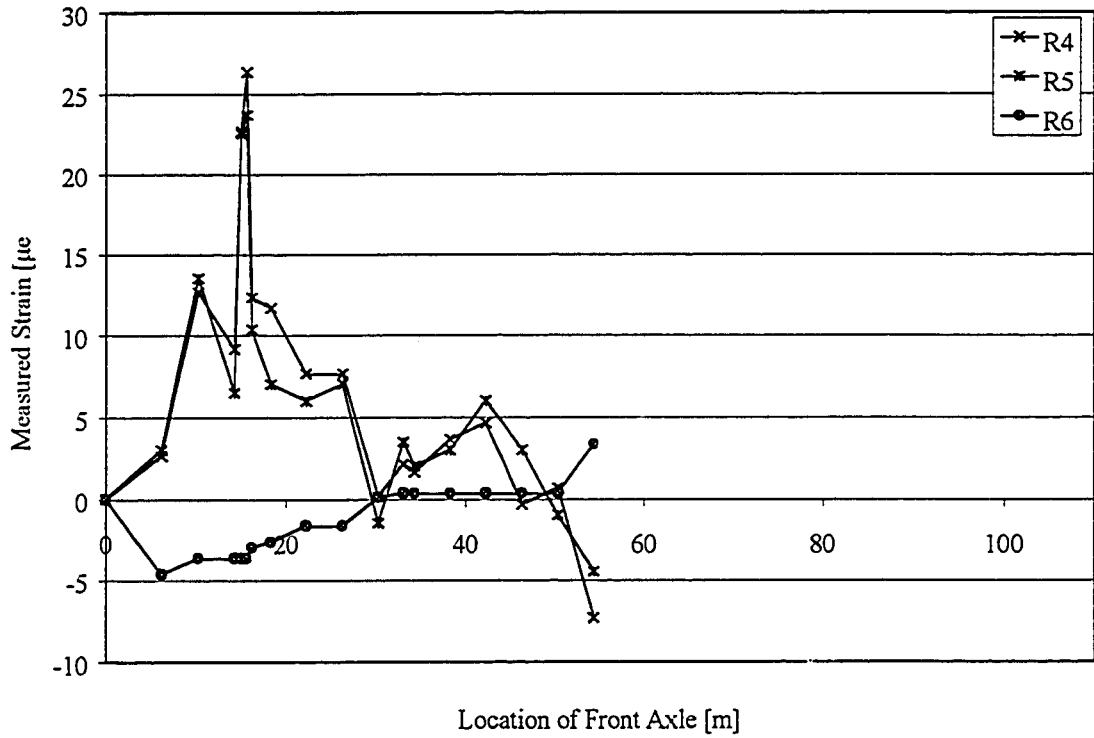


Figure B29: Static Load Test, August '98 for C-Bar at Cantilever

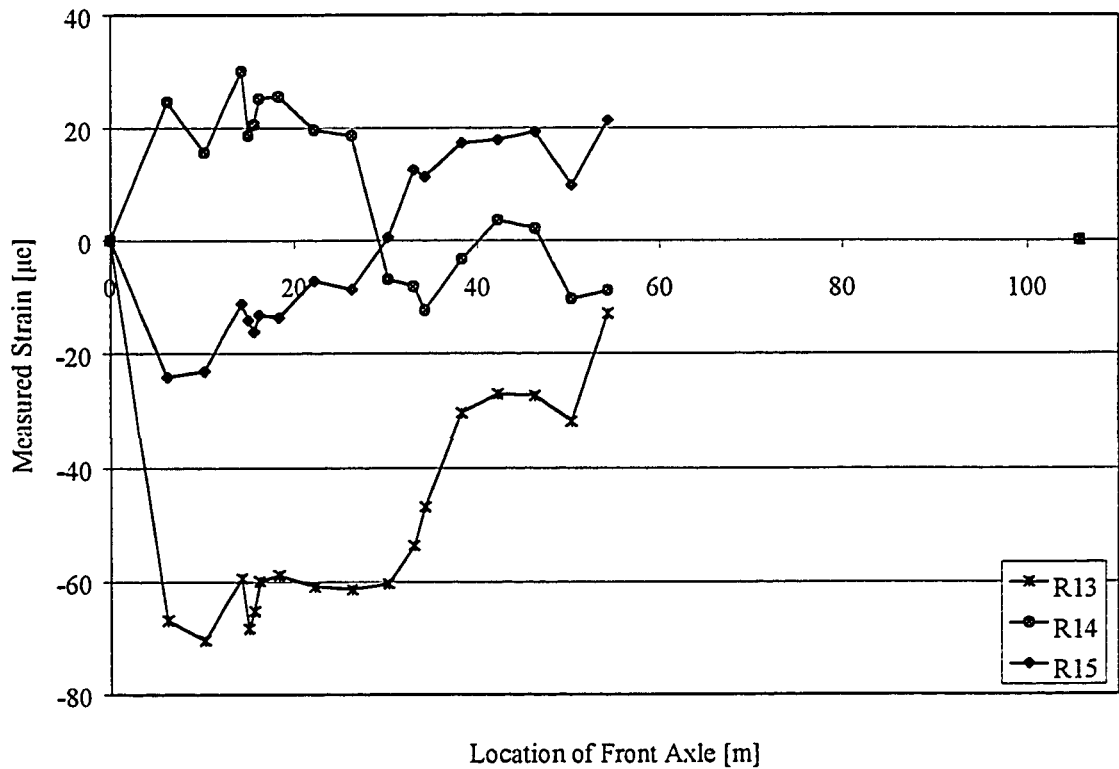


Figure B30: Static Load Test, August '98 for C-Bar at Pier No.1

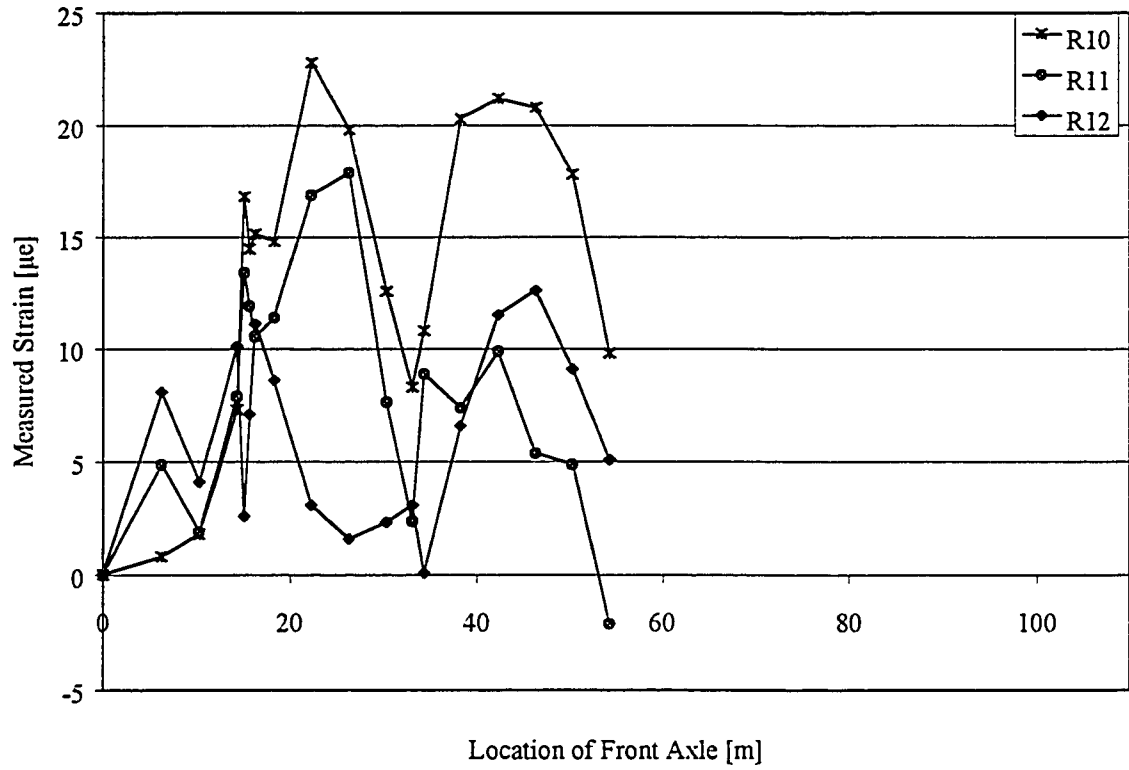


Figure B31: Static Load Test, August '98 for C-Bar at Pier No.1

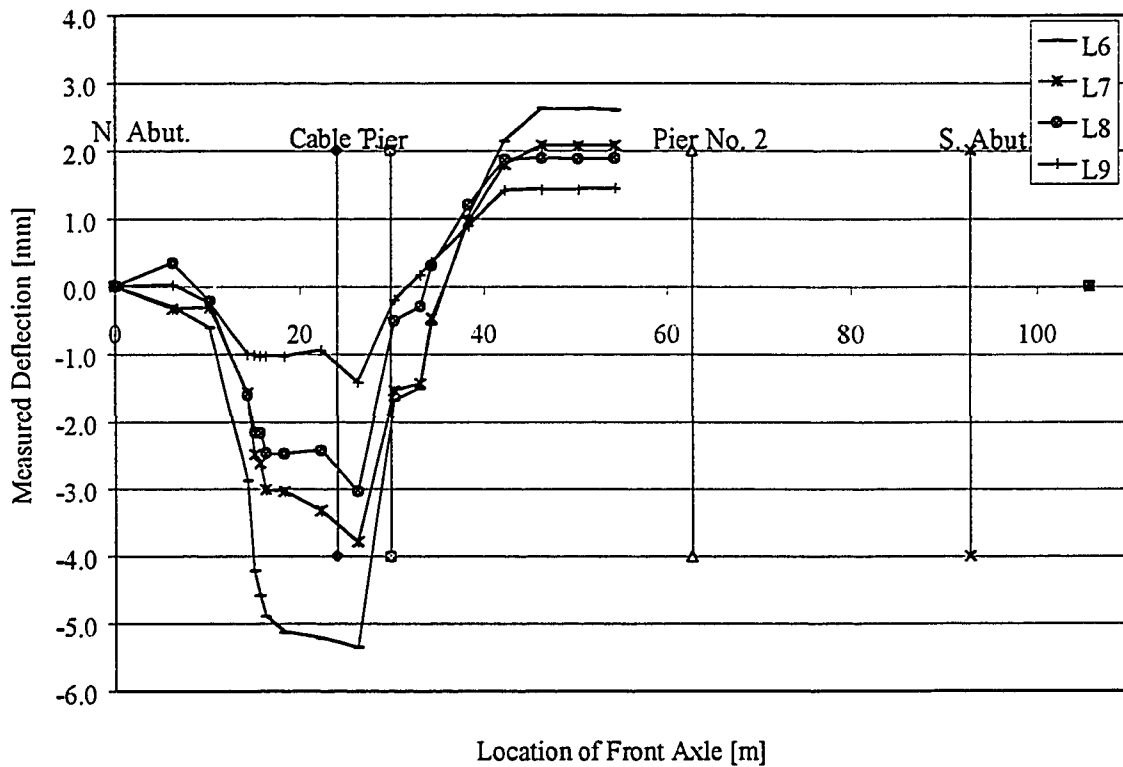


Figure B32: Static Load Test, August '98 for Cable Transducers at Strap #21

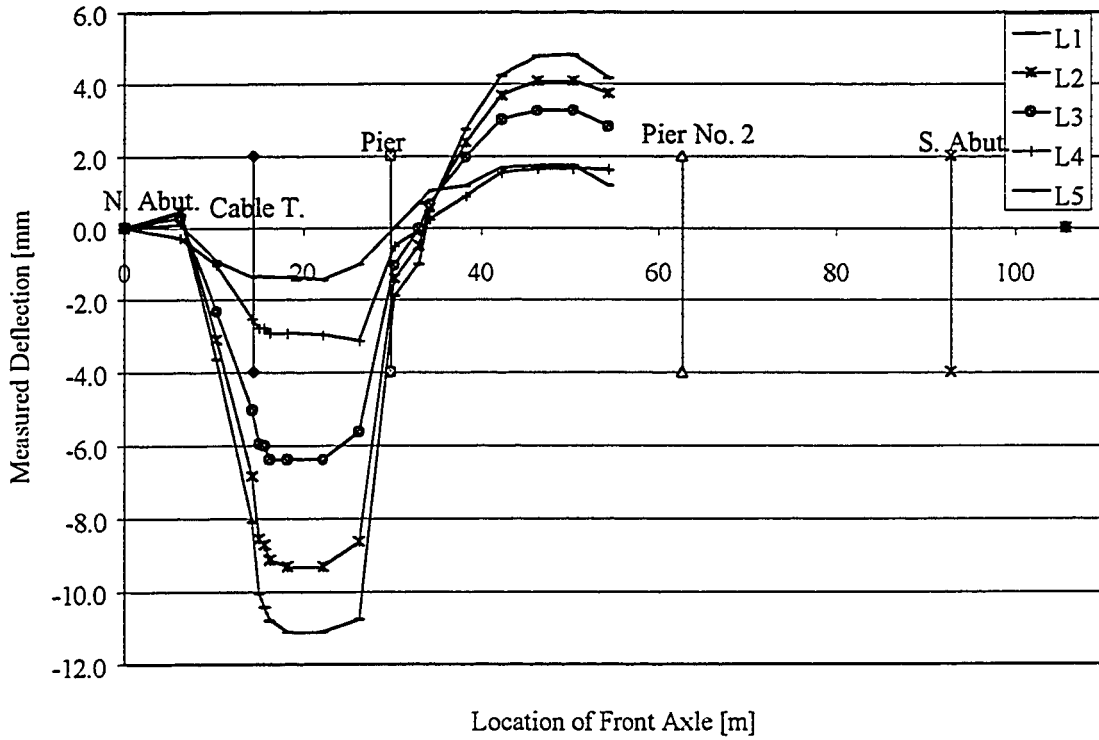


Figure B33: Static Load Test, August '98 for Cable Transducers at Strap #13

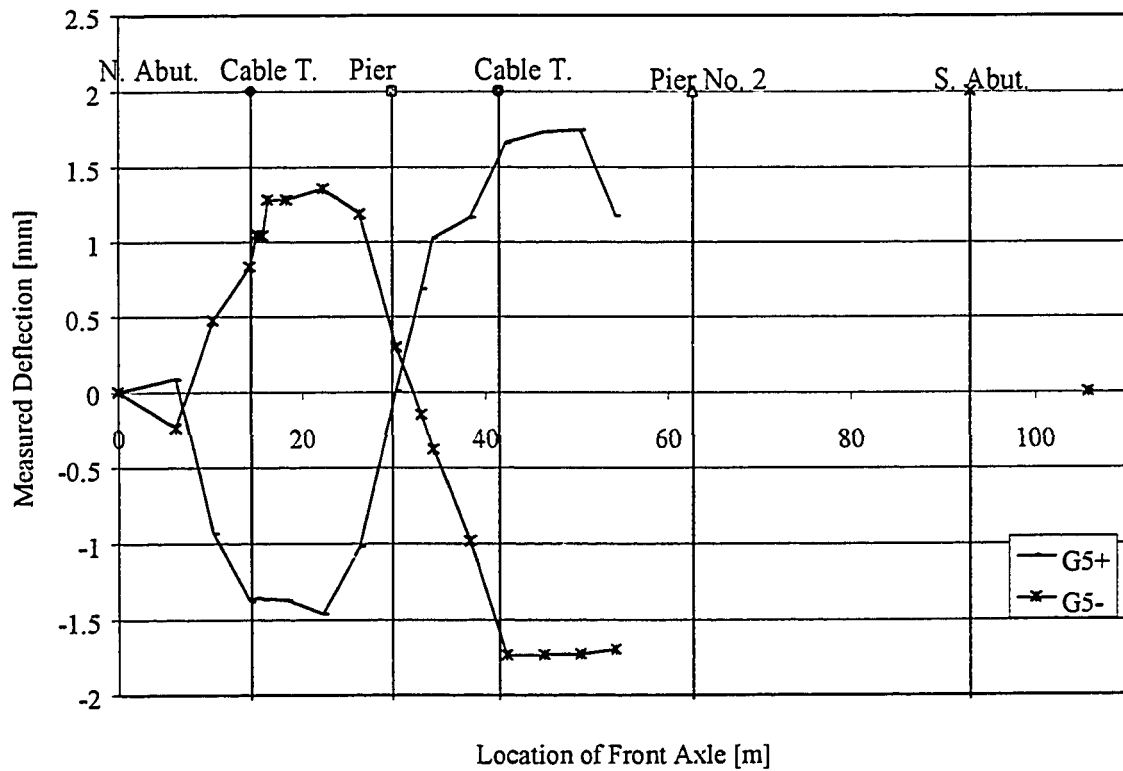


Figure B34: Static Load Test, August '98 for Cable Transducers on Girder 5

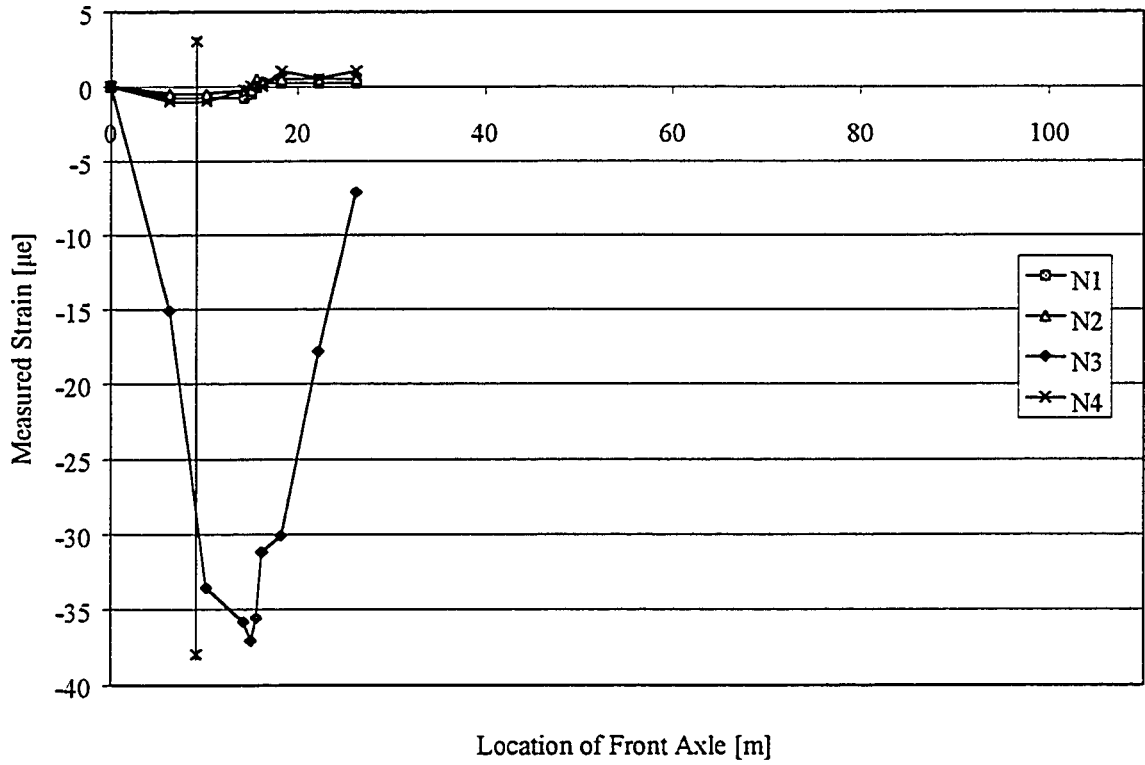


Figure B35: Static Load Test, August '98 for Gauges on NEFMAC & Stainless Bar

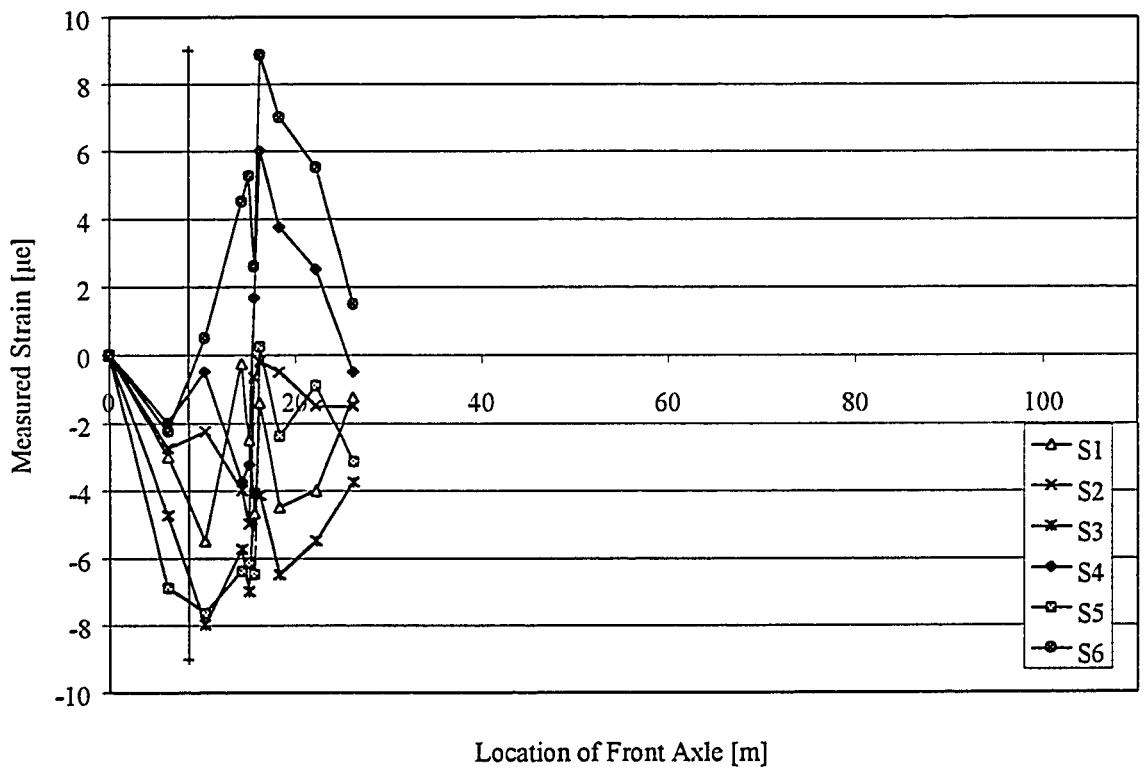


Figure B36: Static Load Test, August '98 for Gauges on Shear Stud

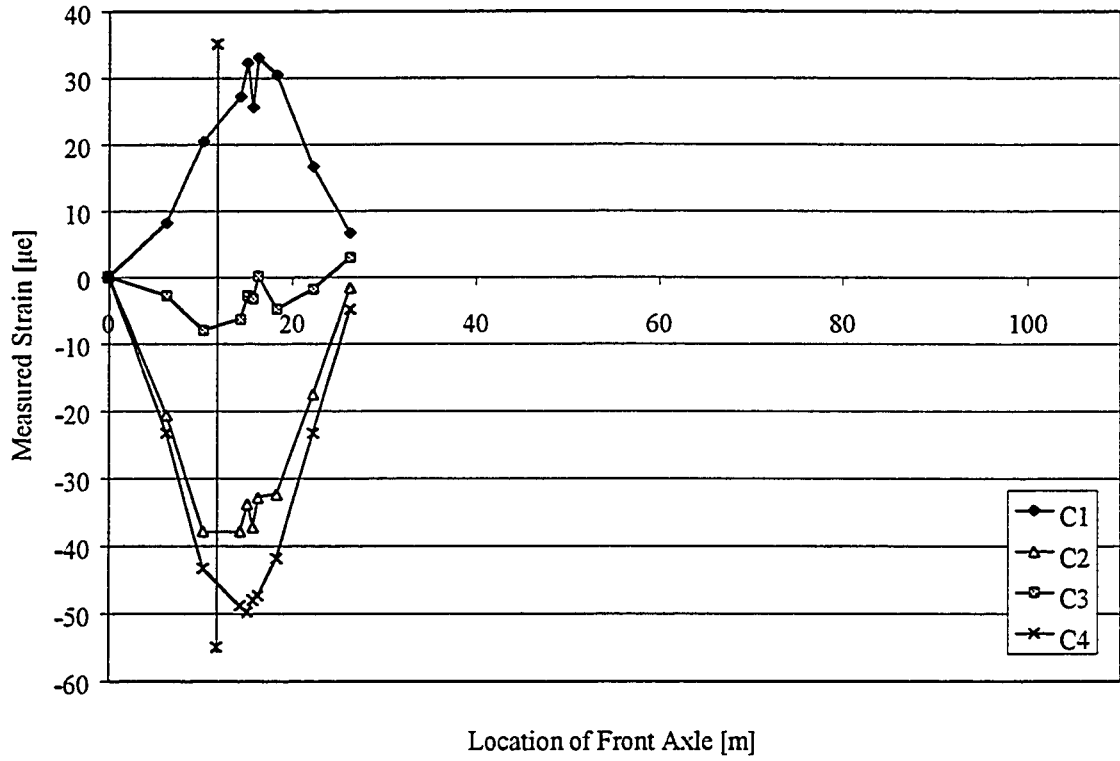


Figure B37: Static Load Test, August '98 for Gauges on Cross Frame

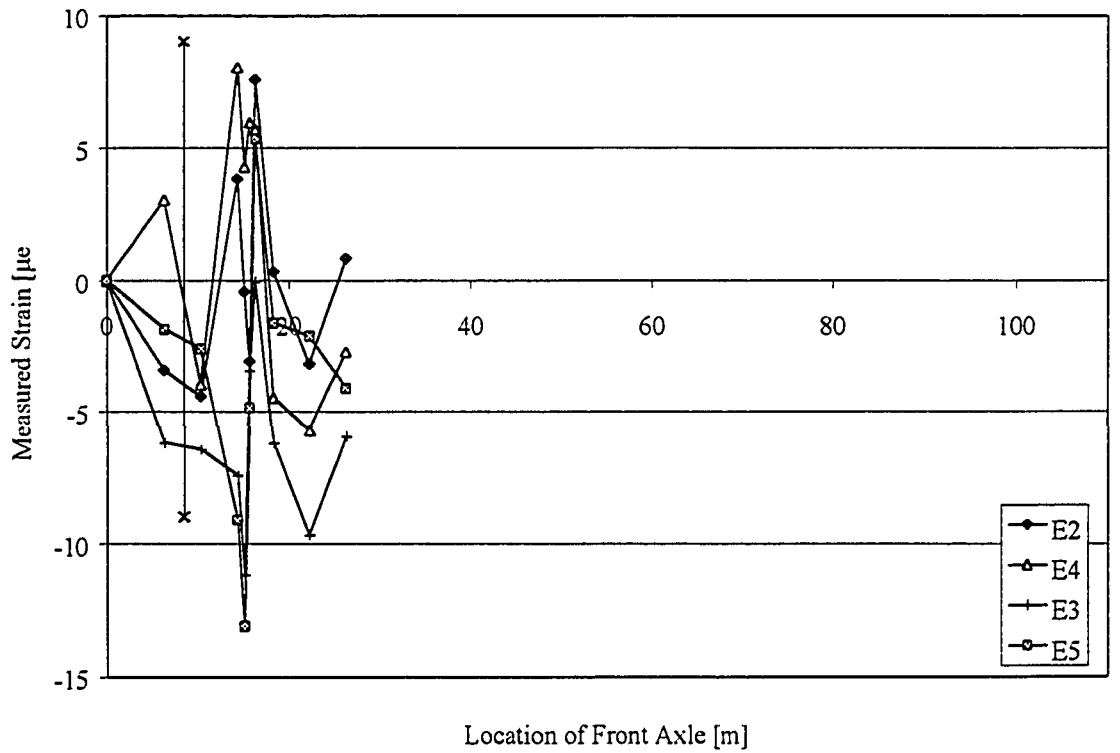


Figure B38: Static Load Test, August '98 for Embedded Concrete Gauges

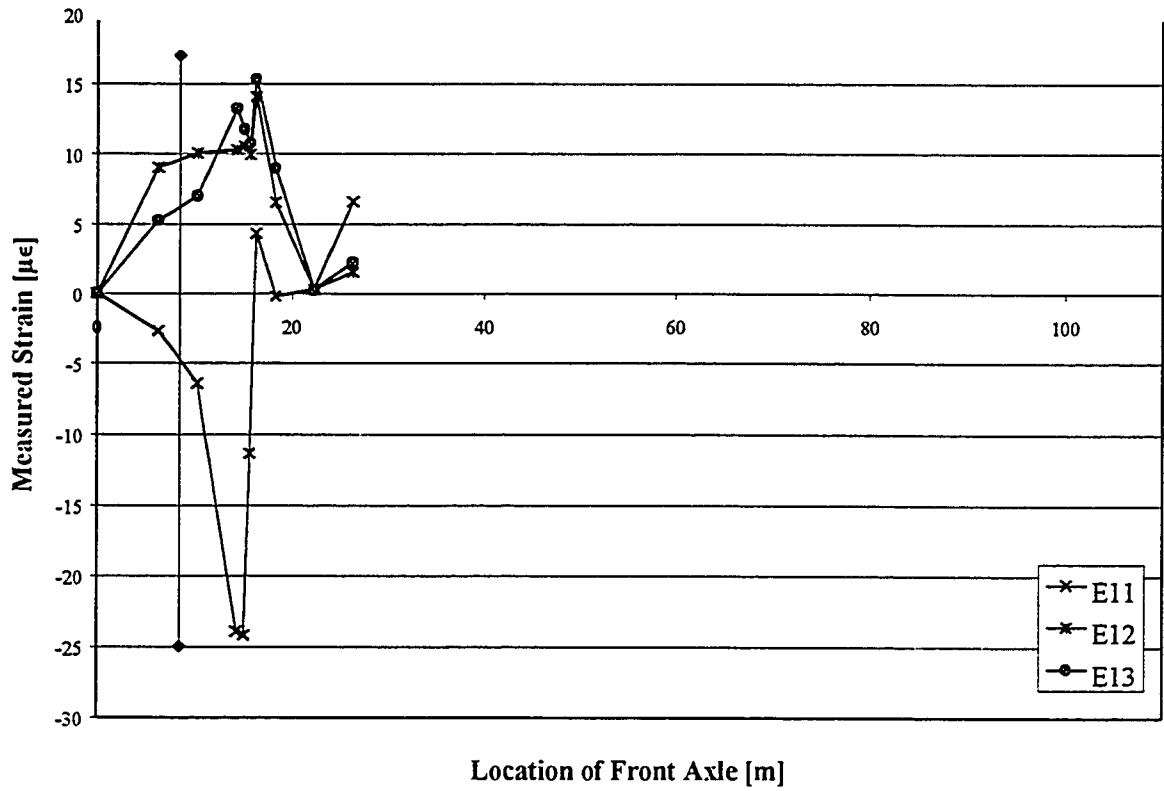


Figure B39: Static Load Test, August '98 for Embedded Concrete Strain Gauges

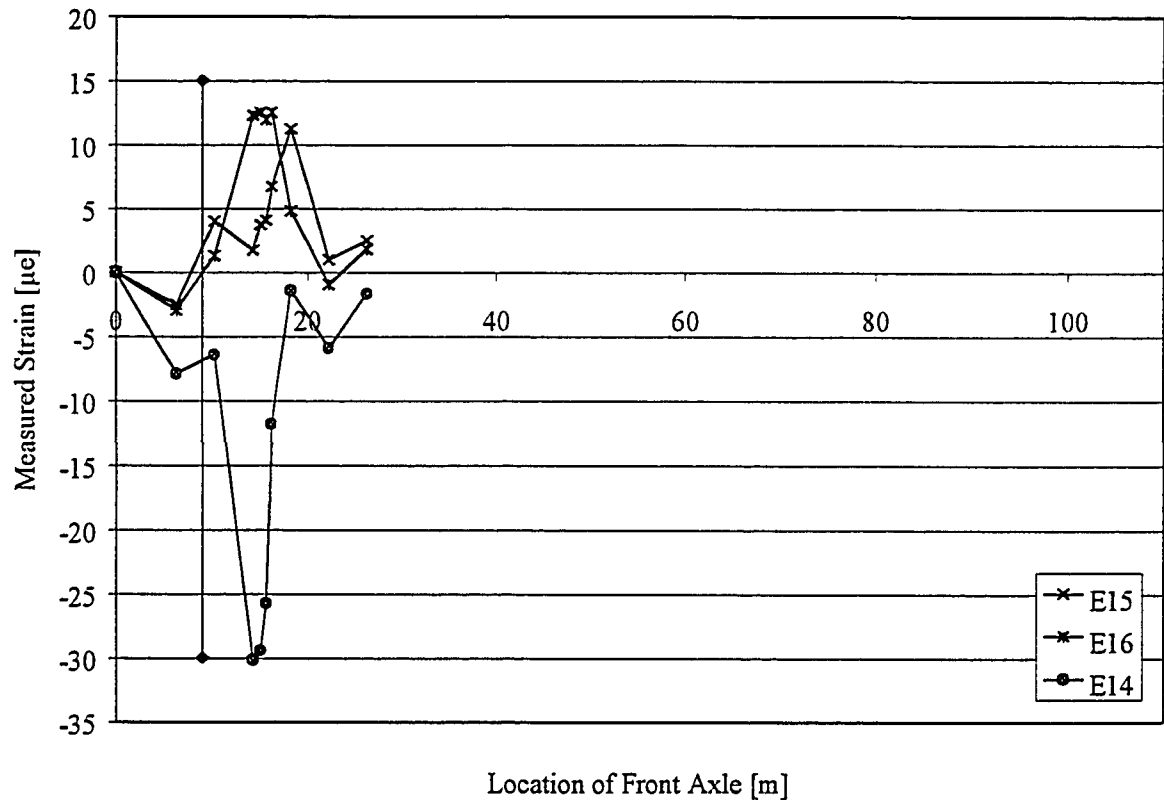


Figure B40: Static Load Test, August '98 for Embedded Concrete Strain Gauges

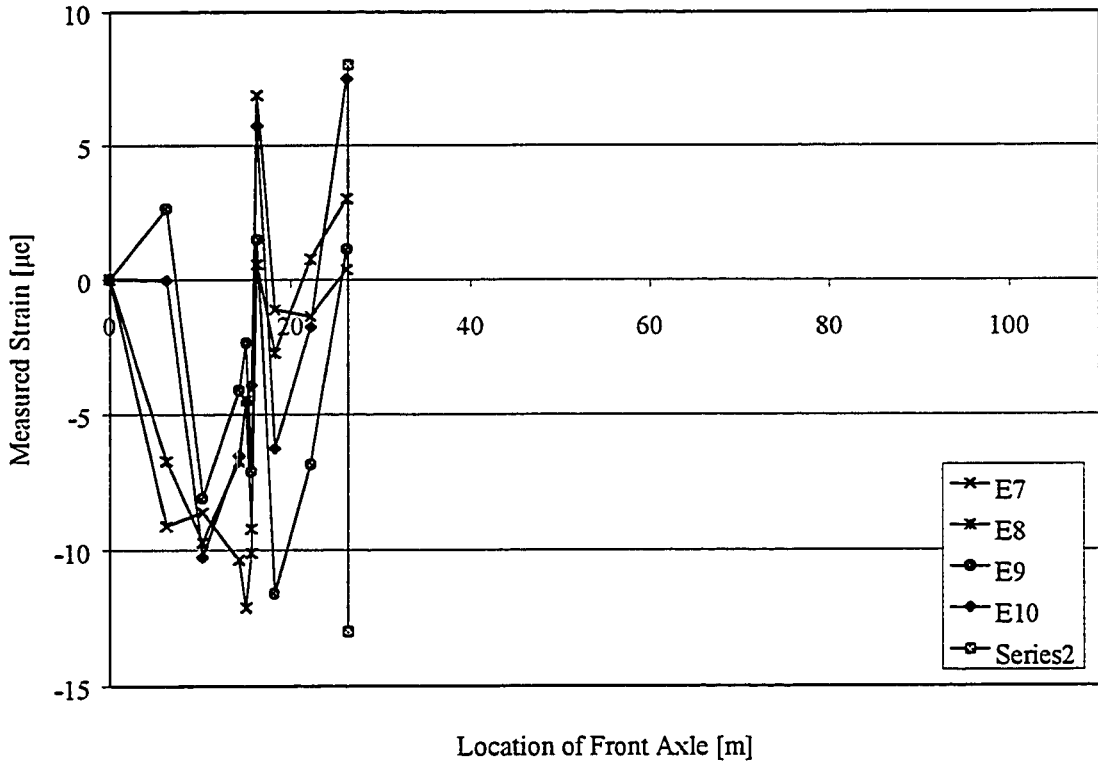


Figure B41: Static Load Test, August '98 for Embedded Concrete Strain Gauges

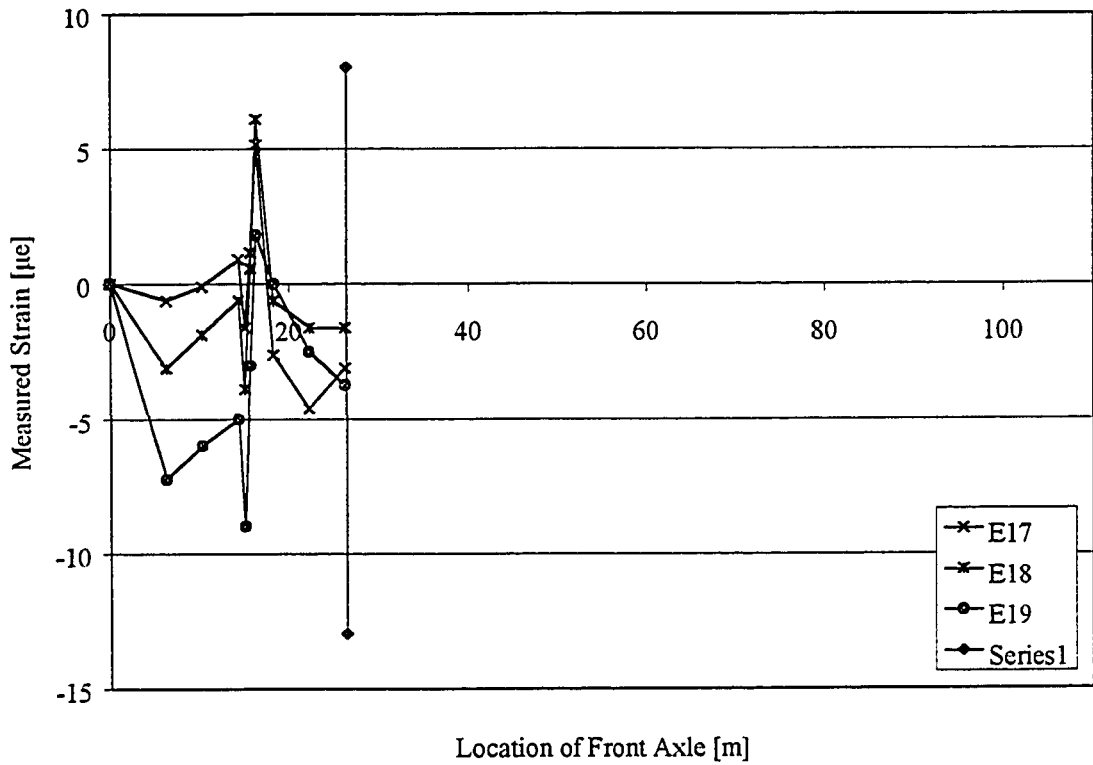


Figure B42: Static Load Test, August '98 for Embedded Concrete Strain Gauges

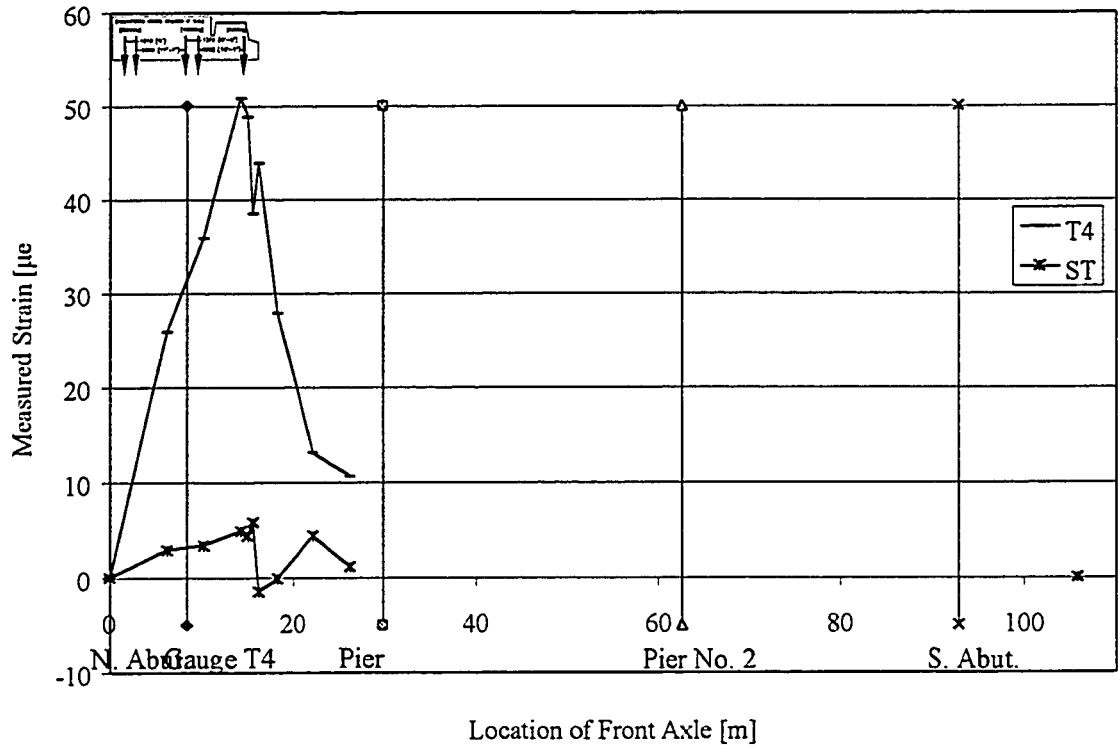


Figure B43: Static Load Test, August '98 for T4 and St Gauges

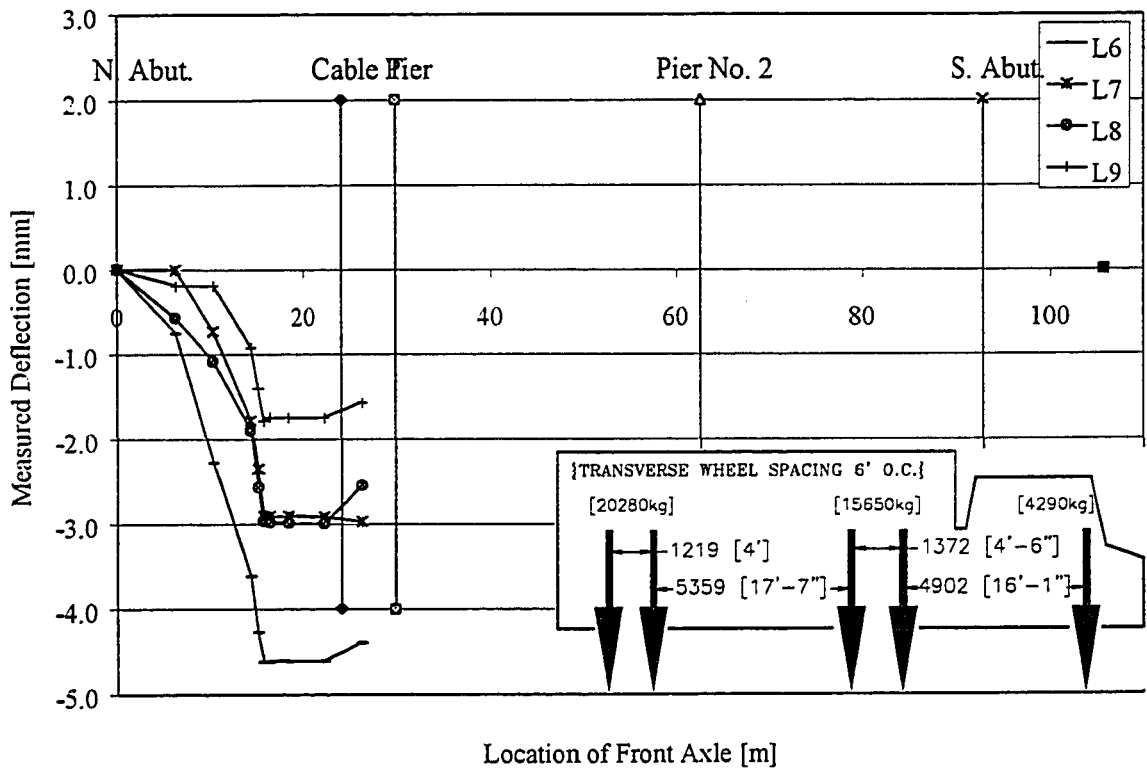


Figure B44: Static Load Test, August '98 for Cable Transducers at Strap #21

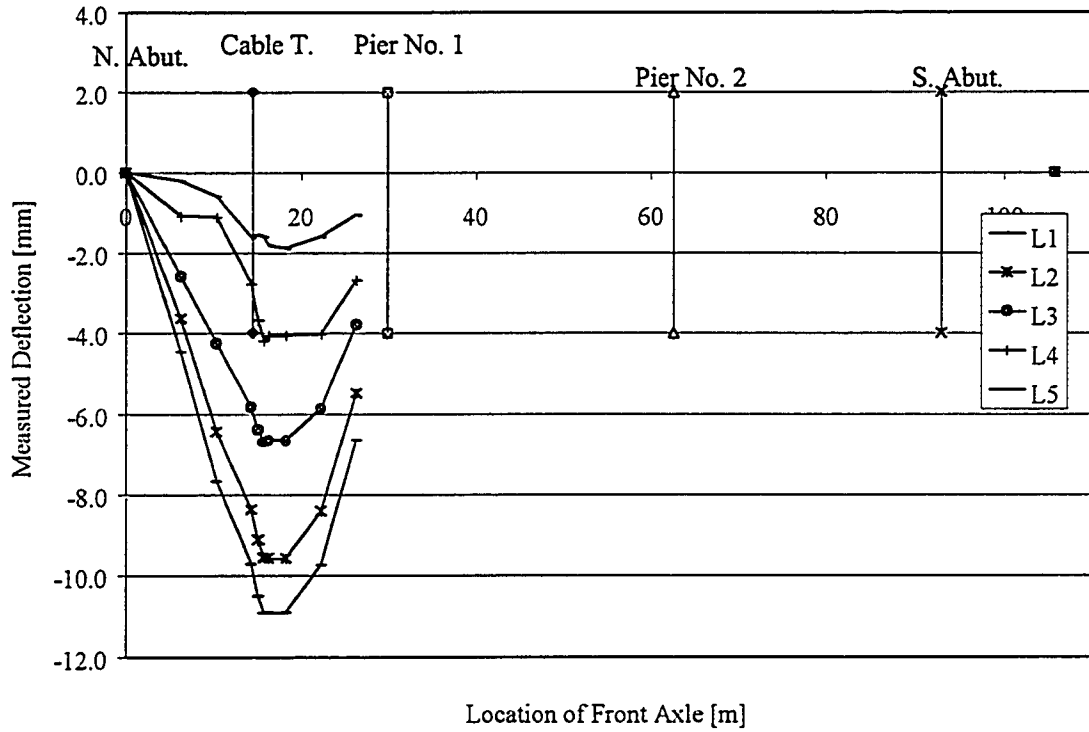


Figure B45: Static Load Test, August '98 for Cable Transducers at Strap #13

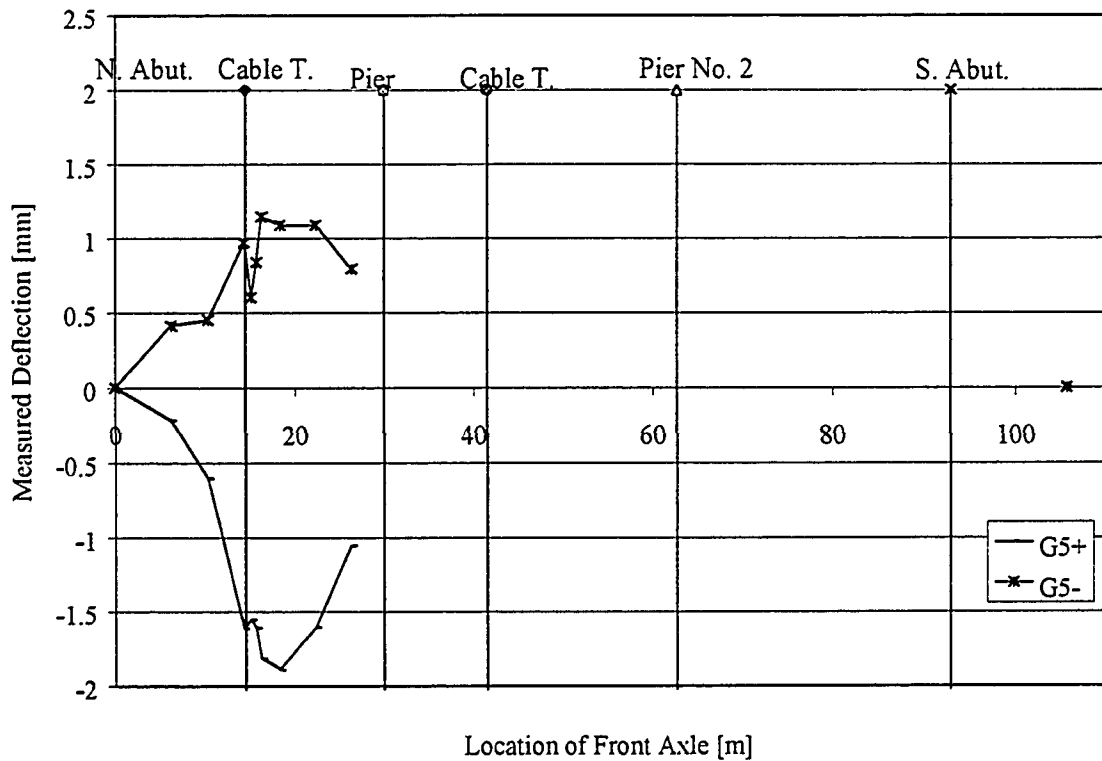


Figure B46: Static Load Test, August '98 for Two Cable Transducers on Girder 5

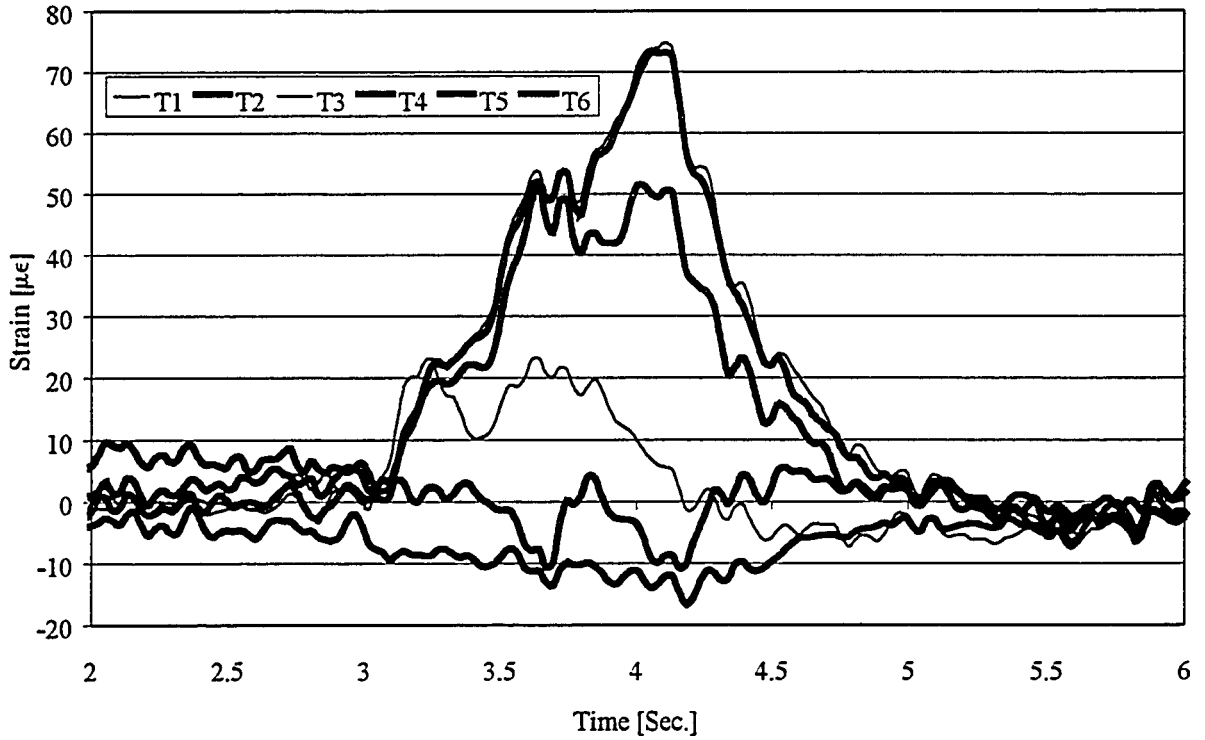


Figure B47: 55 km/hr Test, August '98 for Strap #8 in Positive Moment Region

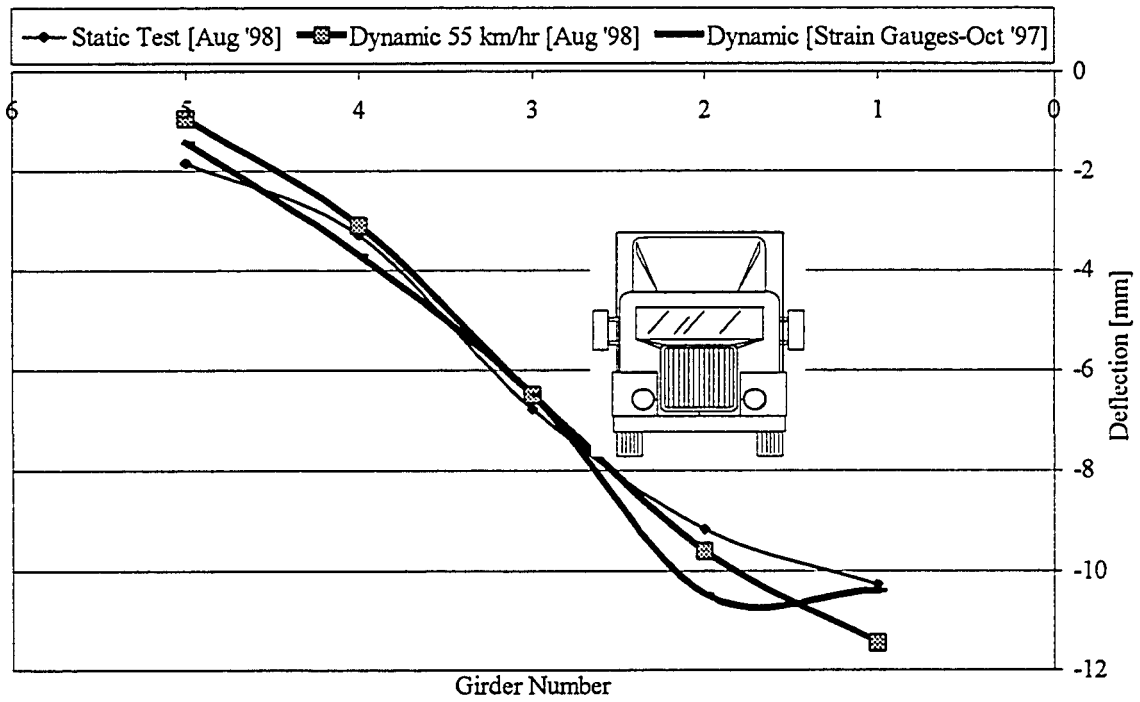


Figure B48: Comparison of Load Sharing in the Positive Moment Region

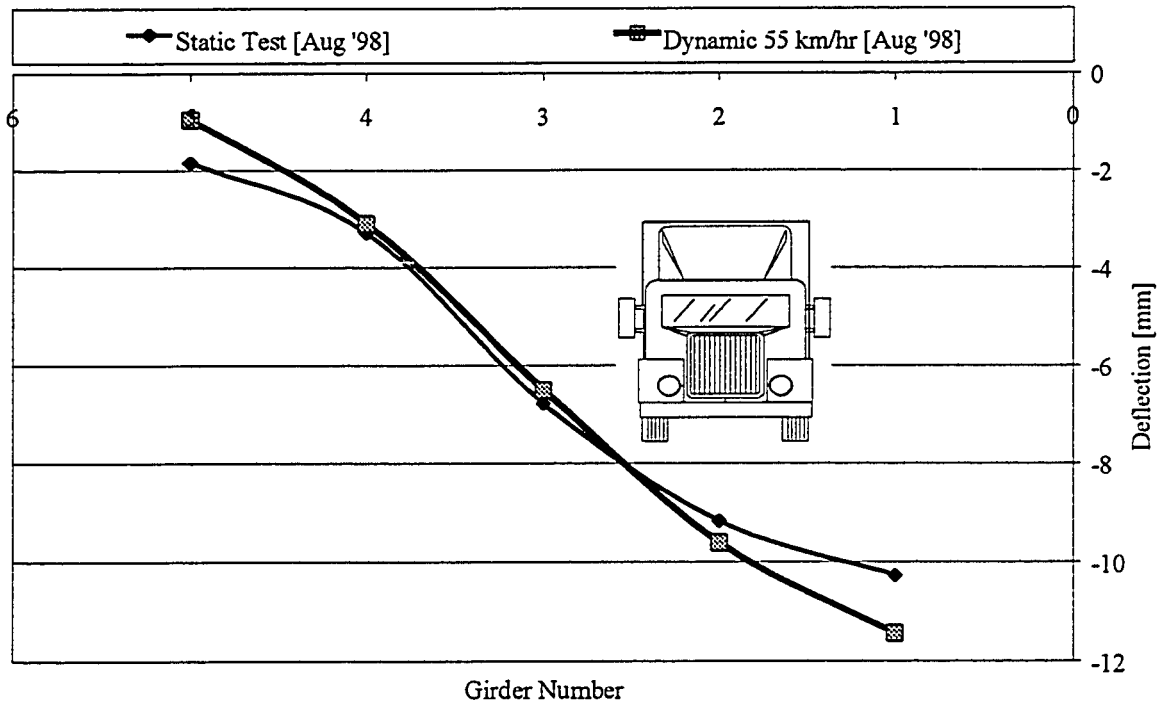


Figure B49: Comparison of Load Sharing in the Positive Moment Region

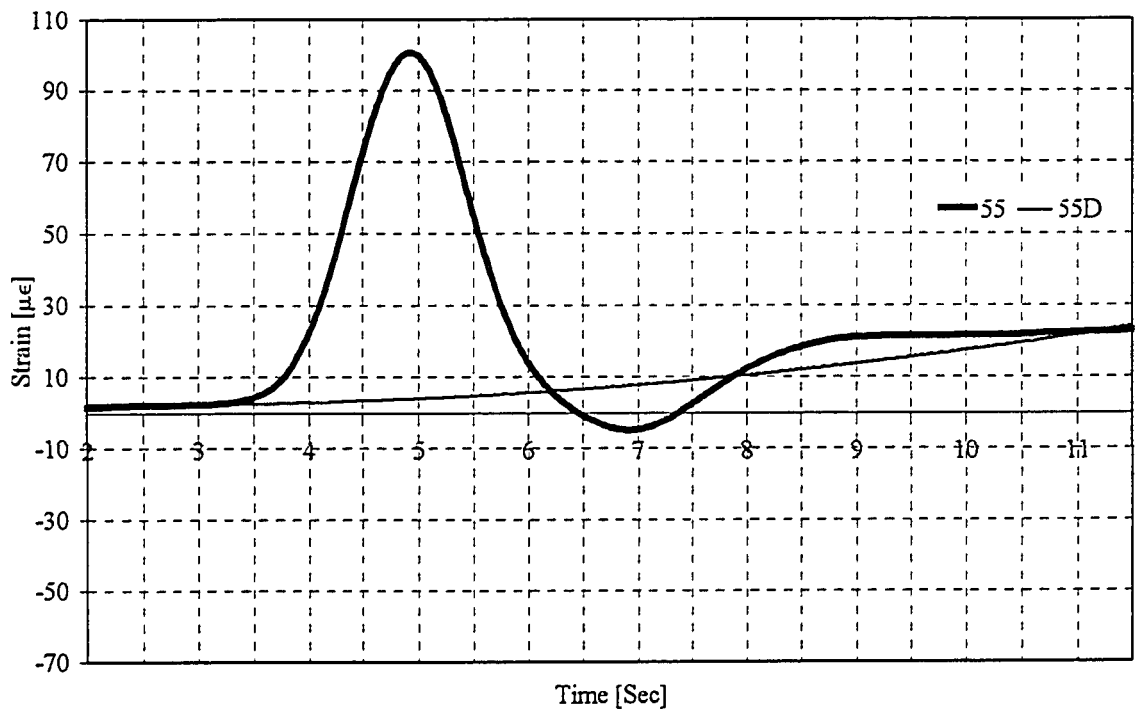


Figure B50: 55 km/hr Test, August '98 for Gauge G3

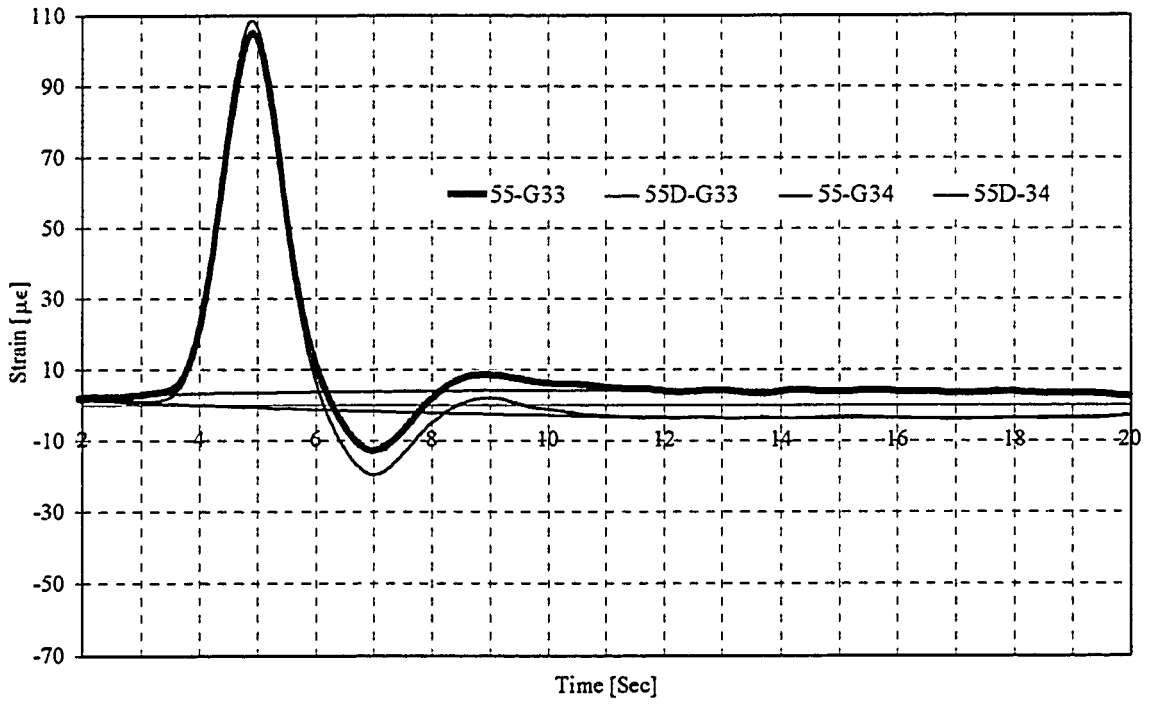


Figure B51: 55 km/hr Test, August '98 for Gauge G33 & G34

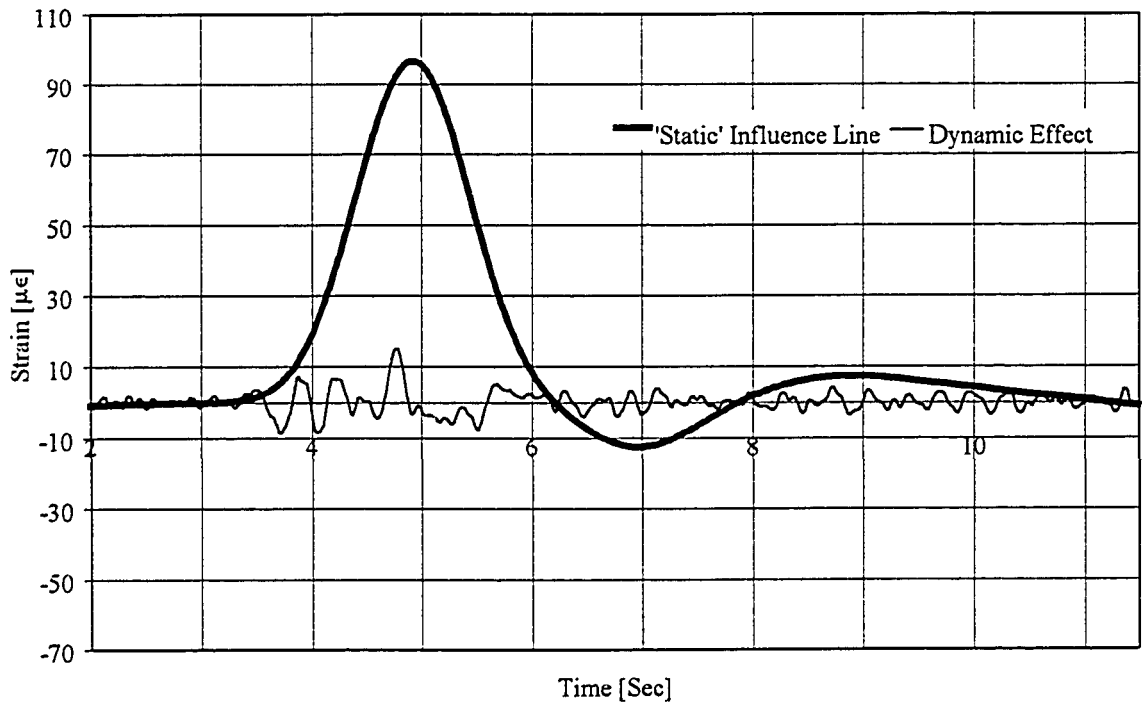


Figure B52: 55 km/hr Test, August '98 for Gauge G3 Filtered Data

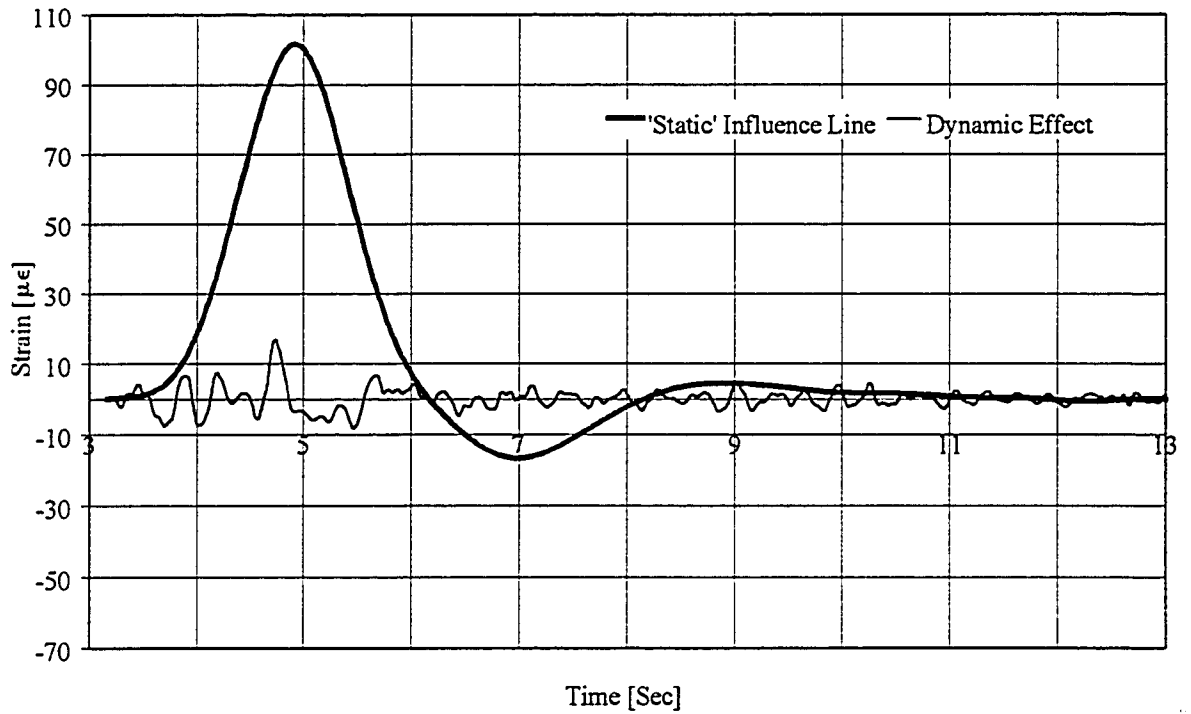


Figure B53: 55 km/hr Test, August '98 for Gauge G33 Filtered Data

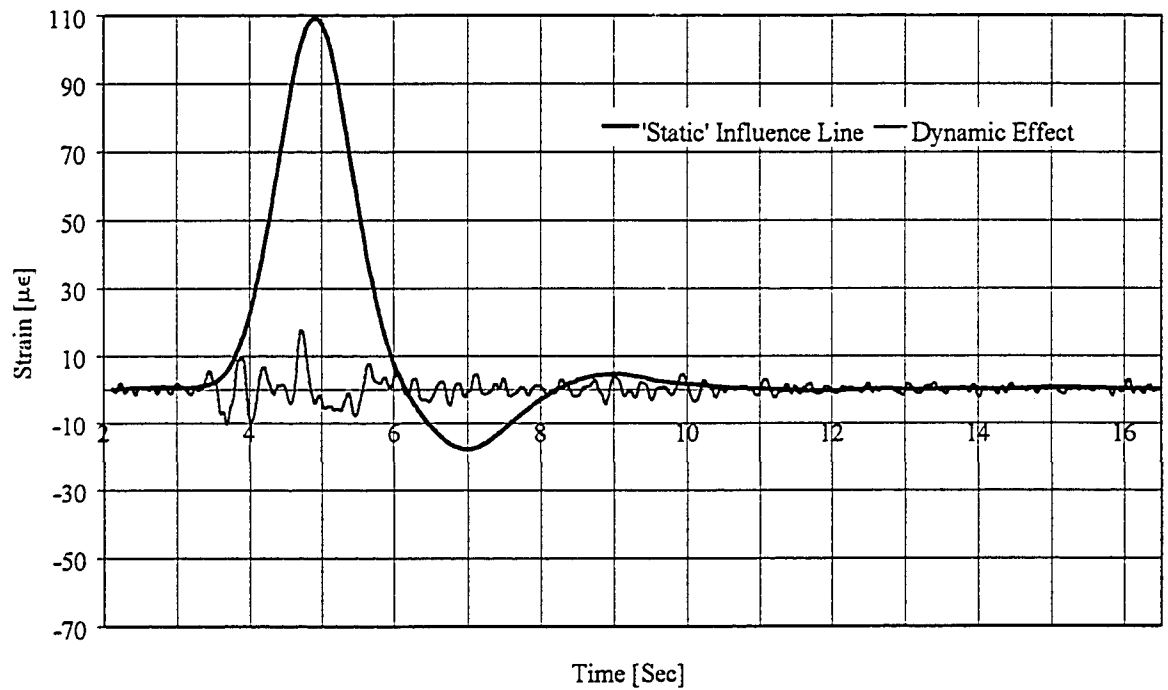


Figure B54: 55 km/hr Test, August '98 for Gauge G34 Filtered Data

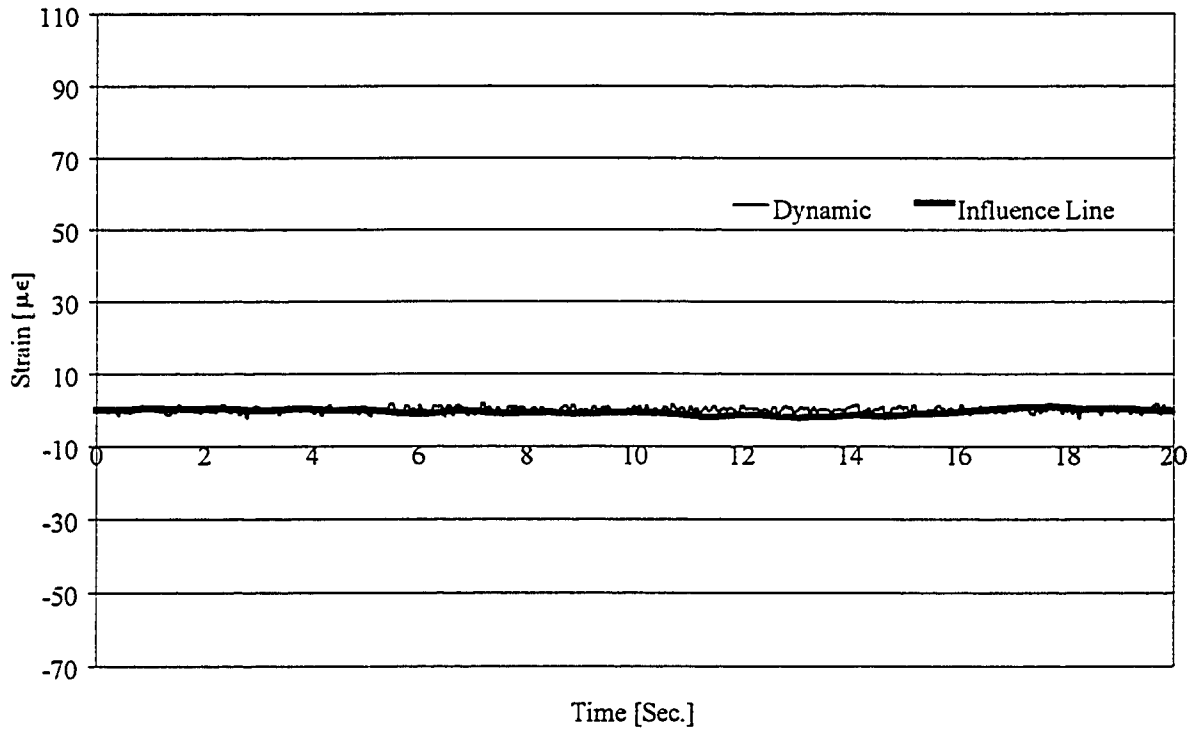


Figure B55: 55 km/hr Test, August '98 for Gauge ST Filtered Data

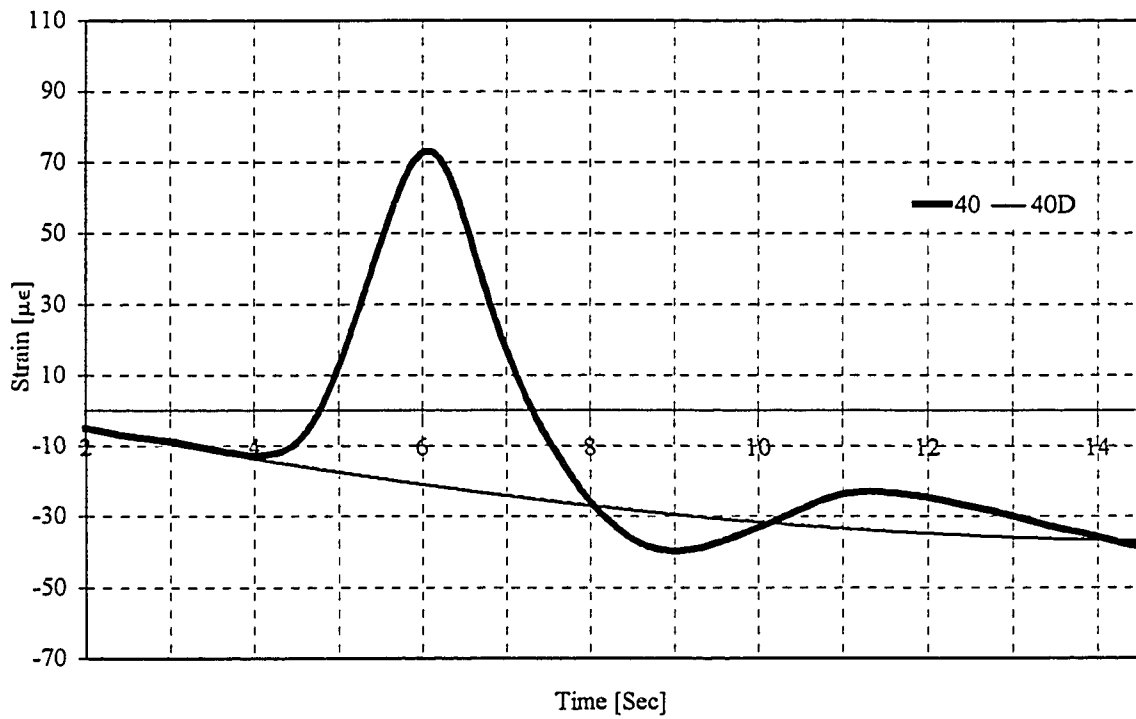


Figure B56: 40 km/hr Test, August '98 for Gauge G3 Filtered Data

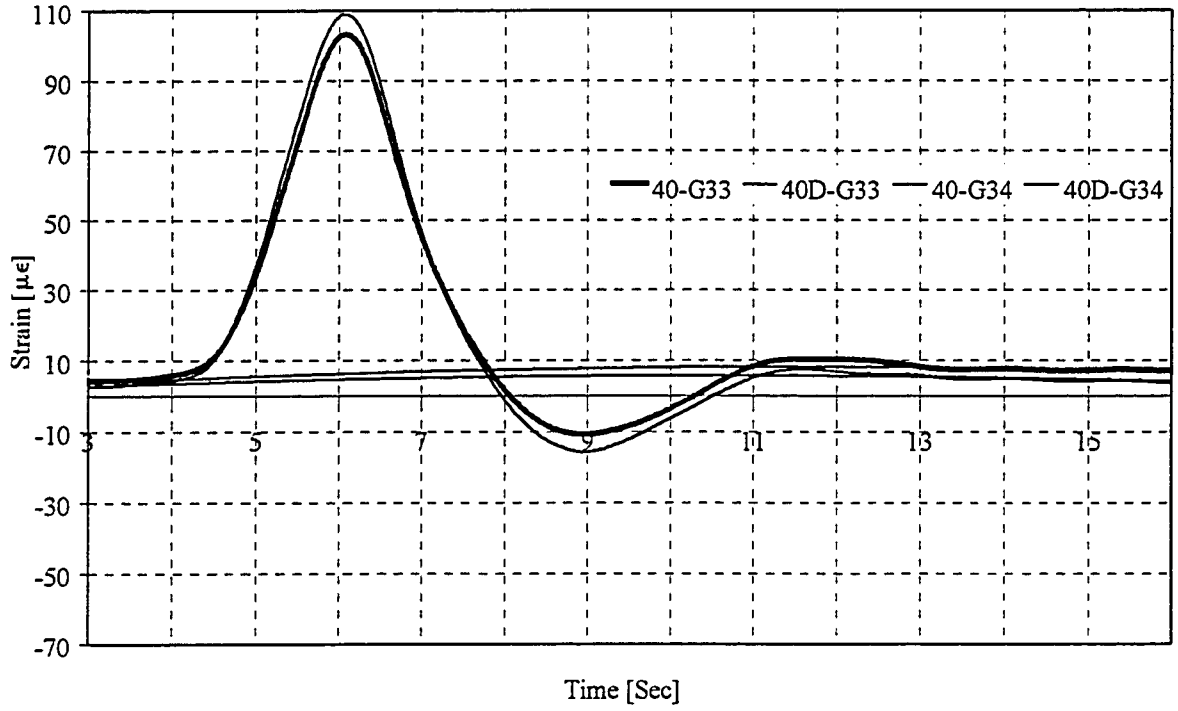


Figure B57: 40 km/hr Test, August '98 for Gauge G33 & G34 Filtered Data

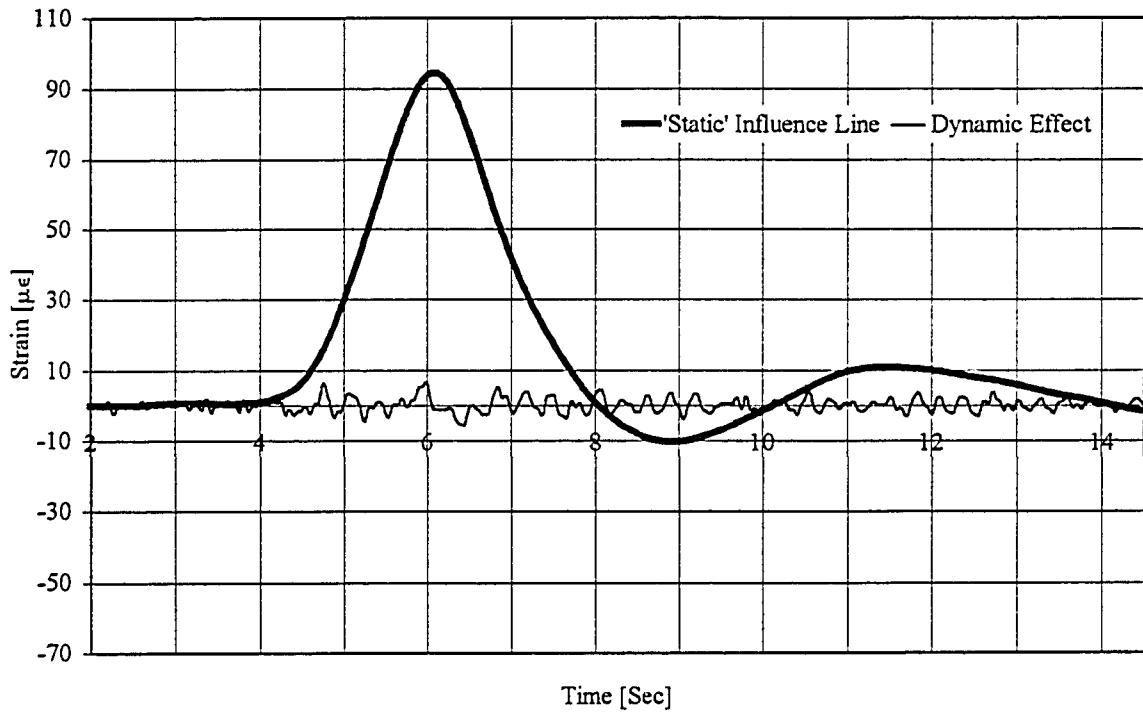


Figure B58: 40 km/hr Test, August '98 for Gauge G3 Filtered Data

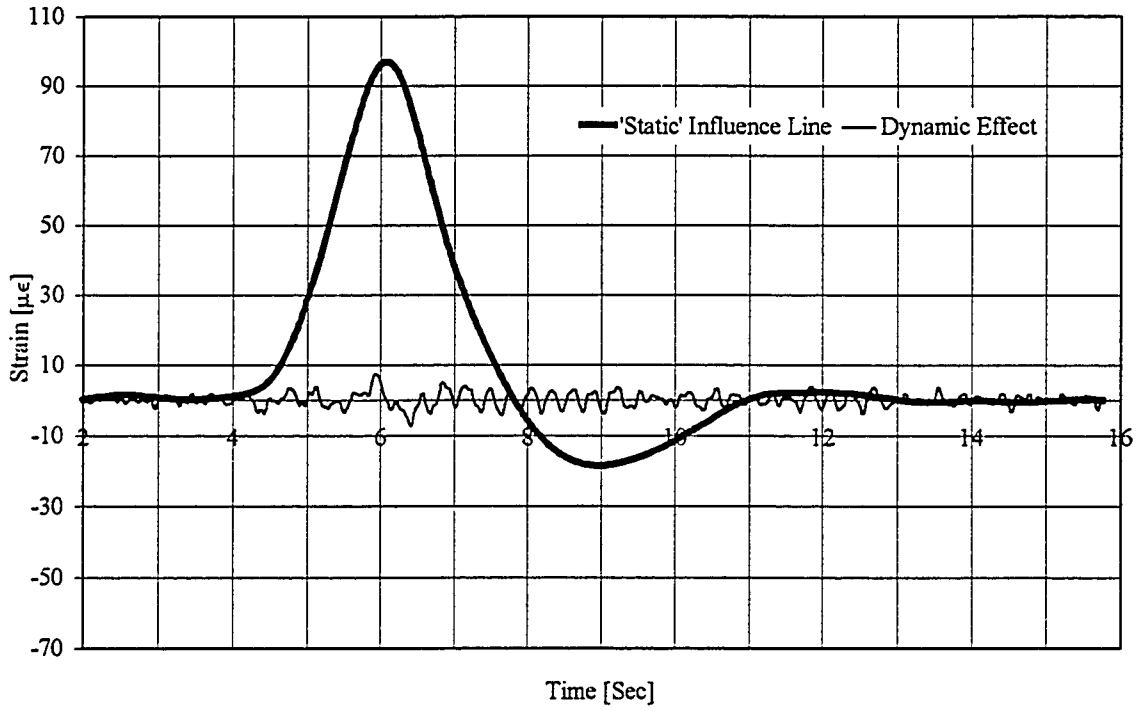


Figure B59: 40 km/hr Test, August '98 for Gauge G33 Filtered Data

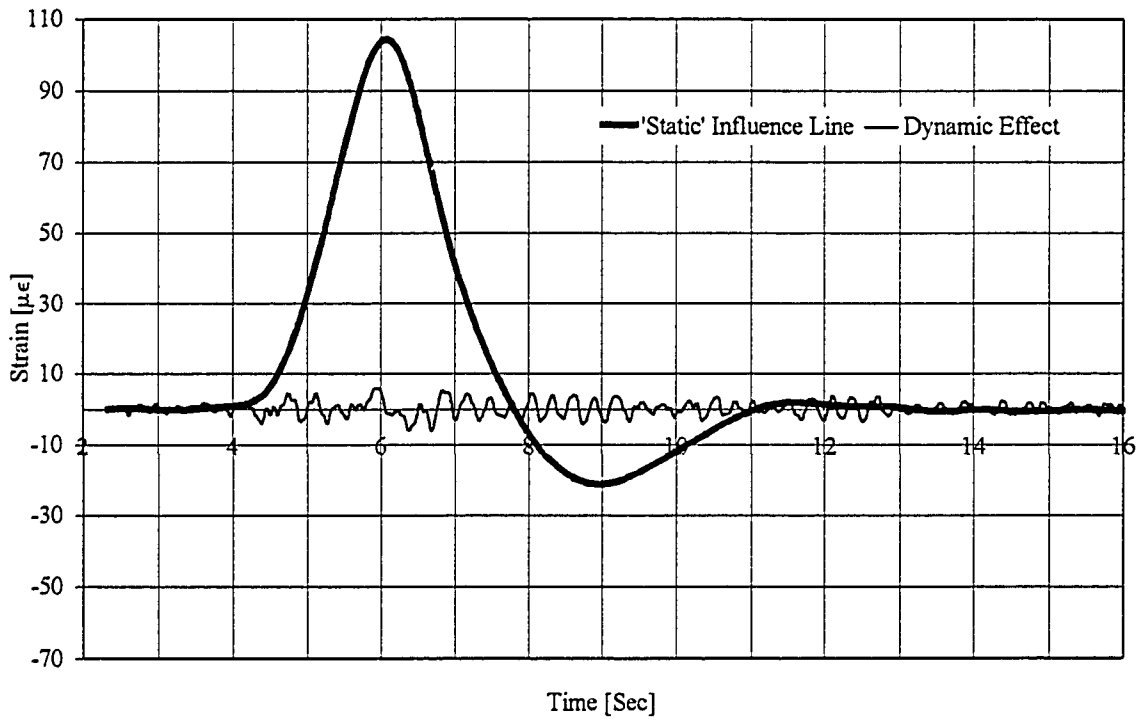


Figure B60: 40 km/hr Test, August '98 for Gauge G34 Filtered Data

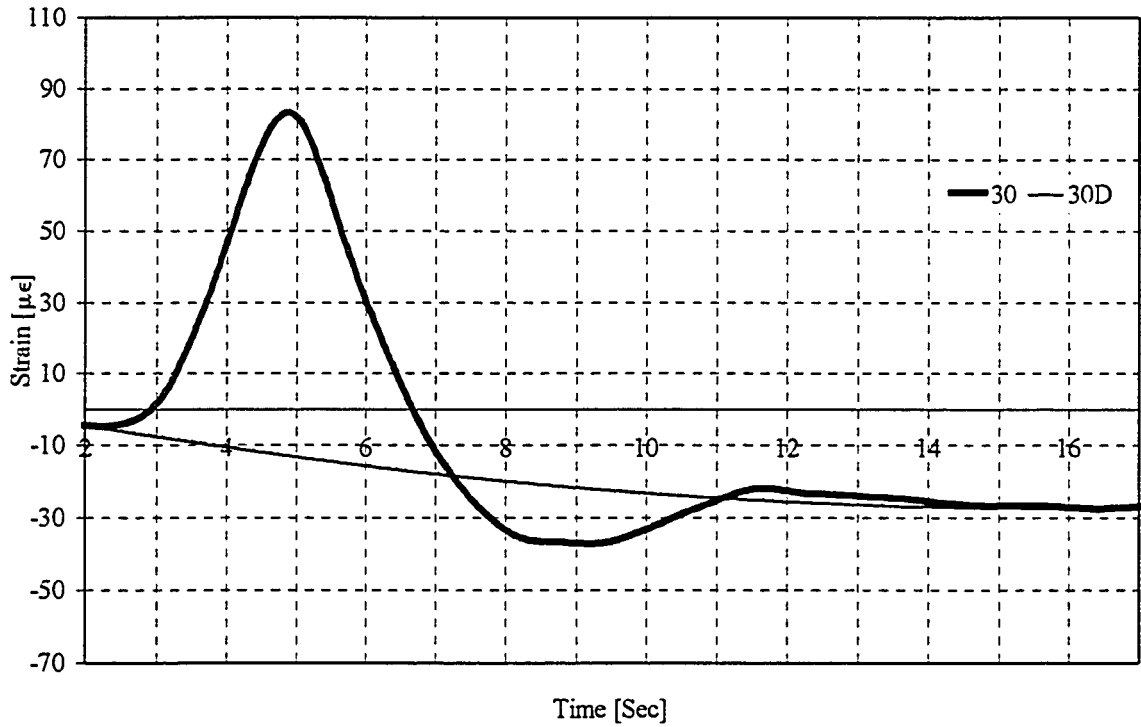


Figure B61: 30 km/hr Test, August '98 for Gauge G3 Filtered Data

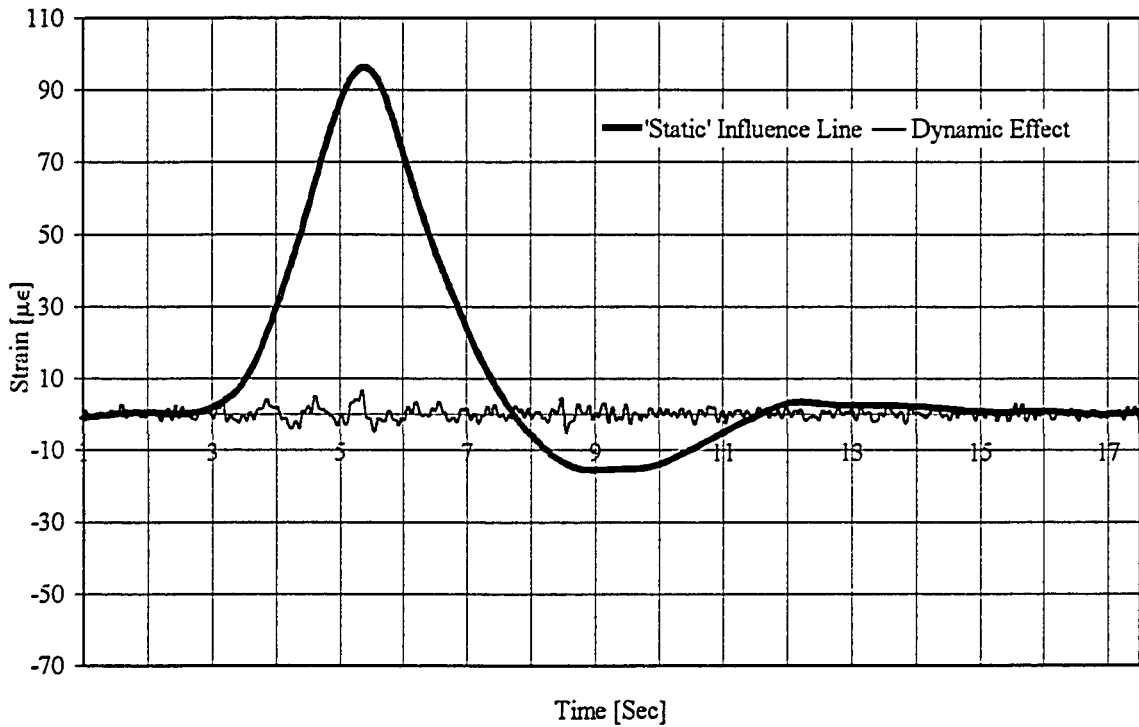


Figure B62: 30 km/hr Test, August '98 for Gauge G3 Filtered Data

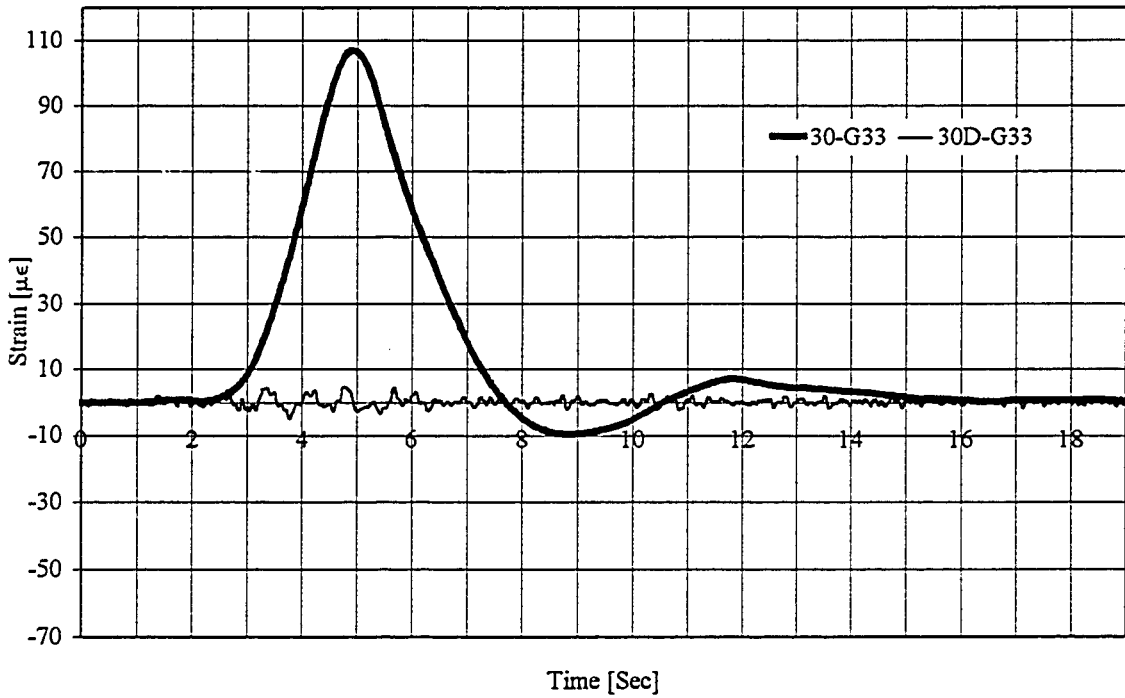


Figure B63: 30 km/hr Test, August '98 for Gauge G33 Filtered Data

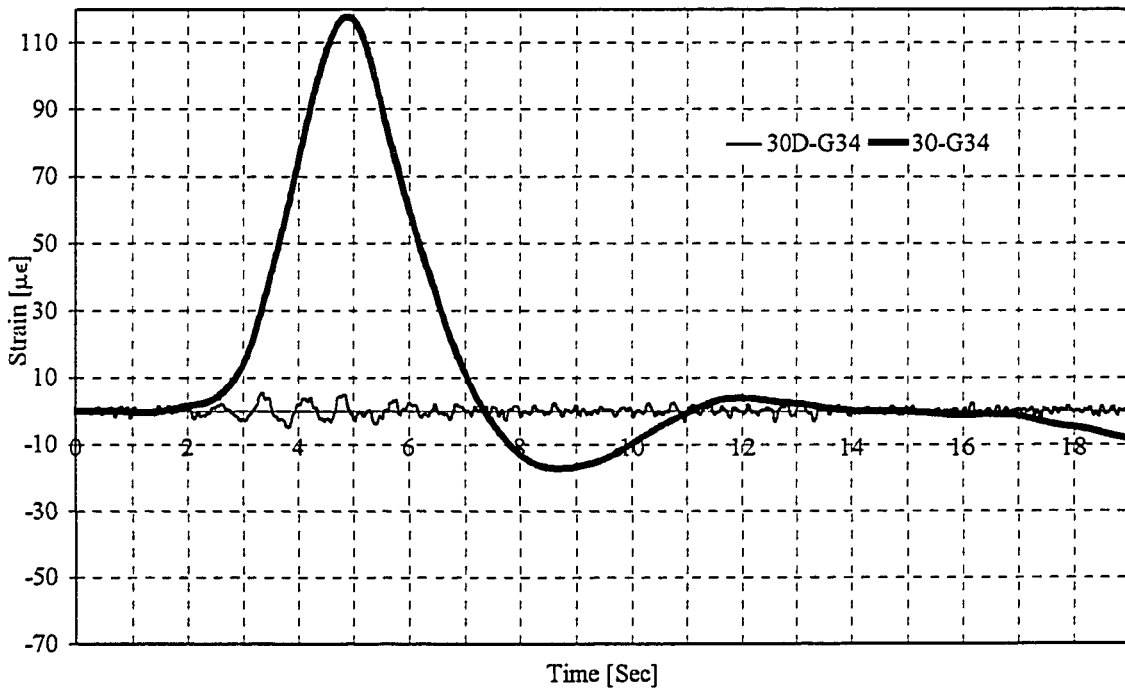


Figure B64: 30 km/hr Test, August '98 for Gauge G33 & G34 Filtered Data

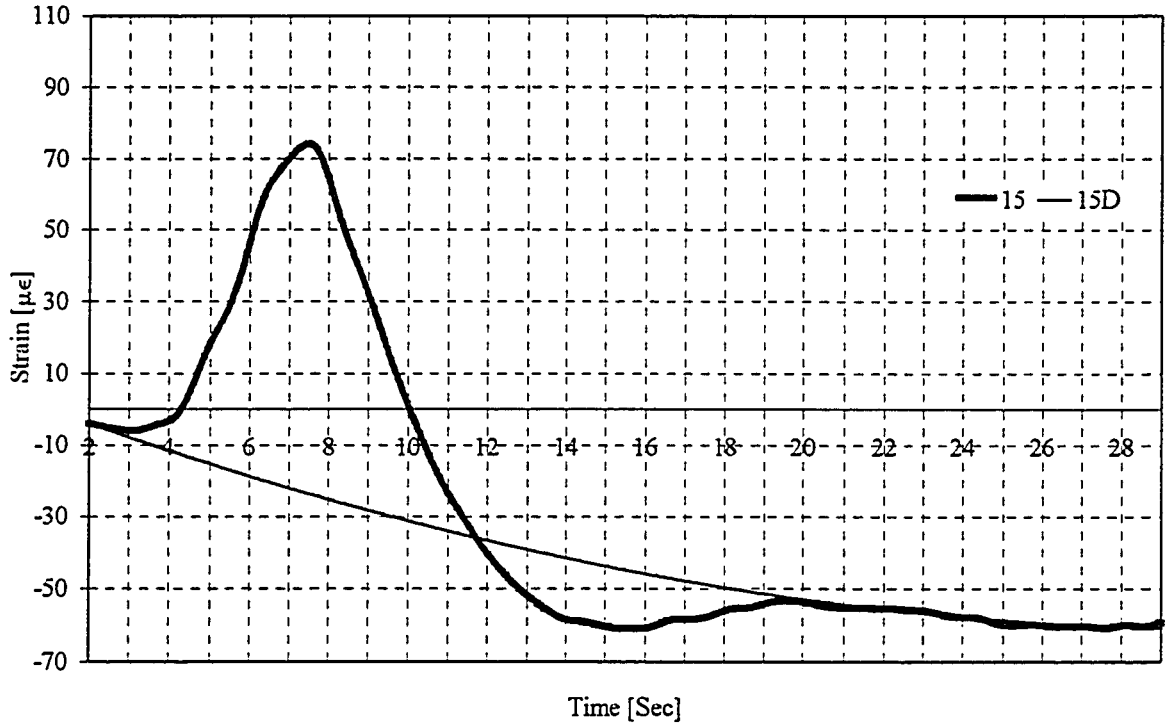


Figure B65: 15 km/hr Test, August '98 for Gauge G3 Filtered Data

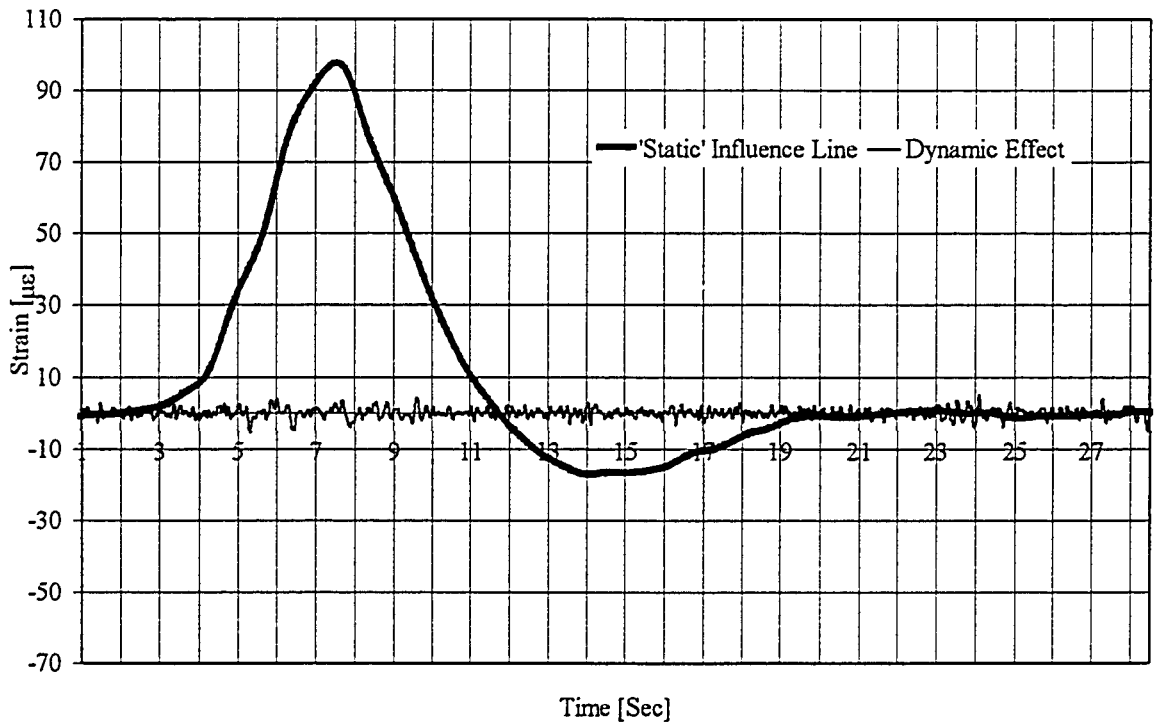


Figure B66: 15 km/hr Test, August '98 for Gauge G3 Filtered Data

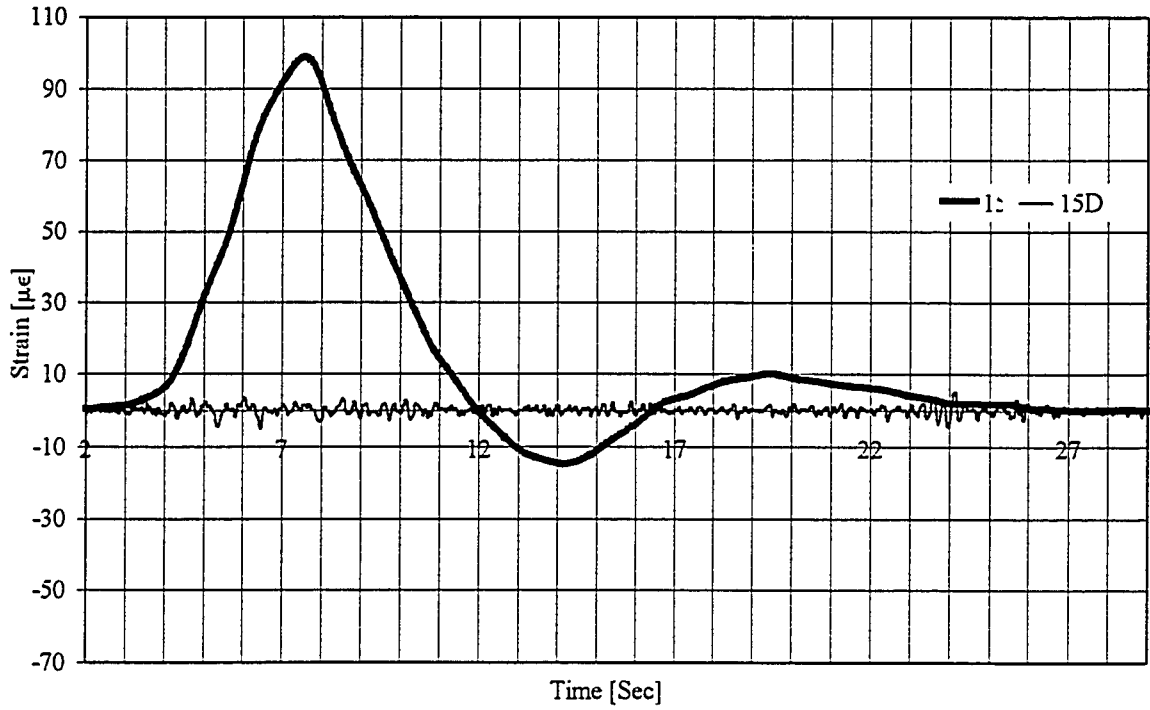


Figure B67: 15 km/hr Test, August '98 for Gauge G33 Filtered Data

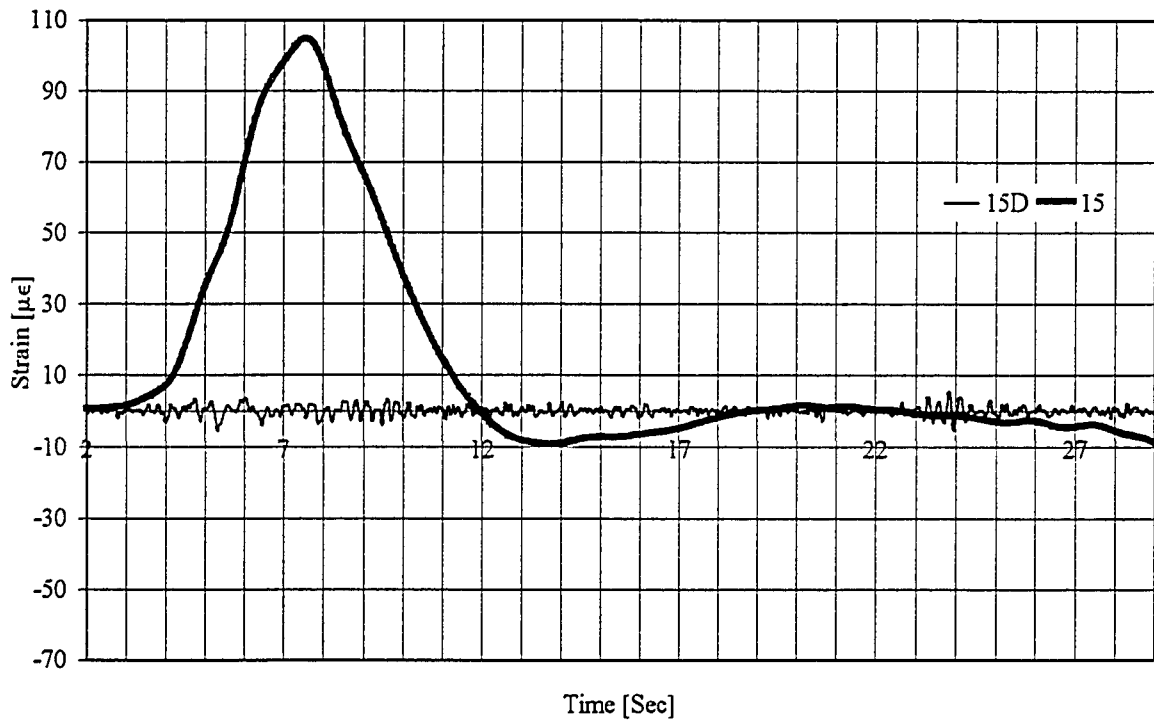


Figure B68: 15 km/hr Test, August '98 for Gauge G34 Filtered Data

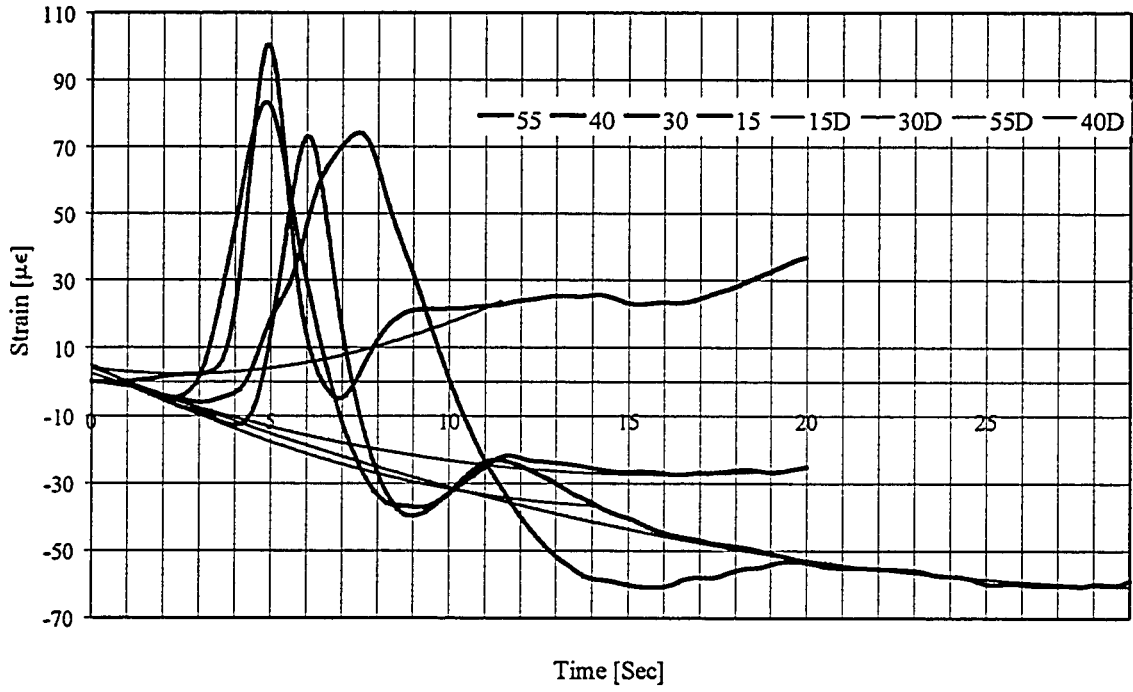


Figure B69: All Four Test Speeds, August '98 for Gauge G3 Filtered Data

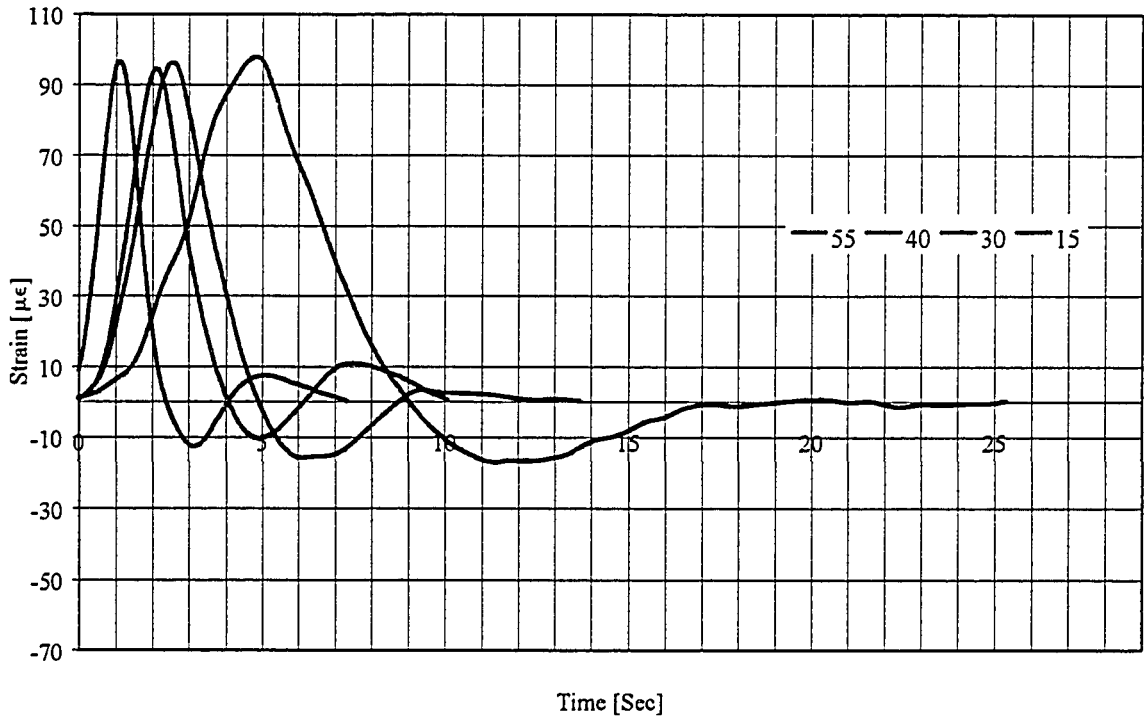


Figure B70: All Four Test Speeds, August '98 for Gauge G3 Filtered Data

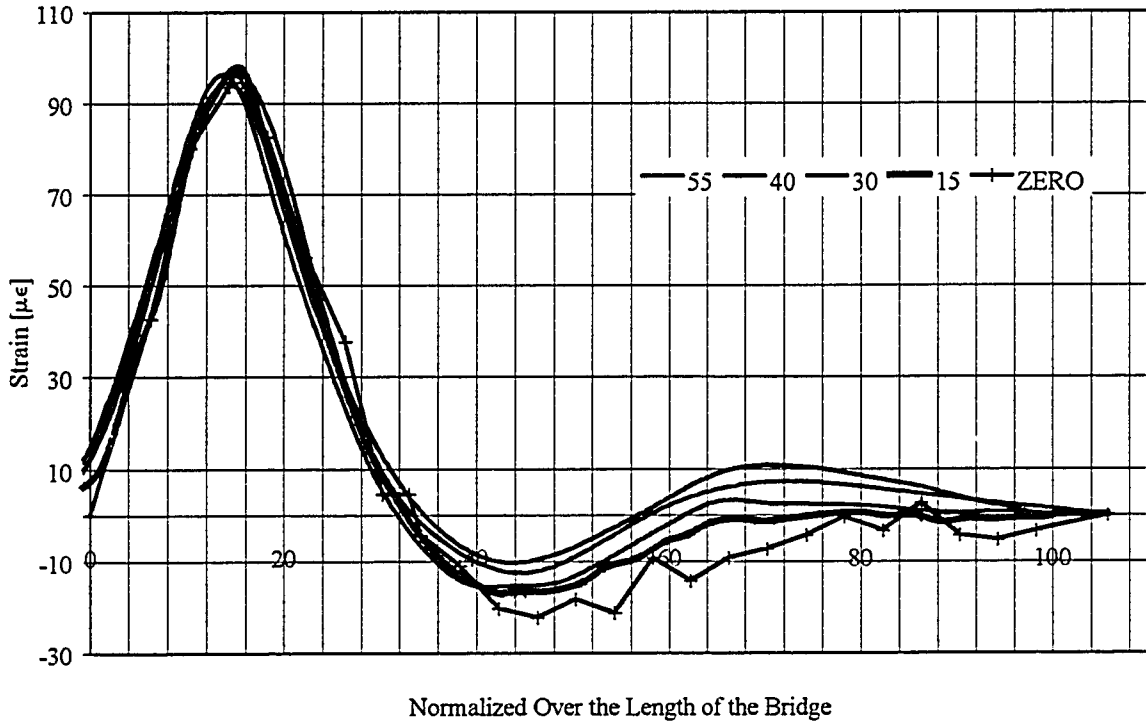


Figure B71: All Four Test Speeds, August '98 for Gauge G3 Filtered Data Superimposed

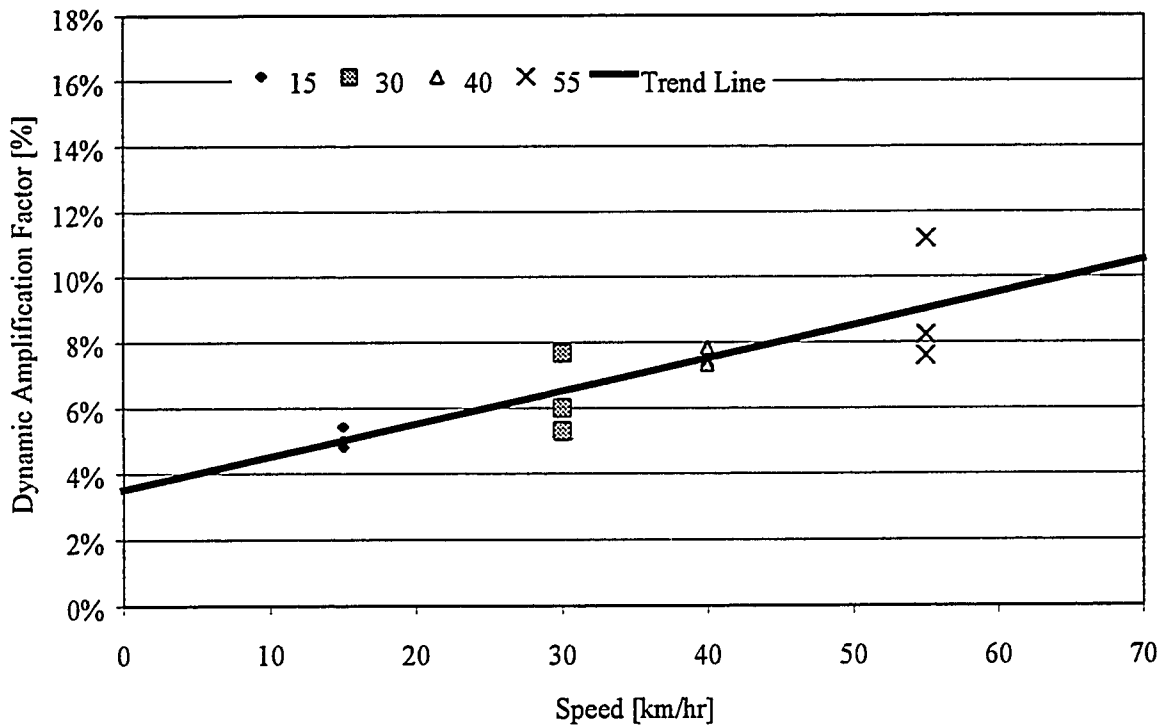


Figure B72: Dynamic Amplification Factor versus Speeds from Cable Transducers

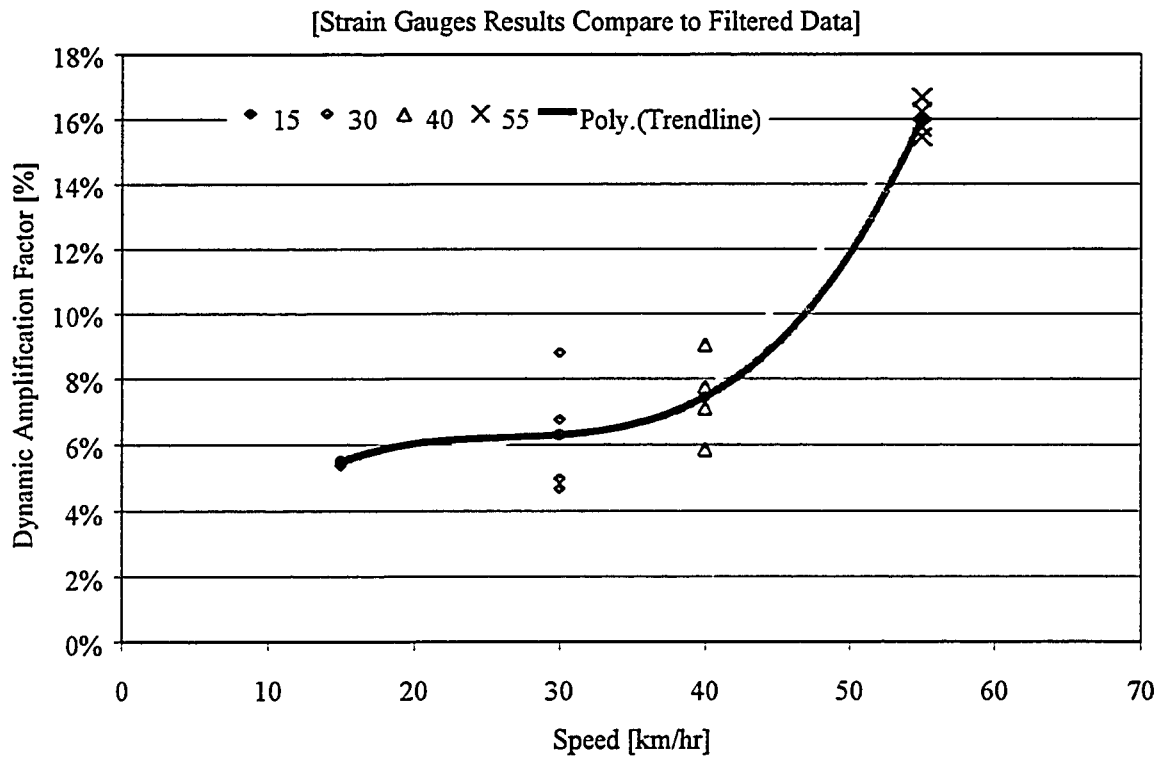


Figure B73: Dynamic Amplification Factor versus Speeds from Strain Gauges

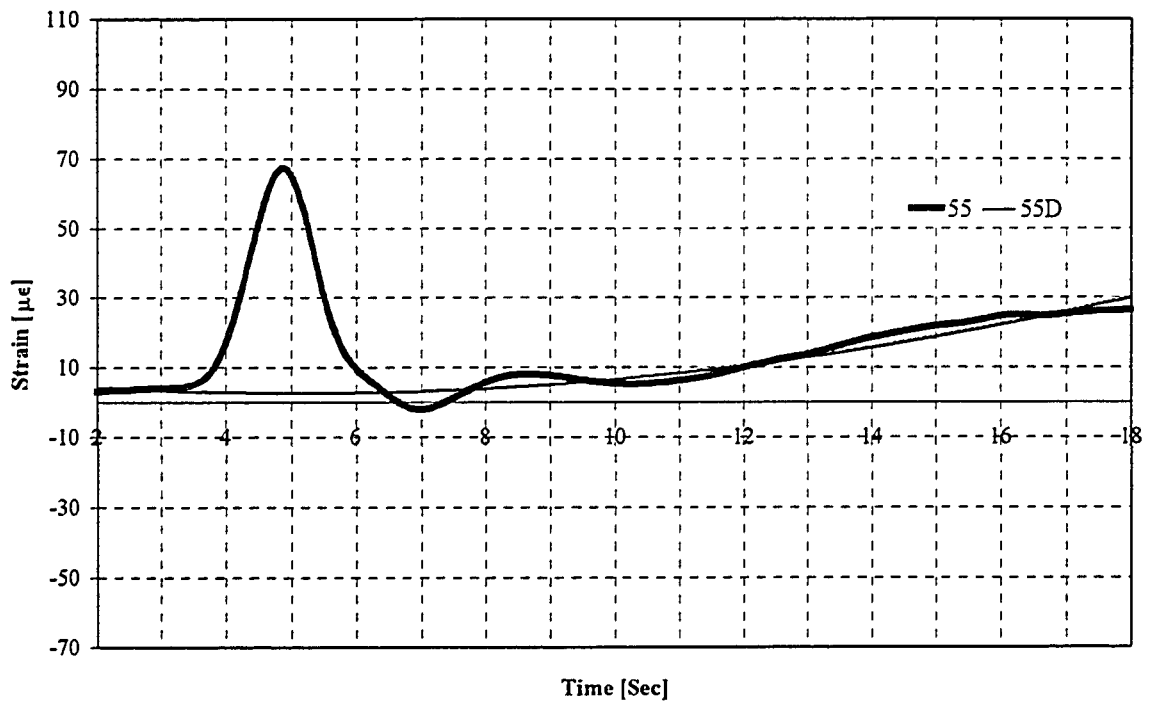


Figure B74: 55 km/hr Test, August '98 for Gauge #6 Before Corrected for Drifts

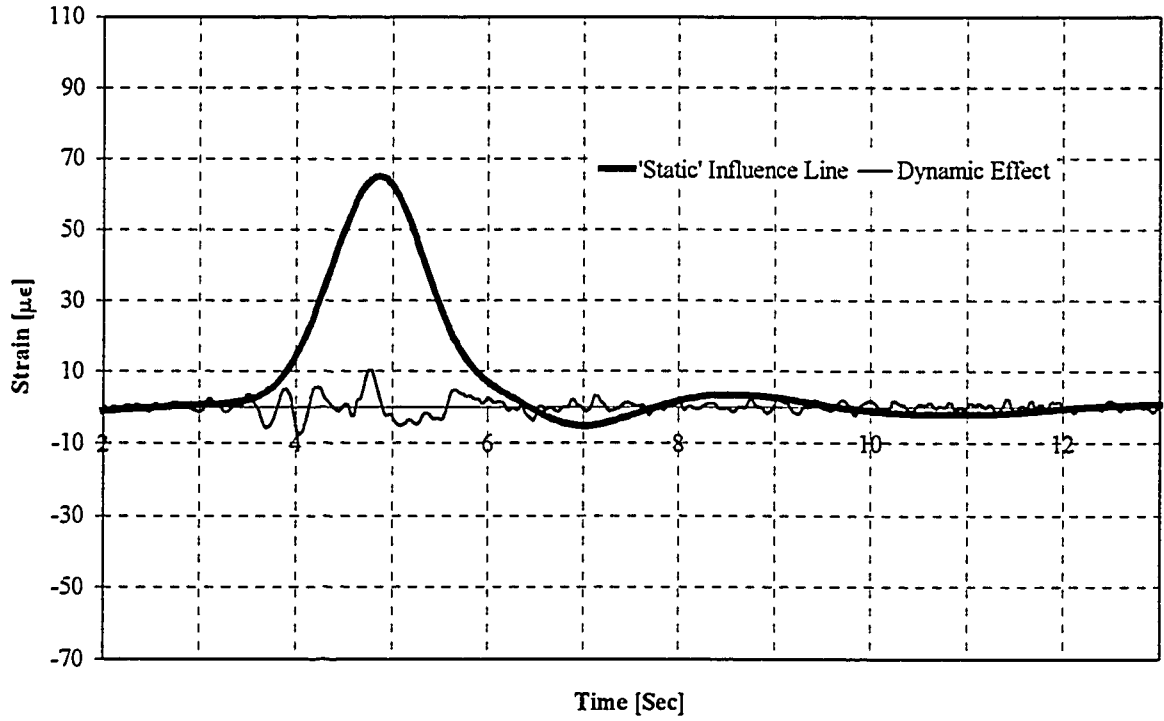


Figure B75: 55 km/hr Test, August '98 for Gauge #6 After Corrected for Drifts

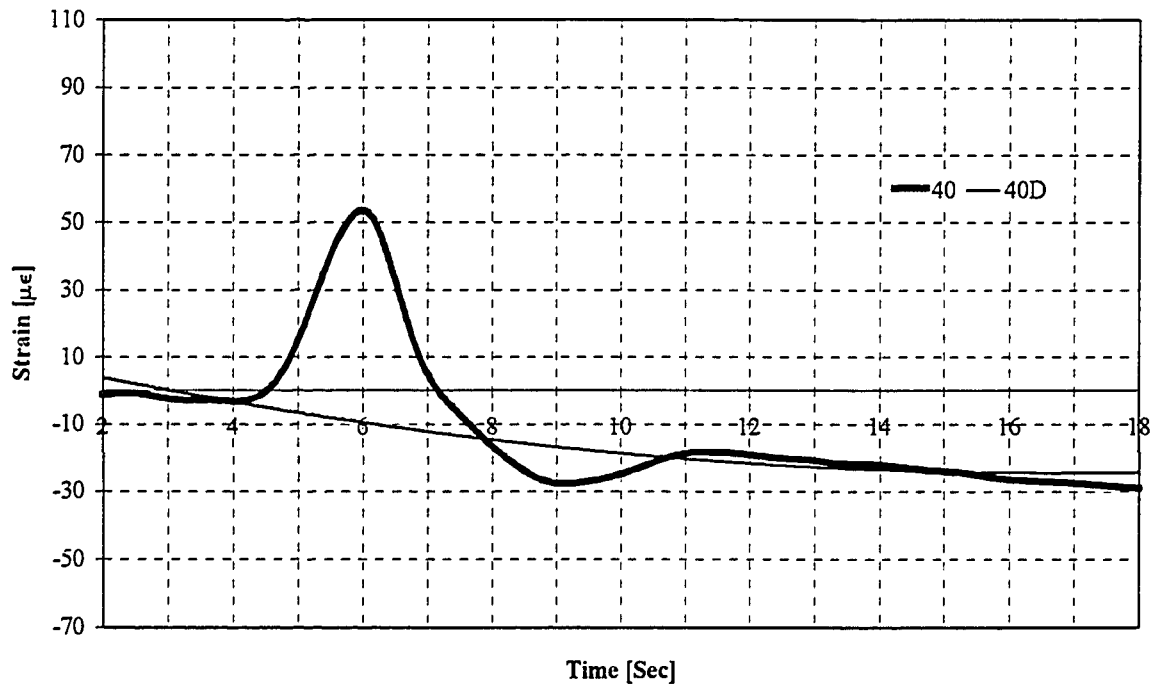


Figure B76: 40 km/hr Test, August '98 for Gauge #6 Before Corrected for Drifts

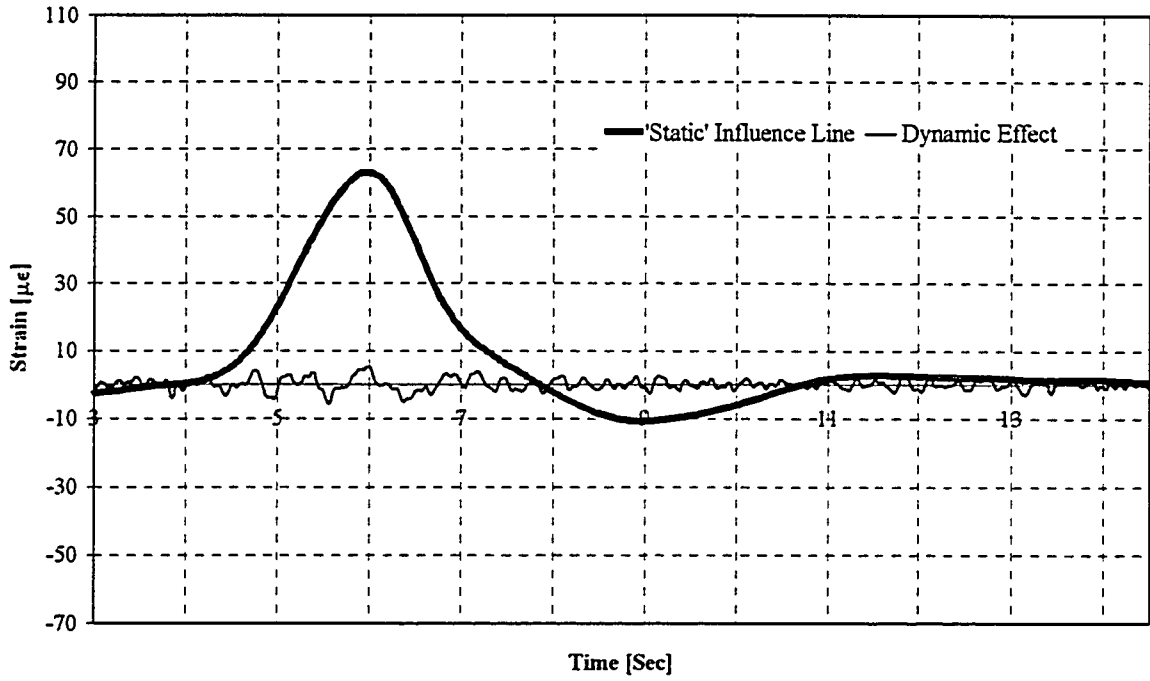


Figure B77: 40 km/hr Test, August '98 for Gauge #6 After Corrected for Drifts

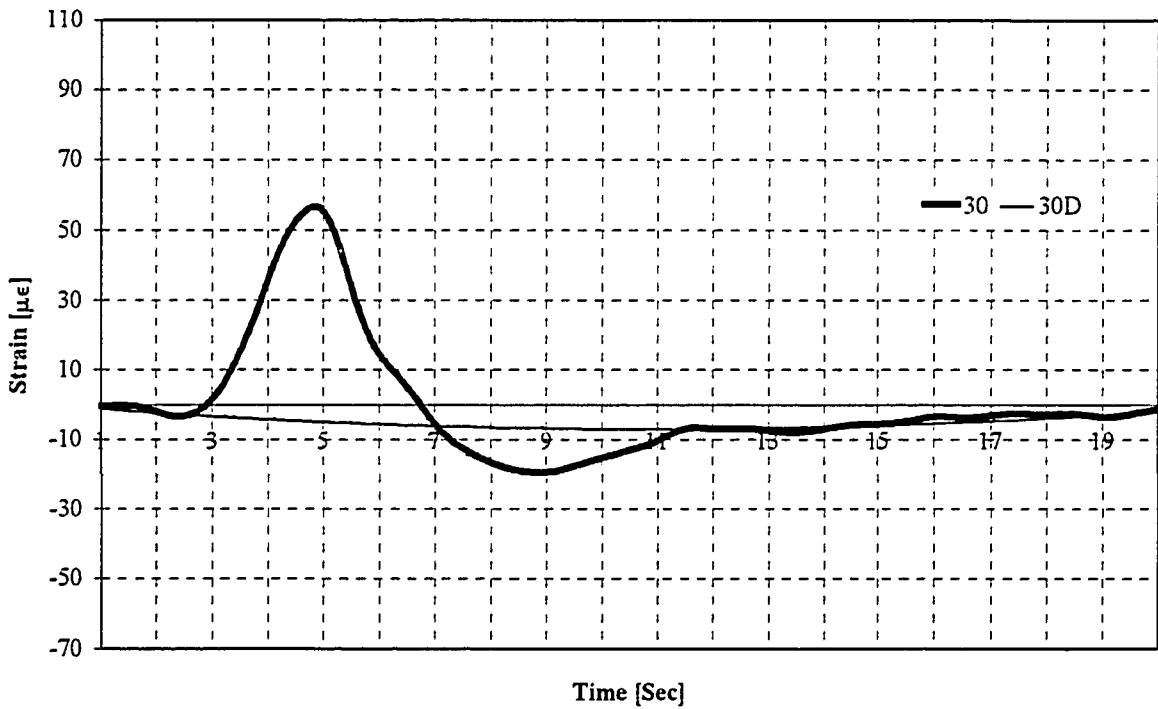


Figure B78: 30 km/hr Test, August '98 for Gauge #6 Before Corrected for Drifts

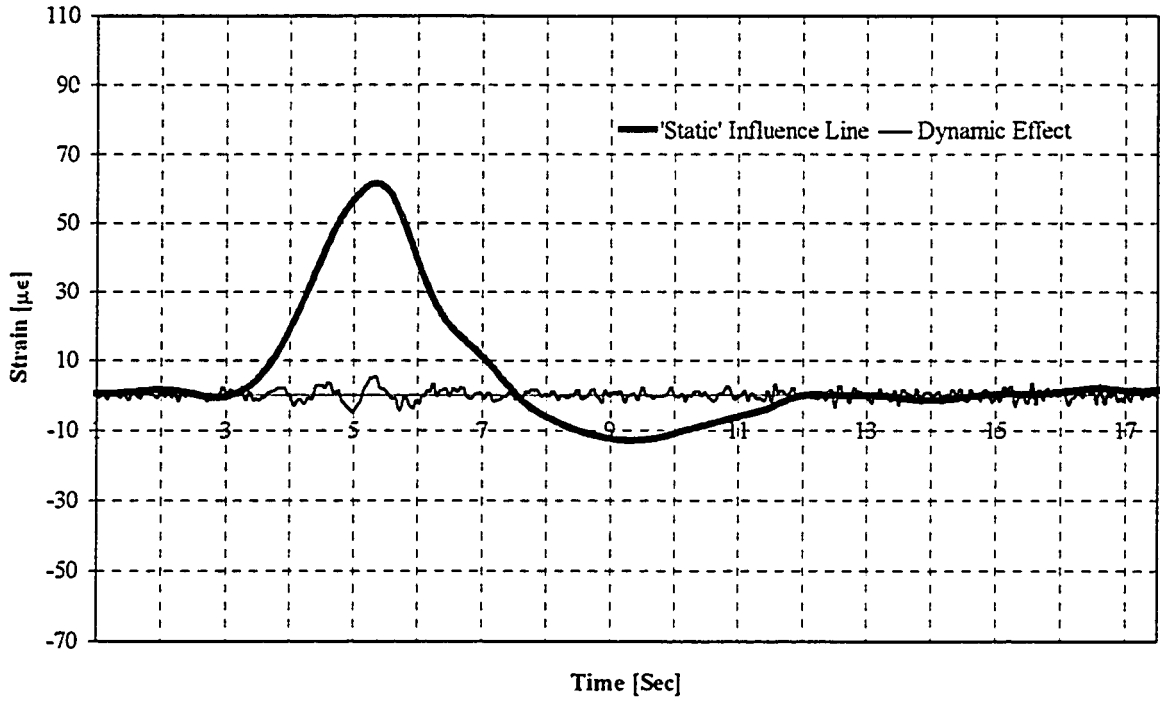


Figure B79: 30 km/hr Test, August '98 for Gauge #6 After Corrected for Drifts

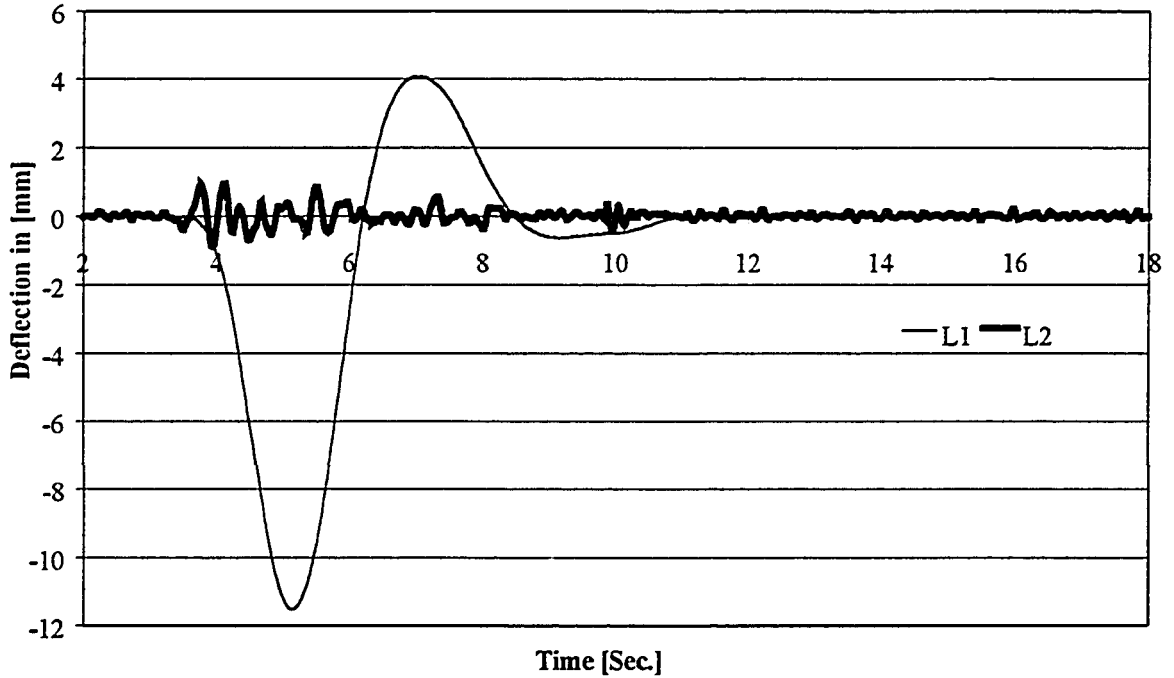


Figure B80: 55 km/hr Test, August '98 for Cable Transducer #1 Filtered Data Set 1

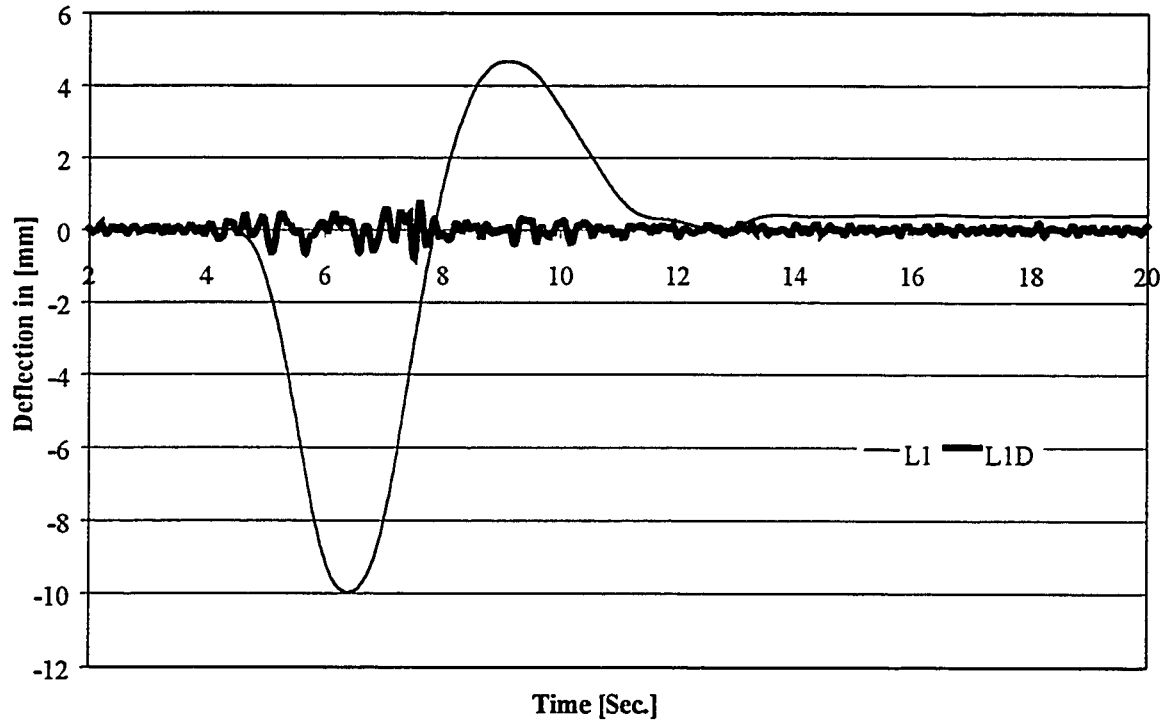


Figure B81: 40 km/hr Test, August '98 for Cable Transducer #1 Filtered Data Set 1

(Cable Transducers #1 on Girder #1 at Strap #13)

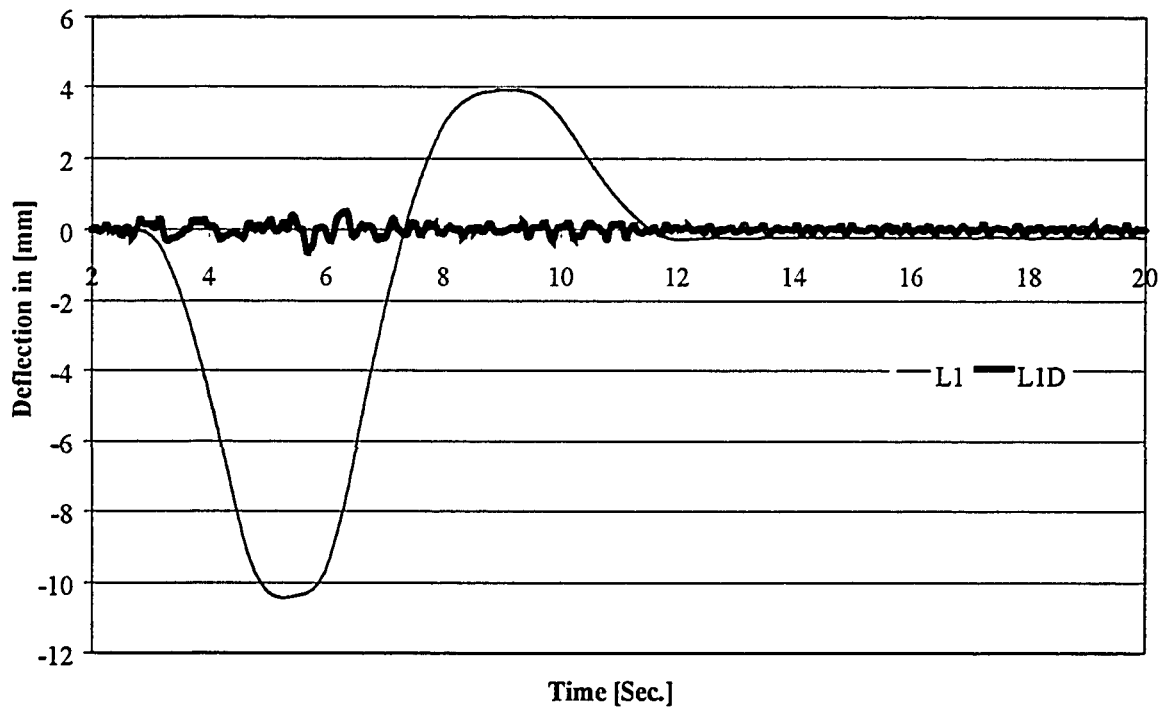


Figure B82: 30 km/hr Test, August '98 for Cable Transducer #1 Filtered Data Set 1

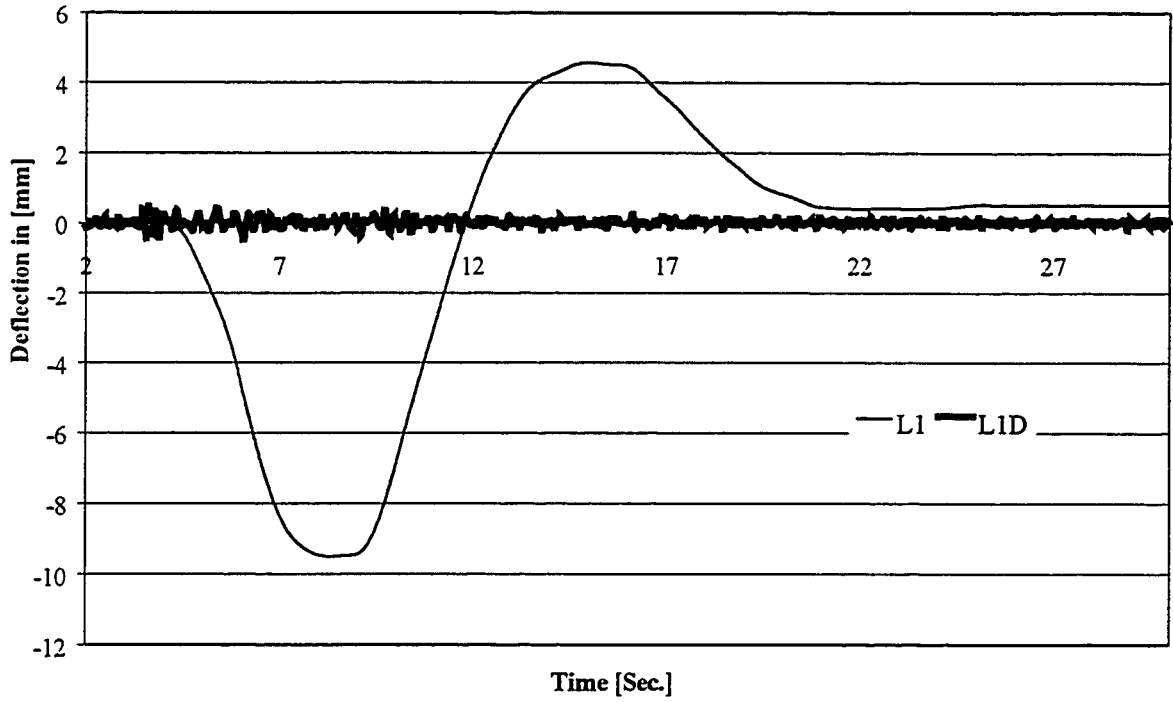


Figure B83: 15 km/hr Test, August '98 for Cable Transducer #1 Filtered Data Set 1

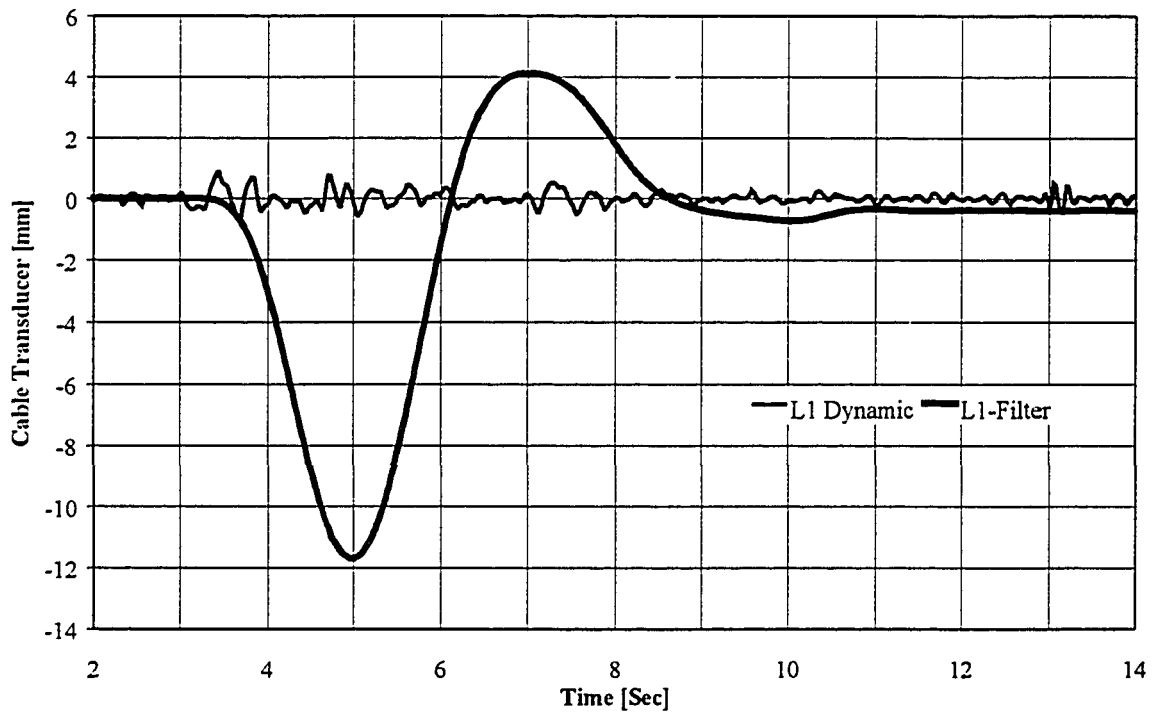


Figure B84: 55 km/hr Test, August '98 for Cable Transducer #1 Filtered Data Set 2

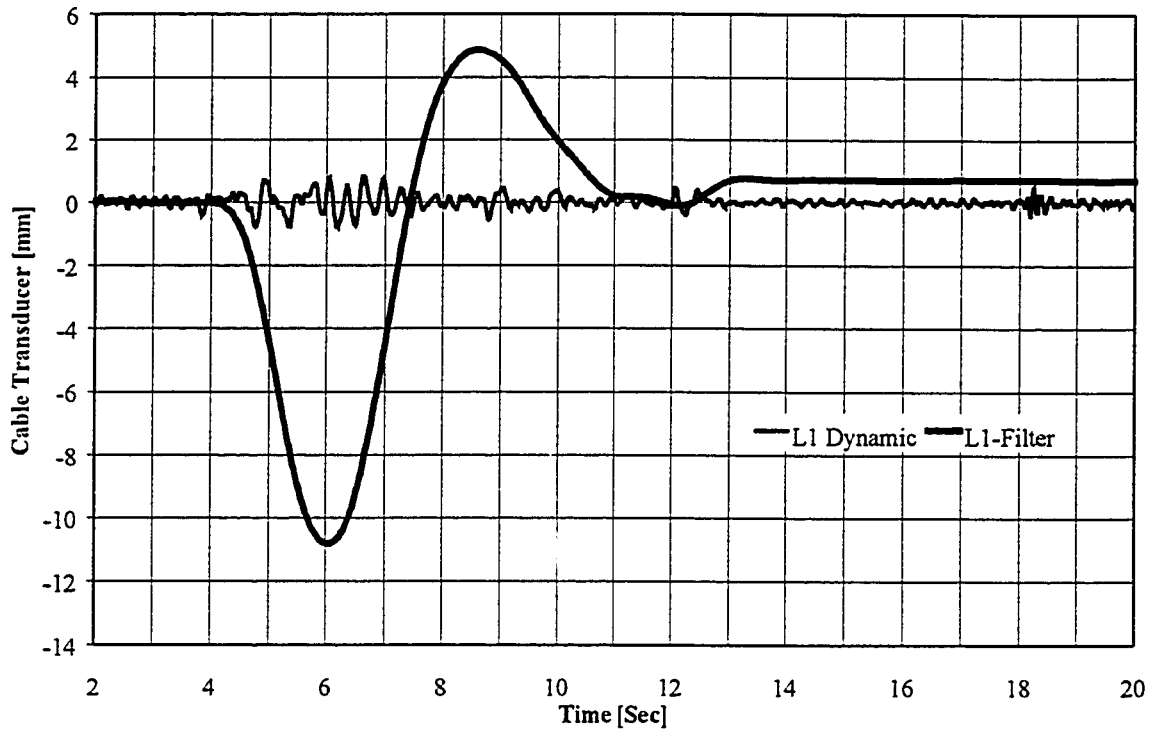


Figure B85: 40 km/hr Test, August '98 for Cable Transducer #1 Filtered Data Set 2

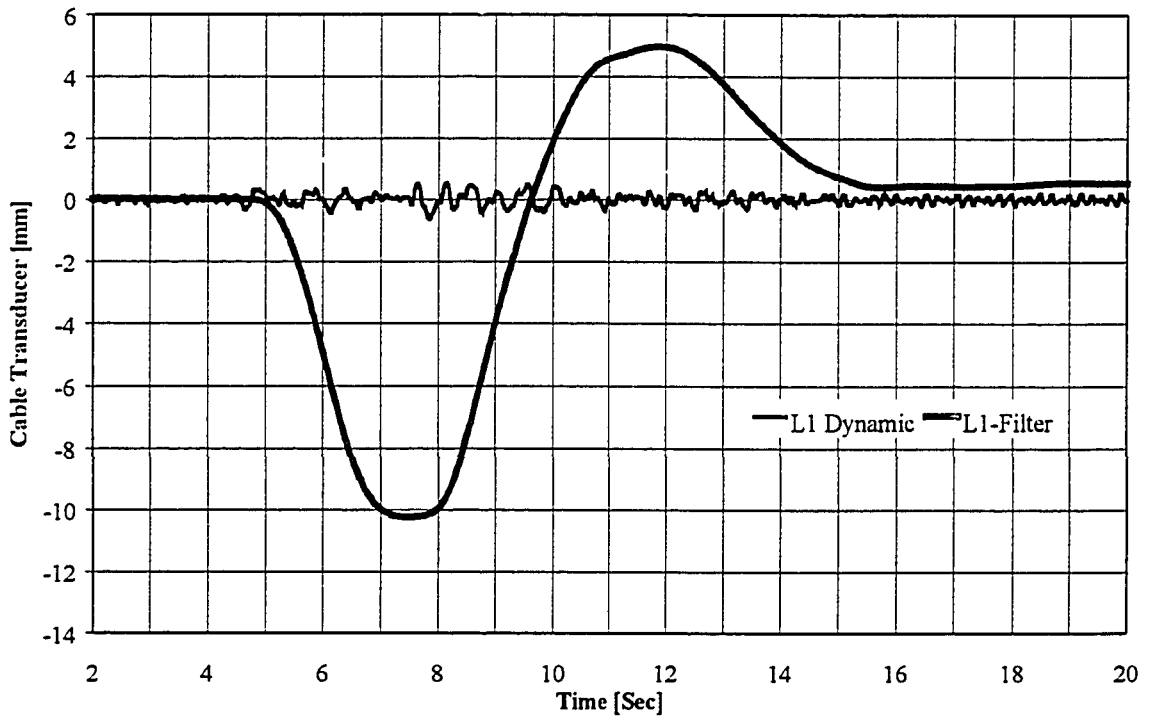


Figure B86: 30 km/hr Test, August '98 for Cable Transducer #1 Filtered Data Set 2

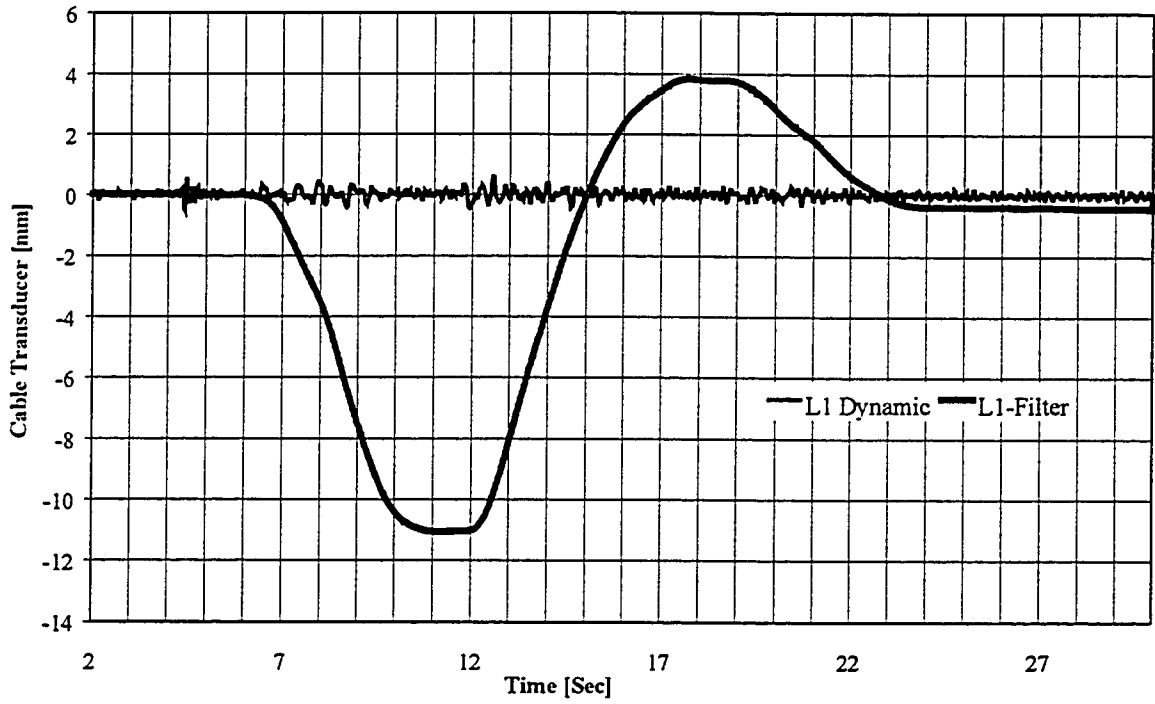


Figure B87: 15 km/hr Test, August '98 for Cable Transducer #1 Filtered Data Set 2

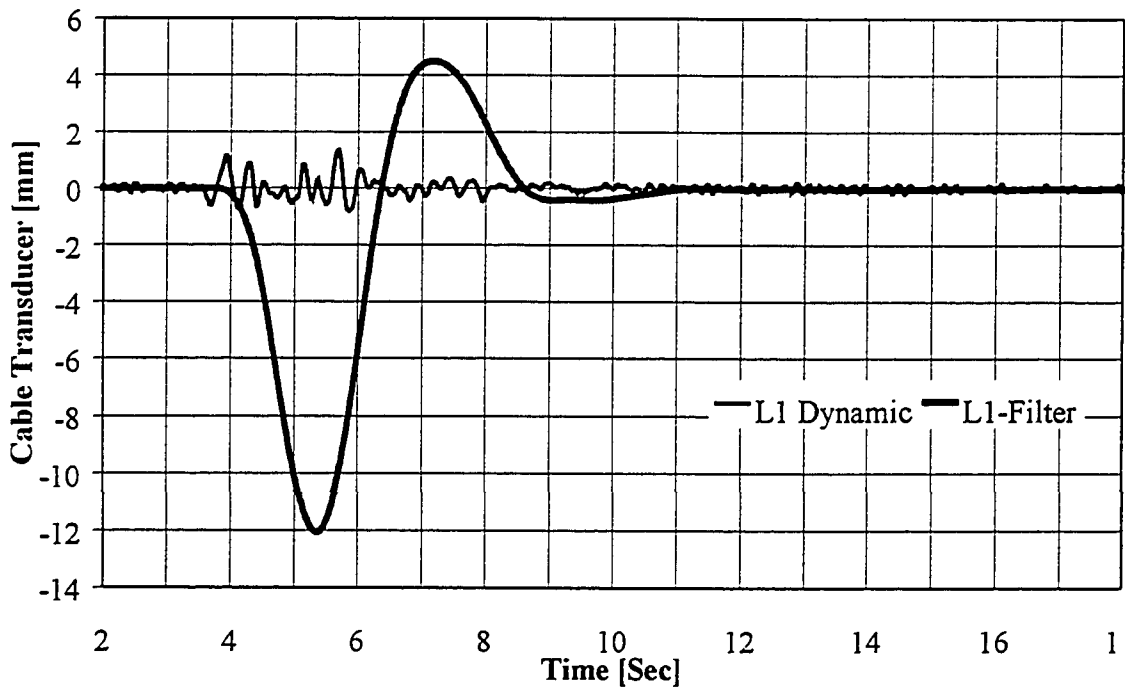


Figure B88: 55 km/hr Test, August '98 for Cable Transducer #1 Filtered Data Set 3

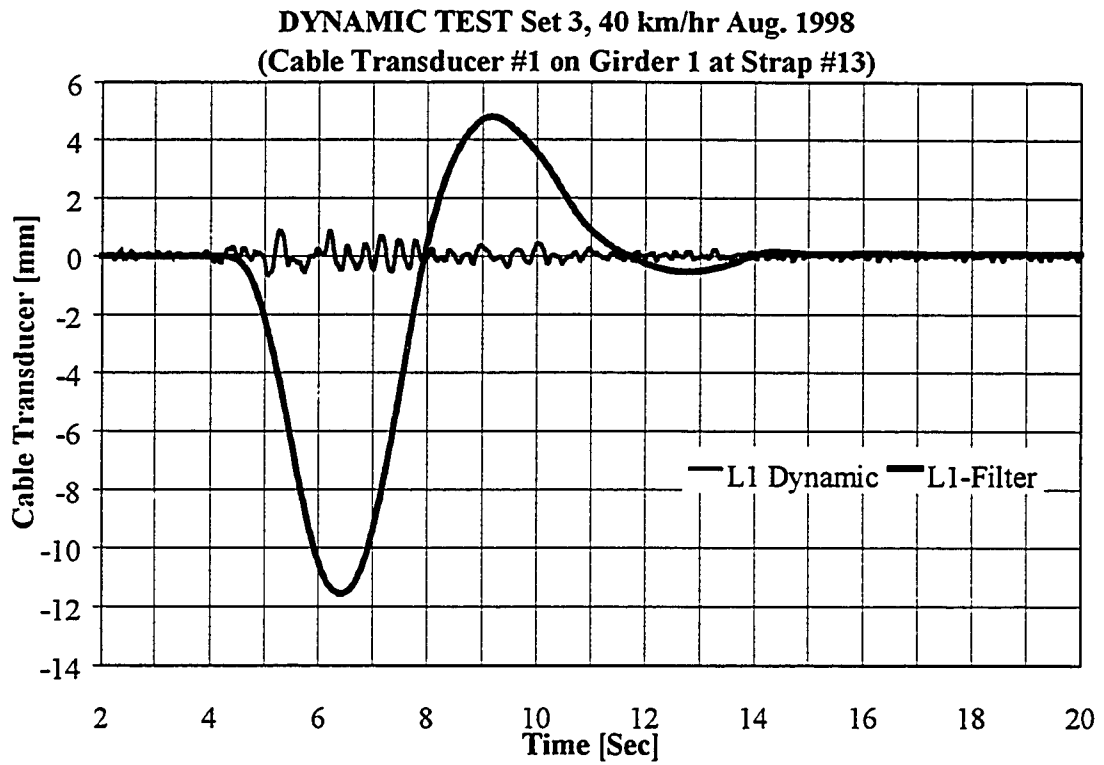


Figure B89: 40 km/hr Test, August '98 for Cable Transducer #1 Filtered Data Set 3

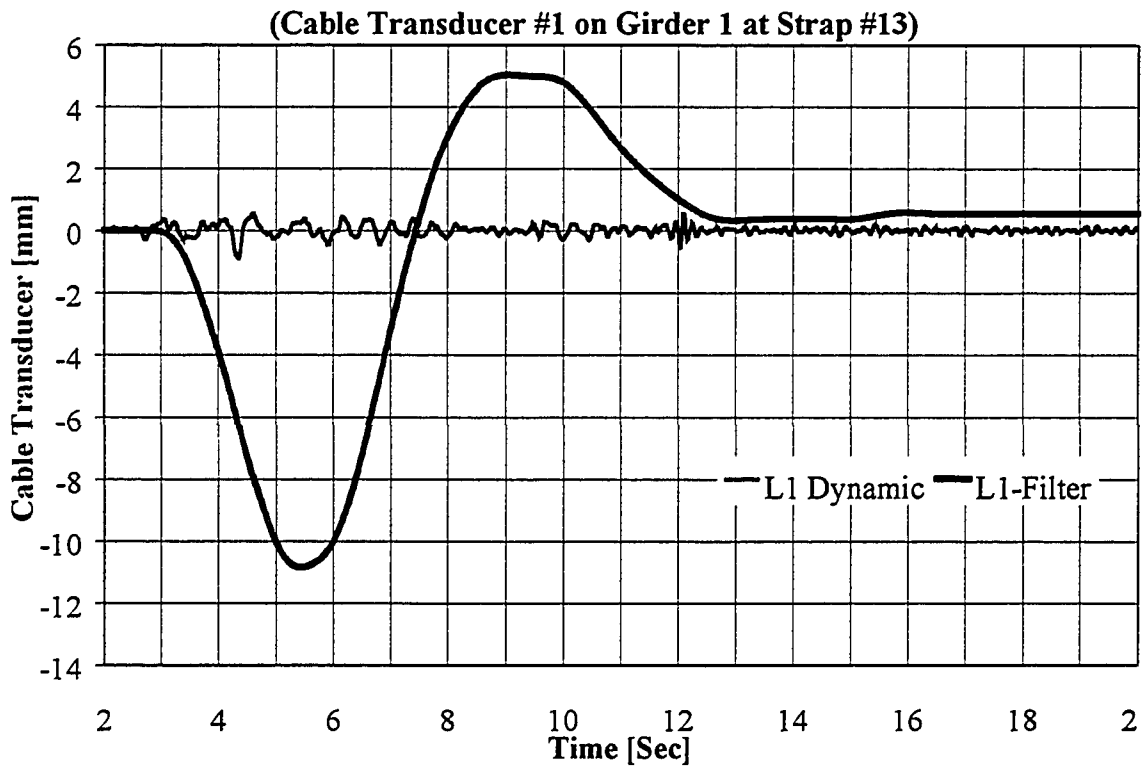


Figure B90: 30 km/hr Test, August '98 for Cable Transducer #1 Filtered Data Set 3

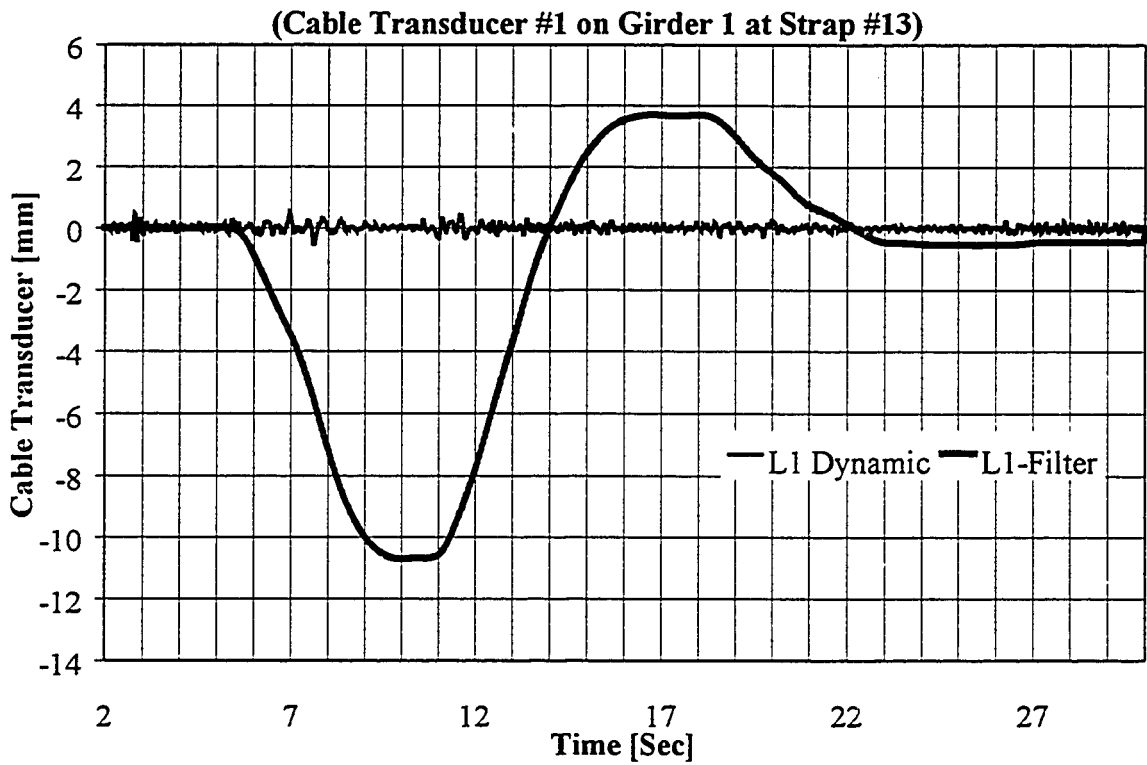


Figure B91: 15 km/hr Test, August '98 for Cable Transducer #1 Filtered Data Set 3

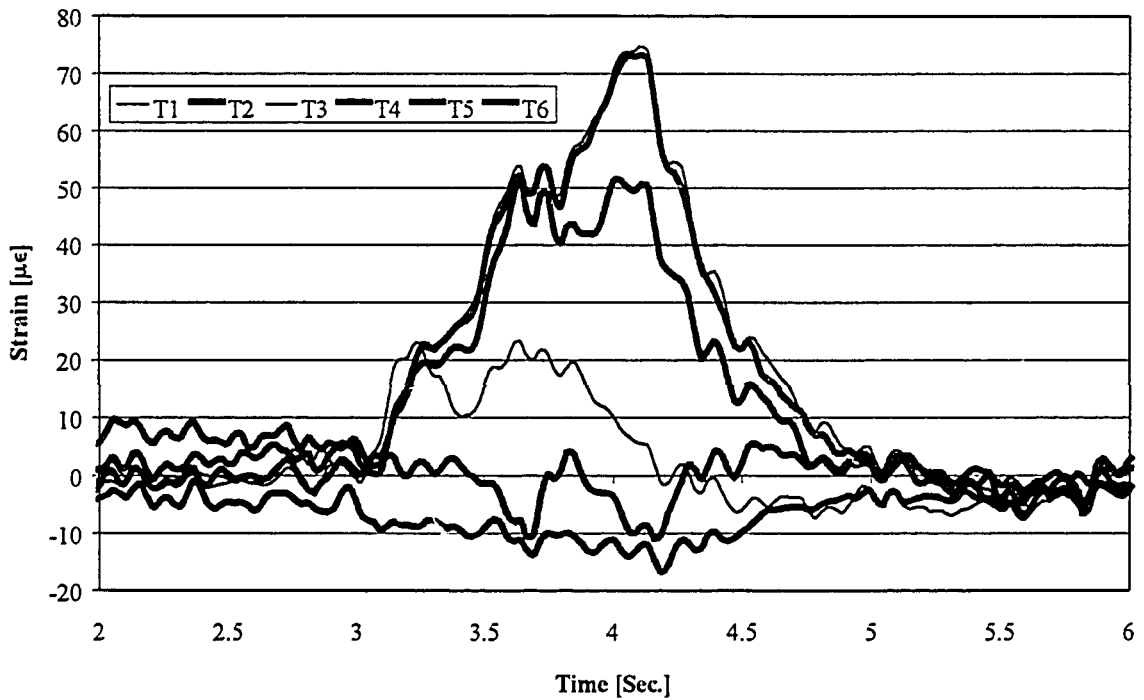


Figure B92: 55 km/hr Test, August '98 for Strain on One Steel Straps, Set 2

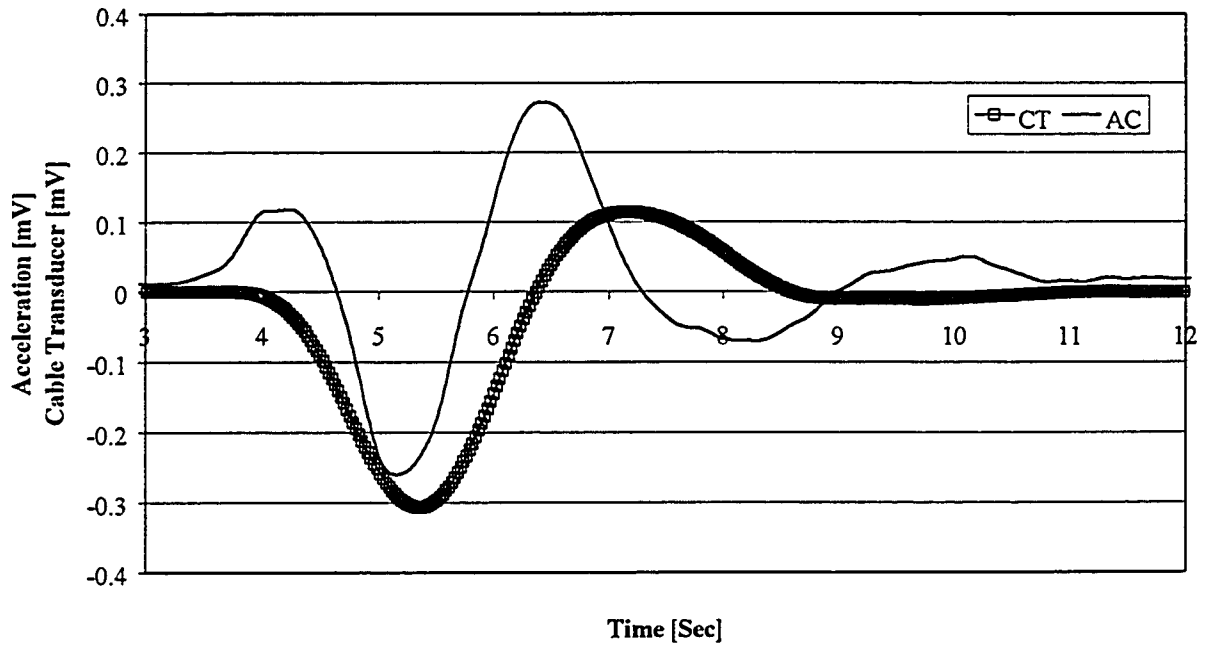


Figure B93: 55 km/hr Test, August '98 for Cable Transducer #1 and Accelerometer #8
 Filtered Data Set 3 for a Low Pass Filtered of 0.8 Hz.

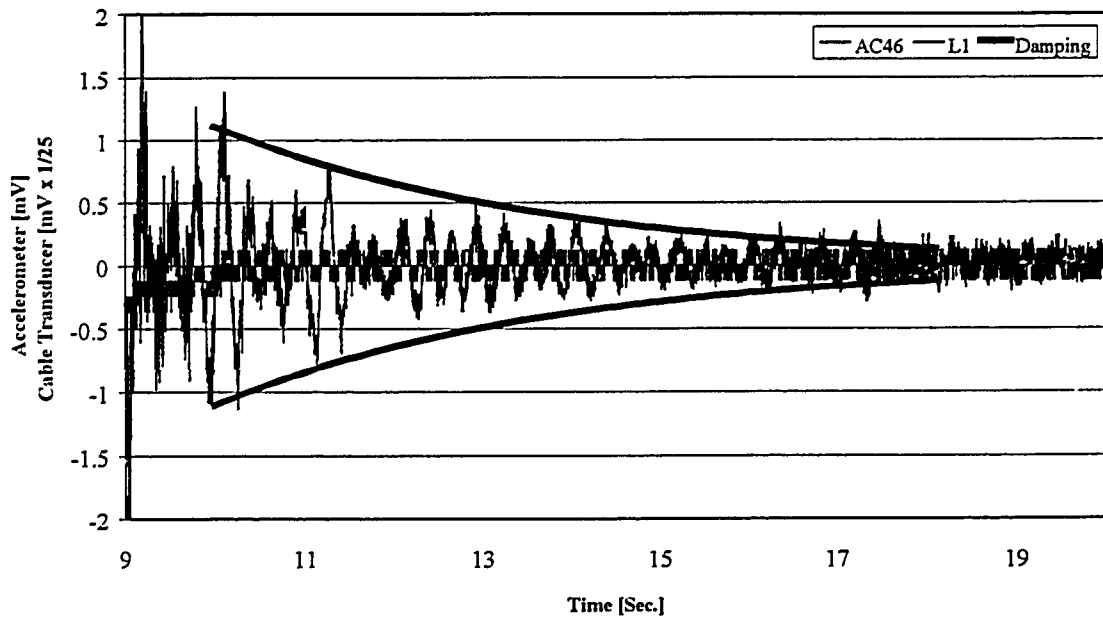


Figure B94: Damping Cure for Free Vibration Phase in Test Set 3

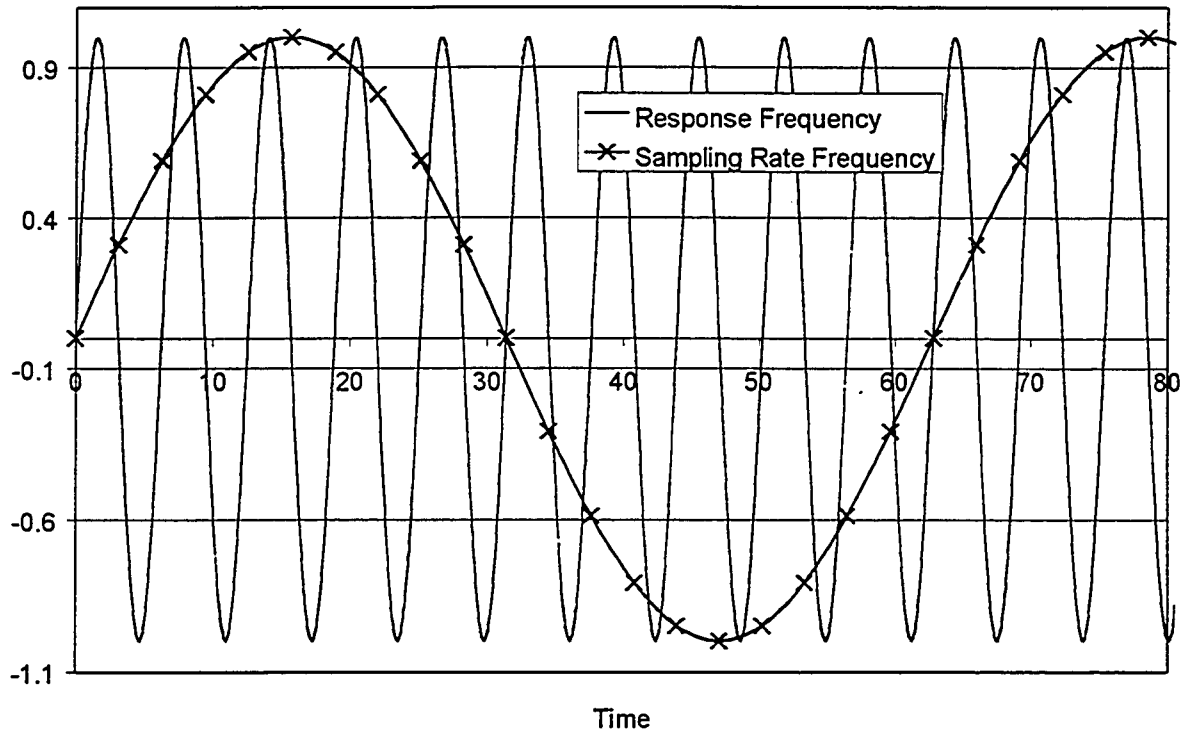


Figure B95: Potential Aliasing Error